

DISS. ETH NO. 17105

**2-D FINITE-DIFFERENCE TIME-DOMAIN  
FULL-WAVEFORM INVERSION  
OF CROSSHOLE GEORADAR DATA**

A dissertation submitted to the  
SWISS FEDERAL INSTITUTE OF TECHNOLOGY ZURICH  
for the degree of

Doctor of Natural Sciences

presented by  
**JACQUES ROBERT ERNST**

Dipl. Natw. ETH (M.Sc.)  
Swiss Federal Institute of Technology, Switzerland  
born January 10, 1973  
citizen of Switzerland

accepted on the recommendation of

Prof. Dr. Alan G. Green, examiner  
Prof. Dr. Hansruedi Maurer, co-examiner  
Prof. Dr. Klaus Holliger, co-examiner  
Prof. Dr. Gerhard Pratt, co-examiner

(2007)



For my parents  
Betty and Robert  
and my sister  
Bettina



# CONTENTS

<b>ZUSAMMENFASSUNG</b>	<b>vii</b>
<b>ABSTRACT</b>	<b>xi</b>
<b>CHAPTER 1: INTRODUCTION</b>	<b>1</b>
1.1. History of radar.....	1
1.1.1. General.....	1
1.1.2. Early radar applications in the earth sciences.....	3
1.2. Georadar a modern technique for subsurface probing .....	3
1.2.1. Numerical modeling of GPR data .....	6
1.2.2. Practical aspects of GPR data acquisition .....	8
1.2.3. Processing and inversion of GPR data .....	9
1.2.3.1. Reflection processing.....	9
1.2.3.2. Deterministic algorithms: Inversion of transmission GPR data .....	9
1.2.3.3. Non-deterministic algorithms: Stochastic evaluation of GPR data ...	11
1.2.4. Advantages and problems associated with the GPR method .....	11
1.3. Goals of this thesis.....	12
<b>CHAPTER 2: REALISTIC FDTD MODELING OF BOREHOLE GEORADAR ANTENNA RADIATION: METHODOLOGY AND APPLI- CATION</b>	<b>15</b>
2.1. Abstract.....	16
2.2. Introduction .....	16
2.3. Methodology.....	17
2.4. Application to air- and water-filled boreholes.....	21
2.4.1. Antenna in a homogeneous half-space .....	22
2.4.2. Antennae in an air-filled borehole .....	23
2.4.3. Antennae in a water-filled borehole .....	23

2.5. Case studies .....	24
2.5.1. Grimsel Rock Laboratory .....	24
2.5.2. Boise Hydrogeophysical Site.....	27
2.6. Conclusions .....	29
Appendix 2.A. UPML absorbing boundaries for cylindrical coordinate systems .....	31
Appendix 2.B. Results of benchmarks .....	34
2.B-1. Influence of the grid-refinement .....	35
2.B-2. Influence of the UPML absorbing boundaries .....	36
2.B-3. Overall validity of the simulation tool .....	36

**CHAPTER 3: FULL-WAVEFORM INVERSION OF CROSSHOLE RADAR  
DATA BASED ON 2-D FINITE-DIFFERENCE TIME-DOMAIN  
(FDTD) SOLUTIONS OF MAXWELL'S EQUATIONS** **39**

3.1. Abstract.....	40
3.2. Introduction .....	40
3.3. Methodology.....	44
3.3.1. Background.....	44
3.3.2. Forward problem .....	44
3.3.2.1. Differential form of Maxwell's equations.....	44
3.3.2.2. Integral form of Maxwell's equations .....	45
3.3.3. Inverse problem .....	46
3.3.3.1. Inversion strategy.....	47
3.3.3.2. Update directions $\gamma_{\hat{\epsilon}}$ and $\gamma_{\hat{\sigma}}$ .....	47
3.3.3.3. Update step lengths $\zeta_{\hat{\epsilon}}$ and $\zeta_{\hat{\sigma}}$ .....	49
3.3.4. Implementation.....	50
3.3.4.1. Stepped inversion for dielectric permittivity and electrical conductivity.....	50
3.3.4.2. Computational issues .....	51
3.4. Applications to synthetic data .....	53
3.4.1. Numerical experiment 1: Single dielectric object in a homogeneous medium .....	55
3.4.2. Numerical experiment 2: Single conductive object in a homogeneous medium .....	56

3.4.3. Numerical experiment 3: Two dielectric-conductive objects in a homogeneous medium .....	58
3.4.4. Numerical experiments 4 - 6: Layered models with and without stochastic variations .....	60
3.4.5. Numerical experiments 7 - 9: Layered models with and without stochastic variations and anthropogenic features .....	62
3.5. Conclusions .....	65

**CHAPTER 4: APPLICATION OF A NEW 2-D TIME-DOMAIN FULL-WAVEFORM INVERSION SCHEME TO CROSSHOLE RADAR DATA** **71**

4.1. Abstract.....	72
4.2. Introduction .....	72
4.3. Full-waveform inversion .....	74
4.4. Application to realistic synthetic data .....	76
4.4.1. Synthetic experiment I: Determining the source wavelet and distributions of $\varepsilon$ and $\sigma$ from true 2-D synthetic data.....	77
4.4.2. Synthetic experiment II: Determining the source wavelet and distributions of $\varepsilon$ and $\sigma$ from pseudo-3-D synthetic data .....	80
4.5. Case study I - Grimsel Rock Laboratory .....	81
4.5.1. Data acquisition .....	81
4.5.2. Data processing, inversions and source-wavelet estimates .....	81
4.5.3. Comparison of radar and seismic P-wave velocity crosshole tomograms .....	84
4.5.4. Interpretation .....	84
4.6. Case study II - Boise Hydrogeophysical Research Site .....	85
4.6.1. Data acquisition .....	85
4.6.2. Data processing, inversions and source-wavelet estimates .....	86
4.6.3. Interpretation .....	86
4.7. Conclusions .....	88
Appendix 4.A. Accounting for 3-D effects.....	90
Appendix 4.B. Source wavelet estimation.....	92
4.B.1. First-arrival pulse method .....	92
4.B.2. Deconvolution method .....	92
4.B.3. Sensitivity of the tomograms to errors in the source wavelet .....	94

<b>CHAPTER 5: CONCLUSIONS AND OUTLOOK</b>	<b>95</b>
5.1. Realistic borehole georadar simulation tool .....	95
5.2. Full-waveform inversion tool .....	96
5.3. Remarks and problems associated with full-waveform inversion in the time-domain .....	98
5.4. Application of the modified georadar waveform inversion scheme to seismic data .....	99
5.5. Frequency-dependent media parameters .....	100
5.6. Future developments and applications .....	100
<b>APPENDIX A: TESTS OF THE 3-D TO 2-D DATA TRANSFORMATION SCHEME</b>	<b>105</b>
A.1. Test 1: Homogeneous media .....	106
A.2. Test 2: Stochastic media with deterministic anomalies.....	107
A.3. Conclusion.....	108
<b>APPENDIX B: REALISTIC MODELING OF BOREHOLE GEORADAR ANTENNA RADIATION</b>	<b>111</b>
B.1. Summary.....	111
B.2. Introduction .....	112
B.3. Modeling approach.....	112
B.4. Validation and application of the algorithm.....	114
B.5. Conclusions .....	117
<b>APPENDIX C: FDTD MODELING OF BOREHOLE GEORADAR DATA</b>	<b>119</b>
C.1. Abstract.....	119
C.2. Introduction .....	120
C.3. Methodology.....	120
C.4. Validation and application of the algorithm.....	122
C.5. Conclusions .....	126



<b>APPENDIX D: FULL-WAVEFORM INVERSION OF CROSSHOLE GEO-</b>	
<b>RADAR DATA</b>	<b>129</b>
D.1. Summary.....	129
D.2. Introduction .....	129
D.3. Methodology.....	130
D.4. Results .....	132
D.5. Conclusions .....	136
<b>BIBLIOGRAPHY</b>	<b>137</b>
<b>CURRICULUM VITAE</b>	<b>151</b>
<b>ACKNOWLEDGMENTS</b>	<b>153</b>



# ZUSAMMENFASSUNG

Bohrloch-Georadar ist mittlerweile eine geophysikalischen Methoden, welche immer häufiger bei der Erkundung des oberflächennahen Untergrundes angewendet wird. Eine typische „Crosshole“-Messanordnung besteht aus zwei Antennen, wobei der Sender im einen Bohrloch und der Empfänger im anderen platziert wird. Die Abstrahlcharakteristik von solchen Antennen ist im Allgemeinen mit jener von analytischen Dipolen vergleichbar. Die im Sender erzeugte elektromagnetische Welle kann durch die Zentral- oder Nominalfrequenz charakterisiert werden und liegt üblicherweise im Bereich von  $\sim 20$  und  $\sim 250$  MHz. Dieser Frequenzbereich entspricht im zu erkundenden Untergrund in etwa Wellenlängen zwischen  $\sim 5$  und  $\sim 0.4$  m. Auf Grund der komplexen Vorgänge die stattfinden, wenn eine elektromagnetische Welle in der Antenne erzeugt und anschliessend ins benachbarte Medium abgestrahlt wird, bietet es sich an, diese Effekte genau zu untersuchen, bevor man sich an die eigentliche Wellenfeldinversion wagt. Dementsprechend habe ich als Erstes ein Tool entwickelt, welches mir erlaubt, die Abstrahlcharakteristik von beliebig komplexen Bohrloch-Antennen zu studieren. Dieses Tool verwendet eine Finite-Differenzen-Approximation der Maxwell-Gleichungen im Zeitbereich (Finite-Differenzen Time-Domain = FDTD), um die elektromagnetische Wellenausbreitung in einem beliebigen Medium zu simulieren. Die Approximationen werden in einem Gitter berechnet, das auf einem zylindersymmetrischen Koordinatensystem beruht. Dieses Koordinatensystem bietet den Vorteil, dass die Energieabstrahlung der Senderantenne eine korrekte 3-D-Charakteristik aufweist, dabei aber nur ein 2-D-Medium benötigt. Eine lokale Gitterverfeinerungstechnik erlaubt eine Untersuchung von sehr kleinen Antennenstrukturen, realistischen Bohrlöchern und Materialien mit hohen Dielektrizitätszahlen (z.B. Wasser). Numerische Experimente zur Untersuchung unterschiedlicher Antennen und deren Energieabstrahlungen in luft- und wassergefüllten Bohrlöchern haben gezeigt, dass die Abstrahlcharakteristik von Wu-King-Antennen mit finiter Länge in etwa jener von infinitesimalen Dipole-Antennen entspricht. Dies ist insofern ein wichtiges Resultat, als dass die infinitesimalen Dipole oft als Approximationen für reale Antennen verwendet werden (z.B. bei Strahlinversionen). Werden dagegen Antennen in wassergefüllten Bohrlöchern zum Vergleich hinzugezogen, so habe ich festgestellt, dass sich die Abstrahlcharakteristik deutlich verändert. Untersuchungen mit realen Daten, gemessen in trockenem Gestein (Grimsel-Felslabor, Schweiz) und in

wassergesättigten Sedimenten (Hydrogeophysikalisches Untersuchungsgebiet, Boise, USA) zeigen, dass bei numerischen Simulationen mit realistischen Wu-King-Antennen und finiten Bohrlöchern die synthetischen Daten deutlich besser mit den beobachteten übereinstimmen, als wenn nur infinitesimale Dipol-Antennen verwendet werden.

Tomographische Inversionen von „Crosshole“-Georadardaten werden üblicherweise mit strahlenbasierten Verfahren berechnet. Diese Verfahren berücksichtigen jedoch nur einen sehr geringen Anteil vom Nutzsignal (z.B. Ersteinsatzeiten und Maximalamplituden vom ersten Wellenzug), wodurch die resultierenden Geschwindigkeits- und Dämpfungs-Tomogramme nur die relativ groben Eigenheiten des Untergrundes zeigen. Bezieht man allerdings einen Grossteil des Wellenfeldes oder sogar das gesamte aufgezeichnete Feld mit in eine entsprechende Inversion ein, so darf angenommen werden, dass die entsprechende Auflösung der resultierenden Tomogramme um bis zu einer Grössenordnung besser sein kann. Solche Auflösungen sind üblicherweise nur mit teuren und sehr lokalen 1-D-Messungen möglich (z.B. Bohrkernmessungen und Direct-Push-Techniken). Trotz des grossen Potentials von Vollwellenfeldinversionen, angewendet auf Georadardaten, gibt es nur sehr wenige entsprechende Veröffentlichungen. Im Gegensatz dazu sind seismische Vollwellenfeldinversionen weit verbreitet. Der Modellierungsteil solcher Inversionen basiert häufig auf FDTD-Approximationen der Wellengleichungen und berücksichtigt automatisch alle möglichen Wellenausbreitungsphänomene (z.B. diffraktierte und gestreute Wellen).

In dieser Dissertation stelle ich eine Vollwellenfeldinversion für „Crosshole“-Georadardaten vor. Die Inversion basiert auf der FDTD-Approximation der Maxwell-Gleichungen in einem 2-D-Kartesischen Koordinatensystem. Diese Wahl, anstelle eines zylindrischen Systems, lässt sich mit der grösseren Flexibilität im Bezug auf die Positionierung von Sendern und Empfängern begründen. Ferner erlaubt ein kartesisches System das Einbinden von sehr effizienten „Generalized Perfectly Matched Layer“ (GPML) absorbierenden Rändern. Das Ziel meines Wellenfeldinversionsalgorithmus ist die detaillierte Rekonstruktion der dielektrischen Permittivität und der elektrischen Leitfähigkeit. Numerische Experimente unter Einbezug von relativ einfachen homogenen Modellen mit einzelnen Anomalien zeigen, dass meine Wellenfeldinversion in der Lage ist, auch sehr kleinen Anomalien zu lokalisieren und deren Form und die Grössenordnung der Materialparameter gut zu rekonstruieren. Verwende ich allerdings kompliziertere Modelle mit stochastischen Verteilungen der Mediumparametern und einzelnen deterministische

Anomalien, so stellt sich heraus, dass diese Anomalien in den Permittivitätstomogrammen nur unwesentlich besser dargestellt werden können, verglichen mit den strahlenbasierten Inversionsresultaten. Dagegen werden die entsprechenden Leitfähigkeitsanomalien mittels der Wellenfeldinversion deutlich besser aufgelöst. Neben diesen relativ einfachen numerischen 2-D-Beispielen habe ich auch 3-D-Experimente durchgeführt. Dabei habe ich zuerst ein Transformationsschema hergeleitet, welches mir die 3-D-Daten zu 2-D-Daten umwandelt. Im Allgemeinen ist das Quellsignal, welches das Aussenden elektromagnetischer Wellen in den Untergrund initiiert, unbekannt und muss entsprechend ermittelt werden. Um dieses Quellsignal zu bestimmen, habe ich ein Tool entwickelt, das auf dem Prinzip der Dekonvolution aufbaut. Dieselben Felddaten, welche ich bereits für die erste Studie über die Abstrahlcharakteristik typischer Antennen verwendet habe, sind für die Vollwellenfeldinversion eingesetzt worden. Dabei stellt man fest, dass die resultierenden Tomogramme, verglichen mit jenen von strahlenbasierten Inversionen, deutlich mehr Details zeigen und die Grenzen zwischen geologischen Einheiten und einzelnen Heterogenitäten klar abbilden. Diese Untersuchungen mit realen Daten zeigen deutlich, dass die Vollwellenfeldinversion gute Resultate liefern kann, welche deutlich mehr Informationen über den untersuchten Untergrund enthalten.



# ABSTRACT

Borehole georadar is an increasingly popular method for probing the shallow subsurface. A typical setup for a crosshole georadar experiment consists of an emitting dipole-type antenna located in a borehole and a corresponding receiver antenna located in a neighboring borehole. The nominal center frequencies of commonly used antennas range from  $\sim 20$  to  $\sim 250$  MHz, which correspond to dominant wavelengths of  $\sim 5$  to  $\sim 0.4$  m, in the subsurface. Prior to developing a full-waveform inversion algorithm it is therefore essential to improve our understanding of the complex electromagnetic wave propagation. To study the radiative properties of borehole georadar antenna systems, I developed a modeling tool based on finite-difference time-domain (FDTD) solutions of Maxwell's equations in cylindrical coordinates. To minimize reflections from the model boundaries, efficient uniaxial perfectly matched layer (UPLM) absorbing boundary conditions are implemented along the top, bottom and right model edges and symmetrical conditions along the cylindrical axis. Using an accurate local refinement technique allows to account for the detailed aspects of borehole radar systems, slim boreholes and materials with very high permittivities (e.g., water). Numerical experiments were conducted to benchmark the modeling tool and to analyze different antenna geometries. Results of these studies reveal that radiation characteristics of finite length Wu-King-type antennas correspond well with typically employed dipole-type approximations as long as they are placed in same environments. In contrast, substantial differences in the radiation characteristics are found when placing antennas in water-filled boreholes. I further studied effects of antennas placed in air- or water-filled boreholes on two real data sets acquired in dry crystalline rock (Grimsel Rock Laboratory in Switzerland) and in water-saturated sediments (Boise Hydrogeophysical Research Site in the USA). Both experiments using realistic transmitter antennas provide better agreements between observed and modeled data than simulations based on infinitesimal dipole transmitters and receivers.

Tomographic inversions of crosshole georadar data have typically been based on ray methods, which typically consider only a very limited portion of the recorded georadar signal, namely the onset time of the first arriving wave trains and the peak amplitudes of the first cycles. The inversion of these data allows the determination of the electromagnetic velocity and attenuation structures of the probed regions, which then can be used to derive dielectric

permittivity and electrical conductivity distributions. As a consequence of using only a limited portion of the recorded data, these methods suffer from a number of inherent limitations. In particular, they can only resolve structures that are relatively large and smooth with respect to the dominant wavelength of the signal. By considering however waveforms of recorded georadar signals and correctly accounting for wave propagation effects in the inversion process, it can therefore be expected to improve the resolution by nearly an order-of-magnitude. The expected sub-meter resolution is comparable to that of expensive and inherently 1-D borehole-based studies (e.g., geophysical logging, core sampling and direct-push techniques). However, full-waveform inversion approaches applied to georadar data are almost unknown so far. In contrast, waveform inversion strategies for seismic data have been available for almost two decades. Many seismic waveform inversion schemes are based on finite-difference solutions of the wave equation. These forward modeling schemes are accurate, can accommodate strongly heterogeneous media and automatically include all wave types of the considered wave propagation regime, such as diffracted or multiply scattered waves.

In my thesis, I present a full-waveform inversion scheme for crosshole georadar data based on FDTD solutions of Maxwell's equations in a 2-D Cartesian coordinate system. Using a Cartesian coordinate system rather than a cylindrical system offers more freedom with respect to placing transmitters and receivers in the model space and allows the implementation of highly accurate and fast generalized perfectly match layers as absorbing boundary conditions. My waveform inversion approach directly considers permittivity and conductivity distributions and has the potential to resolve not only the coarse but also the fine scale features of the probed subsurface. The scheme requires a stepped or cascaded inversion approach in which the first step consists of a permittivity inversion that mainly accounts for the phase information of the data, followed by a conductivity inversion, which focuses on the remaining amplitude information. Numerical experiments demonstrate that my 2-D inversion scheme is capable of adequately resolving, the locations, the shapes and the magnitudes of bodies with spatial extent considerably smaller than a dominant wavelength embedded in homogeneous background media. Similar good results are reported for band-limited Gaussian noise contaminated data. More realistic synthetic experiments consisting of layers and artificial objects (pipes and tunnels) embedded in stochastic background media suggested that dielectric permittivity distributions are only slightly improved compared to corresponding



ray-based results. Generally, the waveform inversion of the electrical conductivity clearly resolves more details of the artificial objects.

In order to invert field data, I developed a 3-D to 2-D transformation scheme that accurately corrects for (i) 3-D geometrical spreading, (ii) a  $\pi/4$  phase shift, and (iii) a frequency scaling effect of  $1/\sqrt{\omega}$ , where  $\omega$  is the angular frequency. The unknown source wavelets are estimated with a scheme that accounts for permittivity and conductivity medium parameter distributions together with deconvolutions of the observed data. The same field data sets are used as for the initial study of the radiation characteristics of different antenna types. The resolution of all full-waveform tomograms is shown to be significantly higher than that of the relevant ray tomograms. Boundaries between distinct geological features and small heterogeneities are sharply imaged in the full-waveform tomograms. These studies demonstrate that waveform inversion is feasible and yields markedly more information about the probed subsurface. It thus may provide key constraints on engineering parameters, such as water content, salinity, porosity, clay fraction or ore grade.



# CHAPTER 1

## INTRODUCTION

Radar (**radio detection and ranging**), a remote sensing technique based on the propagation of electromagnetic waves, is commonly used for air- and ship-traffic management and speed controls conducted by the police. Scientifically oriented applications of radar are found in meteorology (e.g., Brown et al., 1971; Fujita, 1981), the earth sciences (e.g., Gross et al., 2004; Leckebusch, 2005), criminology (e.g., Davenport et al., 1988; Ruffell and McKinley, 2005) and space exploration (e.g., Porcello et al., 1974). In the following, I begin by reviewing historical developments of radar with a special focus on the earth sciences and then describe relevant aspects of the antennas and geological media, insights gained from numerical simulations, acquisition geometries, various data processing and analysis tools, and the advantages and drawbacks of using ground-penetrating radar (GPR or georadar) as an investigation tool. In the final part of the chapter, I outline the goals of my thesis.

### 1.1. HISTORY OF RADAR

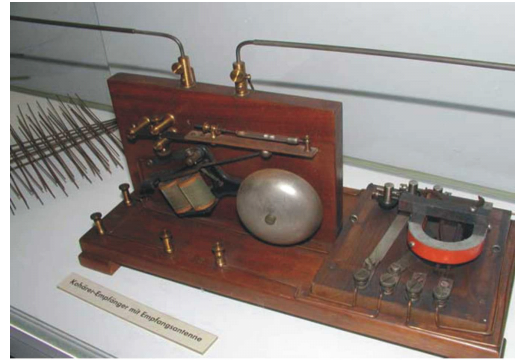
#### 1.1.1. GENERAL

The radar technique was developed, forgotten, and redeveloped several times during the last century. The first development was made in 1904 by the German Christian Hülsmeyer, who constructed a device based on Hertz's experiment (Hülsmeyer, 1904). Hülsmeyer's primary intention was to develop an apparatus for remotely detecting metal objects in the marine environment (e.g., ships and shipwrecks) in order to avoid accidents. The device was designed for non-military purposes. His initial radar system (Figure 1.1), which emitted a constant signal (i.e., non-pulsing, mono-frequency), was able to detect metal objects up to a distance of ~3 km. It was not possible to estimate the distance to the objects due to strong interference between the emitted and received signals (Hollmann, 2001; Coffey et al., 2005). Seven years later, Leimbach and Löwy (1911) filed a patent in Germany for the

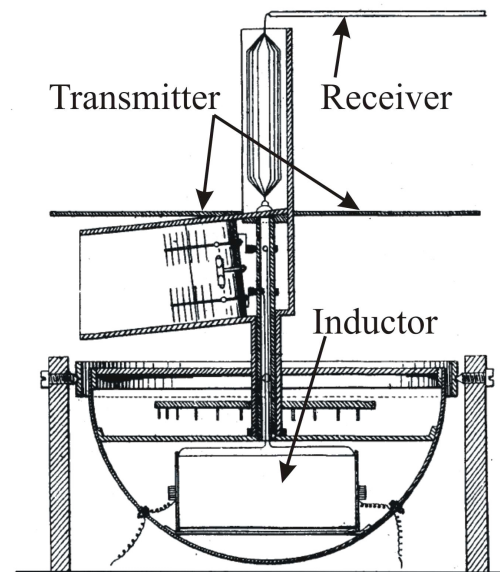
first GPR system that allowed buried metallic ore bodies to be detected. Their tests were based on constantly emitting and receiving antennas placed in 200 m deep neighboring boreholes. In the same year, a US science fiction writer introduced a device in his novels (the actinoscope) that was able to detect and measure the distance to metallic objects using pulsating electromagnetic waves (Gernsbacher, 1911).

Hülsmeier's original concept was essentially rediscovered in different countries during the early 1920's. The following list summarizes the different stages based on a comprehensive review by Bauer (2004):

- 1922 (United States): H. Taylor and L. Young conducted communication experiments across a river. They noticed strong variations in the signals when ships crossed the communication link and thus concluded that it might be possible to detect objects using electromagnetic waves (Brown, 1999).
- 1924 (Great Britain): Appleton and Barnett (1925a), (1925b) performed radio propagation experiments in which they investigated the reflection of electromagnetic waves from atmospheric layers.
- 1926 (Germany): Hülsenbeck & Co (1926) filed a patent for the first pulsed radar system. All previous systems emitted constant energy signals such that large interference between the transmitted and reflected signals was common.
- 1926 (United States): G. Breit and M. A. Tuve used pulsed signals to investigate the ionosphere (Brown, 1999).



(a)



(b)

**Figure 1.1:** First 'radar system' developed by Ch. Hülsmeier. (a) Picture of this apparatus from an exhibition in the "Deutschen Museum" in Munich and (b) technical layout of Hülsmeier's patented work.

- 1928 (United States): Bently (1928) filed a patent for a device that was able to measure the altitude of aircrafts (today known as FM radar).
- 1933-1934 (Germany): Based on the equivalence of the acoustic and electromagnetic wave equations, R. Kühnhold developed a device that was able to detect a test vessel at a distance of 2.1 km.

Radar technology developed quickly during the Second World War, because countries were forced to stay ahead of their respective enemies. For example, one or two radar systems of the type patented by Bently (1928) were mounted on planes in 1943. This allowed other aircraft to be detected, provided a warning to pilots if they were scanned by enemy radar, and enabled friend and foe to be distinguished (Brown, 1999).

### 1.1.2. EARLY RADAR APPLICATIONS IN THE EARTH SCIENCES

Despite more than 30 geophysical-related patents filed between 1936 and 1971 (Olhoeft, 2002), the GPR technique was not developed into a practical tool until the 1970-1990 period. One of the earliest earth science applications was a survey that involved a capacitive method for generating electromagnetic waves (comparable to GPR; Stern, 1929; 1930). It was used in Austria to measure the thickness of a glacier.

During the late 1950's, a number of planes crashed on glaciers due to misinterpretations of the altitude measured by the aircraft-mounted radar systems. These accidents led to new investigations of the subsurface and its response to radar signals. A real boom of GPR developments and new application areas occurred in the middle 1960's and 1970's, with the electromagnetic sounding system of the Apollo 17 mission to the Moon being the most famous (e.g., Porcello et al., 1974). At this time, the first commercial equipment became available (e.g., Morey, 1972). Today, a number of different GPR systems with shielded and unshielded antennas and suitable for surface or borehole studies are available from several companies (e.g., GSSI, Malå, and Sensors and Software Inc).

## 1.2. GEORADAR: A MODERN TECHNIQUE FOR SUBSURFACE PROBING

Radar frequencies vary from 1 MHz to 110 GHz, covering most of the microwave, radio/TV, and amateur radio bands (blue area in Figure 1.2a). Center frequencies used in GPR experiments are typically in the 10 MHz to 3 GHz range. The important media parameters in GPR are dielectric permittivity ( $\varepsilon = \varepsilon_r \varepsilon_0$ , where  $\varepsilon_r$  is the dimensionless relative permittivity

and  $\epsilon_0$  the permittivity of free space,  $\epsilon_0 = 8.854 \cdot 10^{-12}$  As/Vm) and electrical conductivity  $\sigma$  (S/m). Representative values of  $\epsilon_r$  and  $\sigma$  are given in Table 1.1. The GPR response is also slightly sensitive to magnetic permeability  $\mu$  (Vs/Am), but for nearly all practical purposes  $\mu$  can be set to its free-space value  $\mu_0 = 1.257 \cdot 10^{-6}$  Vs/Am;  $\mu$  typically lies between  $1.26 \cdot 10^{-6}$  and  $1.63 \cdot 10^{-6}$  Vs/Am according to the magnetite and pyrrhotite content of the media.

**Table 1.1:** Relative dielectric permittivities and electrical conductivities of different subsurface materials (modified after Knödel et al., 1997)

Material	Permittivity $\epsilon_r$	Conductivity $\sigma$ [mS/m]
air	1	0
water	80	0.01
sea-water	80	30000
dry sand	3 - 5	0.01
saturated sand	20 - 30	0.1 - 1
silt	5 - 30	1 - 100
clay	5 - 40	2 - 1000
limestone	4 - 8	0.5 - 2
shale	5 - 15	1 - 100
granite	6	0.01 - 1
dry salt	~6	0.001 - 0.1
ice	3.18	0.01
oil, asphalt	2 - 3	0.01

Depending on the parameters mentioned above and the center signal frequency, the dominant wavelengths GPR waves in the subsurface range from meters to a few centimeters. For a given wave velocity, the dominant wavelengths decrease and the resolution increases as the center frequencies increase. For high resolution it also is necessary to have broad bandwidths. The bandwidths of many GPR systems are designed to be approximately equal to the dominant frequencies (e.g., for a 100 MHz center-frequency signal, the bandwidth is about 50-150 MHz). As for other wave phenomena, higher frequency GPR signals are attenuated more rapidly than lower frequency ones (Davis and Annan, 1989). Attenuation increases and depth penetration decreases markedly with increases in electrical conductivity.

Figure 1.2a lists diverse electromagnetic techniques together with associated frequencies and wavelengths. GPR is characterized by the highest frequencies amongst the geophysical methods; it provides the highest resolution (i.e., comparable only to well-logging methods like neutron-neutron-, sonic-, and televiewer-logs, see for example Knödel et al., 1997; Paasche et al., 2006; Spillmann et al., 2007), but also the lowest penetration depths (Figure 1.2b).

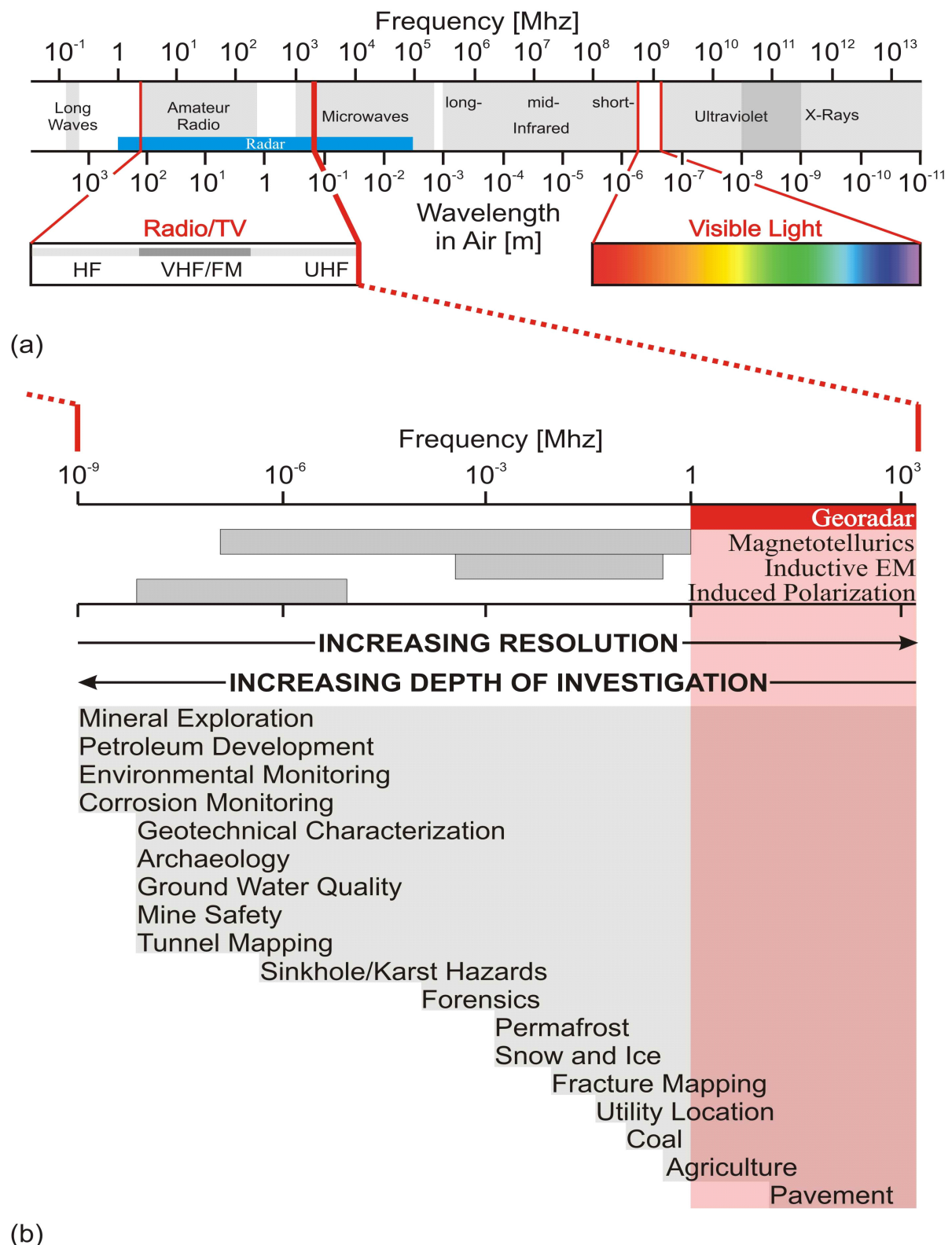


**Figure 1.2:** (a) Electromagnetic spectrum. HF - high-frequency (shortwave broadcast); VHF - very high-frequency (FM and television); UHF - ultra high-frequency (television). (b) Parts of the spectrum used in geophysics. High frequency methods may also be used for investigating areas that appear in the low-frequency regions of the figure [modified from Knödel et al. (1997) and Olhoef (2002)].

GPR surveying yields satisfactory results as long as the electrical conductivity of the subsurface is low to moderate. It is possible to estimate whether or not GPR is likely to yield useful results by comparing the required penetration depths with the dominant signal wavelengths  $\lambda$ . The following rule should be considered before conducting a GPR survey (e.g., Knödel et al., 1997):

$$\sigma < \frac{\pi}{f_c \mu_0 \lambda^2}, \quad (1.1)$$

where  $f_c$  is the center signal frequency. For a typical survey with  $f_c = 100$  MHz and a corresponding  $\sim 1$  m wavelength, the conductivity should be smaller than  $\sim 25$  mS/m. If the conductivity is equal or higher than  $\sim 50$  mS/m, diffusive electromagnetic phenomena dominate, thus preventing efficient radar wave propagation. Such conditions are likely for water-saturated clay and silt, salt-water, and metallic objects.

Applications of GPR have included (i) searching for pipes, cables and metallic/non-metallic barrels (e.g., Grandjean et al., 2000; Hansen and Johansen, 2000), (ii) probing waste disposal sites for leakages (e.g., Guy et al., 2000; Porsani et al., 2004), (iii) mapping geological targets (e.g., sedimentary structures, fractures, fissures or voids; see for example Bano, 1996; Greaves et al., 1996; Gross et al., 2004), (iv) estimating glacier thicknesses and morphology (e.g., Arcone, 1991; Gogineni et al., 2001), (v) measuring the depth to the water-table or degree of water contamination (e.g., Brune and Doolittle, 1990; Chen and Chow, 2007), (vi) determining the water content of soils and buildings (e.g., Tronicke et al., 2002; Irving et al., 2007), and (vii) detecting cavities in pavements (e.g., Hugenschmidt et al., 1998; Saarenketo and Scullion, 2000). In addition to earth scientists and civil engineers (see also Peters et al., 1994), GPR has been used by the police to search for hidden objects (e.g., buried bodies; see also Hammon et al., 2000; Ruffell and McKinley, 2005), by the military to identify the locations of unexploded ordnance, mines and other potential hazards (e.g., Bruschini et al., 1998; Sun and Li, 2003), and by archeologists as well as treasure hunters to find historical graves and foundations of buildings or valuable metallic objects in the subsurface (e.g., coins, sculptures etc.; see also Sternberg and McGill, 1995; Conyers, 2004; Leckebusch, 2005).

### 1.2.1. NUMERICAL MODELING OF GPR DATA

Numerical modeling provides insights into the behavior of electromagnetic waves propagating through the subsurface. With the availability of evermore powerful computers,



increasingly complex modeling techniques have been developed and applied over the past 40 years. The goal of these techniques is to solve the governing Maxwell's equations using numerical methods. The oldest and probably best known approach is based on the finite-difference methods. This approach involves the discretization of the differential operators of Maxwell's equations in the time or frequency domain for 1-, 2- and 3-D models (e.g., Taflove and Hagness, 2000). Integral forms of Maxwell's equations can be solved by using finite-integral approaches (FI, see Hafner, 1999). It is relatively straightforward to code both approaches. They do not require (i) large and expensive mesh generation and management or (ii) the solution of large linear equations or potentially complicated integral equations. To ensure the accuracy of these approaches for modeling complex structures, it may be necessary to employ higher order approximations of the equations or finer grids.

Other techniques, such as the finite-element (FE; e.g., Monk, 2003) and spectral-element methods (SE; e.g., Hesthaven and Warburton, 2002), alleviate accuracy problems at the cost of more complicated formulations and (at least partially) higher computational costs (memory and time). Simulations of subsurface electromagnetic wave propagation may also be performed using the method-of-moments (MoM; e.g., Khalil and Steer, 1999) and boundary-element methods (BE; e.g., Yashiro and Ohkawa, 1985).

Model edges are relatively easy to handle in the method-of-moments and boundary-element methods (e.g., Hafner, 1999), but they require special attention when using most other methods. If the model space was truncated without the application of special boundary conditions, artificial reflections from the boundaries would interfere with the signals of interest. To simulate an open infinite model space, the incident fields at the boundaries need to be efficiently absorbed. Different techniques based on changing material properties or analytical considerations have been developed over the past few years. Absorbing boundary conditions of the first category are, for example, diffusive boundaries characterized by increasing conductivity with increasing distance from the inner limits of the boundaries or Berenger's (1994) perfectly matched layers. Examples of analytic approaches include Engquist and Majda's (1977) and Mur's (1981) absorbing boundary conditions.

Applications of numerical simulation techniques to electromagnetic problems have been made in the military and biological fields as well as in medicine, electrical engineering, and the earth sciences. Numerical modeling of GPR has involved determining: (i) radiation characteristics of different types of antenna, (ii) near-field interactions between antennas and the subsurface, including the effects of guided phases (e.g., inside boreholes), (iii) antenna

coupling on rough terrain, (iv) effects of scattering, (v) optimization of antenna designs, and (vi) radar survey design and optimization (e.g., Goodman, 1994; Carcione, 1996; Taflove and Hagness, 2000; Lampe and Holliger, 2003; Irving and Knight, 2005; Ernst et al., 2006).

### 1.2.2. PRACTICAL ASPECTS OF GPR DATA ACQUISITION

GPR acquisition techniques may be grouped into four major categories:

1. The most common configuration is the surface-to-surface surveying geometry (Figure 1.3a), in which both antennas (shielded or unshielded) are moved across the ground in a common-offset-configuration (i.e., antenna spacing remains fixed). To determine the antenna locations, odometers, GPS's, theodolites or laser positioning systems may be used (e.g., Lehmann and Green, 1999; Grasmueck and Viggiano, 2007).
2. In single-hole GPR measurements, the transmitter and receiver antennas are moved along a borehole in a common-offset-configuration. The locations of the antenna pair in the borehole are typically obtained from distance measurements made with odometers. This acquisition geometry is useful for detecting steeply dipping targets that are difficult or impossible to image using surface-acquisition systems. If non-directional antennas are employed, independent constraints are needed to determine the true locations of the reflectors (Olsson et al., 1992; Spillmann et al., 2007).
3. Vertical radar profiling (VRP) requires one antenna in a borehole and the other on the surface. Measurements using this configuration supply estimates of media parameters and structures within 1-2 m of the borehole (Figure 1.3b). VRP data allows steeply dipping reflectors and the natural layering of the subsurface to be imaged (e.g., Spillmann et al., 2007). A major drawback of this configuration is that the large radiation angles (i.e., the angles between the horizontal and the radiation directions) when combined with the radiation characteristics of typical dipole-type borehole GPR antennas (see Chapter 2) may result in low signal-to-noise data.
4. Having access to two boreholes enables crosshole GPR data to be acquired (Figure 1.3c). Transmitting radar energy in one borehole and recording it in a neighboring borehole yields data that are capable of producing high-resolution images of the media parameters between the boreholes. This acquisition configuration can also be used to image dipping reflectors (e.g., Olsson et al., 1992).

Data recorded using all four recording geometries contain transmitted/refracted, reflected, diffracted, and scattered energy.

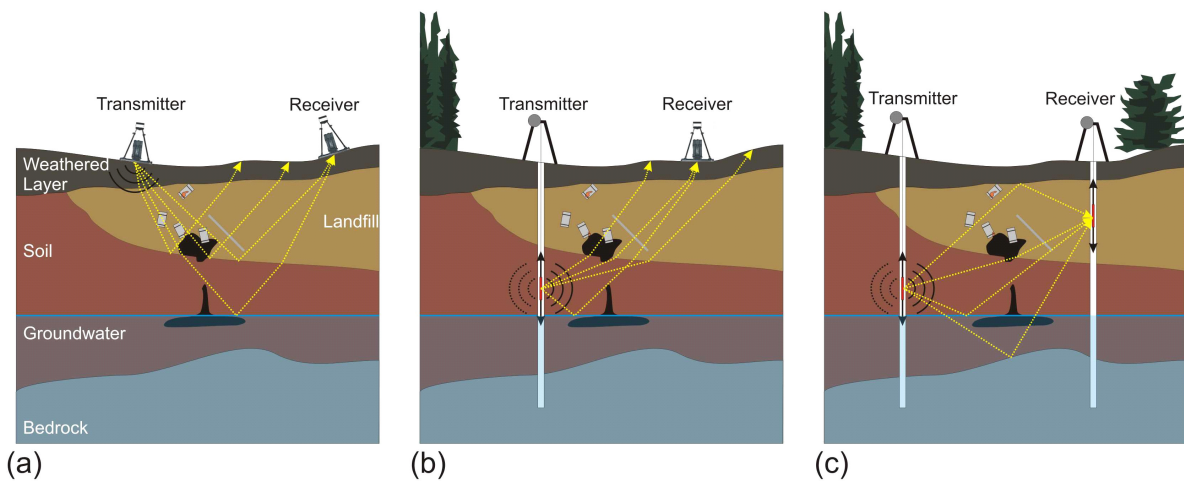


**Figure 1.3:** Different acquisition geometries: (a) Surface to surface profiling, (b) vertical radar profiling (VRP) and (c) crosshole radar surveying.

### 1.2.3. PROCESSING AND INVERSION OF GPR DATA

#### 1.2.3.1. REFLECTION PROCESSING

Reflections in GPR data can be processed using approaches similar to those developed for reflection seismic data (e.g., Fokkema, 2003; Gross et al., 2003; Heincke et al., 2004; Jung-Ho et al., 2005; Streich et al., 2007). Important steps include (i) different types of filtering to reduce noise and enhance the signal, (ii) corrections for topography, (iii) deconvolution, and (iv) migration. Despite the many similarities between elastic and electromagnetic waves, certain seismic data processing algorithms cannot be applied directly to GPR data; they need to be modified to account for the vectorial nature of radar waves and the antenna radiation characteristics (see Chapter 2).

#### 1.2.3.2. DETERMINISTIC ALGORITHMS: INVERSION OF TRANSMISSION GPR DATA

It is generally difficult to extract media properties (i.e., dielectric permittivity and electrical conductivity) from reflection data. In contrast, such properties can be estimated from transmission data by inverting appropriate parts of the recorded traces (e.g., first-arrival traveltimes, first-cycle amplitudes or data that correspond to selected frequencies) or the entire data set. In some cases, in which no explicit formulation of the underlying physics is

required or ad-hoc corrections are sufficient (e.g., ray-based inversion of first-arrival traveltimes and first-cycle amplitudes), it is possible to apply common inversion routines to seismic and GPR data.

Geophysical inverse theory presupposes a physical model that relates the observed data with the unknown media parameters. Depending on the complexity and size of the inverse problem to be solved, the governing mathematical theory can be formulated using a variety of schemes (Tarantola and Valette, 1982; Pratt et al., 1998; Tarantola, 2005), the most common of which are:

- (i) Linear and non-linear least-squares approaches using direct solvers. To apply these approaches, it is necessary to have linear or linearized models that link the data and model parameters. When necessary, linearization is achieved by considering only the first-order terms (i.e., first derivatives) of a Taylor-series representation of the physical model. Typically, the mathematical formulation requires the explicit computation of the Jacobian (i.e., sensitivity) matrix and its inverse.
- (ii) Non-linear least-squares approaches based on descent-type solvers (e.g., conjugate gradient). These approaches are closely related to non-linear least-squares approaches, but they have the advantage of not requiring the explicit computation of the Jacobian matrix, thus making it possible to address very large problems, such as those required for full-waveform time-domain inversions.
- (iii) Full Newton algorithms. Approaches (i) and (ii) only involve first-order terms (in particular, the first derivatives), such that in certain circumstances the inversions may be slow and somewhat inaccurate. By including first- and second-order derivatives (i.e., the Hessian matrix), faster and more accurate Full Newton algorithms may be possible. An inherent drawback of full Newton algorithms is the significant extra mathematical complexity and the associated costly computations.
- (iv) Gauss-Newton and quasi-Newton algorithms. Simplifying the Hessian matrix results in the Gauss-Newton algorithm, which is similar to non-linear least-squares formulations. Since computations of the full Jacobian matrix are expensive, various approximations are employed (e.g., as in the quasi-Newton approach).

Inversion of seismic and GPR data requires the corresponding wave equations to be evaluated. An overview of different inversion techniques is provided in Chapter 3. They

include ray-theoretical (e.g., Olsson et al., 1992), Born-iterative (e.g., Chew and Wang, 1990), diffraction (e.g., Cui and Chew, 2000), wave-equation traveltime (e.g., Cai et al., 1996), and full-waveform (e.g., Moghaddam et al., 1991; Pratt et al., 1998) tomography approaches.

### ***1.2.3.3. NON-DETERMINISTIC ALGORITHMS: STOCHASTIC EVALUATION OF GPR DATA***

Non-deterministic (i.e., stochastic or Monte Carlo) methods involve testing a large number of randomly or pseudo-randomly chosen models. These methods are suitable for solving highly non-linear problems. Tarantola (2005) provides a thorough review of these methods. I only mention the simulated annealing method, which has its origins in thermodynamics. Heating a solid until it melts and then letting it cool very slowly yields a perfect crystal, which is distinguished by having the lowest possible energy state. Adapted to geophysical problems, the goal is the same: to find the one model that represents the minimum state of energy. Applications of simulated annealing methods to the inversion of GPR data have been reported by Gibert et al. (2004), Cassiani et al. (2004) and Tronicke and Holliger (2005). Although stochastic methods are appropriate for strongly non-linear problems, their use is often limited by their high computational costs.

### **1.2.4. ADVANTAGES AND PROBLEMS ASSOCIATED WITH THE GPR METHOD**

GPR has become a popular method for probing the subsurface. Acquisition of surface GPR data requires much less effort than that needed to generate and record surface seismic data, whereas the acquisition of seismic and GPR borehole and crosshole data requires comparable expenditures of field effort.

The broad band of frequencies employed in GPR allow small shallow targets and large moderately deep features to be investigated (Figure 1.2b). The method requires contrasts in dielectric permittivity and/or electrical conductivity. If the conductivities are too large at any location or depth (Equation 1.1), the GPR waves are rapidly attenuated and, as consequence, do not reach the receiver. Furthermore, reflections and diffractions from conductive objects on the surface (e.g., wires, trees, and vehicles) may overwhelm the subsurface images, in particular when non-shielded or inadequately shielded antennas are employed. Unfortunately, shielded antennas usually produce ringy and generally weaker signals.

Difficulties may arise in the processing and inversion of GPR data. The radiation characteristics of GPR transmitter and receiver antennas are strongly dependent on direction,

which contrasts markedly with the spherical or quasi-spherical radiation patterns generated by seismic sources (Figure 1.4). Correct imaging of GPR data requires the antenna radiation patterns to be included in the migration/inversion algorithms.

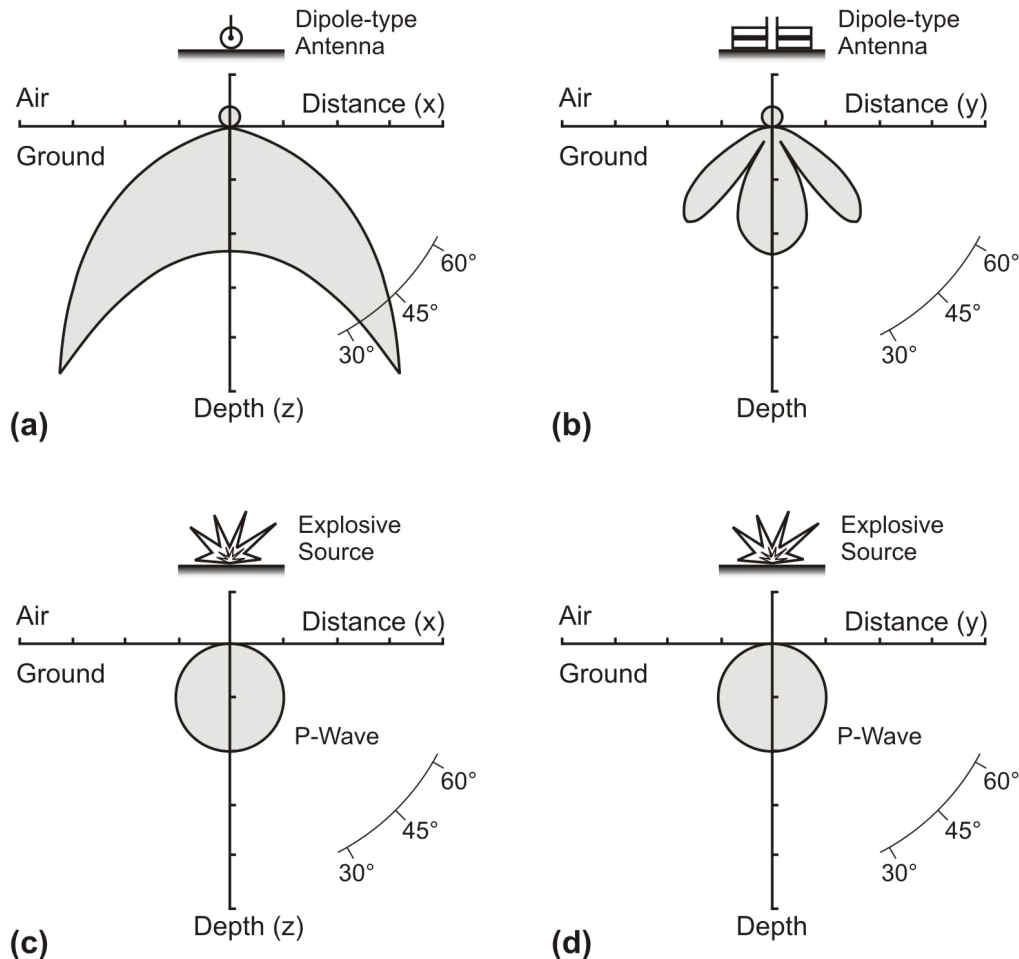


**Figure 1.4:** (a) and (b) Radiation characteristics of dipole-type GPR antennas with axis oriented in y-direction. (a) x-z plane and (b) y-z plane. (c) and (d) Radiation characteristics of a point seismic source. (c) x-z plane and (d) y-z plane.

### 1.3. GOALS OF THIS THESIS

The main goal of my thesis is the development of a full-waveform inversion scheme for crosshole GPR data. Standard ray-based inversion schemes use only up to two pieces of information per recorded trace: the first-arrival traveltimes and the maximum amplitude. The newly developed scheme allows the entire or significant parts of the recorded data to be inverted. As a consequence of including much more information in the inversion process, waveform tomograms contain higher resolution structural information and better constrained contrasts in media parameters than ray tomograms. Estimates of key petrophysical and

hydrogeophysical parameters can be readily derived from the tomograms. In this way, geophysicists and non-geophysicists can better characterize the subsurface.

An inherent limitation of my time-domain approach is computational. It requires access to a cluster-type supercomputer. The choice of a time-domain approach was based on my experience in the field of time-domain modeling, the simplicity of the inversion formalism, and the straightforward nature of the data visualization.

The first two years of my project were concerned with developing and benchmarking a numerical modeling algorithm that allowed the radiation characteristics of borehole GPR antennas to be analyzed. A local grid refinement technique enabled me to represent fine details of the transmitter antennas embedded in much coarser grids representing the geological media. The algorithm was tested on extensive synthetic and observed crosshole GPR data. The results of this research are contained Chapter 2 (*Realistic FDTD modeling of borehole georadar antenna radiation: methodology and application*), which has been published in *Near Surface Geophysics*.

Originally, I planned to implement the algorithm presented in Chapter 2 in the full-waveform inversion scheme. However, using a cylindrical coordinate system in a full-waveform inversion scheme would only be practical in rare cases, namely because transmitters need to be located on the cylinder rotation axis (i.e., generally useless for the back-propagation part). Consequently, for the forward component of the scheme I developed a finite-difference time-domain algorithm in Cartesian coordinates. For the inversion component, I modified various algorithms originally developed for the full-waveform inversion of seismic data. The new scheme allows vertical-component electric-field GPR data to be inverted. To solve the forward problem numerous times, I wrote the code to run on parallel computer systems. As consequence, wave propagation generated by all borehole transmitters is simultaneously simulated, such that the total time required is practically the same as that needed to compute wave propagation due to a single transmitter on a single CPU. The theoretical basis and application of the full-waveform inversion scheme to increasingly complex 2-D synthetic data are presented in Chapter 3 (*Full-waveform inversion of crosshole radar data based on 2-D finite-difference time-domain (FDTD) solutions of Maxwell's equations*), which has been published in *IEEE Transactions on Geosciences and Remote Sensing*.

A comprehensive test of the new scheme applied to two very different field data sets is the principal goal of Chapter 4 (*Application of a new 2-D time-domain full-waveform inversion scheme to crosshole radar data*). Developing a method for (i) inverting 3-D data using a 2-D algorithm that accounts for 3-D antenna radiation characteristics and 3-D media parameter variations and (ii) estimating the unknown source wavelet from the measured data were specific challenges of this component of my thesis. Chapter 4 has been published in *Geophysics*. The results of testing the 3-D to 2-D transformation scheme are presented in Appendix A.

Chapter 5 contains a brief review of the work presented in Chapters 2 to 4 and some general conclusions. Finally, I outline several related topics that are worth pursuing.



## **CHAPTER 2**

### **REALISTIC FDTD MODELLING OF BOREHOLE GEORADAR ANTENNA RADIATION: METHODOLOGY AND APPLICATION**

**Jacques R. Ernst, Klaus Holliger, Hansruedi Maurer and Alan G. Green**

*Slightly modified from the published version.*

Published in: Near Surface Geophysics, 4, 2006, 19-30

## 2.1. ABSTRACT

High-frequency electromagnetic-wave propagation phenomena associated with borehole georadar experiments are complex. To improve our understanding of the governing physical processes and radiative properties of borehole georadar antenna systems, we have developed a modeling tool based on a finite-difference time-domain (FDTD) solution of Maxwell's equations in cylindrical coordinates. The computational domain is bounded by cylindrical symmetry conditions along the left edge of the model and uniaxial perfectly matched layer (UPML) absorbing boundary conditions along the top, bottom and right model edges. An accurate and efficient grid-refinement technique allows us to account for detailed aspects of borehole georadar antenna systems, slim boreholes and materials with very high dielectric permittivities, such as water. Numerical experiments reveal that the radiation patterns of finite-size Wu-King-type antennae and infinitesimal electric dipoles in dry boreholes differ only slightly from the analytic solution of an infinitesimal electric dipole in a homogeneous full-space. In contrast, there are substantial differences between the radiation patterns of antennae placed in water-filled boreholes and their analytic full-space equivalents without boreholes. The effects of placing the antennae in air- and water-filled boreholes are explored using data acquired in crystalline rock and alluvial sediments, respectively. In both cases, simulations based on realistic transmitter antennae located in boreholes and spatially corrected receiver radiation patterns provide better agreement between the observed and modeled data than simulations based on infinitesimal transmitter and receiver dipoles.

## 2.2. INTRODUCTION

Cross-hole georadar is an increasingly popular method for high-resolution probing of the shallow subsurface. A typical experimental setup consists of transmitter and receiver dipole-type antennae located in neighboring boreholes (Peterson, 2001). Tomographic inversions of cross-hole georadar traveltimes and amplitudes provide information about the dielectric permittivity and the electric conductivity structures, respectively (Olsson et al., 1992). This information allows us to constrain the distributions of important environmental, engineering and hydrological parameters (e.g. porosity, water content, salinity, clay fraction, ore grade) within the probed region (Topp et al., 1980; Fullagar et al., 2000).

The tomographic inversion of cross-hole georadar traveltimes is analogous to the well-established seismic approach and is considered to be correspondingly robust. In contrast, ray- and waveform-based inversions of cross-hole georadar amplitudes require a priori knowledge

about the radiative properties of the borehole antennae. A common approach is to assume that the radiation pattern of a dipole-type borehole antenna can be represented by the far-field radiation pattern of an infinitesimal electric dipole in a homogeneous medium (Olsson et al., 1992; Peterson, 2001). To test the validity of this approximation, Holliger and Bergmann (2002) explored the effects of boreholes and their filling media on the radiative properties of infinitesimal electric dipole transmitters located within the boreholes. They found that air-filled boreholes only cause minor distortions of the radiation pattern with respect to the analytical full-space equivalent, whereas water-filled boreholes fundamentally alter the radiative behavior. Since many boreholes are water-filled, this may have important implications for the inversion of cross-hole georadar amplitude data. However, it is not clear to what extent these results can be extended to finite-length borehole georadar antennae.

To answer this question, we have developed a versatile finite-difference time-domain (FDTD) solution of Maxwell's equations in cylindrical coordinates that is capable of accurately simulating typical borehole georadar antenna systems under realistic operating conditions. We first employ the algorithm to investigate the radiation characteristics of resistively loaded borehole georadar antennae in air- and water-filled boreholes. It is then used to model high-quality cross-hole georadar waveforms recorded in (i) dry crystalline rocks (NAGRA's Grimsel Rock Laboratory in Switzerland) and (ii) a water-saturated heterogeneous alluvial aquifer (Boise Hydrogeophysical Research Site in Idaho, USA).

### **2.3. METHODOLOGY**

The inherent cylindrical geometry of boreholes and georadar antennae favors the use of a rotationally symmetric cylindrical-coordinate system. This reduces the computational cost to that of a 2D problem, while correctly accounting for the 3D geometrical spreading and radiation characteristics of dipole-type transmitters. The assumption of cylindrical symmetry does, however, imply that the model exhibits rotational symmetry, that the transmitters can only be located on the symmetry axis and that the borehole axis always coincides with the symmetry axis. For these reasons, only the transmitters can be modeled explicitly. The corresponding radiative properties of the receivers have to be approximated. This latter is achieved by either considering only the vertical component of the transmitted electric field or applying a spatial correction factor that represents the correct radiation characteristics (described briefly in the Case Studies section).

Transforming Maxwell's equations from 3-D Cartesian coordinates to 2-D rotationally symmetric cylindrical coordinates yields two sets of equivalent coupled partial-differential equations known as the transverse electric (TE) mode equations:

$$\frac{\partial E_r}{\partial t} = \frac{1}{\varepsilon} \left[ -\frac{\partial H_\varphi}{\partial z} - \sigma E_r \right], \quad (2.1a)$$

$$\frac{\partial E_z}{\partial t} = \frac{1}{\varepsilon} \left[ \frac{1}{r} \frac{\partial (r H_\varphi)}{\partial r} - \sigma E_z \right], \quad (2.1b)$$

$$\frac{\partial H_\varphi}{\partial t} = \frac{1}{\mu} \left[ \frac{\partial E_z}{\partial r} - \frac{\partial E_r}{\partial z} \right], \quad (2.1c)$$

and the corresponding transverse magnetic (TM) mode equations:

$$\frac{\partial E_\varphi}{\partial t} = \frac{1}{\varepsilon} \left[ \frac{\partial H_r}{\partial z} - \frac{\partial H_z}{\partial r} - \sigma E_\varphi \right], \quad (2.2a)$$

$$\frac{\partial H_r}{\partial t} = \frac{1}{\mu} \left[ \frac{\partial E_\varphi}{\partial z} \right], \quad (2.2b)$$

$$\frac{\partial H_z}{\partial t} = \frac{1}{\mu} \left[ \frac{1}{r} \frac{\partial (r E_\varphi)}{\partial r} \right], \quad (2.2c)$$

with  $E$  and  $H$  the electric and magnetic field components in radial ( $r$ ), vertical ( $z$ ) and azimuthal ( $\varphi$ ) directions,  $\varepsilon$  the dielectric permittivity,  $\sigma$  electric conductivity and  $\mu$  the magnetic permeability. In a typical borehole georadar setup, we are primarily interested in the electric field component parallel to the borehole axis and hence use the TE-mode equations. The equations are discretized using a staggered leap-frog finite-difference scheme that is second-order accurate in both time and space (Yee, 1966; Holliger and Bergmann, 2002). The criteria controlling numerical dispersion and stability of this  $O(2,2)$ -accurate solution are identical to those of corresponding FDTD schemes in 2D Cartesian coordinates (i.e., Courant criterion; see also Bergmann et al., 1996; Holliger and Bergmann, 2002):

$$c_{\max} \cdot \Delta t \sqrt{\frac{1}{(\Delta r)^2} + \frac{1}{(\Delta z)^2}} \leq 1, \quad (2.3)$$

where  $c_{\max} = \sqrt{\varepsilon_{\min} \mu_0}$  is the maximum phase velocity in the finite-difference grid, with  $\varepsilon_{\min}$  being the lowest value of the dielectric permittivity and  $\Delta t$ ,  $\Delta r$  and  $\Delta z$  are discretized intervals corresponding to  $t$ ,  $r$  and  $z$  in (2.1a) to (2.1c) and (2.2a) to (2.2c). In the following, we assume equal grid dimensions in radial and vertical directions (i.e.,  $\Delta r = \Delta z$ ).

To avoid artificial reflections from the model boundaries, we apply cylindrical symmetry conditions along the left model edge and absorbing conditions along the top, bottom and right model edges (Figure 2.1). The symmetry conditions are realized by mirroring the electric and magnetic field components in the immediate vicinity of the cylindrical symmetry axis. For the absorbing boundary conditions, we use the perfectly matched layer approach for a lossless uniaxial anisotropic medium (Berenger, 1994; Gedney, 1996; Taflove and Hagness, 2000). Our uniaxial perfectly matched layer (UPML) method is suitable and computationally efficient for lossless dielectric media, but also works well for electrically resistive heterogeneous media (Appendices 2.A and 2.B).

The realistic simulation of georadar antenna radiation requires accurate discretization of small intricate structures. Doing this with a uniform grid would result in enormous computational costs, because most of the model would be excessively oversampled. This problem can be addressed through grid-refinement techniques, either based on subgridding algorithms (e.g., Umashankar et al., 1987; Chevalier et al., 1997) or through a locally refined

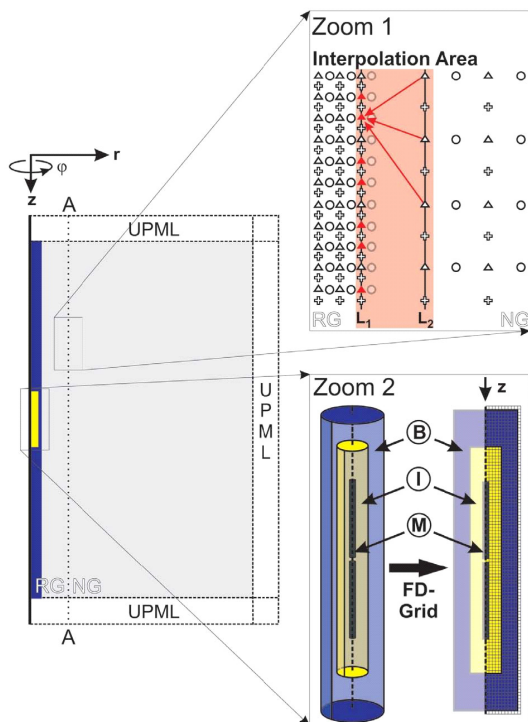


**Figure 2.1:** Sketch of model configuration in a cylindrical-coordinate system. RG: refined grid; NG: normal grid; A-A': border between normal and refined grid; UPML: uniaxial perfectly matched layer absorbing boundary. Zoom 1 shows an example of interpolation between the coarse and fine grids (crosses: radial electric field; circles: vertical electric field; triangles: azimuthal magnetic field). Red components are interpolated, with the red arrows identifying the contributing components (for display purposes, field components along line L1 and L2 are displayed apart, i.e., L1 and L2 are coincident). Zoom 2 shows the discretization of a realistic insulated antenna within a borehole. B: borehole; I: insulation; M: metallic antenna rods.

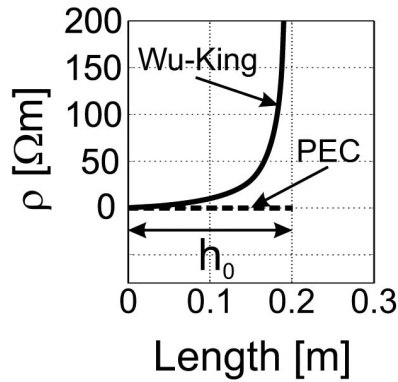


**Figure 2.2:** Sketch of resistance distribution along metallic antenna rods of PEC- and Wu-King-type antennae with  $h_0$  denoting the distance from the central gap to the outer edge of the antenna rod (i.e., the arm length).

grid (e.g., Falk et al., 1996; Robertsson and Holliger, 1997). We employ the latter approach because of its inherent simplicity and suitability for accommodating regions with unusually low velocities, such as water-filled boreholes. The refinement is achieved by splitting the spatial cells (leaving the temporal discretization unchanged), such that the normal-grid spacing is an integer times the refined-grid spacing. Depending on the integer refinement factor and the sequence of the TE-mode equations in our algorithm, either the azimuthal magnetic field components (odd refinement factors) or the azimuthal magnetic and vertical-electric field components (even

refinement factors) have to be interpolated. The different interpolation approaches are a consequence of the staggered-grid layout. When employing odd integer refinement factors, field components to be interpolated only occur on vertical lines of the mesh. If even refinement factors are used, field components need to be interpolated on horizontal and vertical grid-lines.

The grid-refinement concept is illustrated in Figure 2.1 (Zoom 1) for a refinement factor of 3. Compared to the linear interpolation method used by Robertsson and Holliger (1997), the third-order Lagrange interpolation scheme (J.O.A. Robertsson 2003, pers. comm.) employed in our study provides a significant (i.e., up to one order-of-magnitude) reduction in the artificial reflectivity of the boundary between the normal and refined grids without markedly increasing the computational cost. We have successfully tested this approach for refinement factors up to 5.

Using this refinement technique, a wire- or rod-type dipole antenna can be explicitly discretized (Figure 2.1, Zoom 2). The antenna is excited by feeding a compact Gaussian voltage pulse into its central gap:

$$V(t) = V_0 e^{-\frac{1}{2} \left( \frac{t - \tau_g/2}{\tau_p} \right)^2}, \quad (2.4)$$

where  $V_0$  is the peak amplitude of the pulse,  $\tau_g/2$  is the time the pulse needs to reach its maximum amplitude and  $\tau_p$  is the pulse width for  $V(t) = V_0 e^{-0.5}$ .

A wide variety of borehole georadar antennae can be simulated by simply changing the properties of the cells representing their metallic parts. For example, undamped perfect electrical conductor (PEC) antennae can be approximated by using very high conductivities (e.g.  $\sim 5 \times 10^7$  S/m for copper). This corresponds to near-zero resistivity in the cells defining the metallic parts (Figure 2.2). PEC antennae can be regarded as an end-member design of typical georadar antennae. A more realistic end-member antenna design was proposed by Wu and King (1965). In their antennae, the resistive loading increases continuously from the feeding point towards the antenna edges (Figure 2.2), thus eliminating internal reflections or ‘ringing’ typical of PEC or weakly damped antennae.

#### 2.4. APPLICATION TO AIR- AND WATER-FILLED BOREHOLES

Before applying our simulation scheme to air- and water-filled boreholes, extensive testing was carried out to validate the simulation algorithm and determine the performance of the grid-refinement technique and UMPL absorbing boundaries. The results of key benchmark tests are presented in Appendix 2.B.

Our test model space (medium model) is 5.5 m wide and 9 m deep with an UPML-frame thickness of 30 cells (Figure 2.3). The material properties of the model are those of moist sand ( $\epsilon = 10\epsilon_0$ ,  $\mu = \mu_0$ ,  $\sigma = 5$  mS/m). A grid-refinement factor of 3 is used and the boundary between the refined (2 mm) and normal (6 mm) grids is located at a radial distance of 0.3 m from the cylindrical symmetry axis. Unless mentioned otherwise, a 5 cm radius borehole is centered along the cylindrical symmetry axis.

The new algorithm was used to compute the radiative properties of an insulated Wu-King-type antenna and a non-insulated infinitesimal electric dipole located in a homogeneous half-space (Figure 2.4) and located in air- and water-filled boreholes situated within a homogeneous half-space (Figures 2.5 and 2.6). The radiation patterns are quantified in terms of the radial component of the time-averaged

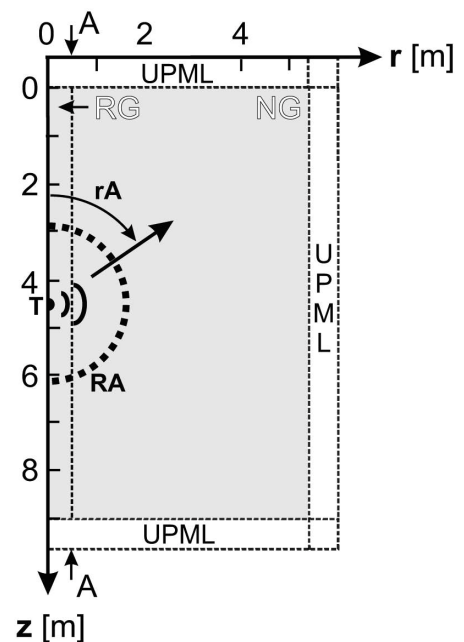


**Figure 2.3:** Sketch of medium model used for computing radiation patterns. RA: receiver array; rA: radiation angle; T: transmitter.

Poynting vector ( $\langle \mathbf{S} \rangle = \langle \mathbf{E} \times \mathbf{H} \rangle$ ), which is a measure of the emitted energy (Lampe and Holliger, 2005). For comparison purposes, Figures 2.4-2.6 also show the analytical radiation pattern of an infinitesimal electric dipole located in a homogeneous full-space, which is the model commonly used for the tomographic inversion of cross-hole georadar amplitude data. A summary of all antenna and medium models is given in Table 2.1.

**Table 2.1:** Summary of models used to benchmark our borehole simulation tool. +: considered, -: not considered.

Antenna models Medium models	Infinitesimal dipole: analytic solution	Insulated Wu-King antenna	PEC antenna: numerical and analytic solutions	Infinitesimal dipole: numerical solution	Figures
Homogeneous half-space	+(in all figures)	+	-	+	2.4
Homogeneous half-space with air-filled borehole	-	+	-	+	2.5
Homogeneous half-space with water-filled borehole	-	+	-	+	2.6
Homogeneous half-space	-	-	-	+	2.12-2.14
	+	-	+	-	2.15

### 2.4.1. ANTENNA IN A HOMOGENEOUS HALF-SPACE

The metallic wire of our Wu-King-type antenna model has a total length of 0.4 m (corresponding to an arm length  $h_0$  of 0.2 m), a radius of 2 mm and exhibits a hyperbolic resistivity distribution. It is surrounded by insulating material ( $\varepsilon = 4\varepsilon_0$ ,  $\mu = \mu_0$ ,  $\sigma = 0$  mS/m)

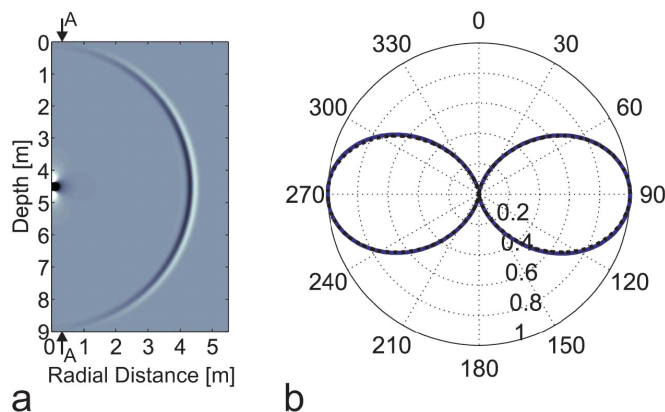


**Figure 2.4:** (a) Snapshot of the vertical-component electric field after 51 ns for an insulated Wu-King-type antenna with a resonance frequency of  $\sim 200$  MHz in a homogeneous full-space. (b) Numerical energy radiation patterns for the same antenna (blue line) and an infinitesimal electric dipole antenna without insulation (red line; not visible due to near-perfect overlap with other solutions) compared to the analytic full-space radiation pattern for an infinitesimal electric dipole (dotted black line). All patterns are normalized to their maximum values at  $90^\circ$ .



that exceeds the length of the antenna rod by 0.1 m on either side and has a radius of 12 mm (these characteristics are typical for some commonly used field antennae; A.P. Annan 2002, pers. comm.). Figure 2.4 demonstrates that the full-space radiative properties of an insulated Wu-King-type antenna in a homogeneous half-space (blue line) is very similar to the numerical (red line) and analytical (dotted black line) radiation patterns of an infinitesimal dipole located in the same medium.

### 2.4.2. ANTENNAE IN AN AIR-FILLED BOREHOLE

Figure 2.5 demonstrates that the fundamental result obtained for an insulated antenna in a homogeneous environment remains essentially valid in the presence of an air-filled borehole ( $\varepsilon = \varepsilon_0$ ,  $\mu = \mu_0$ ,  $\sigma = 0$  mS/m). Only minor differences between the numerical and analytical radiation patterns are observed (Figure 2.5b). The maximum radiated energy is, however, over 36% less than for the corresponding homogeneous full-space environment.

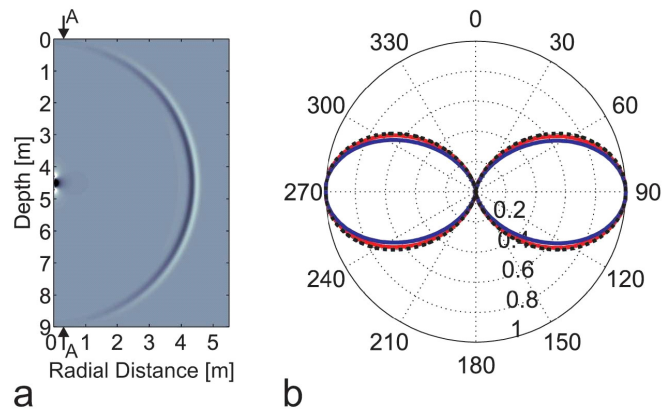


**Figure 2.5:** As for Figure 2.4, but the numerical solutions are for antennae in an air-filled borehole.

### 2.4.3. ANTENNAE IN A WATER-FILLED BOREHOLE

By comparison, the presence of a water-filled borehole ( $\varepsilon = 80\varepsilon_0$ ,  $\mu = \mu_0$ ,  $\sigma = 0.5$  mS/m) significantly influences the character of the snapshot and the radiation pattern (Figure 2.6). The snapshot indicates that a significant amount of energy is trapped in the borehole. Guided waves travel along the borehole with a velocity close to that of the surrounding medium, radiating continuously into this medium. Consequently, a water-filled borehole can be regarded as an extended antenna. Receivers close to the transmitter borehole record much more energy as a result of the guided phases. This yields radiated energy that increases markedly (Figure 2.6b) with decreasing radiation angle (i.e., near  $0^\circ$  and  $180^\circ$ ). The

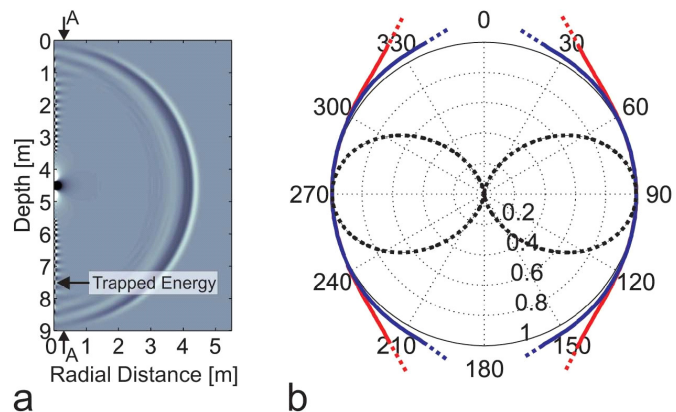


**Figure 2.6:** As for Figure 2.4, but the numerical solutions are for antennae in a water-filled borehole

increases markedly (Figure 2.6b) with decreasing radiation angle (i.e., near  $0^\circ$  and  $180^\circ$ ). The

radiation pattern of the insulated, finite-length antenna is again reasonably well approximated by that of a non-insulated infinitesimal electric dipole in the same medium, but differs fundamentally from the corresponding analytical full-space radiation pattern. Additional tests (not shown here) demonstrated that the overall shapes of the radiation patterns are not affected by the length of the recording used to evaluate the time-averaged Poynting vector. The maximum radiated energy is again significantly (i.e.,  $\sim 18\%$ ) reduced by the presence of the borehole.

In summary, our simulations indicate that the results of Holliger and Bergmann (2002) for an infinitesimal electric dipole in air- and water-filled boreholes are valid for Wu-King-type antenna systems. This has implications for full-waveform modeling/inversion of borehole georadar data, as we shall demonstrate by modeling selected parts of two cross-hole georadar data sets collected in very different environments.

## 2.5. CASE STUDIES

### 2.5.1. GRIMSEL ROCK LABORATORY

We have acquired a cross-hole georadar data set within the NAGRA (Swiss Cooperative for the Storage of Nuclear Waste) Grimsel Rock Laboratory in the central Swiss Alps. The two 10 cm diameter subparallel boreholes were  $\sim 20$  m long, sub-horizontal, air-filled and  $\sim 10$  m apart. Previous geological, geomechanical and seismic investigations of the

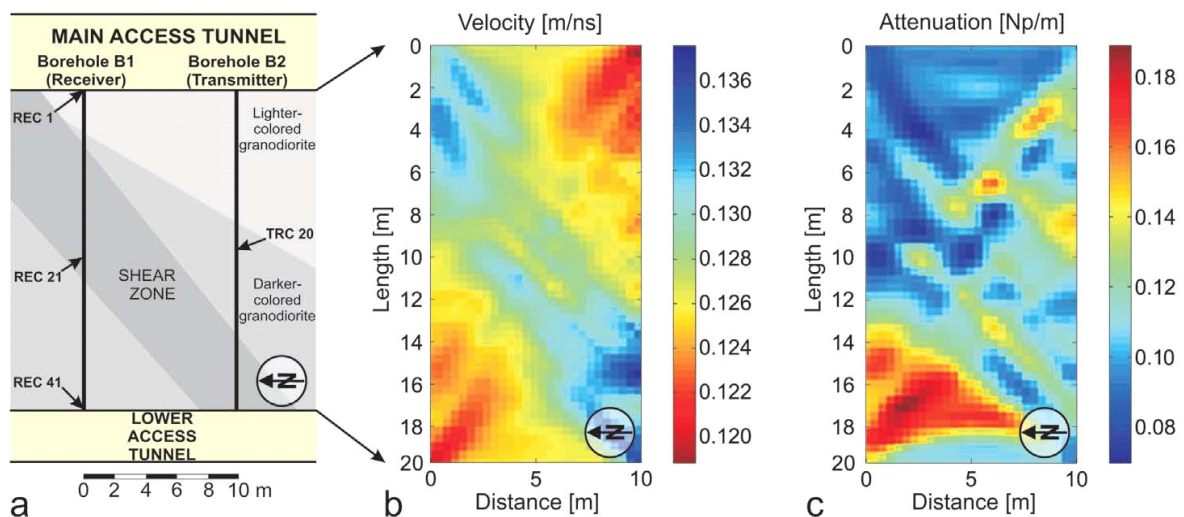


**Figure 2.7:** (a) Sketch of the cross-hole georadar experiment performed at the Grimsel site (Switzerland) superimposed on a structural cross-section (modified from Majer et al., 1990). Thick black lines: horizontal boreholes. REC and TRC indicate receiver and transmitter locations. Ray-based (b) velocity and (c) attenuation tomograms. Np refers to the neper, unit of dimensionless ratio.

area between these boreholes (Majer et al., 1990) revealed the presence of a major cross-cutting shear zone (Figure 2.7a).

The cross-hole georadar survey was carried out using 250 MHz RAMAC borehole georadar antennae with the transmitter antenna located in borehole B2 and the receiver antenna located in borehole B1 (Figure 2.7a). The data were recorded using transmitter and receiver intervals of  $\sim 0.5$  m. There were a total of 40 transmitter and 41 receiver positions, resulting in  $\sim 1600$  traveltimes and amplitudes. Good ray-coverage was obtained over an angular range of  $\sim 30^\circ$ - $150^\circ$  with respect to the borehole axis.

The first-arrival traveltimes were picked semi-automatically and tomographically inverted using an algorithm based on a finite-difference solution of the Eikonal equation (Lanz et al., 1998). To estimate the maximum first-cycle amplitudes of the data, we computed the envelope of each trace and picked the corresponding maximum. Standard ray-based inversion of the amplitude data (Holliger et al., 2001) was performed using the radiation pattern of an infinitesimal vertical electric dipole and the raypaths obtained from the inversion of the traveltimes. Figure 2.7(b,c) shows the resulting velocity and attenuation structures. Lateral variations of velocity and attenuation were rather moderate, amounting to  $\sim 2\%$  and  $\sim 20\%$ , respectively.

The corresponding dielectric permittivity and electric conductivity distributions were obtained by applying high-frequency approximations for the electromagnetic velocity  $v$  and attenuation  $\alpha$ :

$$\varepsilon \approx \frac{1}{\mu_0} v^{-2} \quad (2.5a)$$

and

$$\sigma \approx 2\alpha \sqrt{\frac{\varepsilon}{\mu_0}} \quad (2.5b)$$

The inferred dielectric permittivity and conductivity structures were then used to generate synthetic cross-hole georadar data with our FDTD simulation tool. In the simulations, the transmitting and receiving antennae were represented by insulated Wu-King-type antennae. The wavelet was determined by first averaging the central traces of all source gathers and then extracting the first-cycle of the resulting signal (Zhou et al., 1997).

As an example of our simulations, we consider the source gather generated by the transmitter antenna located at TRC 20 in the centre of borehole B2 (Figure 2.7a). As mentioned in the Methodology section, only the transmitter antenna and borehole can be modeled explicitly. A correction is used to account for the receiver antenna and borehole. This is achieved by applying correction factors to all synthetic traces based on the radiation characteristics of an insulated Wu-King-type antenna located in an air-filled borehole (e.g. as shown in Figure 2.5). The receiver locations in the numerical model are set at those used to record the data in borehole B1 (Figure 2.7a).

In Figure 2.8(a), we compare every second observed trace with its simulated counterpart. Both the observed and the simulated data are normalized with respect to the corresponding maximum amplitude of trace 21. Overall, the agreement between the traveltimes, amplitudes and shapes of the observed and simulated traces is excellent over the first cycles of the traces. The somewhat larger mismatch for trace 41 may be due to the fact that the tunnel wall in the immediate vicinity of this recording is crossed by a large number of electric wires and metallic pipes. Similarly good agreement between observed and synthetic source gathers is obtained for sources at other locations (not shown). Somewhat surprisingly, the boundaries between the different types of granodiorite and the presence of the shear zone do not greatly influence the general pattern of uniformly increasing traveltimes and uniformly decreasing amplitudes away from the central traces.

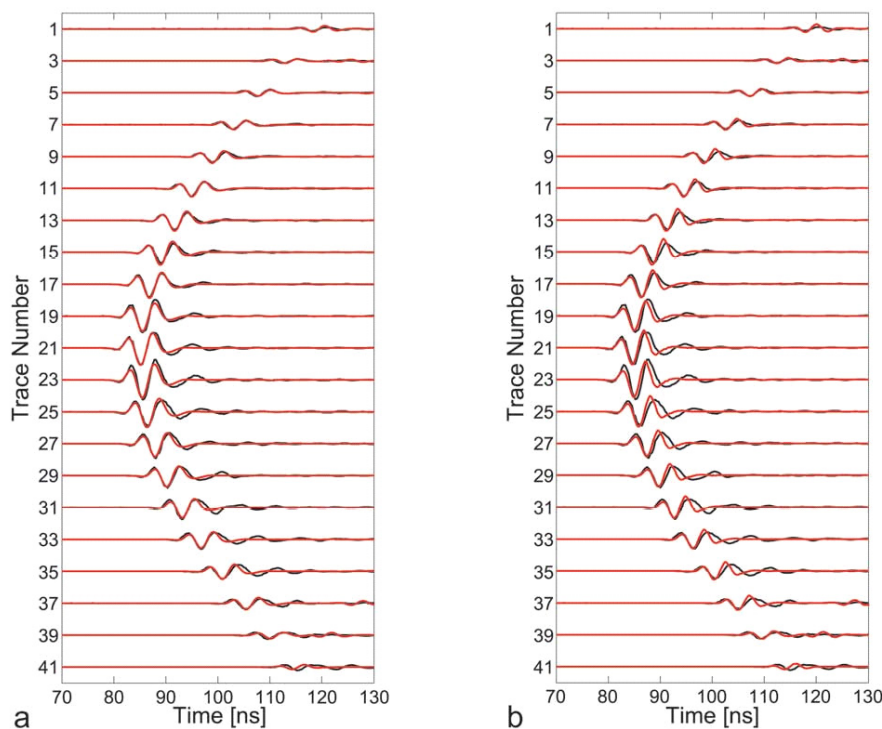


**Figure 2.8:** Comparison of every second observed (black lines) and modeled (red lines) trace for transmitter TRC 20 in the cross-hole georadar experiment shown in Figure 2.7. Simulations are computed for (a) an insulated Wu-King-type transmitter located in an air-filled borehole and (b) an infinitesimal electric dipole transmitter without a borehole. All traces are normalized with respect to the maximum values of the central trace 21.

For comparison, we have repeated this simulation using infinitesimal electric dipole approximations for the transmitter and receivers. The results (Figure 2.8b) for the first cycle of the simulated signal are similar to those obtained for the finite-length-antenna simulations. Following the first cycles, the match between observed and synthetic traces is somewhat better in Figure 2.8(a) than in Figure 2.8(b), but neither antenna implementation explains the detailed characteristics of the observed data. This is consistent with the fact that the model used for the FDTD simulations is based on a ray-theoretical inversion of the traveltimes and amplitudes, which only accounts for the direct transmitted part of the wavefield, ignoring the effects of scattering. Waveform-based inversion approaches are needed to explain the observed data beyond the first arriving wavetrain. As Pratt (1999) and Pratt and Shipp (1999) showed for seismic data, such approaches should enhance the resolution of the tomographic images substantially.

### 2.5.2. BOISE HYDROGEOPHYSICAL SITE

The second cross-hole georadar data set was acquired at the Boise Hydrogeophysical Research Site near Boise, USA (Tronicke et al., 2004). The two 10.2 cm diameter boreholes C5 and C6 were 20 m deep, separated by 8.5 m and slightly tilted with respect to the vertical (Figure 2.9a). They penetrated unconsolidated heterogeneous braided river deposits with layers characterized by varying degrees of porosities (22-26%, in Figure 2.9a; Clement et al., 1999; Barrash and Clemo, 2002). The water table was at 2.96 m depth.

Data acquisition started at a depth of about 4 m using a 250 MHz RAMAC borehole georadar antenna system. Transmitter and receiver antennae were moved at intervals of 0.2 and 0.4 m, respectively. This resulted in a total of 3080 traces, of which 2064 were employed

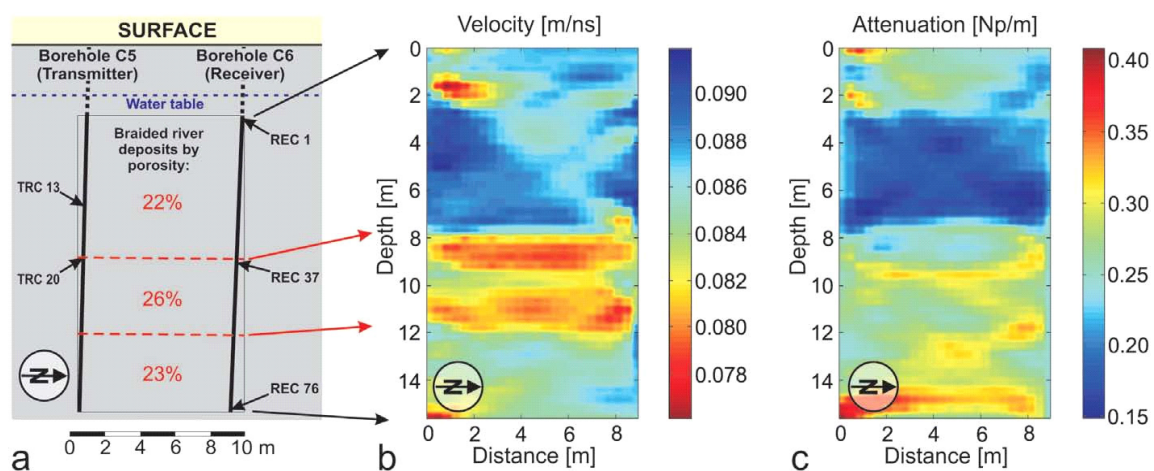


**Figure 2.9:** (a) Sketch of the cross-hole georadar experiment at the Boise site (Idaho). Thick black lines: near-vertical boreholes; REC and TRC indicate receiver and transmitter locations. Ray-based (b) velocity and (c) attenuation tomograms (Tronicke et al., 2004). Np refers to the neper, unit of dimension-less ratio.

for the inversion process (Tronicke et al., 2004). Dense ray coverage was obtained over an angular range of  $\sim 35^\circ$ - $145^\circ$  with respect to the borehole axis. Figure 2.9(b,c) demonstrate that velocity and attenuation variations were comparable to the previous case study, amounting to  $\sim 3\%$  and  $\sim 19\%$ , respectively.

We estimated the distribution of electromagnetic material properties between the two boreholes and the source wavelet in the same manner as for the previous case study. We also used Wu-King-type antennae for the simulations and, again, accounted for the effects of the receiver antenna and borehole using a series of correction factors based on our forward calculations (e.g. Figure 2.6). Two source gathers generated by the transmitter antennae located at TRC 13 and 20 were considered (Figure 2.9b,c). TRC 13 was located within a seemingly homogeneous region, whereas TRC 20 was close to the boundary between two units with quite different porosities, allowing us to study the influence of this boundary.

In Figures 2.10 and 2.11, we show a comparison between every third observed and simulated trace for transmitters located at TRC 13 and 20. All amplitudes are scaled relative to the maximum amplitudes of traces 25 and 37, respectively. For source gather TRC 13, the match between the observed and synthetic waveforms is comparable to that obtained in the previous case study (Figure 2.8a). Again, a somewhat degraded fit to the observed data was achieved when approximating the transmitter and receivers as infinitesimal electric dipoles (Figure 2.10b).

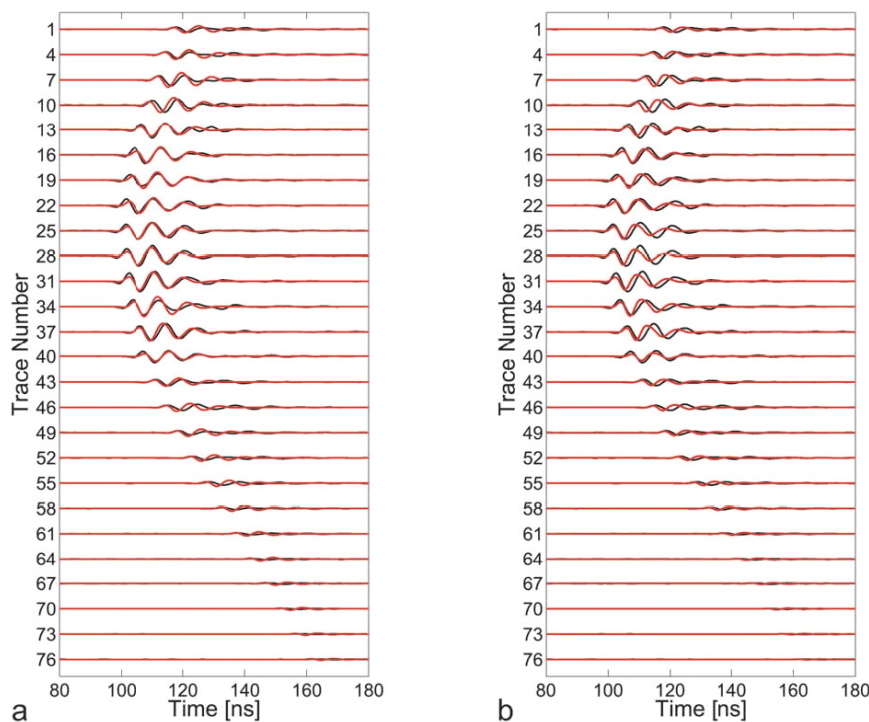


**Figure 2.10:** Comparison of every third observed (black lines) and modeled (red lines) trace for transmitter location TRC 13 in the experiment shown in Figure 2.9. Simulations are computed using (a) an insulated Wu-King-type transmitter located in a water-filled borehole and (b) an infinitesimal electric dipole transmitter without a borehole. All traces are normalized with respect to the maximum value of the central trace 25.

The overall agreement between observed and modeled data is rather poor for source gather TRC 20 (Figure 2.11). We suspect that the velocity and attenuation models in the vicinity of TRC 20 are inaccurate as a result of inherent inadequacies of ray-based tomographic inversion schemes for resolving complex structures. The physical properties of a medium in the immediate vicinity of an antenna significantly influence its radiation characteristics (Holliger et al., 2001). This highlights once more the need for waveform-based inversion approaches for cross-hole georadar data.

## 2.6. CONCLUSIONS

We have developed a FDTD solution of Maxwell's equations in cylindrical coordinates that is suitable for modeling the detailed radiation characteristics of finite-length borehole georadar antennae. The new algorithm could form the basis for (i) estimating more realistic radiation pattern corrections required for ray-based inversions of crosshole georadar amplitude data, (ii) developing full-waveform inversion methods, (iii) improving the planning of field experiments and (iv) designing new borehole georadar antenna systems.

Our results suggest that previous work on the radiative properties of infinitesimal electric dipole transmitters in air- and water-filled boreholes extend to resistively loaded borehole georadar antennae. In particular, radiation patterns of insulated Wu-King-type antennae are closely approximated by those of an infinitesimal electric dipole located in the same transmitting or recording environment. Given that the design of many borehole georadar antennae is based on some form of progressive Wu-King-type resistive loading, this has implications for full-waveform modeling and inversions of borehole georadar data.

We modeled the observed waveforms of two crosshole georadar data sets acquired in very different environments. Generally, the matches between the observed and simulated first-cycles were excellent as long as the effects of the receiver antenna and borehole were correctly accounted for. As expected, the agreement between observed and modeled data was rather poor when the transmitter was located in a strongly heterogeneous part of the model.

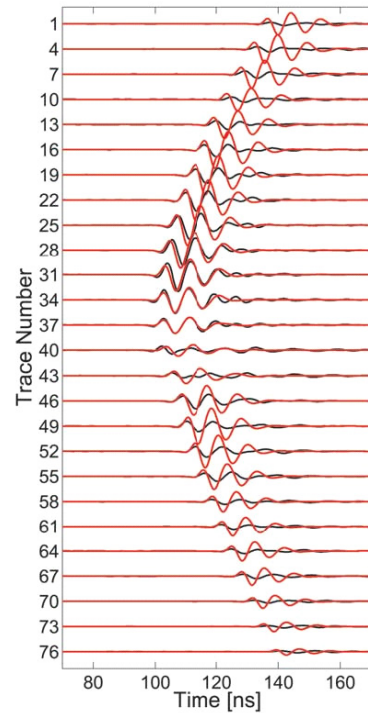


**Figure 2.11:** As for Figure 2.10(a), but for transmitter location TRC 20. Traces are normalized with respect to the maximum value of trace 37.

For such regions, ray-based tomographic models are likely to be inadequate. Together with the poorly matched waveforms following the first recorded cycles on most traces, this points to the need for waveform-based inversion methods. Our algorithm represents a suitable basis for developing such approaches.



## APPENDIX 2.A. UPML ABSORBING BOUNDARIES FOR CYLINDRICAL COORDINATE SYSTEMS

Using a lossless uniaxial anisotropic medium as a perfectly matched layer (PML) allows the non-physical and rather cumbersome split-field notation (Berenger 1996) to be avoided. In 3D Cartesian coordinates, Maxwell's curl equations for the PMLs can be written in the frequency domain as (Gedney, 1996; Taflove and Hagness, 2000)

$$\nabla \times \hat{\mathbf{H}} = j\omega\epsilon\bar{\bar{s}}\hat{\mathbf{E}} \quad (2.A-1a)$$

$$\nabla \times \hat{\mathbf{E}} = j\omega\mu\bar{\bar{s}}\hat{\mathbf{H}} \quad (2.A-1b)$$

where  $\hat{\mathbf{E}}$  and  $\hat{\mathbf{H}}$  are the electric and magnetic field vectors,  $j = \sqrt{-1}$ ,  $\epsilon$  is the dielectric permittivity,  $\mu$  is the magnetic permeability,  $\omega$  is the angular frequency and  $\bar{\bar{s}}$  is the 2D diagonal relative PML medium tensor, with diagonal elements  $s_\phi s_z/s_r$ ,  $s_r s_z/s_\phi$  and  $s_r s_\phi/s_z$ . This tensor is a function of  $\omega$ ,  $\epsilon$  and  $\sigma_B$ , where  $\sigma_B$  is the boundary conductivity function. We choose this approach because of its low computational costs and its ability to reduce artificial boundary reflections efficiently (Appendix 2.B).

Transforming (2.A1a) and (2.A1b) to a rotationally symmetric cylindrical-coordinate system yields a set of three coupled partial-differential equations:

$$-\frac{\partial \hat{H}_\phi}{\partial z} = j\omega\epsilon \frac{s_\phi s_z}{s_r} \hat{E}_r, \quad (2.A-2a)$$

$$\frac{1}{r} \frac{\partial (r \hat{H}_\phi)}{\partial r} = j\omega\epsilon \frac{s_r s_\phi}{s_z} \hat{E}_z, \quad (2.A-2b)$$

$$\frac{\partial \hat{E}_r}{\partial z} - \frac{\partial \hat{E}_z}{\partial r} = -j\omega\mu \frac{s_r s_z}{s_\phi} \hat{H}_\phi, \quad (2.A-2c)$$

where the constitutive parameters  $s_r$ ,  $s_z$  and  $s_\phi$  are defined as

$$s_q = 1 + \frac{\sigma_B(q)}{j\omega\epsilon} \text{ for } q = r, \phi \text{ and } z. \quad (2.A-3)$$

Following Gedney (1996), we define the boundary conductivity function of the PML frame as  $\sigma_B(q) = \sigma_{\max} (q/\delta)^m$ , where  $m$  and  $\delta$  are a polynomial exponent and the thickness of the PML frame, respectively. Optimal values for the exponent  $m$  are model dependent. They have to be determined empirically. For our purposes, values between 1.5 and 3.5 result in very low amplitude boundary reflections. The maximum conductivity  $\sigma_{\max}$  is constrained by analyzing the theoretical reflection error due to a perfect electrical conductor (PEC) wall surrounding the PMLs (Gedney, 1996).

Transforming equations (2.A2a)-(2.A2c) to the time domain leads to convolutions between the parameters  $s_r$ ,  $s_z$  and  $s_\phi$  and the electromagnetic field components, which would be cumbersome to implement and computationally inefficient. To circumvent this problem, the constitutive relationships may be defined in a way that results in a decoupling of the frequency-dependent terms (Taflove and Hagness, 2000). In our case, this yields

$$\hat{D}_r = \varepsilon \frac{s_z}{s_r} \hat{E}_r \quad (2.A-4a)$$

$$\hat{D}_z = \varepsilon \frac{s_\phi}{s_z} \hat{E}_z \quad (2.A-4b)$$

$$\hat{B}_\phi = \mu \frac{s_r}{s_\phi} \hat{H}_\phi \quad (2.A-4c)$$

The set of equations that describe electromagnetic wave propagation in the uniaxial PML (UPML) absorbing boundaries in cylindrical coordinates can then be written as

$$-\frac{\partial H_\phi}{\partial z} = \frac{\partial D_r}{\partial t} + \frac{\sigma_\phi}{\varepsilon} D_r \quad (2.A-5a)$$

$$\frac{1}{r} \frac{\partial (r H_\phi)}{\partial r} = \frac{\partial D_z}{\partial t} + \frac{\sigma_r}{\varepsilon} D_z \quad (2.A-5b)$$

$$-\frac{\partial E_r}{\partial z} + \frac{\partial E_z}{\partial r} = \frac{\partial B_\phi}{\partial t} + \frac{\sigma_z}{\varepsilon} B_\phi \quad (2.A-5c)$$

with the corresponding constitutive relationships being defined as

$$\frac{\partial D_r}{\partial t} + \frac{\sigma_r}{\varepsilon} D_r = \varepsilon \frac{\partial E_r}{\partial t} + \sigma_z E_r \quad (2.A-6a)$$

$$\frac{\partial D_z}{\partial t} + \frac{\sigma_z}{\varepsilon} D_z = \varepsilon \frac{\partial E_z}{\partial t} + \sigma_\varphi E_z \quad (2.A-6b)$$

$$\frac{\partial B_\varphi}{\partial t} + \frac{\sigma_\varphi}{\varepsilon} B_\varphi = \mu \frac{\partial H_\varphi}{\partial t} + \frac{\mu \sigma_r}{\varepsilon} H_\varphi \quad (2.A-6c)$$

Finally, (2.A5a)-(2.A5c) and (2.A6a)-(2.A6c) need to be discretized to obtain the FDTD update equations for the UPML absorbing boundary regions. Using the same staggered  $O(2,2)$ -accurate scheme as for the rest of the grid, this yields for the vertical component  $E_z$  of the electric field and the associated vertical electric flux-density  $D_z$ :

$$\begin{aligned} E_z^{n+1}(i + \frac{1}{2}, k) &= \frac{C^-(\varphi)}{C^+(\varphi)} E_z^n(i + \frac{1}{2}, k) \\ &+ \frac{1}{C^+(\varphi)} \left( C^+(z) D_z^{n+1}(i + \frac{1}{2}, k) - C^-(z) D_z^n(i + \frac{1}{2}, k) \right) \end{aligned} \quad (2.A-7a)$$

$$\begin{aligned} D_z^{n+1}(i + \frac{1}{2}, k) &= \frac{C^-(r)}{C^+(r)} D_z^n(i + \frac{1}{2}, k) \\ &+ \frac{1}{(i + \frac{1}{2}) C^+(r)} \frac{\Delta t}{\Delta r} \left( (i+1) H_z^{n+\frac{1}{2}}(i+1, k) - i H_z^{n+\frac{1}{2}}(i, k) \right) \end{aligned} \quad (2.A-7b)$$

with  $C^\pm(q) = 2\varepsilon \pm \sigma_q(q) \Delta t$  for  $q = r, \varphi$  and  $z$ .

## APPENDIX 2.B. RESULTS OF BENCHMARKS

In the following numerical tests, we first evaluate the influence of the grid-refinement and the UPML absorbing boundaries on wavefields radiated by infinitesimal vertical electric dipoles. Then the overall validity of our antenna simulation algorithm is tested by calculating the radiation patterns for a PEC wire-type antenna. Both transmitter types are excited by a broad-band Gaussian voltage pulse [equation (2.4)]. We use a pulse with a total length  $\tau_g$  of 8.1 ns and a width  $\tau_p$  of 0.4 ns, which for an infinitesimal electric dipole located in a vacuum corresponds to an emitted signal with a dominant frequency of  $\sim 500$  MHz and a bandwidth of 2-3 octaves. Because of the different requirements for these benchmarks, two different medium models are employed. To test thoroughly the grid-refinement and UPML absorbing boundaries, we use various models of a vacuum (Figure 2.12 and Table 2.2), whereas the overall validity of our antenna simulation algorithm is explored using a realistic model of the ground (Figure 2.3, Tables 2.1 and 2.2).

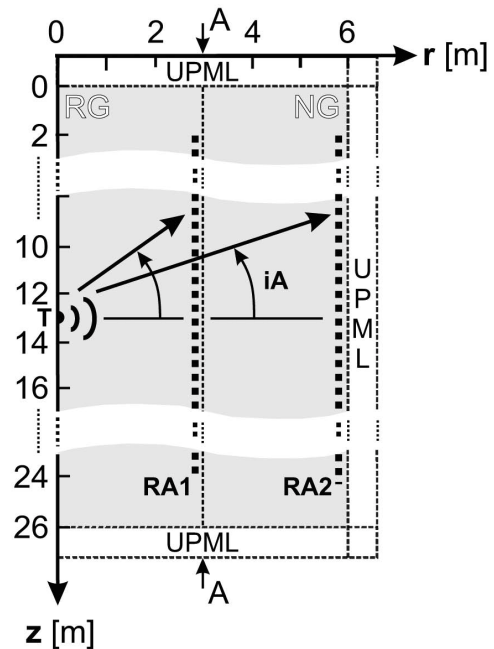


**Figure 2.12:** Sketch of medium model used for evaluating the accuracy of the grid-refinement scheme and the UPMLs.  $iA$ : incidence angle; RA1 and RA2: receiver arrays for the grid-refinement and UPML boundary tests, respectively; T: transmitter.

**Table 2.2:** Model parameters used for testing the grid-refinement, UPML absorbing boundaries and the overall validity of the antenna simulation algorithm.

Bench- marks Model parameters	Grid-refinement		UPML		Overall validity
	Test model	Reference model	Test model	Reference model	
Size [m]	$6 \times 26$	$6 \times 26$	$6 \times 26$	$10 \times 26$	$5.5 \times 9$
Normal grid cell-size [mm]	12.5	2.5	12.5	12.5	6
Refinement factor	3.5	1	1	1	3
UPML [cells]	30	30	15, 20, 30	30	30

### 2.B-1. INFLUENCE OF THE GRID-REFINEMENT

We use  $6 \times 26$  m models of a vacuum ( $\varepsilon = \varepsilon_0$ ,  $\mu = \mu_0$ ,  $\sigma = 0$  mS/m) for evaluating reflections associated with the grid-refinement (Tables 2.1 and 2.2). The normal grid-cell size in the test models is fixed at 0.0125 m (15 gridpoints per minimum wavelength) and refinement factors of 3 and 5 are considered. Results of the grid-refinement tests are compared to simulations based on a reference model with a much smaller grid-cell size of 0.0025 m (75 gridpoints per minimum wavelength). A vertical infinitesimal electric dipole transmitter is located at a depth of 13 m. We distribute 150 receivers along a vertical line, 0.05 m to the left of the boundary between the refined and normal grids (Figure 2.12, receiver array RA1).

Figure 2.13 shows simulated traces that would be recorded at RA1 for the reference model and for the test model with a refinement factor of 5 for incidence angles of  $0^\circ$ ,  $30^\circ$  and  $60^\circ$ . A qualitative comparison suggests excellent agreement between the traces of the two modeling results (Figure 2.13a-c). The lower diagrams in Figure 2.13(a-c) reveal that differences between the two numerical solutions are insignificant. Figure 2.13(d) shows the artificial reflected energy at the boundary between the normal and refined grids as a function of incidence angle. It demonstrates that for refinement factors of 3 and 5, less than  $1.5 \times 10^{-4}\%$  of the energy incident at the boundary is reflected at angles of up to  $60^\circ$ .

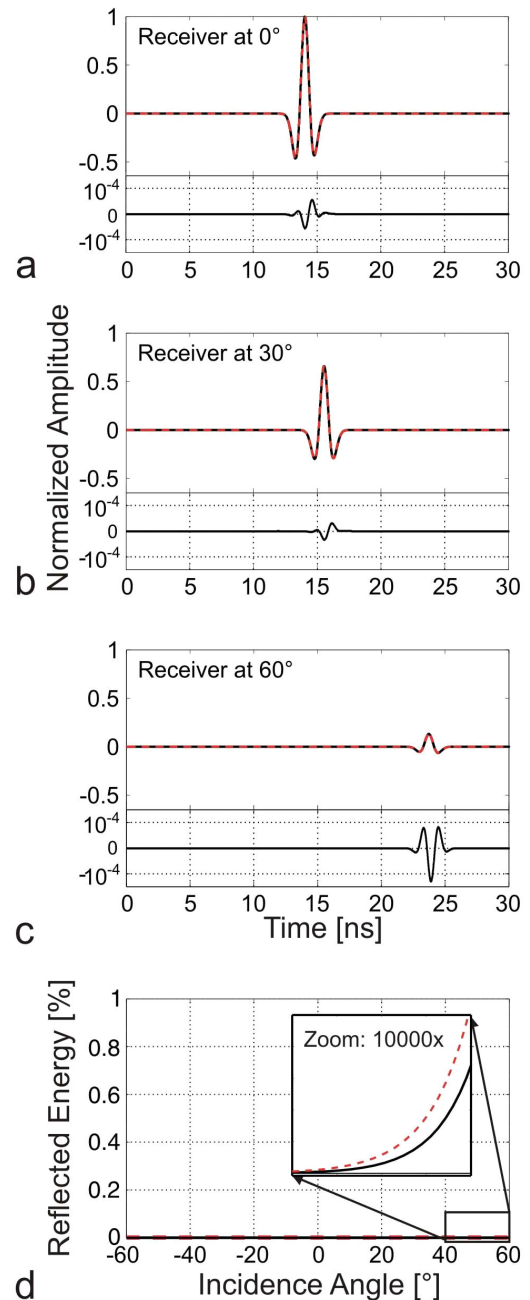


**Figure 2.13:** Test of the grid-refinement scheme. (a)-(c) Traces simulated at RA1 in Figure 2.12 for incidence angles of  $0^\circ$ ,  $30^\circ$  and  $60^\circ$  using a 5-times refined grid (solid red lines) and a medium model with a uniformly fine grid (dashed black lines); amplitudes are normalized with respect to the maximum amplitude at  $0^\circ$ . The differences between each pair of traces are also shown (solid black lines). (d) Energy reflected from the boundary of the refined and normal grids for refinement factors of 3 (black line) and 5 (dashed red line).

## 2.B-2. INFLUENCE OF THE UPML ABSORBING BOUNDARIES

To test the performance of the UPML absorbing boundaries, we use a  $6 \times 26$  m vacuum model with a uniform grid cell size of 0.0125 m and UPML boundaries with thicknesses of 15, 20 and 30 cells (Table 2.2). Our reference for this series of tests is a wider model of  $10 \times 26$  m with a 30-cell UPML boundary. Figure 2.14 (a-c) demonstrate that radargrams simulated 0.05 m to the left of the 30-cell thick UPML boundary in the test model are practically indistinguishable from those simulated at the same location in the reference model. Artificial reflections from 15-, 20- and 30-cell thick UPML boundaries are  $<0.25\%$ ,  $<0.1\%$  and  $<0.05\%$ , of the incident energy for angles of up to  $60^\circ$  (Figure 2.14d).

## 2.B-3. OVERALL VALIDITY OF THE SIMULATION TOOL

To establish the overall validity of our antenna simulation algorithm, we compare computed radiation patterns for a PEC wire-type antenna located within a homogeneous half-space with corresponding analytical solutions (Tables 2.1 and 2.2; Balanis, 1982). The medium model is the same as that used in the main text (Figure 2.3;  $\epsilon = 10\epsilon_0$ ,  $\mu = \mu_0$ ,  $\sigma = 5$  mS/m).

The metallic antenna rod has a half-length  $h_0$  of 0.2 m, a conductivity of  $5 \times 10^7$  S/m and is not insulated (Figure 2.2). It has a resonant frequency of  $\sim 100$  MHz. The transmitter is located at a depth of 4.5 m on the cylindrical symmetry axis and receivers are located at a constant radial distance of 1.6 m, or approximately 3.4 dominant wavelengths from the

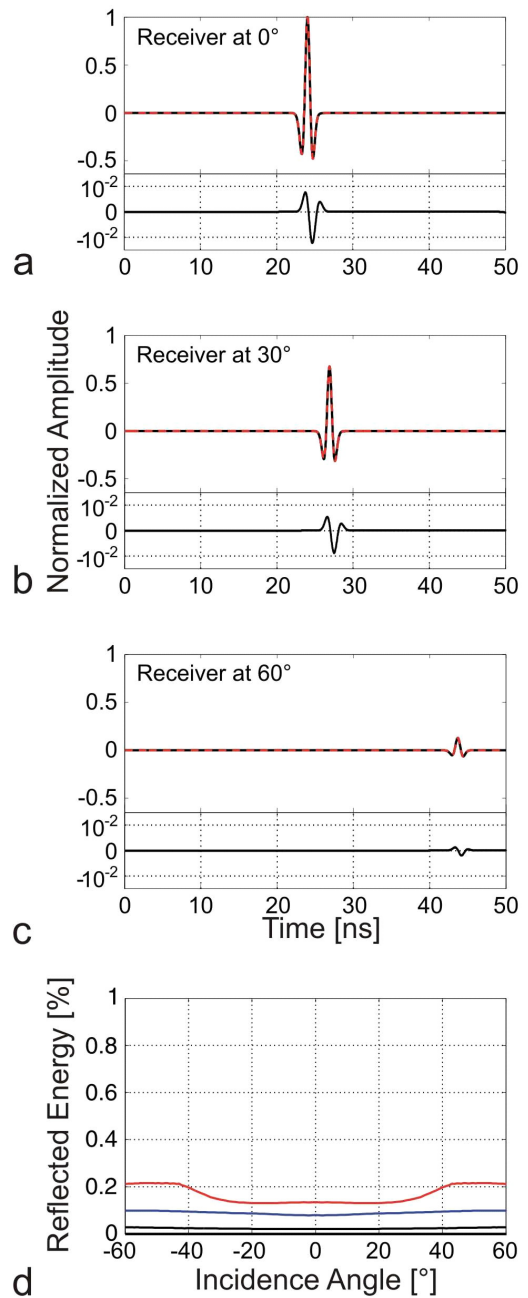


**Figure 2.14:** Test of the UPMLs. (a)-(c) Traces simulated at RA2 in Figure 2.12 for a 30-cell wide (2 minimum wavelengths) UPML (red lines) compared to traces simulated at the same location for a much wider model (dashed black lines). The differences between the pairs of traces are also shown (solid black lines). (d) Energy reflected from 15-cell wide (red line), 20-cellwide (blue line) and 30-cell wide (black line) UPMLs.

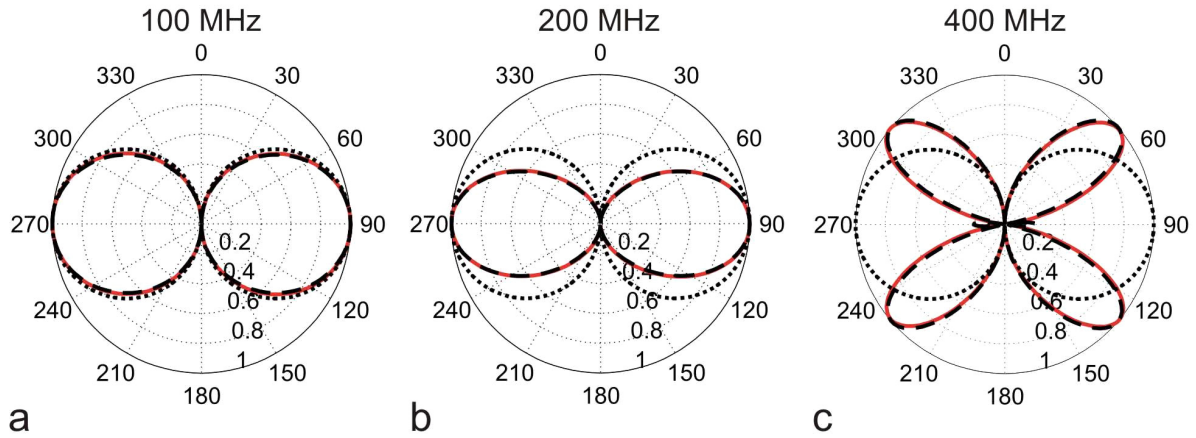


**Figure 2.15:** Radiation patterns for frequencies of (a) 100, (b) 200 and (c) 400 MHz for numerical (red lines) and analytical (dashed black lines) solutions of a PEC antenna with a resonance frequency of  $\sim 100$  MHz, and for the corresponding analytic solutions for an infinitesimal electric dipole in a homogeneous full-space (dotted black lines). Radiation patterns are normalized to the maximum values.

transmitter (Figure 2.3, receiver array RA), thus ensuring that we are dealing with the far-field regime of electromagnetic wave propagation. The radiation patterns are obtained by Fourier transforming the tangential component of the electric field and plotting amplitudes for frequencies of 100, 200 and 400 MHz in polar coordinates. The resulting radiation patterns agree well with their analytical counterparts (compare the solid red and dashed black lines in Figure 2.15), thus demonstrating the overall accuracy of our algorithm.

For comparison, we also show the analytic full-space radiation pattern of an infinitesimal electric dipole (dotted black lines in Figure 2.15). These results illustrate that at low frequencies (100 MHz), the analytic full-space radiation pattern is an acceptable representation of the radiative properties of an undamped  $\sim 100$  MHz wire-type antenna in a homogeneous half-space. At higher frequencies (e.g. 400 MHz), the infinitesimal electric dipole is clearly a poor approximation.





# CHAPTER 3

## FULL-WAVEFORM INVERSION OF CROSSHOLE RADAR DATA BASED ON 2-D FINITE-DIFFERENCE TIME-DOMAIN (FDTD) SOLUTIONS OF MAXWELL'S EQUATIONS

Jacques R. Ernst, Hansruedi Maurer, Alan G. Green and Klaus Holliger

*Slightly modified from the published version.*

Published in: IEEE Transactions on Geoscience and Remote Sensing, **45**, 2007, 2807-2828

### 3.1. ABSTRACT

Crosshole radar techniques are important tools for a wide range of geoscientific and engineering investigations. Unfortunately, the resolution of crosshole radar images may be limited by inadequacies of the ray tomographic methods commonly used to invert the data; since ray methods are based on high-frequency approximations and only account for a small fraction of the information contained in the radar traces, they are restricted to resolving relatively large-scale features. As a consequence, the true potential of crosshole radar techniques has yet to be realized. To address this issue, we introduce a full-waveform inversion scheme based on a finite-difference time-domain solution of Maxwell's equations. We benchmark our new scheme on synthetic crosshole data generated from suites of increasingly complex models. The full-waveform tomographic images accurately reconstruct: (i) the locations, sizes, and electrical properties of isolated sub-wavelength objects embedded in homogeneous media, (ii) the locations and sizes of adjacent sub-wavelength objects embedded in homogeneous media, (iii) abrupt media boundaries and average and stochastic electrical property variations of heterogeneous layered models, and (iv) the locations, sizes and electrical conductivities of water-filled tunnels and closely spaced sub-wavelength pipes embedded in heterogeneous layered models. The new scheme is shown to be remarkably robust to the presence of uncorrelated noise in the radar data. Several limitations of the full-waveform tomographic inversion were also identified. For typical crosshole acquisition geometries and parameters, small resistive bodies and small closely spaced dielectric objects may be difficult to resolve. Furthermore, electrical property contrasts may be underestimated. Nevertheless, the full-waveform inversions usually provide substantially better results than those supplied by traditional ray methods.

**Key Words:** Finite-difference time-domain (FDTD) methods, Maxwell's equations, crosshole radar, full-waveform inversion, dielectric permittivity, electrical conductivity

### 3.2. INTRODUCTION

Crosshole radar surveying is a highly effective technique for mapping subsurface electrical properties. To acquire crosshole radar data, dipole-type antennas generate high-frequency electromagnetic energy in a borehole and sense the resultant wavefields in one or more neighboring boreholes. The nominal or center frequencies of most borehole radar antennas range from 20 - 250 MHz, corresponding to dominant wavelengths of 5.0 - 0.4 m for common earth materials.

Tomographic inversions of crosshole radar data are generally based on ray theory (Carlsten et al., 1995; Fullagar et al., 2000; Bellefleur and Chouteau, 2001; Holliger et al., 2001; Tronicke et al., 2001; Holliger and Maurer, 2004; Irving and Knight, 2005; Clement and Barrash, 2006; Musil et al., 2006; Paasche et al., 2006). Separate inversions of the first-arrival times and maximum first-cycle amplitudes provide electromagnetic velocity and attenuation images of the probed regions. By making certain plausible assumptions, electromagnetic velocity and attenuation are converted to dielectric permittivity and electrical conductivity, parameters closely linked to a variety of environmental- and engineering-relevant subsurface properties (e.g., porosity, water content, salinity, clay fraction, ore grade).

Conventional ray tomography suffers from several critical shortcomings that are a consequence of the small number of signal attributes employed in the inversion process (Nolet, 1987; Wielandt, 1987). For instance, ray tomography usually only resolves features larger than the dominant signal wavelength (e.g., resolution scales approximately with the diameter of the first Fresnel zone Williamson and Worthington, 1993) and it cannot provide reliable information on certain important types of low-velocity structure. These deficiencies are particularly acute for targets that can only be illuminated from a limited number of directions, which is the situation for many crosshole investigations.

Since inversion is important for a wide range of problems in seismic exploration and exploitation, medical imaging, non-destructive testing, tunnel and landmine detection, a number of accurate alternative methods for inverting diverse types of wavefield (e.g., acoustic, elastic, radar, microwave, optical, X-ray) data have evolved over the past two decades. As examples, the following waveform-based tomographic inversion methods have been introduced in exploration seismology:

- Fresnel volume (Cerveny and Soares, 1992; Spetzler and Snieder, 2004);
- wave-equation traveltimes (Luo and Schuster, 1991; Vasco and Majer, 1993; Zhou et al., 1995; Zhou et al., 1997);
- diffraction (Devaney, 1984; Wu and Toksoz, 1987; Pratt and Worthington, 1988; Woodward, 1992; Dickens, 1994; Harris and Wang, 1996);
- full-waveform (Tarantola, 1984a; Tarantola, 1984b; Gauthier et al., 1986; Tarantola, 1986; Mora, 1987; Beydoun et al., 1989; Pica et al., 1990; Pratt, 1990a; Pratt, 1990b;

Pratt and Worthington, 1990; Pratt and Gouly, 1991; Pratt et al., 1991; Song et al., 1995; Reiter and Rodi, 1996; Zhou and Greenhalgh, 1998b; Zhou and Greenhalgh, 1998a; Pratt, 1999; Pratt and Shipp, 1999; Hicks and Pratt, 2001; Dessa and Pascal, 2003; Zhou and Greenhalgh, 2003; Tarantola, 2005).

These methods have been developed for both acoustic and elastic waves generated and recorded at the surface and/or along boreholes. They have included finite-difference and finite-element approaches in both the time- and frequency-domains.

In exploration seismology, waveform-based inversion schemes provide sub-wavelength resolution (Pratt, 1999) and under favorable conditions the resolution is as good as one-half (Wu and Toksoz, 1987) to one-third (Dickens, 1994) of a wavelength. In a direct comparison, Dessa and Pascal (2003) demonstrate that waveform-based inversion of ultrasonic data improves the resolution threshold by an order-of-magnitude relative to that supplied by ray tomography. By considering information contained in relevant parts of the entire recorded signal, waveform-based inversions are capable of providing reliable information on a broad range of structures, including those distinguished by low velocities.

Advances in waveform-based tomographic inversions of radar data have either (i) been made as a result of independent developments in electromagnetism or (ii) implicitly/explicitly followed those made in exploration seismology (i.e., the acoustic/elastic equations have been replaced by Maxwell's equations and the solutions have been appropriately reformulated). Important advances in the first category resulted from various Born iterative methods based on integral representations of Maxwell's equations (Wang and Chew, 1989; Chew and Wang, 1990; Sena and Toksoz, 1990; Moghaddam et al., 1991; Moghaddam and Chew, 1992; Moghaddam and Chew, 1993; Cui et al., 2001). In the second category, Johnson et al. (2005) and Cai et al. (1996) adapted the Fresnel volume and wave-equation traveltimes methods, respectively, and different authors (Strickel et al., 1994; Cui and Chew, 2000; Zhou and Liu, 2000; Cui and Chew, 2002; Cui et al., 2004; Popovic and Taflove, 2004) reported modified diffraction tomography techniques. An early attempt by Moghaddam et al. (1991) to determine the dielectric permittivities of small objects from synthetic data using a suitably modified version of Tarantola's (1984a; 1984b) full-waveform inversion approach was not considered fully satisfactory by the authors, primarily because significant a priori information was required to ensure correct convergence. We have since learned from numerous studies in seismology that a good initial model is required for the successful application of many full-waveform tomographic inversion techniques (e.g., see

review by Dessa and Pascal, 2003). Independently, three groups have recently developed full-waveform time-domain tomographic inversion schemes and tested them on synthetic radar data (Jia et al., 2002; Ernst et al., 2005; Kuroda et al., 2005). All three groups were able to determine the locations and relative permittivities of sub-wavelength bodies located within weakly conductive media.

Despite the considerable advantages compared to ray tomography, most applications of waveform-based inversion techniques to synthetic and observed crosshole radar data have suffered from one or more of the following limitations (e.g., Sena and Toksoz, 1990; Moghaddam et al., 1991; Cui and Chew, 2000; Jia et al., 2002; Takenaka et al., 2003): (i) unrealistic assumptions were made about the background media (e.g., they were assumed to be homogeneous and/or lossless), (ii) the effects of realistic electrical conductivities were ignored, (iii) the conductivities were not determined, (iv) only low contrasts between the target structures and background medium were accommodated (e.g., they were based on the Born or Rytov weak scattering approximations), (v) only one or a few discrete targets were imaged, (vi) target shapes had to be known, (vii) target sizes had to be large relative to the dominant wavelength of the signal, and/or (viii) mono-frequency signals were employed.

In this contribution, we describe a full-waveform time-domain tomographic inversion scheme for crosshole radar data. It provides high-resolution dielectric permittivity and electrical conductivity images of the earth between boreholes by automatically accounting for all phases of the radar signal. The background media may be heterogeneous, the physical property contrasts are not limited by the Born or Rytov weak scattering approximations, and the size of the dielectric/conductive targets may be smaller than the dominant wavelength of the radar signal. As for other full-waveform inversion methods, a good initial model is required to prevent the inversion process converging to local minima in the search space. Accordingly, we employ conventional ray tomography to derive the initial models (Pratt and Goulty, 1991; Pratt, 1999; Pratt and Shipp, 1999; Dessa and Pascal, 2003).

After presenting the theory for the forward and inverse components of our new scheme, key implementation issues are highlighted. We then illustrate the advantages and limitations of the new scheme by applying it to a series of synthetic crosshole data sets generated for increasingly complicated subsurface media and target structures. All full-waveform tomography images are compared with the relevant ray tomography results.

### **3.3. METHODOLOGY**

#### **3.3.1. BACKGROUND**

Although finite-difference time- and frequency-domain computer codes have long been available for the full-waveform inversion of elastic-wave data (e.g., Tarantola, 1984b; Tarantola, 1986; Beydoun et al., 1989; Pratt, 1990a; Pratt, 1990b; Pratt and Gouly, 1991; Pratt et al., 1991), recent crosshole seismic research and case studies have mostly been concerned with acoustic-wave solutions. This limitation is a consequence of the high cost of generating and recording the required data and the huge computing resources needed to perform full-waveform elastic-wave inversions. Yet, we know that many crosshole seismic data sets contain shear-, converted-, and guided-wave phases in addition to the compressional-wave phases.

Finite-difference solutions of Maxwell's equations are computationally comparable to those of the viscoacoustic-wave equations in seismics. Moreover, the responses of radar antennas in dry and water-filled boreholes and the effects of placing them near the earth's surface or other discontinuities can be simulated using suitably modified finite-difference solutions of Maxwell's equations (Holliger and Bergmann, 2002; Ernst et al., 2006).

We use a 2-D finite-difference time-domain (FDTD) solution of Maxwell's equations in Cartesian coordinates for the forward component of our full-waveform inversion scheme. This choice is largely based on our extensive experience in FDTD techniques (Bergmann et al., 1996; Bergmann et al., 1998; Holliger and Bergmann, 1998; Bergmann et al., 1999; Holliger and Bergmann, 2002; Jia et al., 2002; Lampe and Holliger, 2003; Lampe et al., 2003; Lampe and Holliger, 2005; Ernst et al., 2006) and their conceptual simplicity. We have adapted Tarantola's (2005) forward-/back- propagation approach for the inversion component of the code.

#### **3.3.2. FORWARD PROBLEM**

##### ***3.3.2.1. DIFFERENTIAL FORM OF MAXWELL'S EQUATIONS***

For wave propagation in the  $(x, z)$  plane of our Cartesian coordinate system, the transverse electric or TE mode of Maxwell's equation can be written as (Taflove and Hagness, 2000):

$$\frac{\partial E_x}{\partial t} = \frac{1}{\boldsymbol{\varepsilon}} \left( -\frac{\partial H_y}{\partial z} - \boldsymbol{\sigma} E_x \right), \quad (3.1a)$$

$$\frac{\partial E_z}{\partial t} = \frac{1}{\boldsymbol{\varepsilon}} \left( \frac{\partial H_y}{\partial x} - \boldsymbol{\sigma} E_z \right), \quad (3.1b)$$

$$\frac{\partial H_y}{\partial t} = \frac{1}{\mu} \left( \frac{\partial E_z}{\partial x} - \frac{\partial E_x}{\partial z} \right), \quad (3.1c)$$

where  $E_x$  and  $E_z$  are the horizontal and vertical electric field components,  $H_y$  is the magnetic field perpendicular to the propagation plane,  $\boldsymbol{\varepsilon}$  is the dielectric permittivity,  $\boldsymbol{\sigma}$  is the electrical conductivity, and  $\mu$  is the magnetic permeability (assumed in the following to be constant and equal to the free-space permeability  $\mu_0$ ). Bold letters are used to represent vectors and matrices. Equations (3.1a) through (3.1c) can be solved efficiently using FDTD techniques (e.g., Yee, 1966; Taflove and Hagness, 2000) based on staggered-grid finite-difference operators that are second-order accurate in both space and time. Highly efficient generalized perfectly matched layer (GPML) absorbing boundaries (Berenger, 1994; Fang and Wu, 1996) minimize the artificial reflections at the edges of the model space.

### 3.3.2.2. INTEGRAL FORM OF MAXWELL'S EQUATIONS

To determine the update directions required in our inversion procedure, it is useful to work with the integral form of Maxwell's equations. Typical borehole radar systems record the vertical component of the electric field  $E_z$ , such that Maxwell's equations can be recast in a form corresponding to the telegraphy equation:

$$\boldsymbol{\varepsilon} \frac{\partial^2 E_z}{\partial t^2} - \frac{1}{\mu} \frac{\partial^2 E_z}{\partial \mathbf{x}^2} + \boldsymbol{\sigma} \frac{\partial E_z}{\partial t} = \Psi_z, \quad (3.2)$$

where  $\mathbf{x}$  is a vector that refers to location  $(x, z)$  and  $\Psi_z$  is the source function. Solutions of (3.2) can be formally expressed using Green's functions  $G_z$  (Jackson, 1975):

$$E_z(\mathbf{x}, t) = \int_V d\mathbf{V}(\mathbf{x}') \int_0^{T_{\max}} dt' G_z(\mathbf{x}, t; \mathbf{x}', t') \Psi_z(\mathbf{x}', t'), \quad (3.3)$$

where  $V$  is the model space and  $T_{\max}$  is the maximum observation time.

### 3.3.3. INVERSE PROBLEM

#### 3.3.3.1. INVERSION STRATEGY

Our full-waveform tomographic inversion scheme for crosshole radar data involves finding the spatial distributions of  $\boldsymbol{\varepsilon}$  and  $\boldsymbol{\sigma}$  that minimize a functional of the form:

$$S = \frac{1}{2} \left\| E_z(\mathbf{x}_{trn}, \mathbf{x}_{rec}, t, \boldsymbol{\varepsilon}(\mathbf{x}), \boldsymbol{\sigma}(\mathbf{x})) - E_z^{obs}(\mathbf{x}_{trn}, \mathbf{x}_{rec}, t, \boldsymbol{\varepsilon}_{true}(\mathbf{x}), \boldsymbol{\sigma}_{true}(\mathbf{x})) \right\|^2, \quad (3.4)$$

where  $\mathbf{x}_{trn}$  and  $\mathbf{x}_{rec}$  are vectors that identify the transmitter and receiver positions,  $\boldsymbol{\varepsilon}$  and  $\boldsymbol{\sigma}$  are the model permittivity and conductivity distributions, and  $\boldsymbol{\varepsilon}_{true}$  and  $\boldsymbol{\sigma}_{true}$  are the true subsurface parameters.  $E_z$  and  $E_z^{obs}$  are the synthetic (computed) and observed vertical electric fields at the receiver locations. Following Tarantola (2005), we use logarithmically scaled versions of our unknown parameters:

$$\hat{\boldsymbol{\varepsilon}} = \log\left(\frac{\boldsymbol{\varepsilon}}{\boldsymbol{\varepsilon}_0}\right) = \log(\boldsymbol{\varepsilon}_r) \text{ and } \hat{\boldsymbol{\sigma}} = \log\left(\frac{\boldsymbol{\sigma}}{\boldsymbol{\sigma}_0}\right) = \log(\boldsymbol{\sigma}), \quad (3.5)$$

where  $\boldsymbol{\varepsilon}_0$  is the dielectric permittivity of free space,  $\boldsymbol{\varepsilon}_r$  is the relative permittivity, and  $\boldsymbol{\sigma}_0$  is set to 1 S/m. Logarithmic scaling ensures positivity and improves convergence.

We minimize the functional  $S$  in (3.4) using a conjugate-gradient-type scheme based on an algorithm introduced by Polak and Ribiere (1969). It requires the following steps:

1. select an initial model  $\hat{\boldsymbol{\varepsilon}} = \hat{\boldsymbol{\varepsilon}}_{ini}$  and  $\hat{\boldsymbol{\sigma}} = \hat{\boldsymbol{\sigma}}_{ini}$  (these are defined by the results of prior ray tomographic inversions of the first-arrival times and maximum first-cycle amplitudes);
2. compute  $E_z$  in (3.3) and  $S$  in (3.4) using the initial model parameters;
3. compute the update directions  $\boldsymbol{\gamma}_{\hat{\boldsymbol{\varepsilon}}}$  and  $\boldsymbol{\gamma}_{\hat{\boldsymbol{\sigma}}}$ ;
4. compute the step lengths  $\zeta_{\hat{\boldsymbol{\varepsilon}}}$  and  $\zeta_{\hat{\boldsymbol{\sigma}}}$ ;
5. update the model parameters using the conjugate gradient equations (simplified)
 
$$\hat{\boldsymbol{\varepsilon}}_{upd} = \hat{\boldsymbol{\varepsilon}} - \zeta_{\hat{\boldsymbol{\varepsilon}}} \boldsymbol{\gamma}_{\hat{\boldsymbol{\varepsilon}}} \text{ and } \hat{\boldsymbol{\sigma}}_{upd} = \hat{\boldsymbol{\sigma}} - \zeta_{\hat{\boldsymbol{\sigma}}} \boldsymbol{\gamma}_{\hat{\boldsymbol{\sigma}}};$$



6. set  $\hat{\boldsymbol{\varepsilon}} = \hat{\boldsymbol{\varepsilon}}_{upd}$  and  $\hat{\boldsymbol{\sigma}} = \hat{\boldsymbol{\sigma}}_{upd}$  and repeat steps 2 to 6 until convergence is achieved.

Convergence is assumed to have been reached when  $S$  changes by less than 1%. The key challenges of this scheme are to define update directions  $\boldsymbol{\gamma}_{\hat{\boldsymbol{\varepsilon}}}$  and  $\boldsymbol{\gamma}_{\hat{\boldsymbol{\sigma}}}$  and step lengths  $\zeta_{\hat{\boldsymbol{\varepsilon}}}$  and  $\zeta_{\hat{\boldsymbol{\sigma}}}$  that result in a small number of iterations to reach the minimum of  $S$ .

### 3.3.3.2. UPDATE DIRECTIONS $\boldsymbol{\gamma}_{\hat{\boldsymbol{\varepsilon}}}$ AND $\boldsymbol{\gamma}_{\hat{\boldsymbol{\sigma}}}$

To determine the update directions  $\boldsymbol{\gamma}_{\hat{\boldsymbol{\varepsilon}}}$  and  $\boldsymbol{\gamma}_{\hat{\boldsymbol{\sigma}}}$ , we consider a linearized form of the forward problem:

$$E_z(\hat{\boldsymbol{\varepsilon}} + \delta\hat{\boldsymbol{\varepsilon}}, \hat{\boldsymbol{\sigma}} + \delta\hat{\boldsymbol{\sigma}}) = E_z(\hat{\boldsymbol{\varepsilon}}, \hat{\boldsymbol{\sigma}}) + \delta E_z(\delta\hat{\boldsymbol{\varepsilon}}, \delta\hat{\boldsymbol{\sigma}}) = E_z(\hat{\boldsymbol{\varepsilon}}, \hat{\boldsymbol{\sigma}}) + \begin{bmatrix} \boldsymbol{\Gamma}_{\hat{\boldsymbol{\varepsilon}}} & 0 \\ 0 & \boldsymbol{\Gamma}_{\hat{\boldsymbol{\sigma}}} \end{bmatrix} \begin{bmatrix} \delta\hat{\boldsymbol{\varepsilon}} \\ \delta\hat{\boldsymbol{\sigma}} \end{bmatrix}, \quad (3.6)$$

and we take advantage of the scalar products:

$$\langle \delta E_z, \delta E_z \rangle = \left\langle \delta E_z, \boldsymbol{\Gamma}_{\hat{\boldsymbol{\varepsilon}}, \hat{\boldsymbol{\sigma}}} \begin{bmatrix} \delta\hat{\boldsymbol{\varepsilon}} \\ \delta\hat{\boldsymbol{\sigma}} \end{bmatrix} \right\rangle = \left\langle \boldsymbol{\Gamma}_{\hat{\boldsymbol{\varepsilon}}, \hat{\boldsymbol{\sigma}}}^T \delta E_z, \begin{bmatrix} \delta\hat{\boldsymbol{\varepsilon}} \\ \delta\hat{\boldsymbol{\sigma}} \end{bmatrix} \right\rangle, \quad (3.7)$$

where  $\boldsymbol{\Gamma}_{\hat{\boldsymbol{\varepsilon}}}$  and  $\boldsymbol{\Gamma}_{\hat{\boldsymbol{\sigma}}}$  are the Fréchet derivatives with respect to  $\hat{\boldsymbol{\varepsilon}}$  and  $\hat{\boldsymbol{\sigma}}$ ,  $\boldsymbol{\Gamma}_{\hat{\boldsymbol{\varepsilon}}, \hat{\boldsymbol{\sigma}}}$  is short-hand for the matrix containing  $\boldsymbol{\Gamma}_{\hat{\boldsymbol{\varepsilon}}}$  and  $\boldsymbol{\Gamma}_{\hat{\boldsymbol{\sigma}}}$  in (3.6), and  $^T$  indicates the matrix transpose. As shown by Tarantola (2005), the update directions  $\boldsymbol{\gamma}_{\hat{\boldsymbol{\varepsilon}}}$  and  $\boldsymbol{\gamma}_{\hat{\boldsymbol{\sigma}}}$  are given by:

$$\boldsymbol{\gamma}_{\hat{\boldsymbol{\varepsilon}}} = \boldsymbol{\Gamma}_{\hat{\boldsymbol{\varepsilon}}}^T \delta E_z \quad \text{and} \quad \boldsymbol{\gamma}_{\hat{\boldsymbol{\sigma}}} = \boldsymbol{\Gamma}_{\hat{\boldsymbol{\sigma}}}^T \delta E_z. \quad (3.8)$$

We begin by deriving an expression for  $\delta E_z = \boldsymbol{\Gamma}_{\hat{\boldsymbol{\varepsilon}}, \hat{\boldsymbol{\sigma}}} \begin{bmatrix} \delta\hat{\boldsymbol{\varepsilon}} \\ \delta\hat{\boldsymbol{\sigma}} \end{bmatrix}$  and then determine  $\boldsymbol{\gamma}_{\hat{\boldsymbol{\varepsilon}}, \hat{\boldsymbol{\sigma}}} = \boldsymbol{\Gamma}_{\hat{\boldsymbol{\varepsilon}}, \hat{\boldsymbol{\sigma}}}^T \delta E_z$  using (3.7). Explicit computations of the Fréchet derivatives are not required.

In the first step, we apply the perturbations  $\hat{\boldsymbol{\varepsilon}} \mapsto \hat{\boldsymbol{\varepsilon}} + \delta\hat{\boldsymbol{\varepsilon}}$  and  $\hat{\boldsymbol{\sigma}} \mapsto \hat{\boldsymbol{\sigma}} + \delta\hat{\boldsymbol{\sigma}}$  and substitute  $(E_z + \delta E_z)$ ,  $(\hat{\boldsymbol{\varepsilon}} + \delta\hat{\boldsymbol{\varepsilon}})$ , and  $(\hat{\boldsymbol{\sigma}} + \delta\hat{\boldsymbol{\sigma}})$  in (3.2). Using the definitions of (3.5), this yields:

$$\varepsilon_0 \exp(\hat{\boldsymbol{\varepsilon}} + \delta\hat{\boldsymbol{\varepsilon}}) \frac{\partial^2 (E_z + \delta E_z)}{\partial t^2} - \frac{1}{\mu} \frac{\partial^2 (E_z + \delta E_z)}{\partial \mathbf{x}^2} + \exp(\hat{\boldsymbol{\sigma}} + \delta\hat{\boldsymbol{\sigma}}) \frac{\partial (E_z + \delta E_z)}{\partial t} = \Psi_z. \quad (3.9)$$

After subtracting (3.9) from (3.2), representing the resultant exponential terms as power-series, and then ignoring the non-linear terms of the power series, we obtain:

$$\boldsymbol{\varepsilon} \frac{\partial^2 (\delta E_z)}{\partial t^2} - \frac{1}{\mu} \frac{\partial^2 (\delta E_z)}{\partial \mathbf{x}^2} + \boldsymbol{\sigma} \frac{\partial (\delta E_z)}{\partial t} = -\boldsymbol{\varepsilon} \frac{\partial^2 E_z}{\partial t^2} \delta \hat{\boldsymbol{\varepsilon}} - \boldsymbol{\sigma} \frac{\partial E_z}{\partial t} \delta \hat{\boldsymbol{\sigma}}. \quad (3.10)$$

Equation (3.10) is formally identical to (3.2), but with  $\delta E_z$  instead of  $E_z$  on the left side and a source-type term on the right side. A solution of (3.10) in terms of Green's functions can be written as [compare to (3.3)]:

$$\begin{aligned} \delta E_z(\mathbf{x}, t) = & - \int_V dV(\mathbf{x}') \int_0^{T_{\max}} dt' G_z(\mathbf{x}, t; \mathbf{x}', t') \boldsymbol{\varepsilon} \frac{\partial^2 E_z}{\partial t'^2} \delta \hat{\boldsymbol{\varepsilon}} \\ & - \int_V dV(\mathbf{x}') \int_0^{T_{\max}} dt' G_z(\mathbf{x}, t; \mathbf{x}', t') \boldsymbol{\sigma} \frac{\partial E_z}{\partial t'} \delta \hat{\boldsymbol{\sigma}}. \end{aligned} \quad (3.11)$$

In the second step, we consider the integral representations of the scalar products on the left and right sides of (3.7):

$$\langle \delta E_z, \delta E_z \rangle = \sum_{trn} \int_0^{T_{\max}} dt \sum_{rec} \delta E_z \delta E_z, \quad (3.12)$$

and

$$\left\langle \begin{bmatrix} \boldsymbol{\Gamma}_{\hat{\boldsymbol{\varepsilon}}}^T \delta E_z \\ \boldsymbol{\Gamma}_{\hat{\boldsymbol{\sigma}}}^T \delta E_z \end{bmatrix}, \begin{bmatrix} \delta \hat{\boldsymbol{\varepsilon}} \\ \delta \hat{\boldsymbol{\sigma}} \end{bmatrix} \right\rangle = \int_V dV (\boldsymbol{\Gamma}_{\hat{\boldsymbol{\varepsilon}}}^T \delta E_z \cdot \delta \hat{\boldsymbol{\varepsilon}}) + \int_V dV (\boldsymbol{\Gamma}_{\hat{\boldsymbol{\sigma}}}^T \delta E_z \cdot \delta \hat{\boldsymbol{\sigma}}). \quad (3.13)$$

By substituting (3.11) in (3.12), the integral representation of (3.7) becomes:

$$\begin{aligned} \sum_{trn} \int_0^{T_{\max}} dt \sum_{rec} \delta E_z \left[ - \int_V dV \int_0^{T_{\max}} dt' G_z \boldsymbol{\varepsilon} \frac{\partial^2 E_z}{\partial t'^2} \delta \hat{\boldsymbol{\varepsilon}} - \int_V dV \int_0^{T_{\max}} dt' G_z \boldsymbol{\sigma} \frac{\partial E_z}{\partial t'} \delta \hat{\boldsymbol{\sigma}} \right] \\ = \int_V dV (\boldsymbol{\Gamma}_{\hat{\boldsymbol{\varepsilon}}}^T \delta E_z \cdot \delta \hat{\boldsymbol{\varepsilon}}) + \int_V dV (\boldsymbol{\Gamma}_{\hat{\boldsymbol{\sigma}}}^T \delta E_z \cdot \delta \hat{\boldsymbol{\sigma}}). \end{aligned} \quad (3.14)$$

Since (3.14) is valid for arbitrary small values of  $\delta \hat{\boldsymbol{\varepsilon}}$  and  $\delta \hat{\boldsymbol{\sigma}}$ , we can equate the terms containing permittivity and the terms containing conductivity on the left and right sides of (3.14) to yield expressions for  $\boldsymbol{\gamma}_{\hat{\boldsymbol{\varepsilon}}} = \boldsymbol{\Gamma}_{\hat{\boldsymbol{\varepsilon}}}^T \delta E_z$  and  $\boldsymbol{\gamma}_{\hat{\boldsymbol{\sigma}}} = \boldsymbol{\Gamma}_{\hat{\boldsymbol{\sigma}}}^T \delta E_z$ :

$$\gamma_{\hat{\epsilon}} = - \sum_{trn} \int_0^{T_{\max}} dt \left\{ \sum_{rec} \left[ \int_0^{T_{\max}} dt' G_z \cdot \left( \boldsymbol{\epsilon} \frac{\partial^2 E_z}{\partial t^2} \right) \right] \cdot \delta E_z \right\} \quad (3.15a)$$

$$\gamma_{\hat{\sigma}} = - \sum_{trn} \int_0^{T_{\max}} dt \left\{ \sum_{rec} \left[ \int_0^{T_{\max}} dt' G_z \cdot \left( \boldsymbol{\sigma} \frac{\partial E_z}{\partial t} \right) \right] \cdot \delta E_z \right\} \quad (3.15b)$$

For practical purposes, we rewrite (3.15a) and (3.15b) as:

$$\gamma_{\hat{\epsilon}} = \boldsymbol{\epsilon}(\mathbf{x}) \sum_{trn} \int_0^{T_{\max}} dt \frac{\partial E_z}{\partial t}(\mathbf{x}, t) \frac{\partial \tilde{E}_z}{\partial t}(\mathbf{x}, t), \quad (3.16a)$$

$$\gamma_{\hat{\sigma}} = - \boldsymbol{\sigma}(\mathbf{x}) \sum_{trn} \int_0^{T_{\max}} dt \frac{\partial E_z}{\partial t}(\mathbf{x}, t) \tilde{E}_z(\mathbf{x}, t), \quad (3.16b)$$

where

$$\tilde{E}_z(\mathbf{x}, t) = \sum_{rec} \int_0^{T_{\max}} dt' G_z(\mathbf{x}_{rec}, t'; \mathbf{x}, t) \delta E_z(\mathbf{x}_{rec}, t'). \quad (3.16c)$$

The integrands in (3.16a) and (3.16b) can be interpreted as zero-lag cross-correlations (Tarantola, 2005), whereas (3.16c) corresponds to a Green's-function-based solution that describes the electric field  $\tilde{E}_z$  at location  $\mathbf{x}$  and time  $t$ , assuming that the residual fields  $\delta E_z$  at all receiver locations are simultaneously backward propagated in time.

### 3.3.3.3. UPDATE STEP LENGTHS $\zeta_{\hat{\epsilon}}$ AND $\zeta_{\hat{\sigma}}$

The updates to the step lengths  $\zeta_{\hat{\epsilon}}$  and  $\zeta_{\hat{\sigma}}$  follow closely the approach introduced by Pica et al. (Pica et al., 1990), in which:

$$\zeta_{\hat{\epsilon}} = \kappa_{\hat{\epsilon}} \frac{\left( E_z(\hat{\boldsymbol{\epsilon}} + \kappa_{\hat{\epsilon}} \boldsymbol{\gamma}_{\hat{\epsilon}}, \hat{\boldsymbol{\sigma}}) - E_z(\hat{\boldsymbol{\epsilon}}, \hat{\boldsymbol{\sigma}}) \right)^T \left( E_z(\hat{\boldsymbol{\epsilon}}, \hat{\boldsymbol{\sigma}}) - E_z^{obs} \right)}{\left( E_z(\hat{\boldsymbol{\epsilon}} + \kappa_{\hat{\epsilon}} \boldsymbol{\gamma}_{\hat{\epsilon}}, \hat{\boldsymbol{\sigma}}) - E_z(\hat{\boldsymbol{\epsilon}}, \hat{\boldsymbol{\sigma}}) \right)^T \left( E_z(\hat{\boldsymbol{\epsilon}} + \kappa_{\hat{\epsilon}} \boldsymbol{\gamma}_{\hat{\epsilon}}, \hat{\boldsymbol{\sigma}}) - E_z(\hat{\boldsymbol{\epsilon}}, \hat{\boldsymbol{\sigma}}) \right)}, \quad (3.17a)$$

and

$$\zeta_{\hat{\sigma}} = \kappa_{\hat{\sigma}} \frac{\left( E_z(\hat{\boldsymbol{\epsilon}}, \hat{\boldsymbol{\sigma}} + \kappa_{\hat{\sigma}} \boldsymbol{\gamma}_{\hat{\sigma}}) - E_z(\hat{\boldsymbol{\epsilon}}, \hat{\boldsymbol{\sigma}}) \right)^T \left( E_z(\hat{\boldsymbol{\epsilon}}, \hat{\boldsymbol{\sigma}}) - E_z^{obs} \right)}{\left( E_z(\hat{\boldsymbol{\epsilon}}, \hat{\boldsymbol{\sigma}} + \kappa_{\hat{\sigma}} \boldsymbol{\gamma}_{\hat{\sigma}}) - E_z(\hat{\boldsymbol{\epsilon}}, \hat{\boldsymbol{\sigma}}) \right)^T \left( E_z(\hat{\boldsymbol{\epsilon}}, \hat{\boldsymbol{\sigma}} + \kappa_{\hat{\sigma}} \boldsymbol{\gamma}_{\hat{\sigma}}) - E_z(\hat{\boldsymbol{\epsilon}}, \hat{\boldsymbol{\sigma}}) \right)}, \quad (3.17b)$$

where  $E_z(\hat{\boldsymbol{\epsilon}}, \hat{\boldsymbol{\sigma}})$  is the synthetic wavefield at receiver locations  $\mathbf{x}_{rec}$  for the model parameter estimates  $(\hat{\boldsymbol{\epsilon}})$  and  $(\hat{\boldsymbol{\sigma}})$ ,  $\kappa_{\hat{\boldsymbol{\epsilon}}}$  and  $\kappa_{\hat{\boldsymbol{\sigma}}}$  are small numbers, and  $E_z(\hat{\boldsymbol{\epsilon}} + \kappa_{\hat{\boldsymbol{\epsilon}}}\boldsymbol{\gamma}_{\hat{\boldsymbol{\epsilon}}}, \hat{\boldsymbol{\sigma}})$  and  $E_z(\hat{\boldsymbol{\epsilon}}, \hat{\boldsymbol{\sigma}} + \kappa_{\hat{\boldsymbol{\sigma}}}\boldsymbol{\gamma}_{\hat{\boldsymbol{\sigma}}})$  are synthetic wavefields computed for perturbed permittivities and conductivities in the respective update directions  $\boldsymbol{\gamma}_{\hat{\boldsymbol{\epsilon}}}$  and  $\boldsymbol{\gamma}_{\hat{\boldsymbol{\sigma}}}$ . Values of  $\kappa_{\hat{\boldsymbol{\epsilon}}}$  and  $\kappa_{\hat{\boldsymbol{\sigma}}}$  are chosen after the first iteration. For the tests described here,  $\kappa_{\hat{\boldsymbol{\epsilon}}} = 10^{-5}$  and  $\kappa_{\hat{\boldsymbol{\sigma}}} = 1.0$  were found to be suitable.

### 3.3.4. IMPLEMENTATION

#### 3.3.4.1. STEPPED INVERSION FOR DIELECTRIC PERMITTIVITY AND ELECTRICAL CONDUCTIVITY

In principle, we could update the dielectric permittivities and electrical conductivities simultaneously after each iteration. Unfortunately, large differences between the magnitudes of the permittivity and conductivity Fréchet derivatives (even though they are not explicitly calculated) cause the simultaneous inversion process to fail for complex models (for a discussion of the equivalent acoustic problem see (Watanabe et al., 2004)). Because the phases and the amplitudes of the observed signals are primarily controlled by the permittivity and conductivity, respectively, this problem can be circumvented by adopting a stepped approach that involves inverting for the permittivities while keeping the conductivities fixed and then inverting for the conductivities while keeping the permittivities fixed. The procedure may be repeated until satisfactory convergence is achieved. For all examples presented in this paper, only a single computational cycle was required.

For the dielectric permittivities, we suppress the amplitude information by back-propagating the following normalized version of the data residuals (see also Watanabe et al., 2004):

$$\delta E(\mathbf{x}_{rec}, t) = E_z^{obs}(\mathbf{x}_{rec}, t) - \frac{\sqrt{\int_0^{T_{max}} dt [E_z^{obs}(\mathbf{x}_{rec}, t)]^2}}{\sqrt{\int_0^{T_{max}} dt [E_z^{syn}(\mathbf{x}_{rec}, t)]^2}} E_z^{syn}(\mathbf{x}_{rec}, t). \quad (3.18)$$

By including realistic conductivities in the input model (e.g., those obtained with ray amplitude inversion), we partly account for the effects of electrical conductivity on the phases (e.g., Cai et al., 1996). After determining the distribution of permittivities, the residual

wavefield is computed without normalization (i.e., square-root terms in (3.18) are 1) and then used for the conductivity inversion.

### 3.3.4.2. COMPUTATIONAL ISSUES

Our full-waveform inversion scheme requires the forward problem to be solved three times per iteration for each transmitter location: once to evaluate the synthetic data  $E_z$  (step 2 of our implementation of Polak and Ribiere's (1969) algorithm), once to compute the update directions [step 3, (3.16)], and once to determine the step length [step 4, (3.17)]. Consequently, the computational costs of the forward modeling largely control the efficiency of our waveform inversion scheme.

Using FDTD techniques to solve the forward problem for a typical crosshole radar data set requires  $10^5$  to  $10^6$  grid points and a few tens of transmitter positions, for which a few thousand time steps need to be computed. For computation of the update directions (3.16), the complete  $E_z$  fields generated by all transmitters at all grid locations need to be kept in memory. This would require a large core memory of about  $20 \times N_{\text{tm}}$  GBytes, where  $N_{\text{tm}}$  is the number of transmitters. However, the spatial resolution of the data is much lower than the discretization needed for accurate forward modeling, so that a number of forward modeling cells can be represented with a single inversion cell. We include  $3 \times 3$  forward modeling cells within one inversion cell without a loss of resolution in the inversion process. This reduces the memory requirements by roughly an order-of-magnitude, thus making the computations tractable without having to implement time-consuming memory-swapping procedures. Furthermore, because the single transmitter calculations are largely independent of each other, the computational scheme can be implemented efficiently on a distributed computer network comprising one CPU per transmitter plus a master CPU. The overhead for distributing the computations is only about 10%. Accordingly, the total computational time  $T_{\text{comp}}$  required for a complete inversion is given by:

$$T_{\text{comp}} \approx 3 \cdot 1.1 \cdot T_{\text{forward}} \cdot N_{\text{iter}} \quad (3.19)$$

where  $T_{\text{forward}}$  is the time required for a single forward calculation and  $N_{\text{iter}}$  is the number of iterations. On a PC cluster consisting of Opteron 244 processors with 4 GByte of memory, the computational time for a single-parameter inversion with  $10^5$  forward grid points requires 3 hours, whereas that for a two-parameter inversion with  $10^6$  forward grid points requires 18 hours.

**Table 3.1.** Model parameters. Homogeneous models were used as input for all ray tomographic inversions. The relative permittivities and conductivities of these models are provided in the last column.

Model # and numerical experiments (Figures)	Model width & depth [m]	#Transmitters / #receivers	Medium parameters $\epsilon_r$ and $\sigma$ [mS/m]	Anomalous object dimensions [m]	Added noise [%]	Initial parameters for ray tomography $\epsilon_r$ and $\sigma$ [mS/m]
<b>1</b> $\epsilon$ inversion (3.2, 3.3)	10 & 10	21 / 21	$\epsilon_{rm} = 4.0$ ; $\sigma_m = 0.1$ $\epsilon_{ra} = 5.0$ ; $\sigma_a = 0.1$	0.5	0, 5, 20	$\epsilon_r = 4.0$ $\sigma = 0.1$
<b>2</b> $\sigma$ inversion (3.4, 3.5)	10 & 10	21 / 21	$\epsilon_{rm} = 4.0$ ; $\sigma_m = 0.1$ $\epsilon_{ra} = 4.0$ ; $\sigma_a = 10.0$	0.5	0, 5, 20	$\epsilon_r = 4.0$ $\sigma = 0.1$
<b>3</b> $\epsilon$ & $\sigma$ inversions (3.6, 3.7)	10 & 10	21 / 21	$\epsilon_{rm} = 4.0$ ; $\sigma_m = 3.0$ $\epsilon_{rb} = 5.0$ ; $\sigma_b = 10.0$ $\epsilon_{rc} = 3.0$ ; $\sigma_c = 0.1$	0.5 & 0.5	0, 5	$\epsilon_r = 4.0$ $\sigma = 3.0$
<b>4</b> $\epsilon$ & $\sigma$ inversions (3.8, 3.9)	10 & 20	41 / 41	$\epsilon_{r1} = 5.2$ ; $\sigma_1 = 2.8$ $\epsilon_{r2} = 3.7$ ; $\sigma_2 = 2.0$ $\epsilon_{r3} = 5.0$ ; $\sigma_3 = 0.1$	-	0	$\epsilon_r = 3.4$ $\sigma = 1.3$
<b>5</b> $\epsilon$ & $\sigma$ inversions (3.10, 3.11)	10 & 20	41 / 41	As for model 4 plus stochastic variations with standard deviations of $\epsilon_r = 0.1$ , $\sigma = 0.5$ and correlation lengths of $x = 1.0$ m, $z = 0.2$ m	-	0	$\epsilon_r = 3.4$ $\sigma = 1.3$
<b>6</b> $\epsilon$ & $\sigma$ inversions (3.12, 3.13)	10 & 20	41 / 41	As for model 4 plus stochastic variations with standard deviations of $\epsilon_r = 0.3$ , $\sigma = 1.5$ and correlation lengths of $x = 1.0$ m, $z = 0.2$ m	-	0	$\epsilon_r = 3.4$ $\sigma = 1.3$
<b>7</b> $\epsilon$ & $\sigma$ inversions (3.14, 3.15)	10 & 20	41 / 41	As for model 4 plus pipes and tunnel with $\epsilon_{rp} = \epsilon_{rt} = 80.0$ $\sigma_p = \sigma_t = 10.0$	pipes: 0.5, 0.5, 0.5 tunnel: 2.0	0	$\epsilon_r = 3.4$ $\sigma = 1.3$
<b>8</b> $\epsilon$ & $\sigma$ inversions (3.16, 3.17)	10 & 20	41 / 41	As for model 5 plus pipes and tunnel with $\epsilon_{rp} = \epsilon_{rt} = 80.0$ $\sigma_p = \sigma_t = 10.0$	pipes: 0.5, 0.5, 0.5 tunnel: 2.0	0	$\epsilon_r = 3.4$ $\sigma = 1.3$
<b>9</b> $\epsilon$ & $\sigma$ inversions (3.18, 3.19)	10 & 20	41 / 41	As for model 6 plus pipes and tunnel with $\epsilon_{rp} = \epsilon_{rt} = 80.0$ $\sigma_p = \sigma_t = 10.0$	pipes: 0.5, 0.5, 0.5 tunnel: 2.0	0	$\epsilon_r = 3.4$ $\sigma = 1.3$

### 3.4. APPLICATIONS TO SYNTHETIC DATA

We explore the potential and limitations of our full-waveform tomographic inversion scheme using synthetic data generated from a suite of increasingly complex models. The models and acquisition geometries are shown in Figure 3.1 and the key parameters are summarized in Table 3.1. For the first three numerical experiments (Figure 3.1a), two 10-m-deep boreholes are separated by 10 m and the forward and inverse grids have spacings of 0.02 and 0.06 m, respectively. There are 21 equally spaced transmitter antenna locations in the left borehole and 21 equally spaced receiver antenna locations in the right borehole. The model space is surrounded by a 0.8-m-thick GPML frame. For the other experiments (Figure 3.1b), the borehole depths are increased to 20 m depth and the number of transmitters and receivers are increased to 41. All other acquisition parameters are identical to those of the first three experiments.

We employed the same FDTD code to create the synthetic data and to solve the forward problems in the inversion process. The waveform of the source signal corresponded to a Gaussian pulse with a nominal frequency of  $\sim 150$  MHz and a bandwidth of  $\sim 3$  octaves, which yielded a dominant wavelength of  $\sim 1$  m in our models.

To begin the inversion process, we applied conventional ray tomography using the first-arrival times and maximum first-cycle amplitudes (Holliger et al., 2001; Holliger and Maurer, 2004; Musil et al., 2006) to obtain velocity and attenuation tomograms that were converted to corresponding dielectric permittivity and electrical conductivity distributions

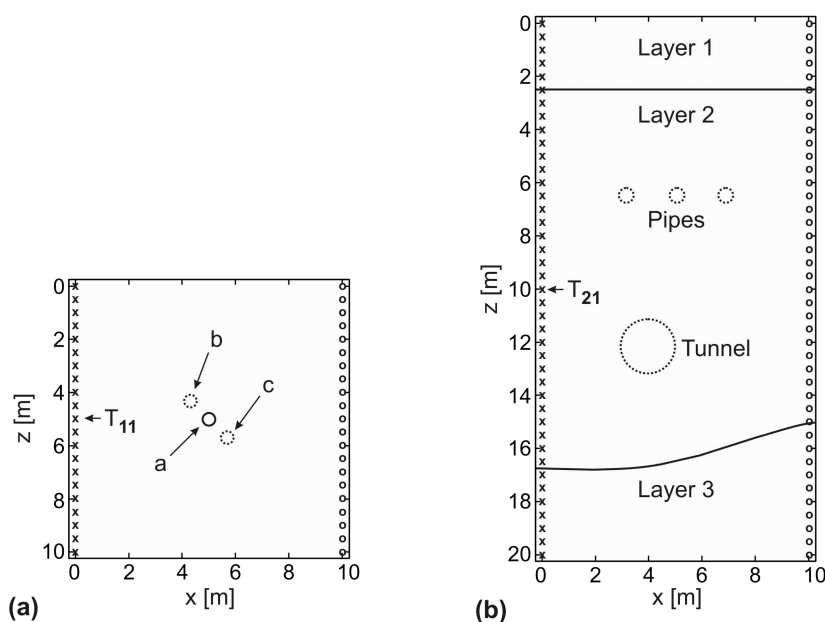


**Figure 3.1:** Generic models and crosshole source-receiver configurations used for all computations. (a) Single anomalous object "a" or double anomalous objects "b" and "c" embedded in various media. (b) Three-layered geological structure containing three pipes and a tunnel. Transmitter (T) and receiver (R) locations are indicated by crosses and open circles. For the various synthetic computations, source gathers are presented for transmitter positions T11 in Figure 3.1a or T21 in Figure 3.1b.

using the following high-frequency approximations:

$$\varepsilon \approx \frac{1}{\mu_0} v^{-2} \quad (3.20a)$$

and

$$\sigma \approx 2\alpha \sqrt{\frac{\varepsilon}{\mu_0}} \quad (3.20b)$$

where  $v$  and  $\alpha$  are velocity and attenuation. The resulting  $\varepsilon$  and  $\sigma$  distributions (our optimum ray tomograms) were then used as the initial models for the full-waveform tomographic inversions. The  $\varepsilon$  and  $\sigma$  computations usually converged after 20 and 10 iterations, respectively. For convenience, we describe our models in the following in terms of the relative permittivity  $\varepsilon_r = \varepsilon / \varepsilon_0$ . Initial  $\varepsilon_r$  and  $\sigma$  values (converted to corresponding velocities

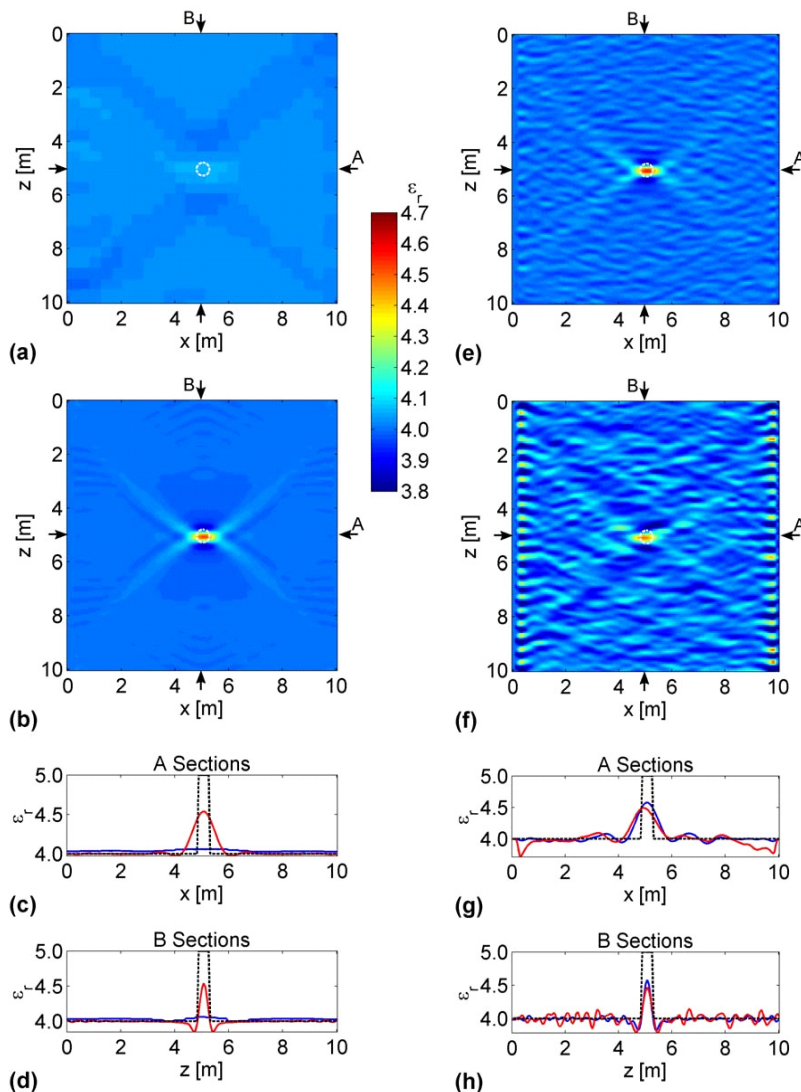


**Figure 3.2:** Relative permittivity ( $\varepsilon_r$ ) tomograms and cross-sections derived from synthetic radar traces generated for input model 1 (Table 3.1) with medium relative permittivity  $\varepsilon_{rm} = 4.0$ , medium conductivity  $\sigma_m = 0.1$  mS/m, and a single small object (a in Figure 3.1a) with  $\varepsilon_{ra} = 5.0$  and  $\sigma_a = 0.1$  mS/m. (a) and (b) Tomograms that result from applying ray-based and full-waveform inversion schemes to noise-free synthetic radar traces. Dashed white circles delineate the object's true location. (c) Blue, red, and black lines are the A cross-sections through the tomogram in (a), tomogram in (b), and input model. (d) Similar to (c), but for the B cross-sections. (e) and (f) Tomograms that result from applying the full-waveform inversion scheme to synthetic radar traces contaminated with 5 and 20% random noise. (g) Blue, red, and black lines are the A cross-sections through the tomogram in (e), tomogram in (f), and input model. (h) Similar to (g), but for the B cross-sections.



and attenuations) used to start the ray tomographic inversions are shown in the last column of Table 3.1.

### 3.4.1. NUMERICAL EXPERIMENT 1: SINGLE DIELECTRIC OBJECT IN A HOMOGENEOUS MEDIUM

Model 1 comprises a high-permittivity circular object (a in Figure 3.1a;  $\epsilon_{ra} = 5.0$ ) embedded in the center of a homogeneous medium ( $\epsilon_{rm} = 4.0$ ). The diameter of the anomalous object is  $\sim 0.5$  m, about half the dominant signal wavelength. Conductivities are low (0.1 mS/m) and homogeneous throughout the model. For two of the inversions, 5% and 20% band-limited white noise is added to the synthetic input traces (Table 3.1). The bandwidth of the noise is chosen to mimic that of observed radargrams.

Relative permittivity tomograms for the noise-free ray and full-waveform inversions are displayed in Figures 3.2a and 3.2b and those for the full-waveform inversions with 5 and

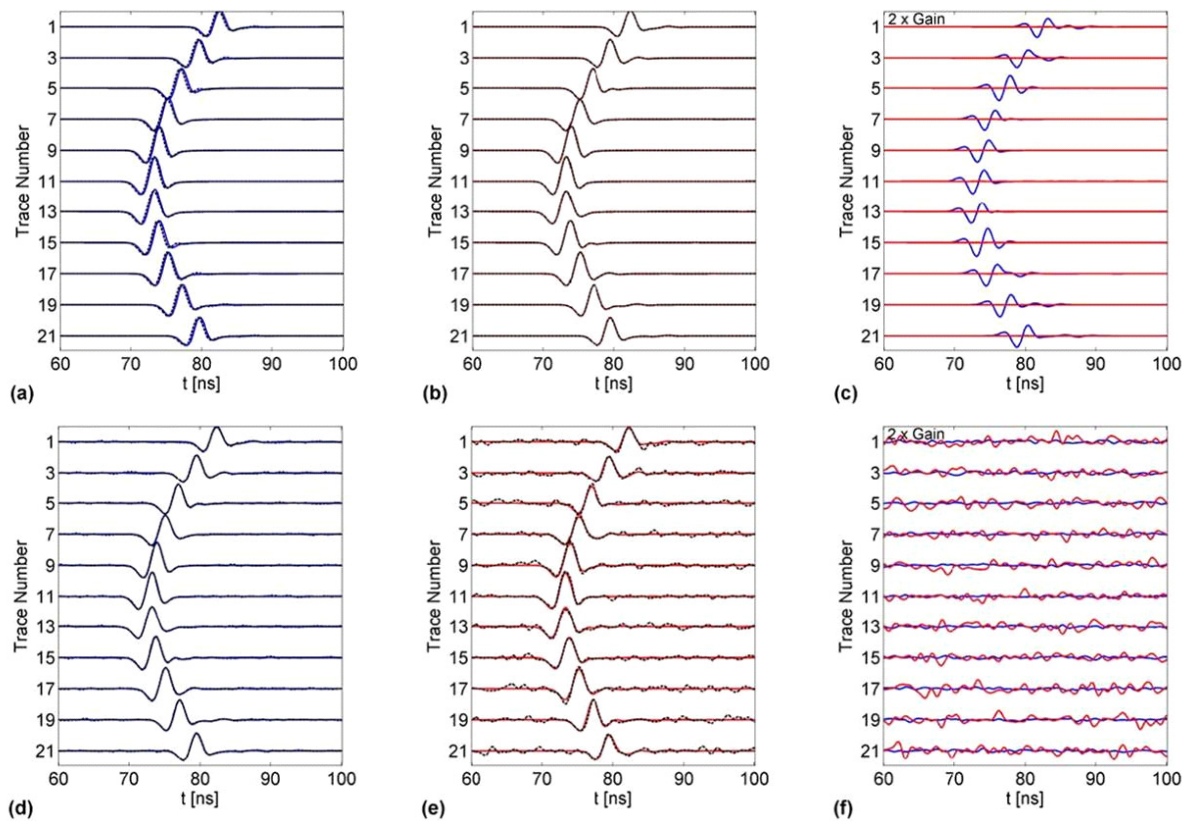


**Figure 3.3:** (a) and (b) For the transmitter located at position T11 in Figure 3.1a, the blue, red, and dashed black lines display every second radar trace generated from the ray tomogram in Figure 3.2a, full-waveform tomogram in Figure 3.2b, and original input model. (c) Blue and red lines show differences between the blue and dashed black lines in (a) and between the red and dashed black lines in (b), respectively. (d) and (e) Similar to (a) and (b), but for the full-waveform tomograms in Figures 3.2e and 3.2f derived from radar traces contaminated with 5 and 20% random noise. (f) Similar to (c), but for the blue, red and dashed black lines in (d) and (e). The amplitudes of all traces in any radar section are normalized with respect to the maximum amplitude of input trace 11. The amplitudes of residuals in (c) and (f) are gained by a factor of 2 relative to the respective radar traces.

20% noise are presented in Figures 3.2e and 3.2f. To quantify better the reconstructed  $\epsilon_r$  values, cross-sections through the tomograms along A and B are shown in Figures 3.2c, 3.2d, 3.2g, and 3.2h. Ray tomography barely detects the presence of the sub-wavelength object, whereas full-waveform tomography successfully recovers its location and size. The object's distorted shape in Figure 3.2b is a consequence of the limited apertures of the transmitter and receiver antenna arrays; additional antennas below and/or above the object would substantially improve the resolution of the shape. The recovered maximum relative permittivity of 4.5 is a little lower than the true 5.0 value. Adding realistic levels of random noise to the data does not significantly affect the convergence and reconstruction capabilities of the full-waveform inversion scheme (Figures 3.2e - 3.2h). To account for the noise, the inversion process introduces scatterers that appear as small-scale fluctuations in the tomograms. These artifacts are most pronounced in the highly sensitive areas of the models (e.g., in the vicinity of transmitters and receivers). Application of appropriate regularization (e.g., Tarantola, 2005) might reduce the effects of these artifacts. As a further check, we also invert for conductivity, which remained even after a few iteration unchanged (not shown).

Selected traces extracted from FDTD simulations of radar waves traveling through the tomograms of Figure 3.2 are compared to the original model input traces (Figure 3.3). Traces based on the ray tomogram (blue lines in Figure 3.3a) have a slight phase shift relative to the input traces (dashed black lines in Figure 3.3). Close inspection of radargrams demonstrates that the automatic routine for recognizing signal onsets mis-identifies the true first breaks by  $\sim 0.2$  ns (2 - 3 samples). Traces based on the full-waveform tomograms (red lines in Figure 3.3b) are practically identical to the input traces (dashed black lines in Figure 3.3b). These similarities and differences are emphasized in Figure 3.3c, which shows residual traces (i.e., differences between the simulated and input data) for simulations based on the ray and full-waveform tomograms.

Figures 3.3d and 3.3e compare simulated traces based on the tomograms of Figures 3.2e and 3.2f with the two suites of noisy input data. The corresponding residual traces in Figure 3.3f are dominated by moderately high-frequency fluctuations, demonstrating the robustness of the full-waveform inversion scheme to the presence of random noise.

### **3.4.2. NUMERICAL EXPERIMENT 2: SINGLE CONDUCTIVE OBJECT IN A HOMOGENEOUS MEDIUM**

For model 2, we replace the sub-wavelength dielectric object of model 1 with a conductive one (a in Figure 3.1a and Table 3.1) and repeat the series of computations (Figures

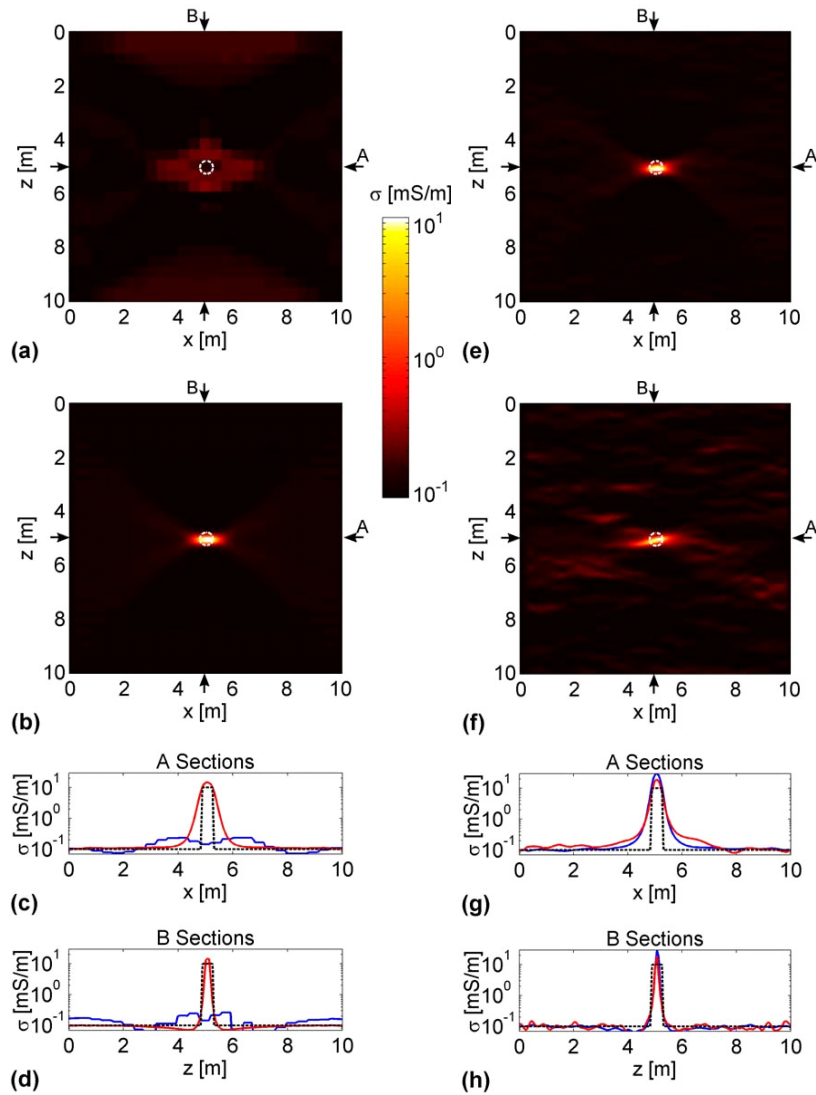


**Figure 3.4:** Conductivity ( $\sigma$ ) tomograms and cross-sections derived from synthetic radar traces generated for input model 2 (Table 3.1) with medium relative permittivity  $\epsilon_{rm} = 4$ , medium conductivity  $\sigma_m = 0.1$  mS/m, and a single small object (a in Figure 3.1a) with  $\epsilon_{ra} = 4$  and  $\sigma_a = 10.0$  mS/m. All other details are explained in the caption to Figure 3.2.

3.4 and 3.5). The constant permittivity ( $\epsilon_{rm} = 4.0$ ) throughout the model results in straight ray paths. Although the anomalous object is 100 times more conductive than its host medium (10 mS/m versus 0.1 mS/m), there are only tiny differences between synthetic traces computed for this model and those computed for a uniform homogeneous model (not shown). The conductivity tomogram and cross-sections in Figures 3.4a, 3.4c and 3.4d show that ray tomography, again, barely detects the presence of the anomalous object. By comparison, the anomaly's location, size, and conductivity are satisfactorily reproduced in the full-waveform tomograms, even in those based on the noisy traces (Figures 3.4b to 3.4h). As in numerical experiment 1, the shape of the reconstructed object is somewhat distorted.

Since we are primarily interested in the role played by conductivity in this experiment, we use the correct constant permittivity to simulate traces based on the conductivity ray tomogram of Figure 3.5a (note the absence of anomalous phase shift in this figure). Even though differences between the simulated and input traces in Figure 3.5a are quite small (the

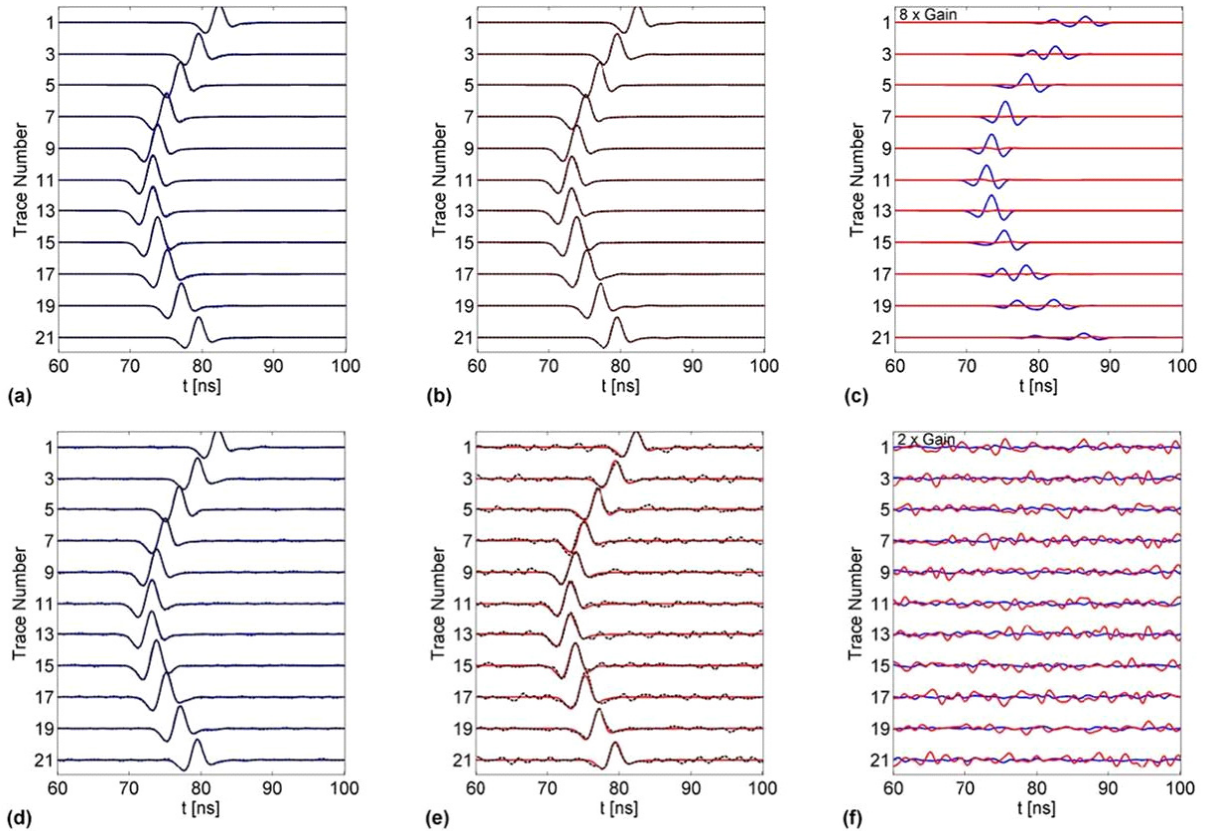


**Figure 3.5:** Similar to Figure 3.3, but showing radar sections and residuals for the inversion results illustrated in Figure 3.4. The amplitudes of residuals in (c) and (f) are gained by factors of 8 and 2 relative to the respective radar traces.

differences are magnified by a factor of 8 in Figure 3.5c), the resolution of the conductivity tomogram is poor (Figure 3.4a). In contrast, the even smaller differences between simulated and input traces in Figure 3.5b (see also Figure 3.5c) result from the high-resolution waveform-based tomogram of Figure 3.4b. Furthermore, traces based on the full-waveform tomograms derived from the noisy data match well with the input noisy traces (Figures 3.5d to 3.5f).

### 3.4.3. NUMERICAL EXPERIMENT 3: TWO DIELECTRIC-CONDUCTIVE OBJECTS IN A HOMOGENEOUS MEDIUM

Model 3 contains two sub-wavelength objects: a high-permittivity/high-conductivity object (b in Figure 3.1a and Table 3.1) intended to represent a water-saturated porous zone and a low-permittivity/low-conductivity object (c in Figure 3.1a and Table 3.1) intended to represent an air-filled porous zone. The two 0.5-m-diameter objects are separated by  $\sim 1.5$  m in an otherwise homogeneous background medium. The first-break times for the ray inversion are picked from noise-free traces, whereas the input traces for the full-waveform inversion contain 5% noise.

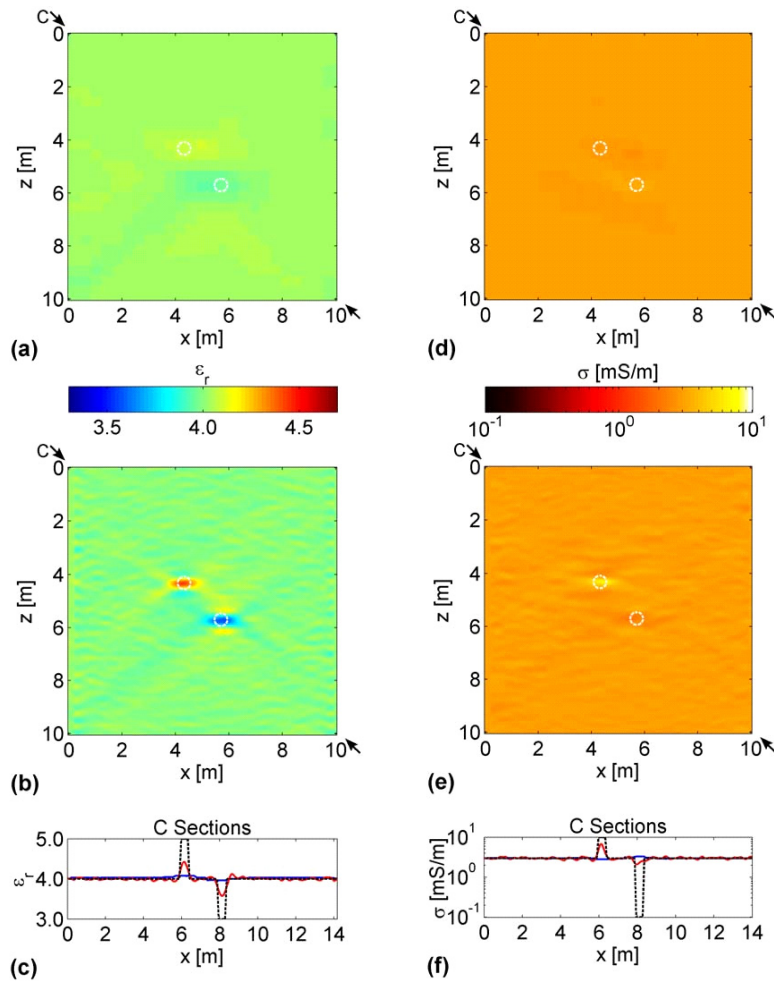


**Figure 3.6:** Relative permittivity ( $\epsilon_r$ ) and conductivity ( $\sigma$ ) tomograms and cross-sections derived from synthetic radar traces generated for input model 3 (Table 3.1) with medium relative permittivity  $\epsilon_{rm} = 4.0$ , medium conductivity  $\sigma_m = 3.0$  mS/m, and two small objects (b and c in Figure 3.1a), the upper with  $\epsilon_{rb} = 5.0$  and  $\sigma_b = 10.0$  mS/m and the lower with  $\epsilon_{rc} = 3.0$  and  $\sigma_c = 0.1$  mS/m. (a) and (d)  $\epsilon_r$  and  $\sigma$  tomograms that result from applying the ray-based inversion scheme to noise-free synthetic radar traces. (b) and (e) Similar to (a) and (d), but showing the results of applying the full-waveform inversion scheme to radar traces contaminated with 5% random noise. (c) Blue, red, and black lines are diagonal cross-sections C through the tomogram in (a), tomogram in (b), and input model. (d) Blue, red, and black lines are diagonal cross-sections C through the tomogram in (d), tomogram in (e), and input model. Dashed white circles in (a), (b), (d), and (e) delineate the objects' true locations.

Neither object is clearly distinguishable in the permittivity and conductivity ray tomograms (Figures 3.6a, 3.6c, 3.6d and 3.6f). Although there is additional smearing relative to the model 1 and 2 results, the permittivity and conductivity full-waveform tomograms successfully predict the location and size of the high-permittivity/high-conductivity object (Figures 3.6b, 3.6c, 3.6e and 3.6f). The low-permittivity/low-conductivity object is also well resolved in the permittivity full-waveform tomogram, but it only appears as a small deviation from noisy background values in the conductivity tomogram (Figure 3.6f). We also note that the predicted permittivity and conductivity contrasts for both objects are notably smaller than the original model. Nevertheless, traces simulated from the full-waveform tomograms correspond closely to the input traces (Figures 3.7b and 3.7c), demonstrating that we are approaching the resolution limits of the full-waveform inversion scheme with this combination of model and borehole geometry.

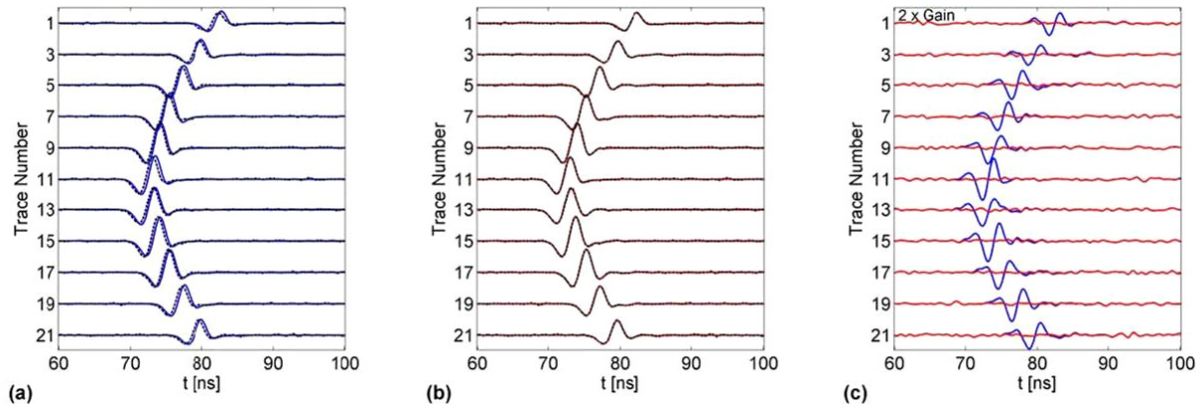


**Figure 3.7:** (a) and (b) For the transmitter located at position T11 in Figure 3.1a, the blue, red, and dashed black lines show every second radar trace generated from the ray tomograms in Figures 3.6a and 3.6d, full-waveform tomograms in Figures 3.6b and 3.6e, and original input model. (c) Blue and red lines show differences between the blue and dashed black lines in (a) and between the red and dashed black lines in (b), respectively. The amplitudes of residuals in (c) are gained by a factor of 2 relative to the radar traces.

#### 3.4.4. NUMERICAL EXPERIMENTS 4 - 6: LAYERED MODELS WITH AND WITHOUT STOCHASTIC VARIATIONS

Many subsurface environments are distinguished by physical properties that vary substantially over a wide range of scales. Generally, the large-scale structures can be treated in a deterministic fashion, but many small-scale features need to be handled as stochastic phenomena (Hewett, 1986; Goff and Jennings, 1999; Tronicke and Holliger, 2005). For the next three numerical experiments, we estimate the electrical properties and boundaries of three models that contain three distinct layers with different permittivity and conductivity distributions (Figures 3.8, 3.10 and 3.12). The average media properties for all three models are: layer 1,  $\epsilon_{r1} = 5.2$  and  $\sigma_2 = 2.8$  mS/m; layer 2,  $\epsilon_{r2} = 3.7$  and  $\sigma_2 = 2.8$  mS/m; layer 3,  $\epsilon_{r3} = 5.0$  and  $\sigma_3 = 0.1$  mS/m (models 4 - 6 in Table 3.1). Layers in model 4 and the lowermost layer of models 5 and 6 are homogeneous. Stochastic variations of relative permittivity and conductivity characterized by exponential covariance functions with 0.1 and 0.5 mS/m standard deviations and 1.0 m horizontal and 0.2 m vertical correlation lengths are added to the upper two layers of model 5. For model 6, we increase the standard deviations to 0.3 and 1.5 mS/m. The synthetic input data used for these numerical experiments are noise-free. Figure 3.1b shows the source-receiver geometries.

For all three synthetic data sets, ray-based inversions of the automatically picked first-arrival times reproduce the permittivities and approximate depths and shapes of the layer boundaries (compare Figures 3.8a and 3.8b, 3.10a and 3.10b, and 3.12a and 3.12b), whereas inversions of the maximum first-cycle amplitudes produce only poor representations of the

conductivity distributions (compare Figures 3.8d and 3.8e, 3.10d and 3.10e, and 3.12d and 3.12e). In these examples, the amplitude ray tomography is clearly deficient. The conductivities do not move sufficiently far from the initial value of 1.3 mS/m (see last column of Table 3.1). As a consequence, the first-cycle amplitudes of some traces are inadequately explained by the ray tomograms (Figures 3.9a - 3.13a and 3.9c - 3.13c).

Many fine details of the stochastic permittivity and conductivity variations and reliable information on the layer boundaries are provided by the full-waveform tomograms (Figures 3.8c, 3.8f, 3.10c, 3.10f, 3.12c, and 3.12f). The estimated permittivities and conductivities throughout the well-sampled areas of the middle layer are accurate and those of the sparsely sampled upper and lower layers are good approximations. The full-waveform tomograms are distinguished by correctly located layer boundaries that are sharper than those in the ray tomograms. Traces generated from the full-waveform tomograms are very similar to the

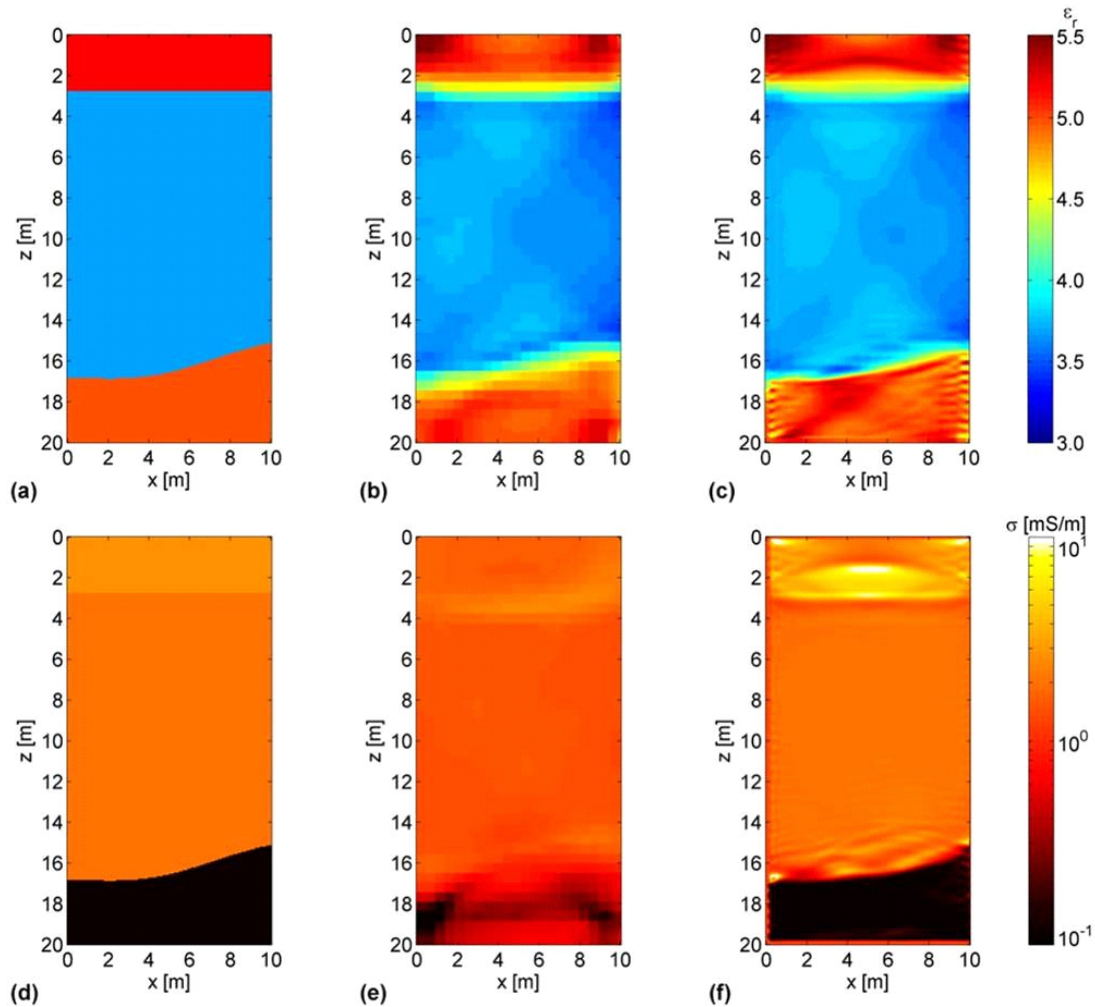


**Figure 3.8:** (a) and (d) Input  $\epsilon_r$  and  $\sigma$  values for model 4 (similar to Figure 3.1b, but without the pipes and tunnel; Table 3.1). Parameters of the 3 layers are:  $\epsilon_{r1} = 5.2$  and  $\sigma_1 = 2.8$  mS/m,  $\epsilon_{r2} = 3.7$  and  $\sigma_2 = 2.0$  mS/m, and  $\epsilon_{r3} = 5.0$  and  $\sigma_3 = 0.1$  mS/m. (b) and (e)  $\epsilon_r$  and  $\sigma$  tomograms that result from applying the ray-based inversion scheme to noise-free synthetic radar traces generated from model 4. (c) and (f) Similar to (b) and (e), but for the results of the full-waveform inversions.

original synthetic data (Figures 3.9b - 3.13b and 3.9c - 3.13c). Small-scale fluctuations near the transmitters and receivers in Figures 3.8c, 3.8f, 3.10c, 3.10f, 3.12c, and 3.12f are again artifacts that result from not using regularization in the full-waveform inversion process.

Increasing the level of stochastic fluctuations eventually results in the layer boundaries being poorly resolved in the original models. Nevertheless, the full-waveform tomographic inversion scheme can still resolve most of the significant permittivity and conductivity variations.

### 3.4.5. NUMERICAL EXPERIMENTS 7 - 9: LAYERED MODELS WITH AND WITHOUT STOCHASTIC VARIATIONS AND ANTHROPOGENIC FEATURES

For our final numerical experiments, we include three small collinear pipes and a tunnel in the three different layered models (models 7 - 9 in Figures 3.14 - 3.19 and Table 3.1). The 0.5-m-diameter pipes and 2.0-m-diameter tunnel are filled with conductive water ( $\epsilon_{tp} = \epsilon_{tt} = 80.0$ ;  $\sigma_p = \sigma_t = 10.0$  mS/m), such that they are high-attenuation, low-velocity targets.

The presence of the pipes and tunnels only slightly change the average and stochastic electrical properties and layer-boundary depths and shapes in the ray and full-waveform

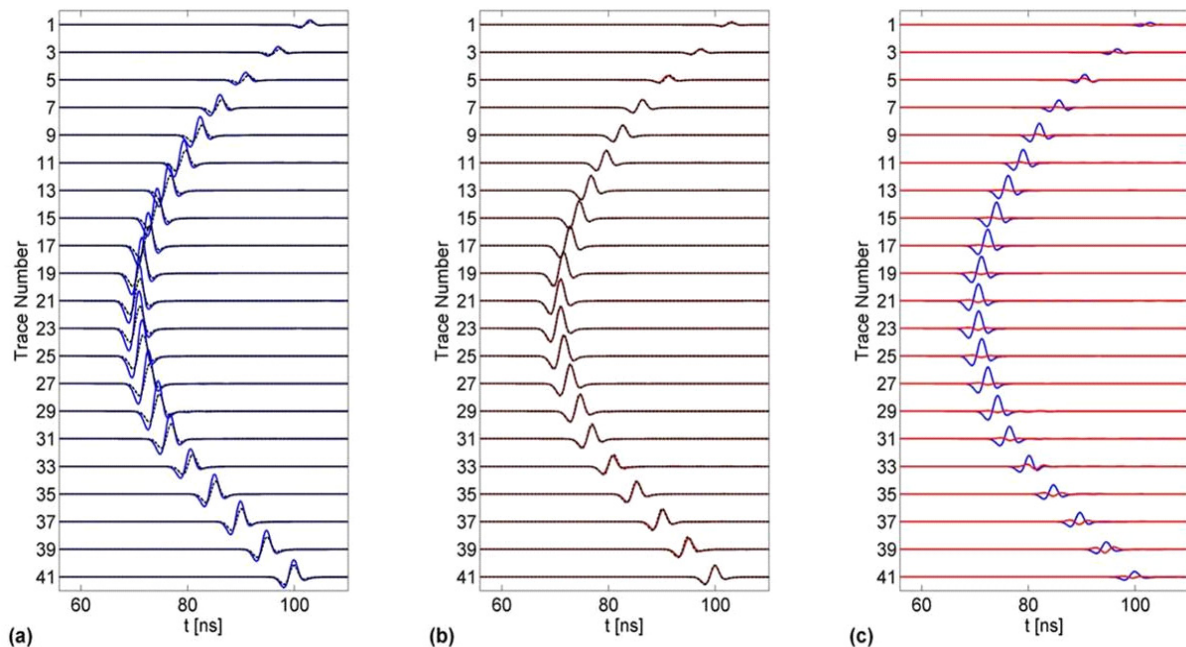


**Figure 3.9:** (a) and (b) For the transmitter located at position T21 in Figure 3.1b, the blue, red, and dashed black lines show every second radar trace generated from the ray tomograms in Figures 3.8b and 3.8e, full-waveform tomograms in Figures 3.8c and 3.8f, and original input model. (c) Blue and red lines show differences between the blue and dashed black lines in (a) and between the red and dashed black lines in (b), respectively. The amplitudes of residuals in (c) are gained by a factor of 2 relative to the radar traces.



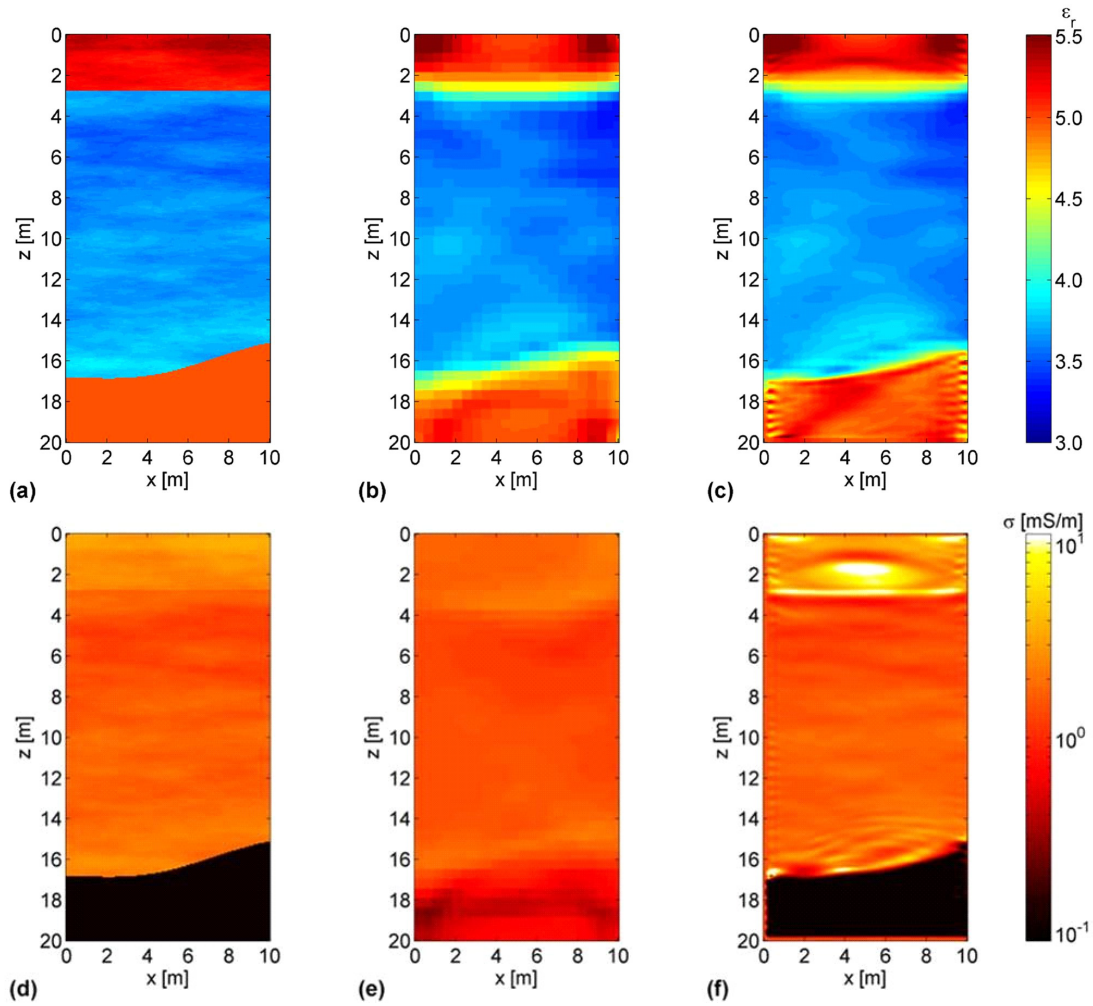


**Figure 3.10:** Similar to Figure 3.8, but with stochastic  $\epsilon_r$  and  $\sigma$  variations added to the top two layers with standard deviations of  $\epsilon_r = 0.1$  and  $\sigma = 0.5$  mS/m and correlation lengths in the  $x$  and  $z$  directions of 1 m and 0.2 m (model 5 in Table 3.1).

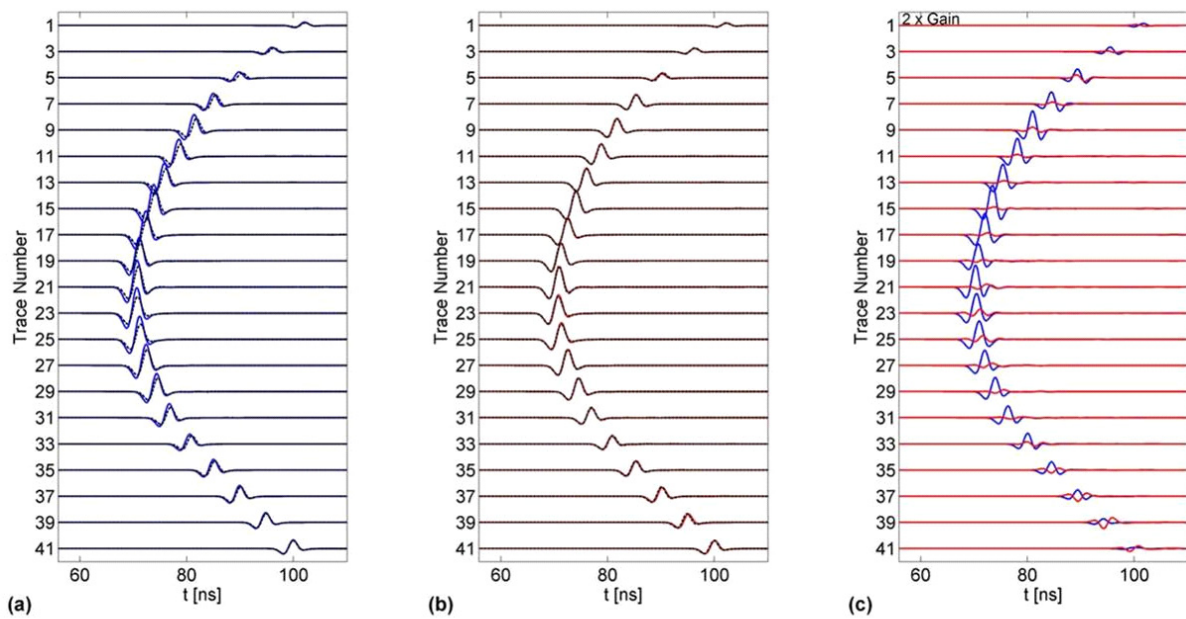


**Figure 3.11:** Similar to Figure 3.9, but for the tomograms in Figure 3.10.

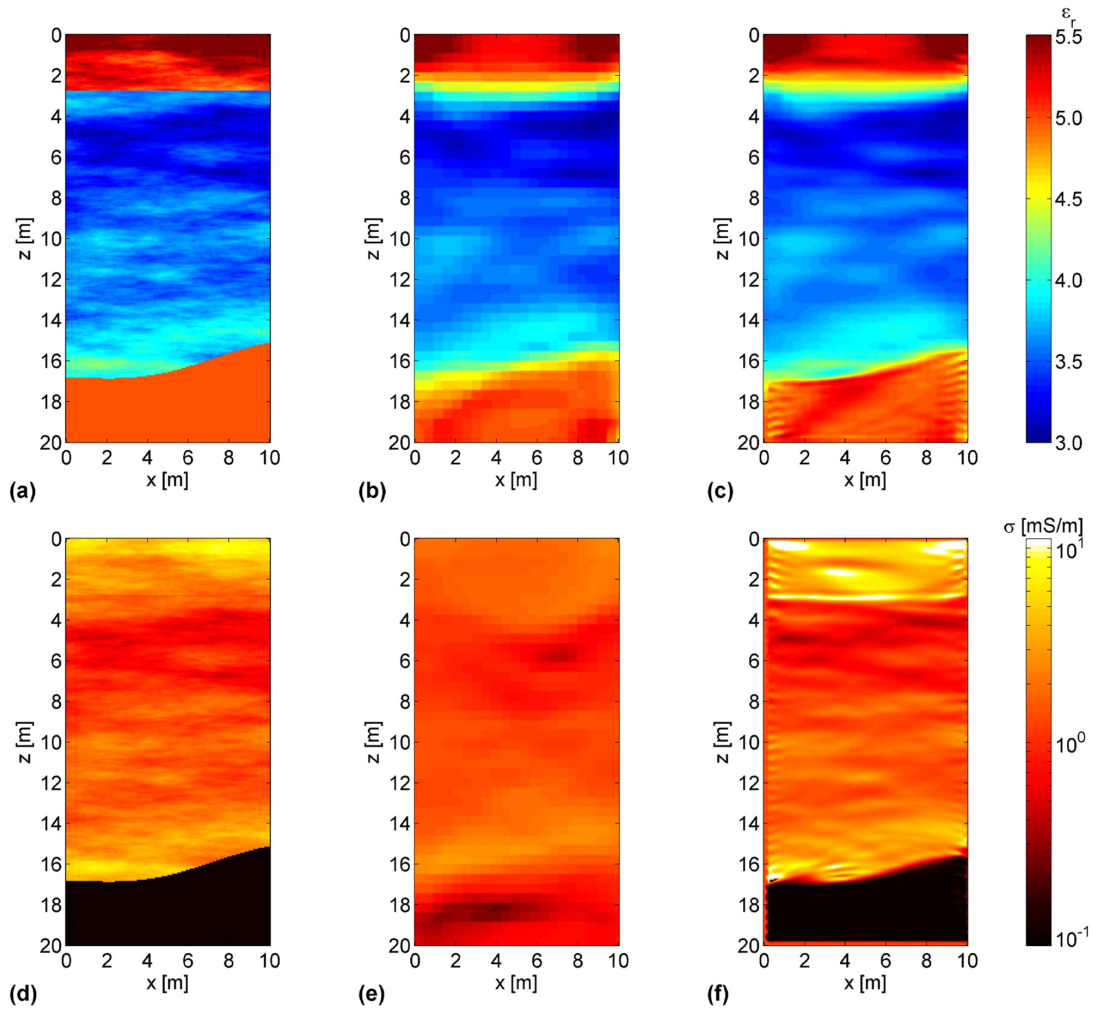


**Figure 3.12:** Similar to Figure 3.8, but with stochastic  $\epsilon_r$  and  $\sigma$  variations added to the top two layers with standard deviations of  $\epsilon_r = 0.3$  and  $\sigma = 1.5$  mS/m and correlation lengths in the  $x$  and  $z$  directions of 1 m and 0.2 m (model 6 in Table 3.1).

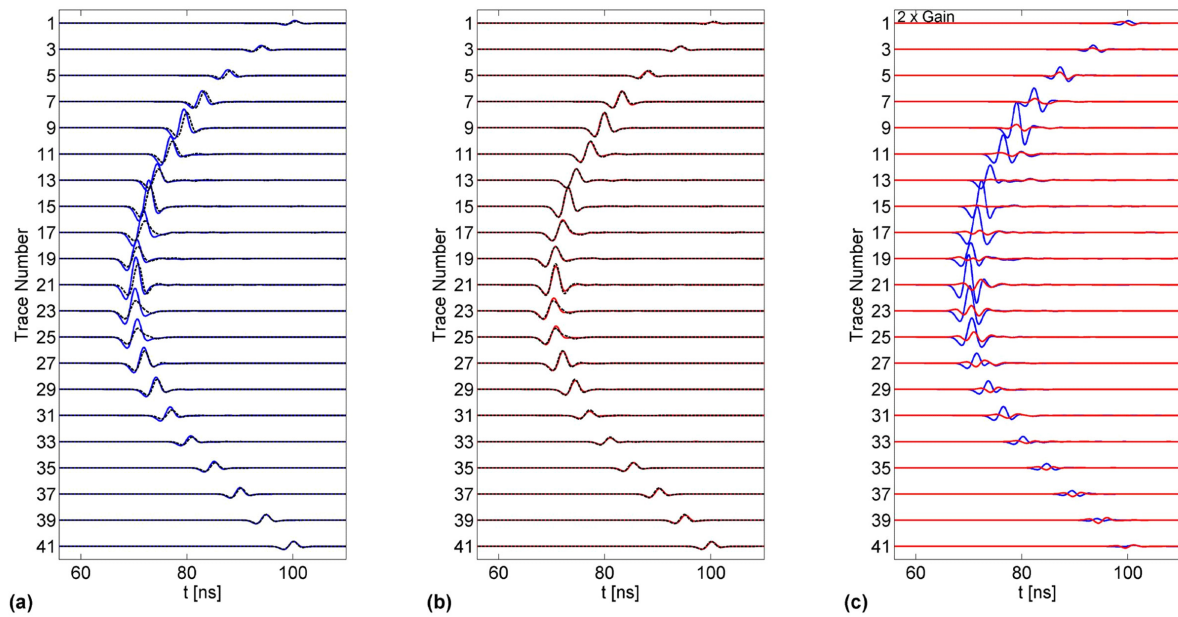


**Figure 3.13:** Similar to Figure 3.9, but for the tomograms in Figure 3.12.

tomograms (compare Figures 3.8, 3.10, and 3.12 with Figures 3.14, 3.16, and 3.18), and the correlations between predicted and original radar traces in Figures 3.15, 3.17, and 3.19 are similar to those in Figures 3.9, 3.11, and 3.13.

Images of the anthropogenic features are very similar in the permittivity tomograms produced by the ray and full-waveform inversions of all three synthetic data sets. Interestingly, for these models the full-waveform permittivity tomograms are only slightly better (i.e., sharper) than the ray-based tomograms. Yet, the full-waveform traces correspond much more closely to the input traces than the ray-based ones (Figures 3.15, 3.17, and 3.19). The size of the circular tunnel is approximately correct in all six permittivity images (Figures 3.14b, 3.14c, 3.16b, 3.16c, 3.18b, and 3.18c), but, as in the examples in Figures 3.2, 3.4, and 3.6, it is slightly elongated in a horizontal direction. Moreover, its relative permittivity is much too low ( $\sim 4.3$  versus 80). A single low-contrast elongated anomaly represents the three collinear pipes in the ray and full-waveform permittivity tomograms of Figures 3.14b, 3.14c, 3.16b and 3.16c, but they are not seen in Figures 3.18b and 3.18c. Considering the dimensions and magnitudes of artifacts in all permittivity tomograms, it is unlikely that the permittivity anomalies caused by the pipes would have been identified as meaningful in a field data set. Identification of the individual collinear pipes embedded in the layered structure appears to be beyond the resolution limits of the full-waveform permittivity inversion.

There are hints of the anthropogenic features in the ray conductivity tomograms, with the size of the tunnel being overestimated and its conductivity contrast underestimated ( $\sim 3$  mS/m versus 10 mS/m; Figures 3.14b - 3.18b). An overly large elongated feature occurs at the depth level of the pipes. In contrast, the sizes, shapes, and conductivity contrasts of the tunnels and individual pipes are accurately reproduced in the full-waveform conductivity tomograms derived from all three synthetic data sets ( $\sim 11$  mS/m for the tunnel and  $\sim 25$  mS/m for the pipes; Figures 3.14c - 3.18c). Considering the relatively poor resolution of the pipes in the full-waveform permittivity tomograms (Figures 3.14c - 3.18c), the high-quality images of the three pipes in the equivalent conductivity tomograms are somewhat surprising (Figures 3.14f - 3.18f).

### 3.5. CONCLUSIONS

We have developed a full-waveform tomographic inversion scheme for crosshole radar data based on a finite-difference time-domain solution of Maxwell's equations and Tarantola's (1984a; 2005) inversion technique. To avoid convergence to local minima in the

search space, ray tomography was used to supply suitable starting models. The new scheme implemented on a PC cluster was applied to synthetic data generated from homogeneous and heterogeneous models containing targets ranging in size from half to twice the dominant signal wavelength.

Our three suites of numerical experiments provided details on the potential and limitations of the new scheme. Full-waveform tomography reproduced the locations, sizes and electrical properties of small (half the dominant signal wavelength) dielectric and conductive objects embedded in a homogenous medium. Neither object was resolved in the ray tomograms. Adding significant levels of band-limited white noise to the radar traces did not markedly degrade the full-waveform tomographic images. Comparably good estimates of target locations and sizes were observed in full-waveform tomograms obtained for a pair of adjacent small objects embedded in a homogeneous medium, one with relatively high permittivity and high conductivity and one with relatively low permittivity and low conductivity. For this model, deviations of the electrical properties were significantly underestimated, yet traces simulated from the full-waveform tomograms were nearly identical to the input traces. We conclude that this particular model and acquisition geometry had approached the resolution limits of the full-waveform inversion scheme.

Results of the second suite of numerical experiments demonstrated the ability of the full-waveform tomographic inversion scheme to reconstruct sharp media boundaries and average and stochastic electric properties of heterogeneous layered models. By comparison, the ray inversion method yielded tomograms in which the media boundaries were generally blurred and the stochastic variations of dielectric permittivity and the average and stochastic variations of electrical conductivity were poorly determined.

Our final suite of numerical experiments involved inserting a horizontal line of small pipes and a relatively large (twice the dominant wavelength) tunnel into the layered models and then inverting the synthetic radar data generated from the resultant composite models. The pipes and tunnel were filled with conductive water. Addition of the anthropogenic features only marginally affected the media boundaries and the average and stochastic electrical properties in the full-waveform and ray tomograms. The location and size of the tunnel were reproduced in all tomograms, with the most accurate estimates being provided by the full-waveform conductivity tomograms. The permittivity of the water was substantially underestimated, whereas its electrical conductivity was correctly reproduced. The collinear pipes were not well resolved in the permittivity tomograms. Instead, they appeared as a single

linear feature in permittivity images with low degrees of stochastic heterogeneity and were not observed in an image with a high degree of heterogeneity; resolution of the individual pipes was clearly beyond the limits of the permittivity tomograms. By comparison, the locations, sizes and conductivities of the individual pipes were faithfully reproduced in the full-waveform conductivity tomograms for all levels of tested stochastic heterogeneity.

By exploiting the complete information content of the synthetic crosshole radar data, full-waveform tomographic inversion is capable of yielding dependable, high-resolution dielectric permittivity and electrical conductivity images. For many applications, the sub-wavelength resolution may be comparable to that supplied by borehole geophysical logging, core sampling, and direct-push techniques. The synthetic tests considered in this study suggest that the new scheme will be a valuable tool for diverse geological, hydrological, archeological, and civil engineering investigations.

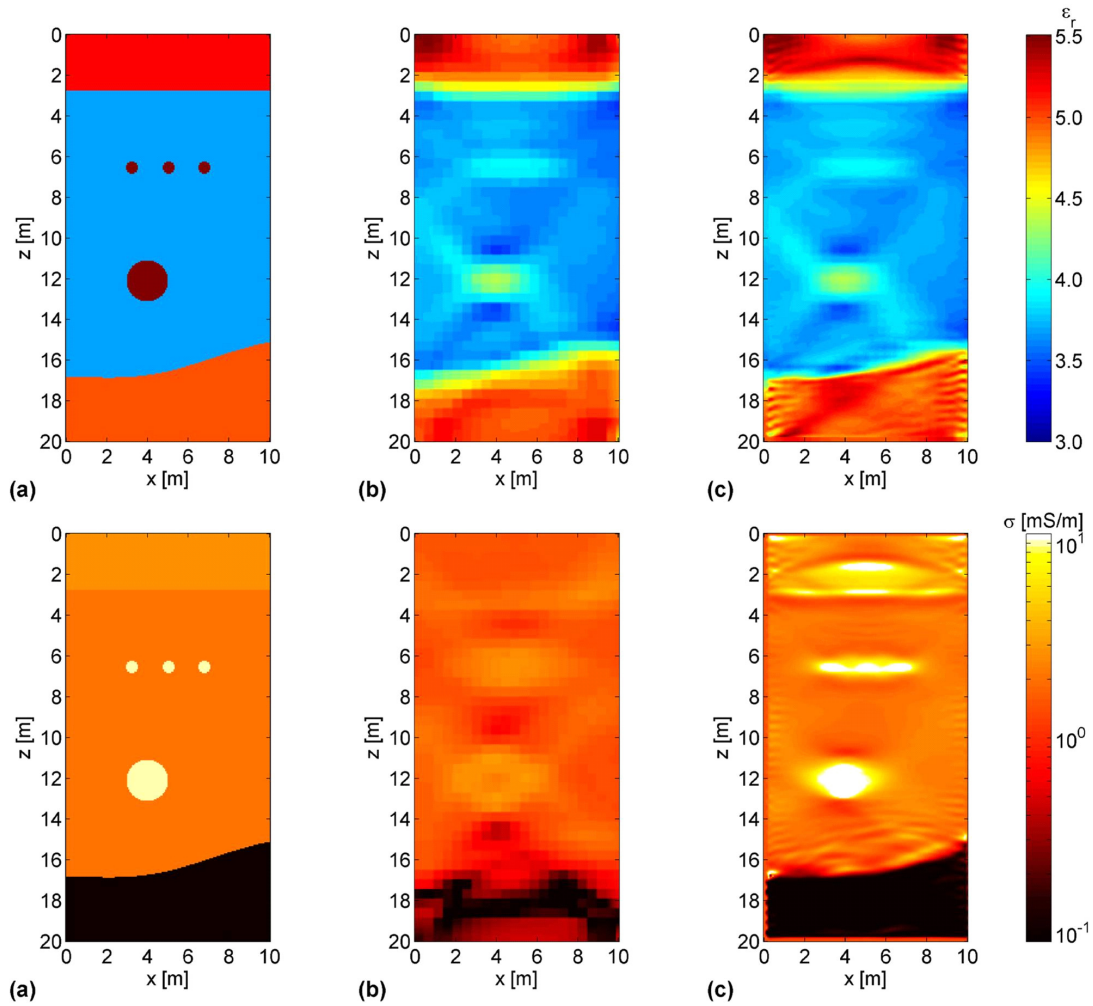


**Figure 3.14:** Similar to Figure 3.8, but with the addition of three pipes and a tunnel filled with moderately conductive water (Figure 3.1b; model 7 in Table 3.1). For the pipes and tunnel  $\epsilon_{rp} = \epsilon_{rt} = 80$ ,  $\sigma_p = \sigma_t = 10.0$  mS/m.

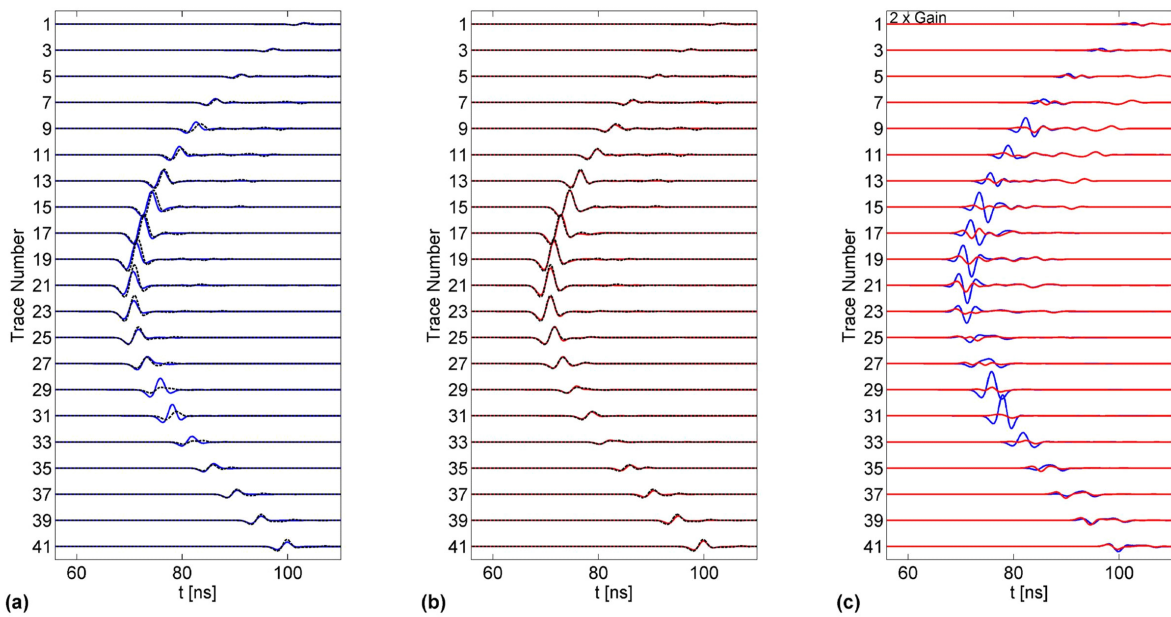


**Figure 3.15:** Similar to Figure 3.9, but for the tomograms in Figure 3.14.

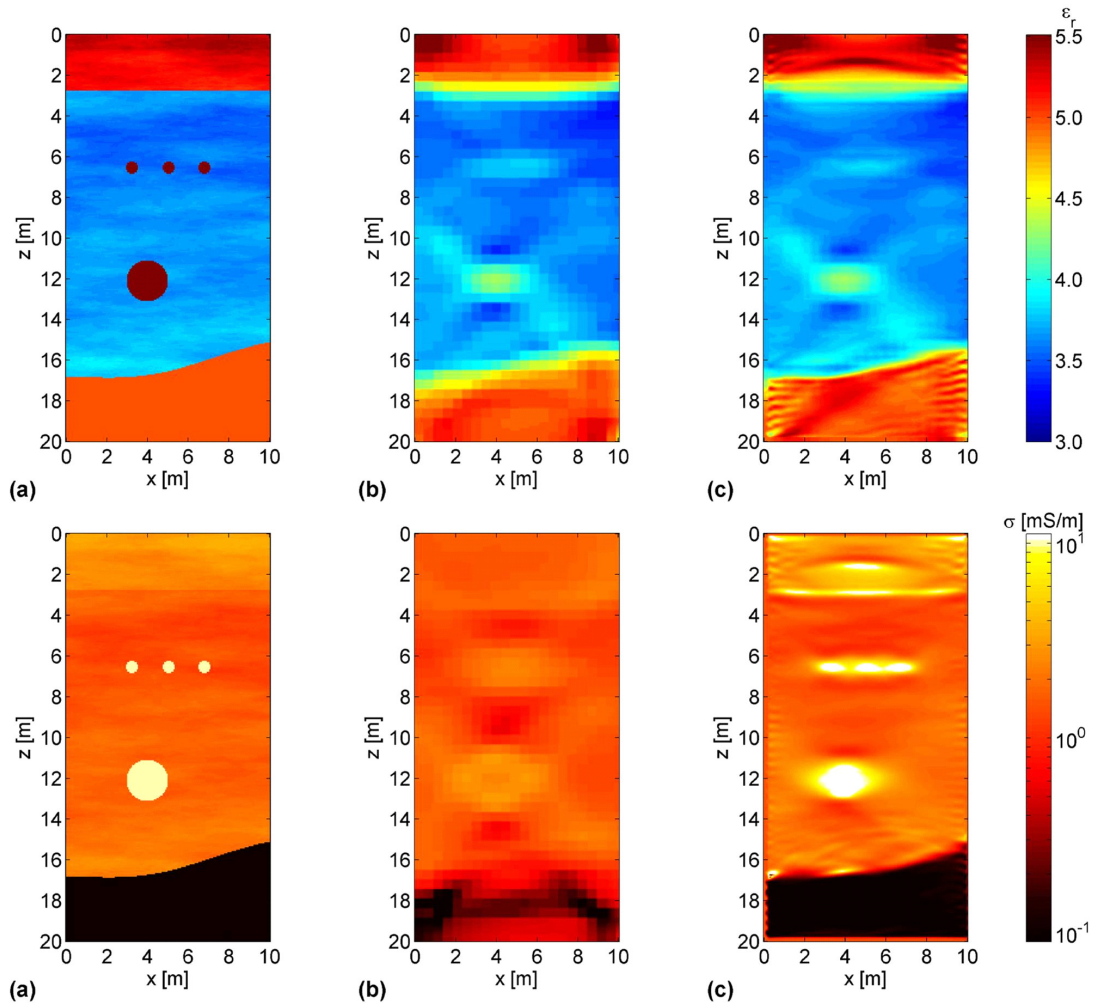


**Figure 3.16:** Similar to Figure 3.10, but with the addition of three pipes and a tunnel filled with moderately conductive water (Figure 3.1b; model 8 in Table 3.1). For the pipes and tunnel  $\epsilon_{rp} = \epsilon_{rt} = 80$ ,  $\sigma_p = \sigma_t = 10.0$  mS/m.

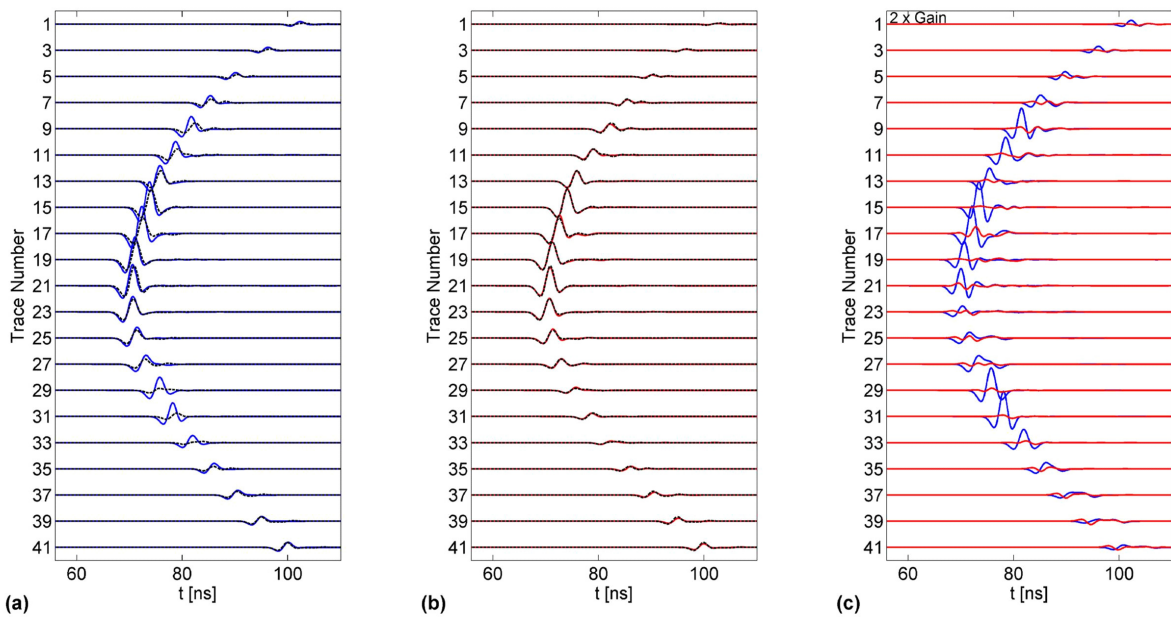


**Figure 3.17:** Similar to Figure 3.9, but for the tomograms in Figure 3.16.

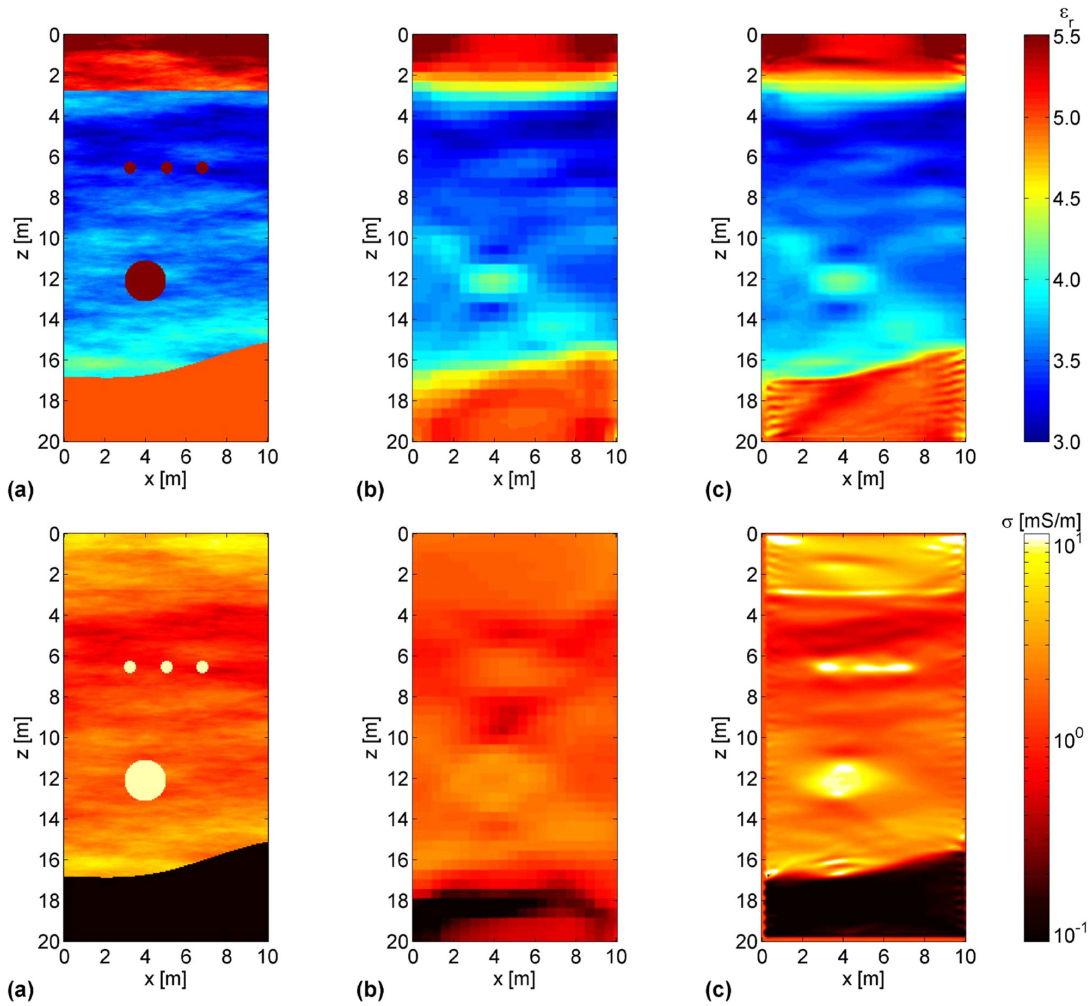


**Figure 3.18:** Similar to Figure 3.12, but with the addition of three pipes and a tunnel filled with moderately conductive water (Figure 3.1b; model 9 in Table 3.1). For the pipes and tunnel  $\epsilon_{rp} = \epsilon_{rt} = 80$ ,  $\sigma_p = \sigma_t = 10.0$  mS/m.

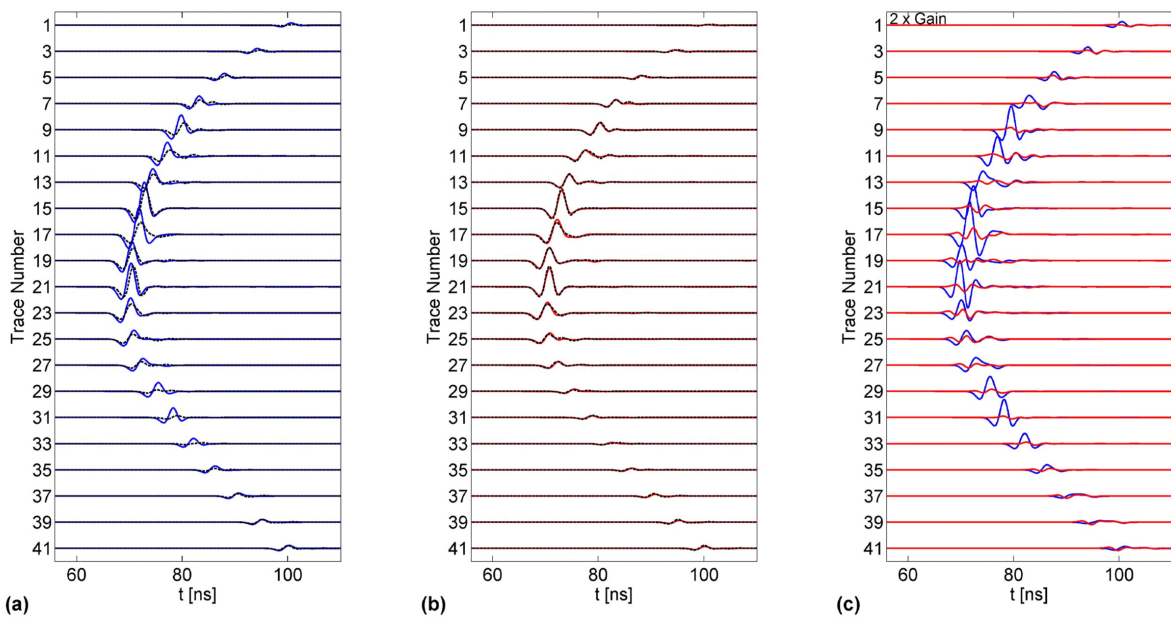


**Figure 3.19:** Similar to Figure 3.9, but for the tomograms in Figure 3.18.



# **CHAPTER 4**

## **APPLICATION OF A NEW 2-D TIME-DOMAIN FULL-WAVEFORM INVERSION SCHEME TO CROSSHOLE RADAR DATA**

**Jacques R. Ernst**, Alan G. Green, Hansruedi Maurer and Klaus Holliger

*Slightly modified from the published version.*

Published in: *Geophysics*, **72**, 2007, J53-J64

#### 4.1. ABSTRACT

Crosshole radar tomography is a useful tool in diverse geological, hydrological, engineering, and archeological investigations. Conventional tomograms provided by standard ray-based techniques have limited resolution, primarily because only a fraction of the information contained in the radar data (i.e., the first-arrival times and maximum first-cycle amplitudes) is included in the inversion. To increase the resolution of radar tomograms, we have developed a versatile full-waveform inversion scheme that is based on a finite-difference time-domain solution of Maxwell's equations. This scheme accounts for the 3-D nature of radar-wave propagation and includes an efficient method for extracting the source wavelet from the radar data. After demonstrating the potential of the new scheme on two realistic synthetic data sets, we apply it to two crosshole data sets acquired in very different geological / hydrological environments. These are the first applications of full-waveform tomography to observed crosshole radar data. The resolution of all full-waveform tomograms is shown to be markedly superior to that of the relevant ray tomograms. Boundaries between distinct geological / hydrological units and small features, a fraction of the dominant radar wavelength, are sharply imaged in the full-waveform tomograms.

**Key Words:** Full-waveform inversion, finite-difference time-domain (FDTD) methods, Maxwell's equations, crosshole radar, synthetic and field data.

#### 4.2. INTRODUCTION

Crosshole radar methods are capable of providing reliable subsurface tomographic images of dielectric permittivity  $\varepsilon$  and electrical conductivity  $\sigma$ , two properties intimately linked to local hydrological conditions, salinity, clay content, and lithological variations. Acquisition of crosshole radar data involves generating high-frequency (20 - 250 MHz) electromagnetic pulses at numerous locations along one borehole and recording the transmitted and scattered waves at a large number of positions along a second borehole. The pulses have dominant wavelengths of 5.0 to 0.4 m in the subsurface.

The vast majority of published tomographic radar images of the shallow subsurface have been derived from standard ray-based inversions of first-arrival times and maximum first-cycle amplitudes (e.g., Olsson et al., 1992; Carlsten et al., 1995; Fullagar et al., 2000; Bellefleur and Chouteau, 2001; Tronicke et al., 2001; 2004; Irving and Knight, 2005; Clement and Barrash, 2006; Musil et al., 2006; Paasche et al., 2006). Unfortunately, the resolution provided by standard ray tomography is limited by the relatively small amount of information

included in the inversion; resolution scales approximately with the diameter of the first Fresnel zone (Williamson and Worthington, 1993).

To improve the resolution provided by radar methods, a number of waveform-type approaches have been developed over the past sixteen years. They have included various Born iterative methods based on integral representations of Maxwell's equations (Wang and Chew, 1989; Chew and Wang, 1990; Sena and Toksoz, 1990; Moghaddam et al., 1991; Moghaddam and Chew, 1992; 1993; Cui et al., 2001) and wave-equation-traveltime (Cai et al., 1996), Fresnel-volume (Johnson et al., 2005), diffraction-tomography (Cui and Chew, 2000; Zhou and Liu, 2000; Cui and Chew, 2002; Cui et al., 2004), and full-waveform (Moghaddam et al., 1991; Jia et al., 2002; Ernst et al., 2005; Kuroda et al., 2005; Ernst et al., 2007) methods. Almost all of these waveform-type approaches have only ever been tested on synthetic data and not applied to recorded crosshole radar data. A notable exception is Cai et al.'s (1996) application of their wave-equation-traveltime method to observed first-arrival traveltimes.

We have recently introduced a 2-D time-domain full-waveform tomographic scheme for the inversion of crosshole radar data (Ernst et al., 2005; 2007). Our intention here is to demonstrate its potential and limitations via applications to two realistic synthetic data sets and two field data sets, one acquired within a relatively dry granodioritic rock mass (Grimsel Rock Laboratory) and one recorded within a water-saturated alluvial aquifer (Boise Hydrogeophysical Research Site). To our knowledge, these are the first applications of full-waveform tomographic inversion to observed crosshole radar data. In contrast to waveform-type investigations that only involve synthetic data, it is necessary for us to (i) account for the 3-D nature of wave propagation through the probed media and (ii) estimate the source wavelet.

After reviewing briefly the principal features of the new full-waveform tomographic inversion scheme, we summarize key implementation details. Although issues (i) and (ii) are very important, we handle them in Appendices A and B to maintain continuity of the main text. Finally, we present the results of applying the new scheme to the synthetic and field data sets. All full-waveform tomograms are compared to the corresponding conventional ray tomograms.

### 4.3. FULL-WAVEFORM INVERSION

Since Tarantola's (1984a; 1984b; 1986) classic papers appeared on the full-waveform inversion of seismic data, numerous inversion methods have been developed and applied to seismic waves generated and recorded at the surface and/or along boreholes. They have included finite-difference and finite-element approaches based on representations of the acoustic-, elastic-, viscoelastic-, and anisotropic-wave equations in both the time- and frequency-domains (e.g., Mora, 1987; 1988; Pica et al., 1990; Pratt, 1990a; 1990b; Zhou and Greenhalgh, 1998a; Pratt, 1999; Pratt and Shipp, 1999; Zhou and Greenhalgh, 2003; Watanabe et al., 2004; Sinclair et al., 2007). Comparable developments on the full-waveform inversion of radar data have been much more limited (Moghaddam et al., 1991; Jia et al., 2002; Ernst et al., 2005; Kuroda et al., 2005; Ernst et al., 2007). In this contribution, we employ our new 2-D full-waveform tomographic inversion scheme to synthetic and field data. Details on the mathematical formulations and computer realization of this scheme are provided by (Ernst et al., 2007). Here, we describe only the most important elements.

For the forward component of our scheme, we employ a 2-D finite-difference time-domain (FDTD) solution of Maxwell's equations in Cartesian coordinates, and for the inverse component, we adapt Tarantola's (1984a) approach to operate in the electromagnetic wave regime. In typical borehole radar configurations, the electric-field component parallel to the borehole axis dominates, such that the TE-mode Maxwell's equations are appropriate for our purposes. These equations are solved using staggered-grid finite-difference operators that are second-order accurate in both time and space (Taflove and Hagness, 2000). Application of efficient generalized perfectly matched layer (GPML) absorbing boundaries minimizes artificial reflections from the model edges (Fang and Wu, 1996).

During the inversion, a conjugate-gradient technique (Polak and Ribière, 1969) is used to find the minimum of a cost functional that defines the differences between the observed and model-predicted data. An adjoint method determines the update gradient directions and an algorithm described by Pica et al. (1990) supplies optimum estimates of the update step sizes. As a consequence, computationally expensive calculations of the Jacobian matrix are not required.

Before applying our 2-D full-waveform tomographic inversion scheme, we need to account as best we can for the 3-D characteristics of wave propagation through the media and determine an estimate of the source wavelet. These two critical issues are discussed in

Appendices 4.A and 4.B. Implementation of our full-waveform tomographic inversion scheme involves the following principal steps:

- I. apply pre-inversion data processing to reduce high-frequency noise and the effects of out-of-plane energy, and "transform" the crosshole radar data to 2-D (Appendix A);
- II. invert the first-arrival times and maximum first-cycle amplitudes using standard ray tomography;
- III. convert the ray velocity and attenuation tomograms to initial  $\varepsilon$  and  $\sigma$  models;
- IV. compute a synthetic wavefield using the initial  $\varepsilon$  and  $\sigma$  conductivity models and a rough estimate of the source wavelet (boxes 1 and 2 in Figure 4.B-2);
- V. determine a realistic estimate of the source wavelet using the deconvolution method outlined in Appendix B (boxes 3 to 5 in Figure 4.B-2);
- VI. compute the synthetic wavefield using the model parameters and the realistic source-wavelet estimate determined at step V;
- VII. subtract the synthetic data from the observed data to determine the residual wavefield;
- VIII. compute the cost functional;
- IX. use the same model parameters employed at step VI and the residual wavefield to generate the back-propagated synthetic wavefield;
- X. calculate the inversion update directions by cross-correlating the forward- and back-propagated wavefields;
- XI. determine the step length that provides fast, yet stable and accurate inversions;
- XII. update the  $\varepsilon$  and  $\sigma$  model using the derived gradient direction and step length;
- XIII. repeat steps V to XII until convergence is achieved (i.e., the cost functional reaches a predetermined minimum value).

During the inversion, the complete wavefield only needs to be computed three times per iteration (i.e., steps VI, IX, and XI).

Our attempts to invert simultaneously for  $\varepsilon$  and  $\sigma$  fail, primarily because of the large differences between the magnitudes of the  $\varepsilon$  and  $\sigma$  Fréchet derivatives (even though they are not explicitly calculated; Watanabe et al. (2004) discuss the equivalent acoustic problem). This problem is resolved by first inverting for  $\varepsilon$  while keeping  $\sigma$  fixed and then inverting for  $\sigma$  while keeping  $\varepsilon$  fixed (Ernst et al., 2007). Although this sequence can be repeated until convergence is obtained, only a single computational cycle is required for all examples presented in this paper.

#### 4.4. APPLICATION TO REALISTIC SYNTHETIC DATA

In the following, we explore the potential and limitations of our full-waveform inversion scheme using two very similar synthetic data sets, one pure 2-D and one quasi-3-D (other synthetic examples are presented in Ernst et al., 2007). Medium parameters, borehole geometries, and boundaries of the stochastic models used to generate the two data sets are identical (Table 4.1 and Figures 4.1a and 4.1d). For convenience, the models are expressed in terms of relative permittivity  $\varepsilon_r = \varepsilon/\varepsilon_0$ , where  $\varepsilon_0$  is the dielectric permittivity of free space. Average medium properties are  $\varepsilon_r^{\text{mean}} = 10.3$  and  $\sigma^{\text{mean}} = 2.0$  mS/m and the stochastic variations are defined by exponential covariance functions with standard deviations  $\varepsilon_r^{\text{std}} = 0.8$  and  $\sigma^{\text{std}} = 1.7$  mS/m and horizontal and vertical correlation lengths of 1.0 and 0.2 m, respectively. Figures 4.1a and 4.1d show the resultant  $\varepsilon_r$  and  $\sigma$  distributions used to generate the synthetic data. They have distinct subhorizontal fabrics with zones of generally low  $\varepsilon_r$  and low  $\sigma$  within 1 m of the surface and below 16 m depth and a zone of mostly high  $\varepsilon_r$  and high  $\sigma$  between 4 and 10 m depth. The two 20-m-deep boreholes in our models are separated by

**Table 4.1:** Summary of model parameters. Homogeneous initial models were used for all ray-tomographic inversions.

Experiments (Figures)	Model width & depth [m]	#Transmitters / #receivers	Input medium parameters ( $\varepsilon_r$ and $\sigma$ [mS/m])	Grid cell sizes [cm]		2.5-D to 2-D transformation / source estimation & improvement	Initial parameters for ray tomography ( $\varepsilon_r$ and $\sigma$ [mS/m])
				forward	inverse		
<b>Synthetic I</b> (4.1, 4.2a, 4.3)	10 & 20	41 / 41	$\varepsilon_r^{\text{mean}} = 10.3$ ; $\sigma^{\text{mean}} = 2.0$ stochastic variations with standard deviations of	2	6	No / Yes	$\varepsilon_r = 10.3$ $\sigma = 1.4$
<b>Synthetic II</b> (4.2b, 4.4)	10 & 20	41 / 41	$\varepsilon_r^{\text{std}} = 0.8$ , $\sigma^{\text{std}} = 1.7$ and correlation lengths of x = 2.0 m, z = 0.2 m	2	6	Yes / Yes	$\varepsilon_r = 10.3$ $\sigma = 1.4$
<b>Grimsel</b> (4.5, 4.6, 4.7a, 4.8)	10 & 20	41 / 40	?	2	18	Yes / Yes	$\varepsilon_r = 5.6$ $\sigma = 1.4$
<b>Boise</b> (4.7b, 4.9 – 4.11)	8.5 & 20	77 / 40 (see main text)	?	2	14	Yes / Yes	$\varepsilon_r = 12.4$ $\sigma = 4.7$

10 m, with 41 equally spaced transmitter antennas in the left borehole and 41 equally spaced receiver antennas in the right borehole. The grid spacings used for the forward and inverse computations are 0.02 and 0.06 m, and the model space is surrounded by a 0.8-m-thick GPML frame.

We employ an FDTD algorithm in 2-D Cartesian coordinates to generate the true 2-D noise-free data for the first synthetic experiment (Synthetic I in Table 4.1) and an FDTD algorithm in cylindrical coordinates (Ernst et al., 2006) to generate the pseudo-3-D noise-free data for the second experiment (Synthetic II in Table 4.1). The source signal in both experiments is a 100 MHz Ricker wavelet that yields signals with  $\sim 1$  m dominant wavelengths in the models.

#### **4.4.1. SYNTHETIC EXPERIMENT I: DETERMINING THE SOURCE WAVELET AND DISTRIBUTIONS OF $\varepsilon$ AND $\sigma$ FROM TRUE 2-D SYNTHETIC DATA**

Conventional ray-based inversions of the first-arrival traveltimes and maximum first-cycle amplitudes provide the electromagnetic velocity and attenuation tomograms that are converted using relatively standard high-frequency relationships (Holliger et al., 2001) to the  $\varepsilon_r$  and  $\sigma$  ray tomograms shown in Figures 4.1b and 4.1e. The  $\varepsilon_r$  ray tomogram is a somewhat blurred image that portrays well the important broad-scale zoning of the original model (compare Figures 4.1b and 4.1a), but the  $\sigma$  ray tomogram is a rather poor representation of the original model (compare Figures 4.1e and 4.1d).

Despite their shortcomings, the two ray tomograms are the basis for a source-wavelet estimate that practically matches the true wavelet (compare the curves represented by the green and dashed black lines in Figure 4.2a; see Appendix 4.A). Using the two ray tomograms and associated source-wavelet estimate as the initial input parameters, the full-waveform inversion scheme for determining  $\varepsilon_r$  and the related source-wavelet computations converge after 20 iterations. The subsequent full-waveform inversion scheme for  $\sigma$  converges after 10 iterations.

Since the source-wavelet estimate based on the ray tomograms is remarkably good, it is not surprising that the full-waveform inversions produce no noticeable improvements in this regard. By comparison, the full-waveform tomograms are significantly more accurate with much higher resolution than the ray tomograms (compare Figure 4.1c with Figures 4.1a and 4.1b and Figure 4.1f with Figures 4.1d and 4.1e). Whereas the resolution of the ray tomograms is generally no better than  $\sim 1$  m (i.e., the dominant wavelength of the radar

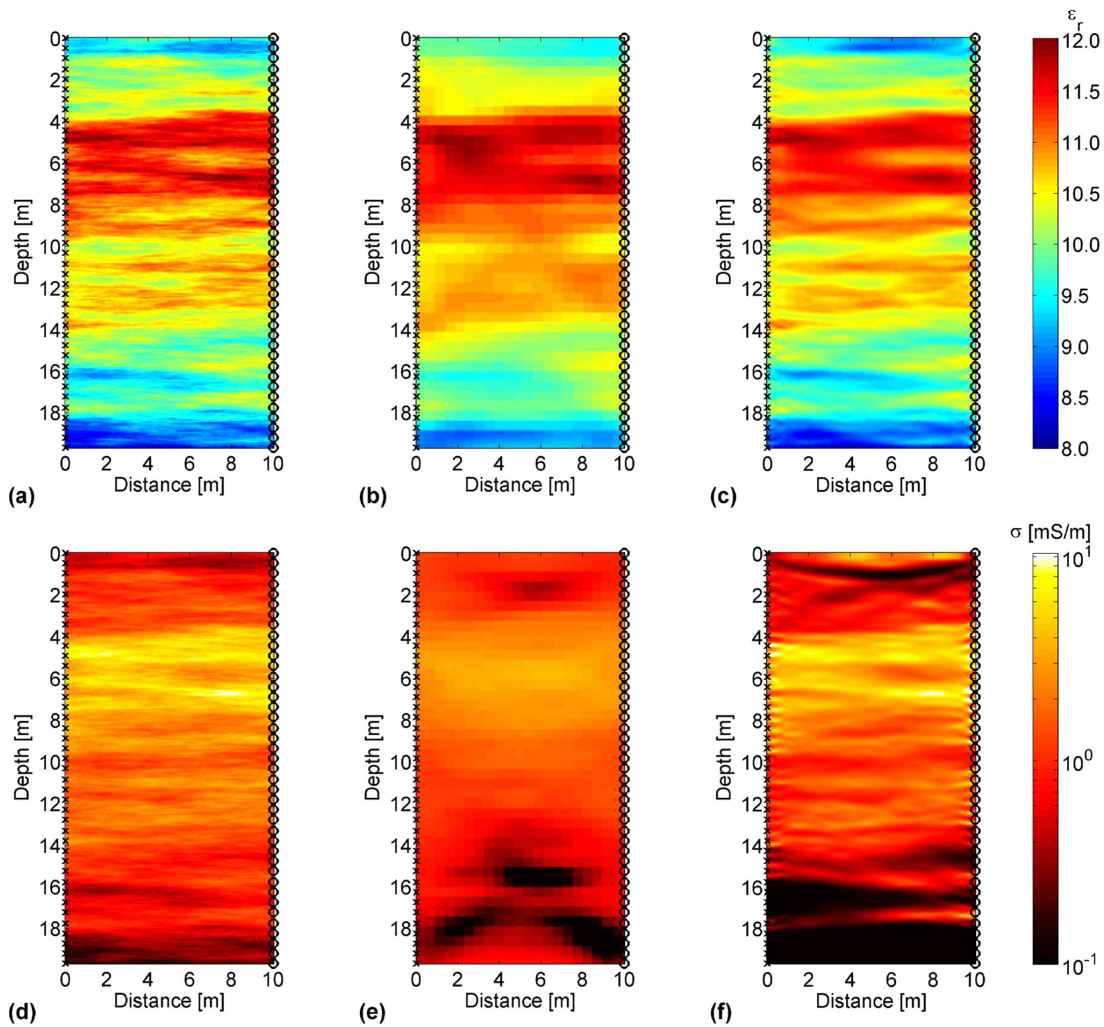
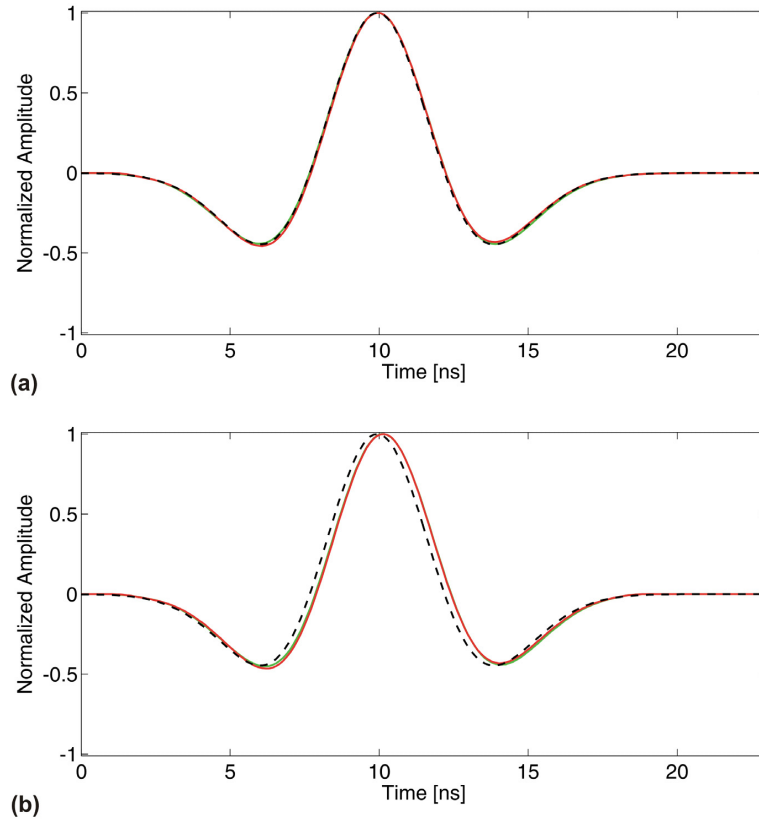


**Figure 4.1:** (a) and (d) input  $\varepsilon_r$  and  $\sigma$  values for the 2-D synthetic data experiment I (Table 4.1). Mean dielectric permittivity and electrical conductivity of the stochastic medium are  $\varepsilon_r^{\text{mean}} = 10.3$  and  $\sigma^{\text{mean}} = 1.4$  mS/m with standard deviations  $\varepsilon_r^{\text{std}} = 0.8$  and  $\sigma^{\text{std}} = 1.7$  mS/m and correlation lengths in the x and z directions of 2 m and 0.2 m. (b) and (e)  $\varepsilon_r$  and  $\sigma$  tomograms that result from applying the ray-based inversion scheme to synthetic traces computed from the model shown in (a) and (d). Data were generated using FDTD approximations of Maxwell's equation in 2-D. (c) and (f) as for (b) and (e) but for the full-waveform inversion. Black crosses and circles are transmitter and receiver locations.

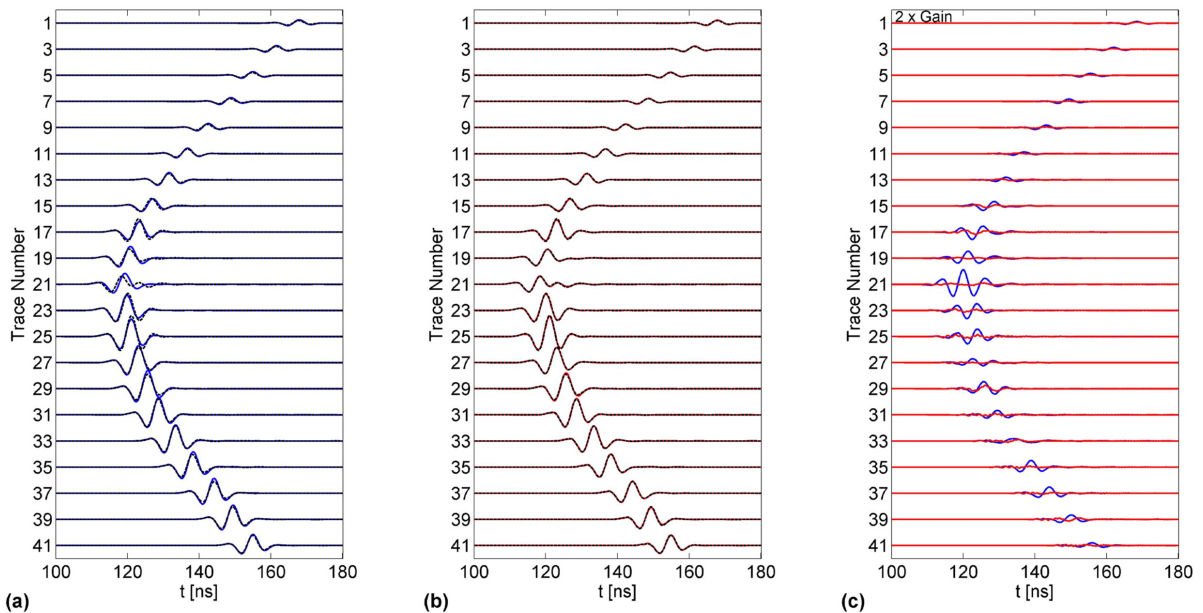
signal), that of the full-waveform tomograms is in the 20-30 cm range. The full-waveform  $\sigma$  tomogram accurately reconstructs small-scale features in regions of the model that are well sampled by multiple crossing wavefronts, but predicts erroneously low  $\sigma$  values at the upper and lower extremities of the model (Figure 4.1f).

Figure 4.3 shows FDTD-generated receiver gathers for the original model and the ray and full-waveform tomograms. First-arrival traveltimes and maximum first-cycle amplitudes of traces generated from the ray tomograms are quite close to those generated from the original model, but there are small but important differences in the waveforms that are exemplified in the difference plots of Figure 4.3c. Traces generated from the full-waveform tomograms are practically identical to those generated from the original model.





**Figure 4.2:** Source wavelets determined for the tomographic inversions shown in (a) Figure 4.1 and (b) Figure 4.4. Dashed black line is the true source wavelet, and green and red lines are the first and final source wavelets determined by the deconvolution method outlined in Appendix B. Amplitudes are normalized with respect to the maximum values for display purposes.



**Figure 4.3:** (a) and (b) are transmitter gathers for a location along the left model edge at 10.1 m depth in Figure 4.1. Dashed black and solid blue and red lines show every second radar trace generated from the original input model in Figures 4.1a and 4.1d, the ray tomograms in Figures 4.1b and 4.1e, and the full-waveform tomograms in Figures 4.1e and 4.1f. (c) Blue and red lines show differences between the blue and dashed black lines in (a) and between the red and dashed black lines in (b), respectively. Amplitudes in (a) and (b) are normalized with respect to the maximum amplitude of the input data. Amplitudes of residuals in (c) are amplified by a factor of 2 relative to the radar traces.

#### 4.4.2. SYNTHETIC EXPERIMENT II: DETERMINING THE SOURCE WAVELET AND DISTRIBUTIONS OF $\epsilon$ AND $\sigma$ FROM PSEUDO-3-D SYNTHETIC DATA

We use the second synthetic data set created with Ernst et al.'s (2006) FDTD code in cylindrical coordinates to demonstrate the efficacy of our approach for minimizing the effects of 3-D wave-propagation phenomena on the 2-D inversion scheme. To simulate realistic conditions, we only invert 20 ns of each trace starting at the first-arrival onsets. After employing equation 4.A-1 in Appendix 4.A to account for the 3-D radiation effects, we follow the same procedures as described previous synthetic experiment. Figure 4.2b shows that the reconstructed source wavelet is slightly phase shifted relative to the true wavelet. Nevertheless, the full-waveform tomograms in Figure 4.4 are very similar to those derived from the pure 2-D data set in Figures 4.1c and 4.1f, and the correspondence between receiver gathers generated from the full-waveform tomogram and original model is as good as that obtained for Synthetic experiment I; small imperceptible differences in the ray tomogram compensate for the small phase shifts in the estimated source wavelet (Figure 4.2b; see the sensitivity analysis in Appendix 4.B).

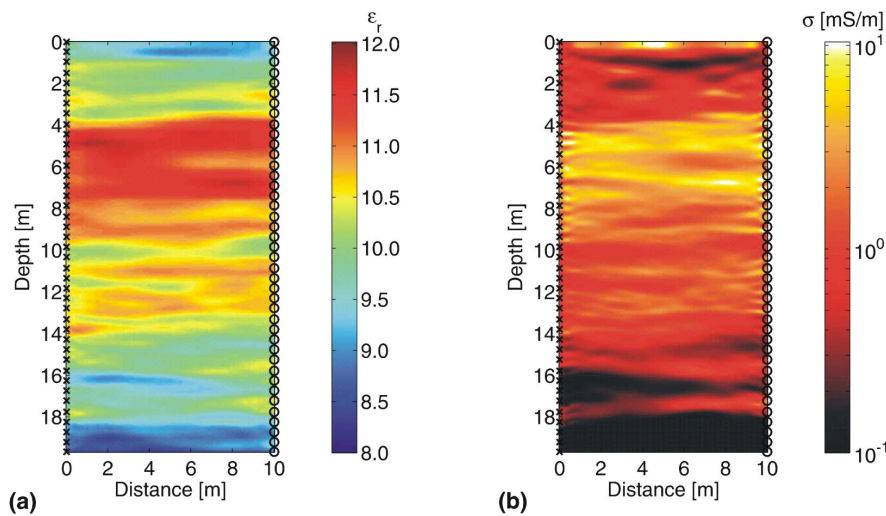


**Figure 4.4:** (a) and (b)  $\epsilon_r$  and  $\sigma$  tomograms that result from applying the full-waveform inversion scheme to synthetic traces generated from a cylindrically symmetric version of the model shown in Figures 4.1a and 4.1b (Synthetic II, Table 4.1). This is referred to as a 2.5-D model. Data generated using FDTD approximations of Maxwell's equations in 2.5-D were transformed to 2-D in the Cartesian coordinate system for use in the full-waveform inversion scheme. Black crosses and circles are transmitter and receiver locations.

#### 4.5. CASE STUDY I - GRIMSEL ROCK LABORATORY

We have acquired crosshole radar data within the Grimsel Rock Laboratory in the central Swiss Alps. Previous geological, geomechanical, and seismic investigations at the study site identified two marginally different types of foliated granodiorite cross-cut by a fractured mylonitic shear zone (Figure 4.5; Majer et al., 1990; Vasco, 1991; Vasco et al., 1998). Both the foliation and shear zone trend in a northeast-southwest direction. The poorly defined boundaries shown in Figure 4.5 are based on extrapolations of observations along the Main Access Tunnel in the east and the Lower Access Tunnel in the west and information extracted from boreholes (dashed black lines). Very different degrees of fracturing at neighboring locations along the tunnels and boreholes suggest that the shear zone is extremely heterogeneous.

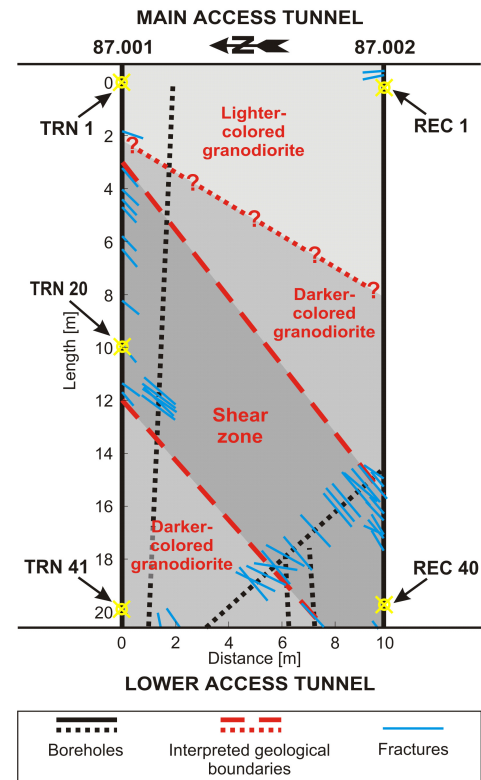


**Figure 4.5:** Sketch of the crosshole radar experiment performed at the Grimsel site (Switzerland). The geological cross-section is based on borehole information (modified from Majer et al., 1990). TRN and REC are transmitter and receiver locations.

##### 4.5.1. DATA ACQUISITION

For our crosshole radar survey, we took advantage of two subhorizontal boreholes linking the two tunnels (87.001 and 87.002 in Figure 4.5). These 0.1-m-diameter dry boreholes were ~21 m long and separated by a constant distance of ~10 m. Along ~20 m lengths of the boreholes, 41 transmitter locations and 40 receiver locations were established at ~0.5 m intervals. Our 250-MHz RAMAC borehole antennas produced radar waves with a surprisingly low dominant frequency of ~125 MHz, which corresponded to wavelengths of 0.9 - 1.1 m in the granodioritic rock.

##### 4.5.2. DATA PROCESSING, INVERSIONS AND SOURCE-WAVELET ESTIMATES

To avoid artifacts associated with rapid variations in the antenna radiation patterns, we only considered data for which the angles between the borehole axes and lines connecting the transmitter and receiver antennas were  $>45^\circ$ . Moreover, because seismic data recorded between the two boreholes had a background anisotropy of 7-10% (Majer et al., 1990; Vasco, 1991; Tura et al., 1992; Vasco et al., 1998), we tested the crosshole radar data for anisotropy.

Linear and polar plots of apparent velocity (i.e., transmitter-receiver distance divided by first-arrival traveltime) versus transmitter-receiver angle (relative to the borehole axes) revealed negligible anisotropy (i.e.,  $< 2.5\%$ ) in the radar data.

Ray tomograms that resulted from inverting the semi-automatically picked first-arrival traveltimes and maximum first-cycle amplitudes are presented in Figures 4.6a and 4.6c. For the source-wavelet determination and the full-waveform inversion, we selected 42 ns of each trace starting at the first-arrival onsets and then followed the same procedures as described for the synthetic data.

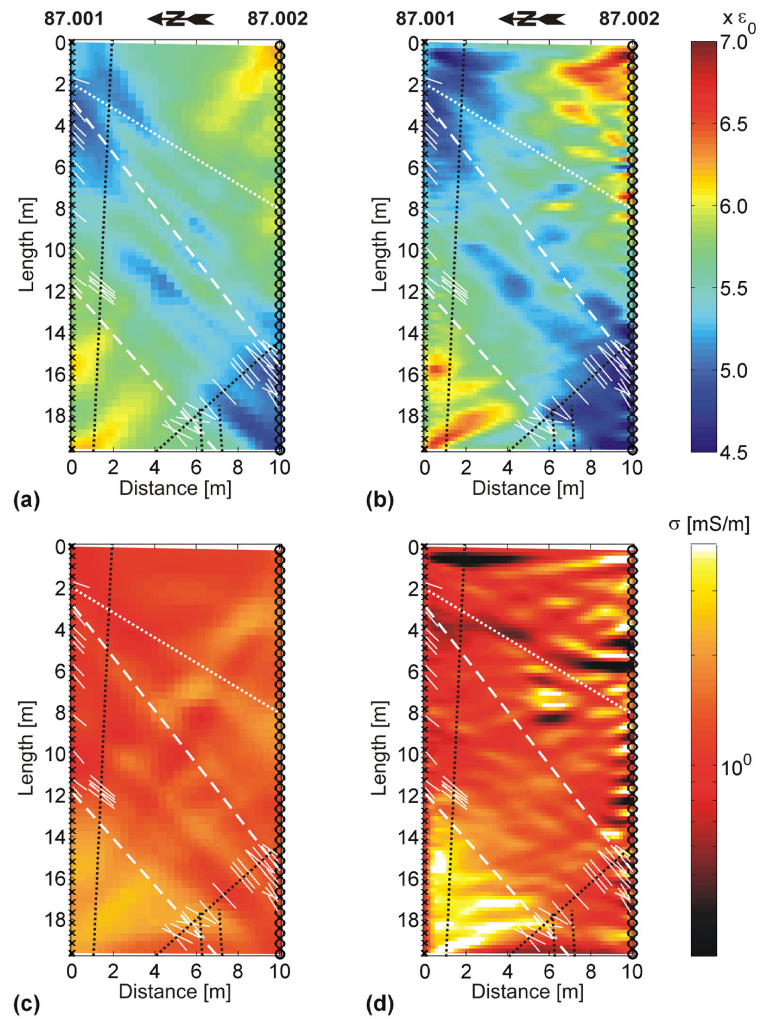


**Figure 4.6:** (a) and (c)  $\epsilon_r$  and  $\sigma$  tomograms that result from applying the ray-based tomographic inversion method to the Grimsel crosshole radar traces after application of equation (4.A-1). (b) and (d) as for (a) and (c) but for the full-waveform inversion. Black crosses and circles are transmitter and receiver locations. White lines are the structural elements and black dashed lines are the additional boreholes shown in Figure 4.6.

Whereas maximum cell sizes of forward-modeling grids are determined by numerical stability criteria (Bergmann et al., 1996; Holliger and Bergmann, 2002), there is no corresponding rule for the inversion cell sizes (Ernst et al., 2007). There are two competing requirements to satisfy in defining the inversion cell sizes: (i) a sufficient number of grid points is needed to represent the radar signal, and (ii) the number of grid points per antenna interval should be limited, otherwise artifacts are generated near the transmitters and receivers as a result of their strong influence on the gradient-computation component of the inversion process (i.e., step X in the section "FULL-WAVEFORM INVERSION"). Considering the 0.9 - 1.1 m radar wavelengths and the  $\sim 0.5$  m source and receiver spacing, a 0.18 m cell size is a reasonable compromise for the inversion of the Grimsel crosshole radar data. As for the

synthetic data examples, we use a conservative 0.02 m cell size for the forward modeling and the model space is surrounded by a 0.8-m-thick GPML boundary.

After 20 iterations for  $\varepsilon_r$  and 10 iterations for  $\sigma$ , the full-waveform tomograms of Figures 4.6b and 4.6d are obtained. Very similar tomograms are obtained for inversion cell sizes ranging from 0.06 to 0.24 m. The small artifacts along the lengths of the boreholes are a consequence of the aforementioned high sensitivities near the transmitters and receivers. Artifacts could be reduced by increasing the inversion cell size, because this would distribute sensitivities over larger areas. However, this would decrease the resolution in better sampled regions of the tomogram. Increasing the density of transmitter and receiver locations would be the correct way to eliminate these artifacts.

The source wavelets based on the ray and full-waveform tomograms are practically identical (Figure 4.7a). They are characterized by two main cycles with a dominant frequency of  $\sim 125$  MHz. Despite these similarities and the good correspondence between observed and ray-based first-arrival traveltimes and maximum first-cycle amplitudes, there are important differences between the observed and FDTD-generated radar traces derived from the ray

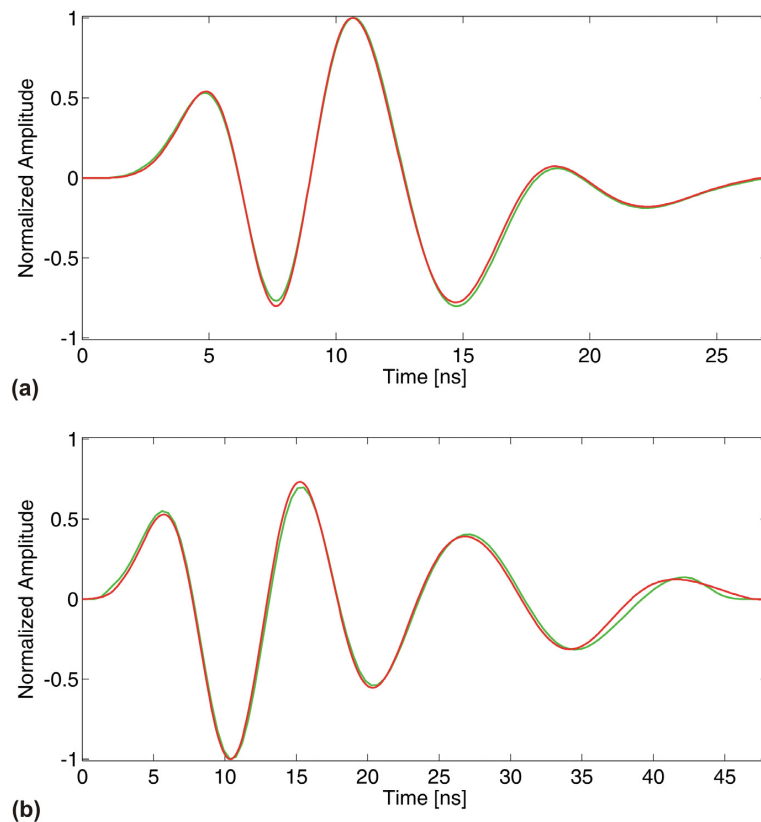


**Figure 4.7:** Source wavelets determined for the tomographic inversions shown in (a) Figure 4.6 (Grimsel data set) and (b) Figure 4.10 (Boise data set). Green and red lines are the first and final source wavelets determined by the deconvolution method outlined in Appendix B. Amplitudes are normalized with respect to the maximum values for display purposes.

tomograms (Figures 4.8a and 4.8c). In contrast, the radar traces generated from the full-waveform tomogram match closely the observed ones (Figures 4.8b and 4.8c).

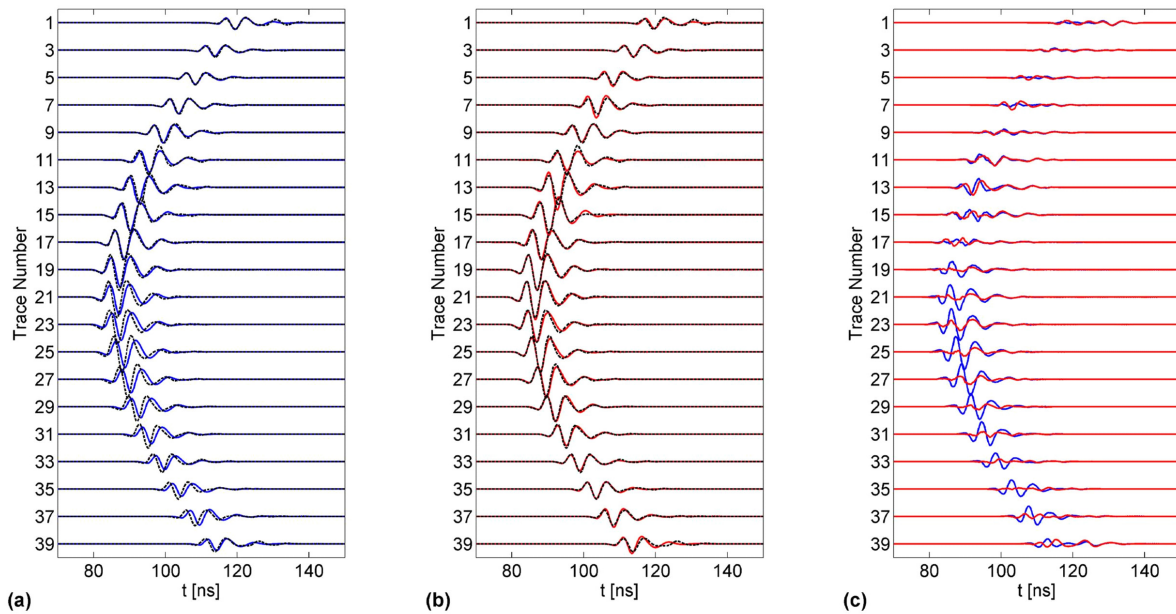


**Figure 4.8:** (a) and (b) are transmitter gathers for location TRN 20 in Figure 4.5. The dashed black and solid blue and red lines show every second observed radar trace and data generated from the ray tomograms in Figures 4.6a and 4.6c and full-waveform tomograms in Figures 4.6b and 4.6d, respectively. (c) Blue and red lines show differences between the blue and dashed black lines in (a) and between the red and dashed black lines in (b). Amplitudes in all panels are normalized with respect to the maximum amplitude of the input data.

### 4.5.3. COMPARISON OF RADAR AND SEISMIC P-WAVE VELOCITY CROSSHOLE TOMOGRAMS

Both  $\varepsilon_r$  tomograms in Figure 4.6 include regions of relatively high  $\varepsilon_r$  values in the northwest and southeast separated by a prominent broad band of low  $\varepsilon_r$  values. This pattern is very similar to that revealed in the Grimsel P-wave velocity tomograms of Vasco (1991), Tura et al. (1992), and Vasco et al. (1998), except that moderately high seismic velocities coincide with low radar velocities (i.e., high  $\varepsilon_r$  values) and low seismic velocities coincide with high radar velocities (i.e., low  $\varepsilon_r$  values).

### 4.5.4. INTERPRETATION

As for the synthetic data examples, the resolution of the Grimsel full-wave radar tomograms is markedly superior to that of the ray tomograms; smaller features are imaged and the  $\varepsilon_r$  and  $\sigma$  contrasts are stronger and sharper. In both suites of tomograms, a pattern of low  $\varepsilon_r$  values follows the northeast-southwest trend of the shear zone. According to the full-wave tomograms, its northwest boundary is distinguished by relatively abrupt changes from

$\varepsilon_r \approx 4.75 - 5.75$  within the shear zone to  $\varepsilon_r \approx 5.75-6.50$  outside. If relatively low  $\varepsilon_r$  values are caused by fracturing, then the full-waveform  $\varepsilon_r$  tomogram (Figure 4.6b) suggests that the southeast boundary of the shear zone is also relatively abrupt and occurs  $\sim 4$  m further to the southeast than shown in Figure 4.5.

Although  $\sigma$  changes from generally less than 1.5 mS/m to mostly more than 2.5 mS/m across the northwest boundary of the shear zone, evidence for the shear zone is less obvious in the  $\sigma$  tomograms than in the  $\varepsilon_r$  tomograms. Since  $\sigma$  is controlled by the highest conductivity component of a system, the presence of relatively dry fractures that do not interrupt current flow through the matrix does not significantly influence the average conductivity distribution.

The evidence from the radar and seismic tomograms is consistent with the ubiquitous presence of fractures within the cross-cutting shear zone. These fractures are likely filled or partially filled with air or other low  $\varepsilon_r$ , low to moderate  $\sigma$ , and low P-wave velocity material.

#### **4.6. CASE STUDY II - BOISE HYDROGEOPHYSICAL RESEARCH SITE**

Our second crosshole radar data set was collected at the Boise Hydrogeophysical Research Site in Idaho (Tronicke et al., 2004). A dense array of boreholes at this site has been used for diverse geological, geomechanical, hydrogeological, and geophysical experiments (Clement et al., 1999; Barrash and Clemo, 2002; Barrash and Reboulet, 2004; Tronicke et al., 2004; Clement and Barrash, 2006). The geology comprised an approximately 20-m-thick deposit of braided-river gravel and sand and an underlying clay layer. The water table was at 2.96 m depth at the time of the measurements.

##### **4.6.1. DATA ACQUISITION**

Tronicke et al.'s (2004) data were acquired in two 0.1 m-diameter boreholes that were  $\sim 20$  m deep and separated by  $\sim 8.5$  m (C6 and C5 in Figure 4.9). The boreholes, which were slightly tilted with respect to the vertical, penetrated three distinct pebble- and cobble-dominated layers with 21, 26, and 26% porosities (Figure 4.9). Data acquisition extended from  $\sim 4$  to  $\sim 19.4$  m depth, with 77 transmitter locations at 0.2 m intervals and 40 receiver locations at 0.4 m intervals. Although the 250-MHz RAMAC borehole antennas produced even lower frequencies than at Grimsel, the dominant  $\sim 80$  MHz radar waves had similar 0.9 - 1.1 m wavelengths in the high- $\varepsilon_r$  (low velocity) sediments.

#### 4.6.2. DATA PROCESSING, INVERSIONS AND SOURCE-WAVELET ESTIMATES

The data processing, inversions and wavelet estimate procedure applied to the Boise data set were very similar to those described for the synthetic and Grimsel data sets. We only considered data for which the angles between the borehole axes and lines connecting the transmitter and receiver antennas were  $>45^\circ$ , anisotropy was determined to be negligible (i.e.,  $<2\%$ ), and 78 ns of each trace starting at the first-arrival onsets was included in the inversion. Forward modeling and inverse grid cell sizes were 0.02 m and 0.14 m, and the model space was surrounded by a 0.8-m-thick GPML boundary.

The resultant ray tomograms are displayed in Figures 4.9a and 4.9c, and the full-waveform tomograms after 30 iterations for  $\varepsilon_r$  and 8 iterations for  $\sigma$  are presented in Figures 4.9b and 4.9d. Like the synthetic and Grimsel examples, the source wavelets based on the ray and full-waveform tomograms are practically identical (Figure 4.7b). The somewhat ringy character of the source wavelet is a result of the Boise boreholes being water filled (Ernst et al., 2006).

There are notable misfits between the observed and FDTD-generated radar traces derived from the ray tomograms, particularly in the central regions of the receiver gather of Figures 4.11a and 4.11c. The radar traces generated from the full-waveform tomogram correspond closely to the observed ones in Figures 4.11b and 4.11c, but the match is not quite as good as for the synthetic and Grimsel examples (Figures 4.3 and 4.8).

#### 4.6.3. INTERPRETATION

The full-waveform tomograms contain sharp images throughout the investigated volume, whereas the ray tomograms are rather blurred (Figure 4.10). Again, greater detail and larger  $\varepsilon_r$  and  $\sigma$  contrasts are observed on the full-waveform tomograms than on the ray tomograms. The boundary between the 21% and 26% porosity units seems to be gradational on the ray tomograms, with changes in  $\varepsilon_r$  and  $\sigma$  appearing  $\sim 0.5$  m above the boundary

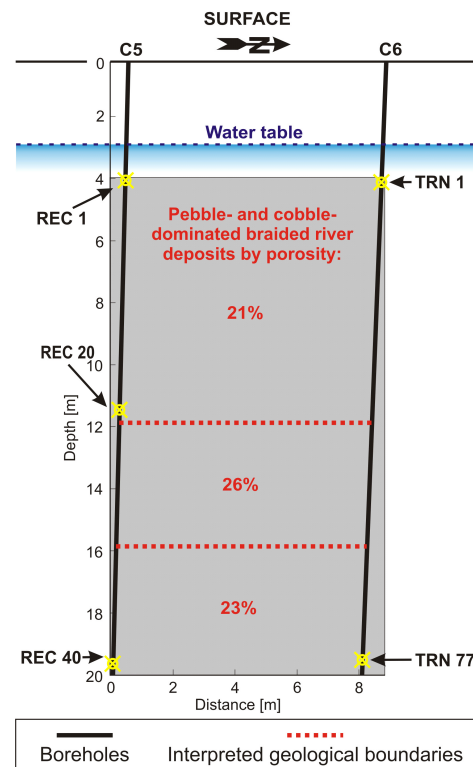


**Figure 4.9:** Sketch of the crosshole radar experiment performed at the Boise site (Idaho). Geological boundaries are based on porosity logs (Tronicke et al., 2004). TRN and REC are transmitter and receiver locations.



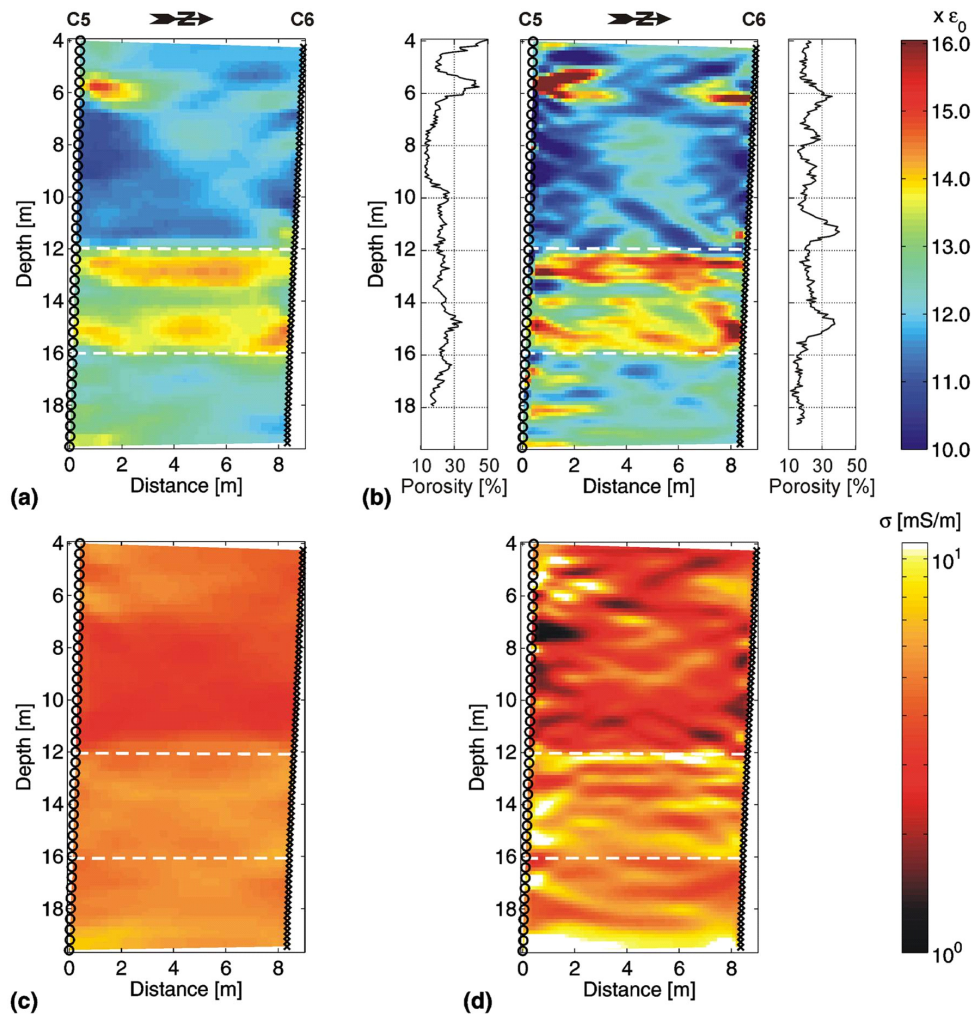


**Figure 4.10:** (a) and (c)  $\varepsilon_r$  and  $\sigma$  tomograms that result from applying the ray-based tomographic inversion method to the Boise crosshole radar traces after application of equation (4.A-1). (b) and (d) as for (a) and (c) but for the full-waveform inversion. Neutron-neutron (porosity) logs measured in the two boreholes are displayed to the left and right of the  $\varepsilon_r$  tomogram in (b). A capacitive resistivity log measured in borehole C6 is shown to the right of the  $\sigma$  tomogram in (d). Black crosses and circles are transmitter and receiver locations. White lines are the boundaries shown in Figure 4.11.

mapped in the boreholes (see also Figure 7 of Tronicke et al., 2004). By comparison, abrupt changes in  $\varepsilon_r$  and  $\sigma$  are observed in the full-waveform tomograms at the mapped boundary. The lower limit of the 26% porosity unit is also better defined on the full-waveform  $\varepsilon_r$  tomogram than on the ray  $\varepsilon_r$  tomogram, but it is not observed as a distinct feature on either  $\sigma$  tomogram.

Since  $\varepsilon_r$  and neutron-neutron counts are both proxies for water content, we plot the neutron-neutron logs measured in the two boreholes (Barrash and Clemo, 2002; Tronicke et al., 2004) alongside the full-waveform  $\varepsilon_r$  tomogram in Figure 4.10b. The correspondence between the two types of data ranges from very good to poor. There are close correlations between high  $\varepsilon_r$  values and high porosities (i.e., values of  $\sim 30\%$  or greater) at  $\sim 5.7$  m,  $\sim 14.8$  m, and  $\sim 16.5$  m in borehole C5 and at  $\sim 6.1$  m,  $\sim 11.3$  m, and  $\sim 14.8$  m in borehole C6.

There are several moderately high porosity values in the two logs that have no expression in the tomogram and the zone of high  $\varepsilon_r$  values that spans the tomogram at  $\sim 12.5$  m depth has no expression in either neutron-neutron log. We note, however, that the zone of high  $\varepsilon_r$  values at  $\sim 12.5$  m depth thins as it approaches both boreholes.

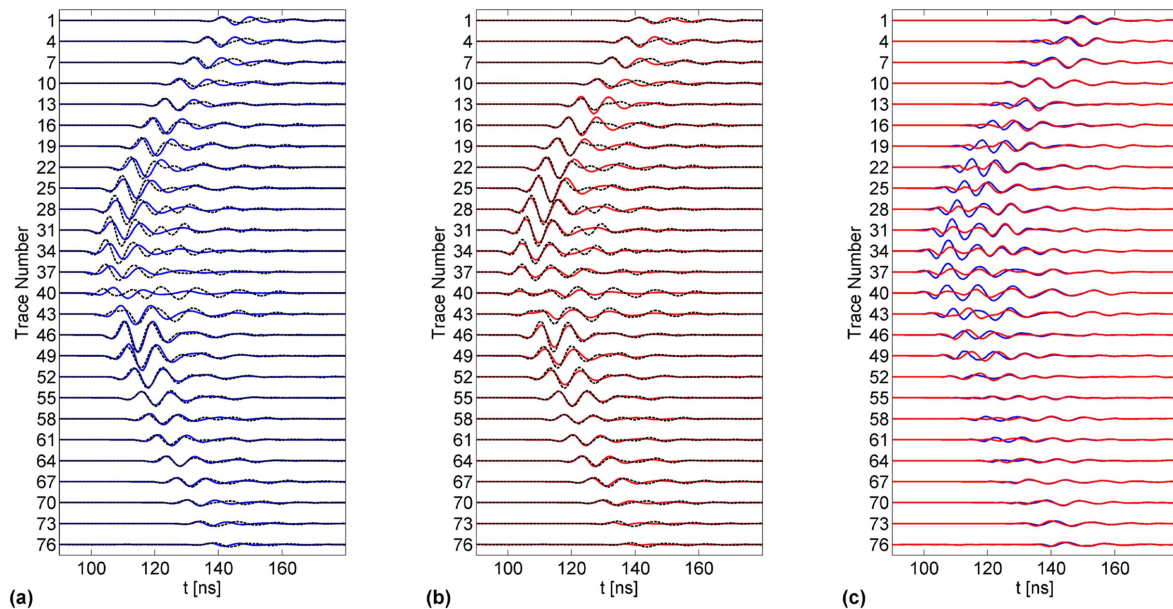


**Figure 4.11:** (a) and (b) are receiver gathers for location REC 20 in Figure 4.9. The dashed black and solid blue and red lines show every third observed radar trace and data generated from the ray tomograms in Figures 4.10a and 4.10c and full-waveform tomograms in Figures 4.10b and 4.10d, respectively. (c) Blue and red lines show differences between the blue and dashed black lines in (a) and between the red and dashed black lines in (b). Amplitudes in all panels are normalized with respect to the maximum amplitude of the input data.

#### 4.7. CONCLUSIONS

We have outlined the essential elements of a new 2-D full-waveform tomographic inversion scheme and described simple methods to account for 3-D radar-wave propagation effects and estimate the source wavelet (Appendices A and B). The new scheme has been applied to realistic pure 2-D and pseudo-3-D synthetic data as well as field data acquired in relatively dry crystalline rock and water-saturated unconsolidated sediments. In all four examples, the resolution of the full-waveform tomograms was significantly superior to that of the respective ray tomograms. Boundaries between structural units were sharply focused and features with dimensions as small as 0.3 - 0.5 of the dominant radar wavelength were clearly imaged in the full-waveform tomograms.

Although transmitter and receiver intervals of half the dominant wavelength proved to be suitable for the synthetic case studies, the results of inverting the field data suggested that

the intervals should be approximately half this value to avoid artifacts near the antennas. In an investigation of potential trade-offs between source-wavelet estimates and the full-waveform tomograms (Appendix B), we found that plausible timing errors in the source wavelets are unlikely to have major effects on  $\varepsilon$  tomograms, but plausible amplitude errors may result in moderately inaccurate  $\sigma$  tomograms.

The ray-based inversions required about 0.5 hours on a single 32-bit Intel Xeon 2.4 GHz processor and the full-waveform inversions required less than 12 hours on N+1 64-bit AMD 244 1.8 GHz processors, where N is the number of transmitters. Clearly, users must decide whether the significant improvement in resolution is worth the extra computational effort required for the full-waveform inversions.

Considering that the source wavelet may vary along the length of a borehole according to local conditions (Holliger and Bergmann, 2002; Ernst et al., 2006), future developments may include the possibility of determining and using a source wavelet for each transmitting regime of a borehole.

#### APPENDIX 4.A. ACCOUNTING FOR 3-D EFFECTS

Crosshole radar data are invariably influenced by 3-D wave-propagation phenomena, including both out-of-plane and radiation effects. Because most crosshole radar data are acquired with single-component non-directional antennas, there is generally insufficient information to discriminate between out-of-plane and in-plane events. Nevertheless, for media characterized by moderate velocity heterogeneity, the vast majority of energy contributing to the first few cycles of a recorded trace likely originates from within the plane containing the transmitter and receiver antennas; for typical crosshole experiments, the initial pulse can only contain energy from within a wavelength or two of this plane. Consequently, to minimize contamination from out-of-plane energy, we only consider time windows that include the first few cycles of the recorded traces in the inversion (see discussions by Pratt, 1999; Pratt and Shipp, 1999).

In applying 2-D computational codes in many disciplines of geophysics, sources and structures are assumed to extend to infinity on either side of the observation plane. In our FDTD algorithm, the sources are effectively modeled as infinite lines of point dipoles. Yet, we know that real antennas radiate energy in three dimensions (Ernst et al. (2006) have shown that the radiation pattern of a point dipole closely approximates that of the common insulated Wu–King-type antenna). An algorithm that explicitly incorporates 3-D wave propagation in a medium that varies in only two dimensions would be one way of addressing this issue (e.g., Zhou and Greenhalgh, 1998b). Implementation of such an approach in our time-domain scheme would be computationally very costly. We have thus chosen an alternative approach proposed by Bleistein (1986), in which appropriate corrections are made for 3-D geometrical spreading, a  $\pi/4$  phase shift, and a frequency scaling effect of  $1/\sqrt{\omega}$ , where  $\omega$  is the angular frequency. The corrections are made to the observed data in the frequency domain as follows:

$$E^{2D}(\mathbf{x}_{\text{trn}}, \mathbf{x}_{\text{rec}}, \omega) = E^{\text{obs}}(\mathbf{x}_{\text{trn}}, \mathbf{x}_{\text{rec}}, \omega) \sqrt{\frac{2\pi T(\mathbf{x}_{\text{trn}}, \mathbf{x}_{\text{rec}})}{-i\omega \varepsilon^{\text{mean}} \mu}}, \quad (4.A-1)$$

where  $E^{2D}(\mathbf{x}_{\text{trn}}, \mathbf{x}_{\text{rec}}, \omega)$  is the corrected data for a transmitter at location  $\mathbf{x}_{\text{trn}}(x, z)$  and a receiver at  $\mathbf{x}_{\text{rec}}(x, z)$ ,  $E^{\text{obs}}(\mathbf{x}_{\text{trn}}, \mathbf{x}_{\text{rec}}, \omega)$  is the original recorded data,  $T(\mathbf{x}_{\text{trn}}, \mathbf{x}_{\text{rec}})$  is the traveltime,  $i^2 = -1$ ,  $\varepsilon^{\text{mean}}$  is the mean dielectric permittivity of the media, and we set  $\mu = \mu_0$ , the magnetic permeability of free space. Thorough testing of this approach on synthetic crosshole

---

radar data demonstrates good agreement between corrected 3-D and corresponding pure 2-D data, as long as the data are generated for far-field regimes.

## APPENDIX 4.B. SOURCE WAVELET ESTIMATION

### 4.B.1. FIRST-ARRIVAL PULSE METHOD

Our first attempt to determine the source wavelet is based on analyses of the first-arrival pulses. The following relationship links the source current  $J_{\text{tm}}$  we employ in our FDTD algorithm to the recorded electric field in the far-field regime  $E^{\text{obs}}$  (de Hoop, 1995):

$$J_{\text{tm}}(\mathbf{x}_{\text{tm}}, t) \propto \int_{t'} E^{\text{obs}}(\mathbf{x}_{\text{rec}}, t') dt' \quad (4.B-1)$$

where  $t$  is time. We avoid problems associated with radiation-angle variations by only considering data from shortest-path transmitter-receiver pairs (i.e., those with radiation angles  $\approx 90^\circ$ ). To obtain a single estimate of the source wavelet, we integrate the radar data according to equation 4.B-1 and then compute the average of the extracted first-arrival pulses. An example of applying this procedure to synthetic data set I (Figures 4.1 - 4.3 and Table 4.1) is shown by the blue curve in Figure 4.B-1. Although the shape of this source-wavelet estimate is generally similar to that of the true source wavelet (black dashed line in Figure 4.B-1), it is not close enough; the resultant tomograms are unsatisfactory. This method performs poorly on all synthetic and observed data sets.

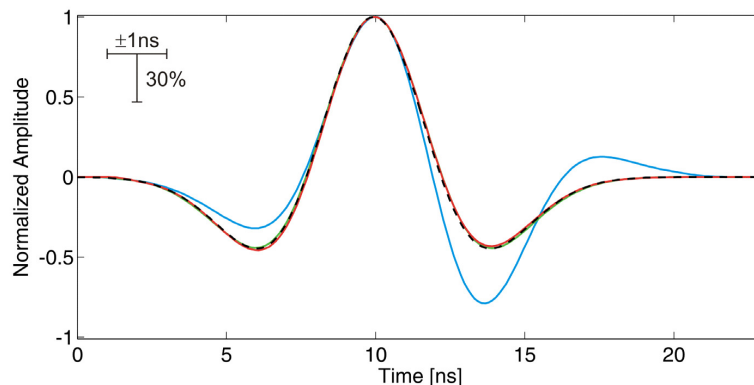


**Figure 4.B-1:** Source wavelet reconstructions for the 2-D synthetic data (Figure 4.1). Dashed black line is the true source wavelet, blue line is the source wavelet based on the first-pulse method, and the green and red lines are the first and final source wavelets based on the deconvolution method outlined in Figure 4.B-2. Amplitudes are normalized with respect to the maximum values for display purposes. The  $\pm 1$  ns and 30% bars indicate the phase shifts and amplitude variations used in the sensitivity analyses.

### 4.B.2. DECONVOLUTION METHOD

The key steps of our second attempt to determine the source wavelet are outlined in Figure 4.B-2. Our radar data can be represented mathematically as the convolution of the true source wavelet with the true impulse response (i.e., suite of spike radargrams) of the region of

Earth under investigation. In principle, the true source wavelet can be obtained by deconvolving the radar data with the true impulse response of the Earth. Of course, we do not know the latter. Fortunately, very good estimates of the source wavelet can be obtained by deconvolving the recorded data with our best estimates of the Earth's impulse response.

At the beginning of the full-waveform inversion, our best estimates of the  $\varepsilon$  and  $\sigma$  distributions are provided by the ray tomograms. It is not possible to compute directly the Earth's impulse response using our FDTD code, because an infinitesimal grid spacing would be required for computations involving a spike source. To circumvent this problem, we first employ the FDTD code to compute a suite of synthetic radargrams  $\mathbf{E}^{\text{syn}}(\varepsilon_{k=0}, \sigma_{k=0}, S_{k=0}(t), t)$  using the  $\varepsilon_{\text{ray}}$  and  $\sigma_{\text{ray}}$  distributions defined by the ray tomograms and a plausible source wavelet  $S_{k=0}(t)$  (boxes 1 and 2 in Figure 4.B-2), where  $k$  is the

iteration number. We use the source wavelet  $S_{\text{ini}}(t)$  determined from the analysis of the first-arrival pulses for this purpose, but any source wavelet with comparable length and frequency content would be sufficient at this stage. After Fourier transformation, we deconvolve (i.e., division in the frequency domain) the synthetic data  $\hat{\mathbf{E}}^{\text{syn}}(f)$  with  $\hat{S}_{k=0}(f)$  to give a frequency-domain estimate of the Earth's impulse response  $\hat{\mathbf{M}}(f)$ , where  $\hat{\phantom{x}}$  indicates a frequency-domain parameter and  $f$  is frequency (box 3 in Figure 4.B-2). Finally, deconvolution of the frequency-

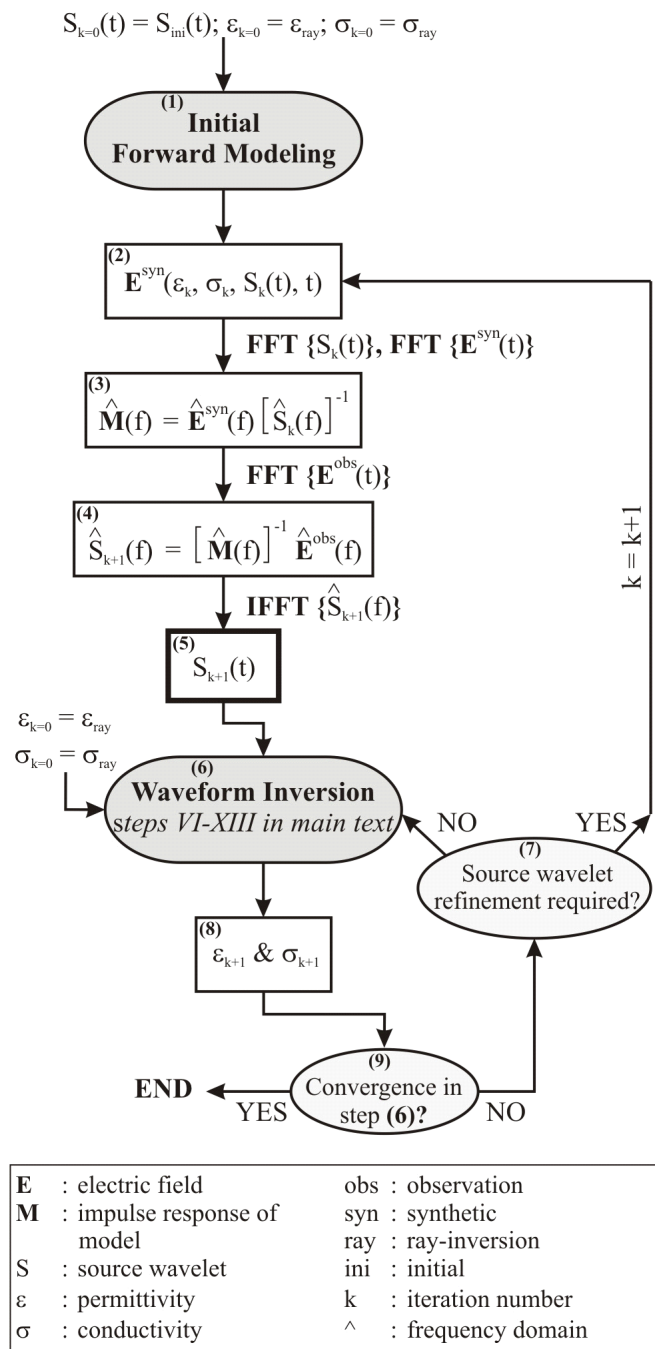


**Figure 4.B-2:** Flow chart outlining the deconvolution source-wavelet estimation method. See text for details.

domain version of the observed data  $\hat{\mathbf{E}}^{\text{obs}}(\mathbf{f})$  with  $\hat{\mathbf{M}}(\mathbf{f})$  and inverse Fourier transformation provides an estimate of the source wavelet  $S_{k=1}(t)$  (boxes 4 and 5 in Figure 4.B-2).

Since the equation in box 4 of Figure 4.B-2 describes an over-determined problem, in which far more data than unknowns are available, we estimate  $\hat{S}_{k=1}(\mathbf{f})$  by fitting the observations in a minimum least-squares sense. Although the process represented by steps 2-5 can be repeated using progressively improved full-waveform tomograms,  $\hat{S}_{k=1}(\mathbf{f})$  already matches closely the true source wavelet in Figure 4.B-1 (compare the solid green and dashed black lines). Indeed, source wavelets based on the ray tomograms are uniformly very close to those based on the best full-waveform tomograms for all of our synthetic and field data sets (compare the green and red lines in Figures 4.2, 4.7 and 4.B-1).

#### **4.B.3. SENSITIVITY OF THE TOMOGRAMS TO ERRORS IN THE SOURCE WAVELET.**

The potential exists for trade-offs between the properties of the source wavelet and those of the tomograms. We test the effects of these trade-offs using the source wavelet of synthetic data set I. Introduction of  $\pm 1$  ns phase shifts to the source wavelet (the form and amplitude of the wavelet are not changed), which correspond to  $\sim 10$  data samples and would be very visible in the radargrams (Figure 4.B-1), results in root-mean-square (RMS) differences of  $\sim 2.3\%$  between the final full-waveform  $\varepsilon$  tomogram and the original input model. For no phase shift, the RMS difference is 1.6%. Artificially reducing the amplitude of the source wavelet by  $\sim 30\%$  (the form and phase of the wavelet are not changed) results in a 13% RMS difference between the logarithm of the final full-waveform  $\sigma$  tomogram and the original input model, whereas the RMS difference is only 5% for the true source wavelet.



## 5. CONCLUSIONS AND OUTLOOK

### 5.1. REALISTIC BOREHOLE GEORADAR SIMULATION TOOL

The first part of my thesis research was dedicated to the development of a simulation tool for studying the detailed responses of borehole radar antennas that range from simple infinitesimal dipole-type to complex insulated finite-length antennas (e.g., Wu-King, PEC). The numerical scheme was based on a finite-difference time-domain discretization of the governing Maxwell's equations in cylindrical coordinates. This coordinate system allowed the 3-D radiation characteristics of the transmitter antennas to be correctly simulated using the computational efficiency of 2-D codes. To model accurately small antenna features (e.g., thin metallic wires), insulation, and intricate borehole structures, while keeping computational costs low, a simple but efficient local grid-refinement technique was implemented. Reflections from the boundaries of the model were markedly reduced by employing uniaxial perfectly matched layer absorbing boundaries.

The scheme was tested using a variety of antenna realizations and different borehole fillings (e.g., air and water). There were strong similarities in the radiation characteristics of infinitesimal dipole- and Wu-King-type antennas as long as the antennas were placed in the same media and internal reflections in the metallic rods of the finite-length antennas were small. As for the results of previous studies, I concluded that under these circumstances infinitesimal dipole-type antenna radiation patterns, which can be described by analytic expressions, are suitable approximations for real damped antennas.

Real antennas are usually designed to minimize reflections within the antenna wires while emitting enough energy into the subsurface. Accordingly, the optimal damping model for well-designed antennas lies somewhere between perfectly damped (i.e., no internal reflections: Wu-King-type antennas) and undamped (i.e., perfect electrical conductors that result in many internal reflections: PEC-type antennas). As a consequence, the radiation characteristics of infinitesimal dipole- and Wu-King-type antennas can only be used as first-order approximations to those of real georadar antennas.

The type of material filling of the boreholes was found to have a substantial effect on the antenna radiation patterns. For example, the radiation characteristics of antennas placed in water-filled boreholes were significantly influenced by guided phases that propagated along the boreholes. These guided waves dissipated energy along large portions of the boreholes, not just in the vicinity of the transmitters.

Knowledge gained from the numerical studies was applied to analyses of crosshole radar measurements made in the dry crystalline rock of the Grimsel Rock Laboratory (Switzerland) and in the water-saturated sediments of the Boise Hydrogeophysical Research Site (USA). Ray-based velocity and attenuation tomograms generated from these observed data sets were used in my full-waveform modeling scheme for the computation of suites of synthetic data for different antenna types and borehole fillings. Infinitesimal dipole- and Wu-King-type antennas yielded similarly good results for the air-filled (i.e. Grimsel) borehole experiments. In contrast, for the water-filled (i.e. Boise) borehole experiments, synthetic data generated for the Wu-King-type antennas matched closer the observed traces than those generated for the infinitesimal dipole-type antennas.

## **5.2. FULL-WAVEFORM INVERSION TOOL**

For the second part of my thesis, I developed a new 2-D full-waveform inversion scheme that allowed subsurface dielectric-permittivity and electrical-conductivity variations to be determined from crosshole radar data (Figure 5.1). Unlike the modeling approach presented in the first part of the thesis, the new scheme was built around finite-difference time-domain solutions of Maxwell's equations in 2-D Cartesian coordinates. The boundary conditions were improved by employing highly efficient generalized perfectly matched layer absorbing boundaries. The inversion component of the new scheme was adapted from methods developed in seismology. Cross-correlation of the forward-propagated vertical-electric wavefields with the back-propagated residual wavefields provided the update directions. This approach was particularly suitable for large data sets and models, because explicit calculations of the sensitivity matrix and its inverse were not required. To avoid convergence to local minima, reasonably accurate initial models were necessary. For this purpose, ray-tomographic reconstructions of the permittivity and conductivity distributions were found to be sufficient.

The new full-waveform inversion scheme was tested on synthetic data generated from 2-D models that contained different degrees of complexity. In general, the new scheme

produced good to excellent reconstructions of the original permittivity and conductivity models. For example, the locations, shapes, and physical-property contrasts of dielectric and/or conductivity bodies that were 0.3 - 0.5 of the dominant radar wavelength were well resolved within homogeneous background models, even when realistic random noise was added to the data. By comparison, these bodies were either not seen or were only barely perceptible in the corresponding ray tomograms. The new scheme was less successful in resolving discrete dielectric bodies embedded in heterogeneous (i.e., stochastic) background models; the full-waveform tomograms did not resolve these bodies much better than the ray tomograms. In contrast, the new scheme determined the key parameters of small and large conductive bodies embedded in heterogeneous media.

Application of the new inversion scheme to the Grimsel and Boise data sets required some additional technique developments (Figure 5.1). To account for 3-D effects, I designed and implemented a transformation scheme that accounted for 3-D geometrical spreading, a  $\pi/4$  phase shift, and a frequency scaling effect of  $1/\sqrt{\omega}$ , where  $\omega$  is angular frequency. Tests of the scheme on synthetic data resulted in good agreement between tomograms determined from true 2-D and transformed pseudo-3-D data. To estimate the source wavelet from the

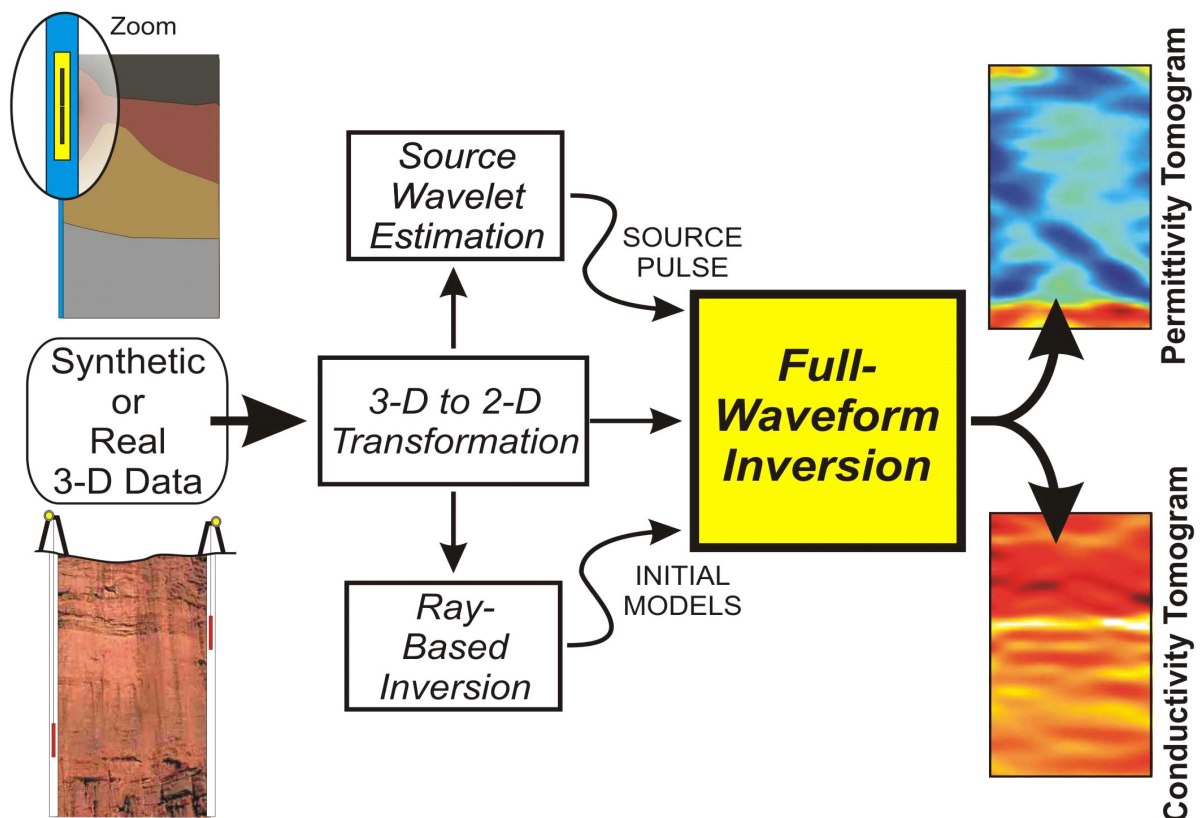


**Figure 5.1:** Summary of the different steps required to invert crosshole radar data using the new full-waveform inversion scheme. Prior to full-waveform inversion, the data are transformed to 2-D and then used to estimate the source wavelet and generate the initial ray tomograms.

observed data, I derived a deconvolution method that used selected traces of the observed data and the ray-based permittivity and conductivity tomograms. The accuracy of this method was verified on pertinent synthetic data.

After application of the two new techniques, full-waveform inversions of the two field data sets produced permittivity and conductivity tomograms that contained much higher resolution information than the respective ray tomograms; boundaries between structural units were more focused and the permittivity and conductivity contrasts were noticeably greater. Small-scale features that were 0.3 - 0.5 of the dominant radar wavelengths were clearly imaged in the full-waveform tomograms.

### **5.3. REMARKS AND PROBLEMS ASSOCIATED WITH FULL-WAVEFORM INVERSION IN THE TIME-DOMAIN**

My full-waveform inversion scheme requires 2-D data or at least data that are effectively transformed to 2-D and realistic estimates of the source wavelets. I have proposed solutions to both points.

Although the transformation scheme generates reasonably good results, it is an approximation that yields progressively poorer results with increasing traveltimes. Transformation of the observed data could be avoided by using quasi-3-D or full 3-D forward modeling algorithms. A quasi-3-D scheme would be computationally less expensive than a 3-D one, because the 3-D character of the transmitters and receivers would be accommodated while assuming the media to be 2-D. Unfortunately, quasi-3-D schemes are cumbersome to implement in the time-domain (Williamson and Pratt, 1995). A better approach would be to implement a quasi-3-D scheme in the frequency-domain, such that the wavefield modeling would concentrate on carefully chosen wavenumber components (e.g., Zhou and Greenhalgh, 1998). A full 3-D approach at this time is probably not feasible, because of high computational costs (e.g., Takenaka et al., 2003; Zhou et al., 2003).

Source wavelets are unknown at the beginning of radar field studies. They need to be estimated from the observed data. Although there is a wide variety of different approaches that address this problem (e.g., Mora, 1987; Zhou et al., 1997; Pratt, 1999), there is no single "best" solution. Even if the ideal source wavelet were to be determined in laboratory studies (e.g., Streich and Van der Kruk, 2006), there are a number of field-related effects (e.g., different borehole configurations and variable near-antenna radiation characteristics) that

would need to be accommodated in the numerical simulations. This is certainly possible, as I have shown in the first part of my thesis, but it increases the computational costs significantly.

#### 5.4. APPLICATION OF THE MODIFIED GEORADAR WAVEFORM INVERSION SCHEME TO SEISMIC DATA

The electromagnetic and acoustic wave equations are very similar (e.g., Carcione and Cavallini, 1995). As a consequence, it is relatively straightforward to modify my scheme for the full-waveform inversion of seismic data. Florian Belina, who completed his masters research under my supervision, has derived the necessary formulas for models with constant density, constant attenuation and variable velocity. He suitably modified my full-waveform inversion scheme and tested it on relevant synthetic crosshole seismic data (see Belina, 2006).

His study demonstrated that the similarities between the electromagnetic and acoustic situations are based on similarities between dielectric permittivity and compressibility and between the vertical-electric and acoustic-pressure fields. Accordingly, the modified modeling code can be used to simulate pressure and particle-velocity fields of acoustic waves propagating through heterogeneous models. The modeling domain is delimited by absorbing boundaries (e.g., Yuan et al., 1997) that are similar to those implemented in my electromagnetic code.

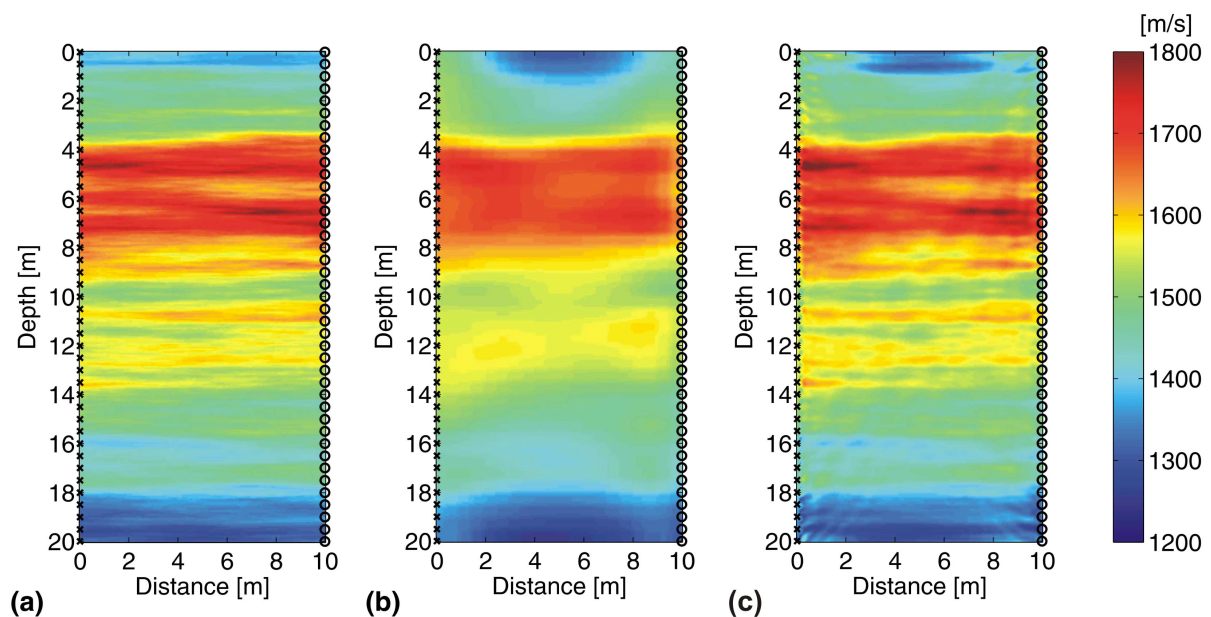


**Figure 5.2:** (a) Input acoustic velocity values (see main text). (b) Velocity tomogram that results from applying the ray-based inversion scheme to first-arrival traveltimes picked from the synthetic seismic data. (c) Velocity tomogram that results from applying a modified version of my full-waveform inversion scheme (see Belina, 2006).

Belina (2006) has applied the seismic version of the full-waveform inversion scheme to a range of increasingly complex models. It yielded accurate high-resolution tomograms that were noticeably superior to the standard ray tomograms. Figure 5.2 shows the original model and the resultant ray and full-waveform tomograms for one example (note, that compressibility was transformed to phase velocity using high frequency approximations). Pressure data were generated from a 10 x 20 m model characterized by a stochastic compressibility distribution (mean compressibility =  $4.44 \times 10^{-10} \text{ m}^2/\text{N}$  and standard deviation =  $6.74 \times 10^{-11} \text{ m}^2/\text{N}$ ) using 41 source and 41 receiver locations (density =  $1000 \text{ kg/m}^3$  and attenuation =  $0 \text{ Np/m}$ ). Clearly, the full-waveform tomogram in Figure 5.2 shows markedly more detail than the corresponding ray tomogram.

In its current form, the modified full-waveform inversion scheme is only capable of inverting the phase information (i.e., only acoustic velocities are determined). However, with further modifications, it should be possible to estimate attenuation distributions by inverting the amplitudes.

### **5.5. FREQUENCY-DEPENDENT MEDIA PARAMETERS**

A possible step to enhance the capabilities of the full-waveform radar inversion scheme would be to include material dispersion, such that the media parameters would be frequency dependent. This addition would be relevant to studies involving water-saturated environments (e.g., water-filled boreholes, porous materials). Taflove and Hagness' (2000) approach for accommodating different types of material dispersion in finite-difference time-domain algorithms could easily be implemented in my full-waveform inversion scheme. However, I suspect that it may only be possible to determine dispersion parameters at locations where the structures are very simple and the data are exceptionally good.

### **5.6. FUTURE DEVELOPMENTS AND APPLICATIONS**

In the following, I identify research topics that I consider important for future work.

Application of the 2-D full-waveform inversion scheme to untransformed 3-D synthetic data yielded tomograms (not shown) that were surprisingly similar to those based on the transformed data. Admittedly, the original source wavelet used to generate the synthetic data was noticeably simpler than those determined from the field data (see Chapter 4) and the estimated source wavelet differed somewhat from the original. I suspect that the estimated source wavelet partially accounted for the missing transformation (i.e., there are trade-offs

between the source-wavelet estimation algorithm and the 3-D to 2-D transformation), but this issue requires further investigation.

The advantages and disadvantages of inverting data in the time and frequency domains need to be explored further, perhaps via applications to suites of variably complex synthetic data. The two approaches would require similar computational efforts if all frequencies were to be considered in the frequency-domain inversions. However, a well-known advantage of frequency-domain approaches is that a limited number of frequencies may be sufficient to reconstruct satisfactorily the media properties, such that the computational time can be markedly reduced. By comparison, visualization of intermediate inversion results is more complicated in the frequency domain than in the time domain and understanding computational processes in the frequency-domain is challenging for the non-specialist.

Various authors have suggested that good initial models are required for successful full-waveform inversions. Unfortunately, there is currently no criteria for determining how good the models need to be. Models of (i) small conductive and dielectric bodies embedded in homogeneous media and (ii) models of small conductive bodies embedded in heterogeneous (stochastic) media can be accurately reconstructed by using quite simple starting models in the full-waveform inversion scheme, even if moderate levels of noise are added to the synthetic data. The situation is very different for small dielectric bodies embedded in heterogeneous media (see Chapter 3). Even the ray tomograms may not be sufficiently close to the true model for convergence to satisfactory results. What are the reasons for the poor results and what needs to be done to resolve better the dielectric bodies? Tarantola (2005) recommends using various starting models obtained from Monte Carlo simulations, but this is very expensive.

Determining suitable source wavelets is a critical component of full-waveform inversion schemes. The following stepwise modifications to my scheme could lead to closer fits of the model-predicted and observed data and generally more accurate tomograms:

1. In Chapter 2, I demonstrated that the borehole filling markedly influences the radiation characteristics, independent of the source type (e.g., infinitesimal dipole or finite length antennas). Accordingly, models of realistic boreholes with corresponding fillings should be included in the new scheme. This procedure would be straightforward to implement, although it may require variable grids (e.g., a locally refined grid; Chapter 2) or a different discretization technique (e.g., finite-element).

2. It may be advantageous to determine a source wavelet for each transmitter location (G. Pratt, personal communication). This would be appropriate for partially water-filled boreholes or for situations where the antenna-borehole coupling varies substantially (e.g., due to cavities).
3. Transmitter and receiver antenna locations are often imprecisely known. Although the coordinate errors may be quite small, they may result in significant artifacts in the tomograms (e.g., Peterson, 2001). To minimize these artifacts, Maurer (1996) and Maurer and Green (1997) included the seismic source and receiver coordinates in their ray-based inversion scheme. A similar approach could be included in my full-waveform inversions scheme.
4. In Chapter 4, I found artifacts to be created near transmitter and receiver locations, if the inversion cell size is too small with respect to the signal wavelength. My approach was, to choose cell sizes such that the artifact generation was minimal by still providing high-resolution tomograms. Another solution to minimize artifacts may be to add additional (virtual) transmitter and receiver positions by using interpolated recordings between current antenna locations. Methods have been introduced and successfully applied in radar as well as seismic data processing (e.g., f-x-y domain trace interpolation method; see Spitz, 1991; Wang, 2002; Heincke et al., 2005).

These enhancements could lead to improved dielectric permittivity and electrical conductivity tomograms by decreasing the artifacts and increasing resolution in poorly constrained areas of the models, in particular in the vicinity of the boreholes.

The full waveform inversion I have presented in this work is based on a cascaded or stepped inversion approach (i.e., first I invert for the permittivity and after convergence for the conductivity). The drawback of such a stepped scheme is that for example effects of electrical conductivity on the phase are mostly ignored (see Chapter 2). Using a simultaneous inversion approach, for example by inverting for the complex velocity (i.e., a function of permittivity and conductivity), would account for these effects, but typically fails to converge (e.g., Watanabe et al., 2004). However, a more sophisticated approach based on the subspace method has been proposed by several authors and successfully applied to a variety of seismic full-waveform inversion problems (e.g., Kennett et al., 1988; Sambridge et al., 1991; Pratt et al., 1998). This approach is particularly suitable for problems with different inversion parameter types (e.g., source wavelet, permittivity and conductivity). Instead of considering



completely detached (as in a stepped inversion) or merged decent vectors (as in a simultaneous inversion), the subspace technique uses a gradient approach (e.g., Tarantola, 1986) for the different parameters in their subspaces and then tries to find the best combination of these parameters types based on a well-constraint small scale matrix inversion. It is thus a hybrid between a gradient and a matrix inversion scheme (for a step-by-step explanation see Sambridge et al., 1991).

My full-waveform inversion scheme is optimized for crosshole geometries. However, the scheme could be modified to include surface measurements by making use of VRP or surface-to-surface configurations. Presently, only the transverse electrical (TE) mode equations are included in the modeling part of the scheme (i.e., antennas at the surface would have to be parallel to the tomographic plane). However, VRP and surface-to-surface studies would benefit from including measurements made with antennas oriented perpendicular to the observation plane. This would require solving the transverse magnetic (TM) mode equations and corresponding additions to the inverse part of my scheme. For investigations that include surface-to-surface measurements, it may be necessary to include a distance-dependent gradient scaling factor to account for amplitude decay (see Gauthier et al., 1986).

The full-waveform inversion scheme presented in this thesis has been applied to diverse synthetic and field data sets. Although of markedly better reconstructions of the subsurface permittivity and conductivity parameter distributions when compared to the corresponding standard ray-based inversion results, modifications to the scheme may eventually be required on the basis of experience gained by applying it to other data sets.



# APPENDIX A

## TESTS OF THE 3-D TO 2-D DATA TRANSFORMATION SCHEME

Finite-difference time-domain modeling based on crosshole radar configurations may be computationally expensive, especially if 3-D geometries in combination with a large number of transmitter locations are involved. In most cases, however, only the 3-D nature of the transmitter and receiver antennas needs to be considered, the media between the boreholes can be assumed to have 2-D characteristics (i.e., the media extends unchanged to infinity on either side of the observation plane). This situation is referred to as a 2.5-D or quasi-3-D problem (Bleistein, 1986; Williamson and Pratt, 1995). In the frequency domain, quasi-3-D solutions of Maxwell's equations are relatively easy to handle. They require the frequency-dependent wavefield to be computed for a given set of wavenumbers (e.g., Song and Williamson, 1995; Song et al., 1995; Zhou and Greenhalgh, 1998a, for the waveform modeling of seismic data). The corresponding approach in the time domain is only feasible if a cylindrical coordinate system is used (see Chapter 2) and the transmitters are located along the symmetry axis. Realistic synthetic data can be computed for single antennas or for transmitter/receiver antennas located along a borehole that coincides with the cylindrical

**Table A-1:** Media parameters used for testing the quasi-3-D to 2-D transformation.

Tests and Dependencies		Figures	Model width & depth [m]	Number of Receivers	Media parameters $\epsilon_r$ and $\sigma$ [mS/m]	Anomalous object dimensions [m] ( $r$ = radius; $w$ = width; $h$ = height)	Distances [m] and angles [°] tested
1a	Distance	A-1a A-2a	23 & 10.5	9	$\epsilon_{rm} = 5.0$ ; $\sigma_m = 0.5$	-	0.5 – 8.5
	1b	Angle		A-1a A-2b			41
2a	Distance	A-1b A-3a	23 & 10.5	9	$\epsilon_{rm}^{\text{mean}} = 3.7$ ; $\sigma_m^{\text{mean}} = 1.6$ with $\epsilon_r^{\text{std}} = 0.5$ , $\sigma^{\text{std}} = 0.3$ and $x = 1.0$ m, $z = 0.2$ m; deterministic anomalies: $\epsilon_{rA1} = 10.0$ ; $\sigma_{A1} = 10.0$ $\epsilon_{rA2} = 2.0$ ; $\sigma_{A2} = 3.0$ $\epsilon_{rA3} = 1.0$ ; $\sigma_{A3} = 0.0$ $\epsilon_{rA4} = 5.0$ ; $\sigma_{A4} = 0.1$	$r_{A1} = 0.5$ $w_{A2} \times h_{A2} = 1.0 \times 2.0$ $w_{A3} \times h_{A3} = 1.9 \times 2.8$	0.5 – 8.5
	2b	Angle		A-1b A-3b A-4			41

symmetry axis (see Chapter 4). Because the residual fields required for back-propagation need to be emitted simultaneously at all receiver locations, a time-domain inversion code operating in cylindrical coordinates would only work if at least one of the boreholes is parallel to the cylinder symmetry axis.

Taking into account the above points and the need to compute the complete wavefields multiple times during each waveform iteration, I came to the conclusion that pure 2-D calculations would be more accurate and faster. Consequently, to invert crosshole radar data using the 2-D full-waveform scheme required transformations that account for the 3-D nature of the antenna radiation patterns and media. I adopted the transformation approach proposed by Bleistein (1986), in which quasi-3-D data are effectively converted to 2-D line-source-type data (see Chapter 4, Appendix 4.A). In initial tests of the transformation scheme, I generated two quasi-3-D synthetic data sets using Maxwell's equations in cylindrical coordinates (see Chapter 2) and converted them to 2-D using Bleistein's (1986) approach. The quasi-3-D and the transformed quasi-3-D to 2-D radar sections were compared to true 2-D data computed for the same models (i.e., by using a 2-D modeling code).

### A.1. TEST 1: HOMOGENEOUS MEDIA

The first tests of the quasi-3-D to 2-D transformation were conducted on a simple model with homogeneous dielectric permittivity  $\epsilon_m = 5.0$  and conductivity  $\sigma_m = 0.5$  mS/m (Tests 1a and 1b in Table A-1; Figure A-1). Transmitter and receiver antennas were modeled as infinitesimal vertical electric dipoles. A realistic Ricker-type source pulse with a center frequency of 150 MHz was simulated for transmitter location TRN and receivers in the REC Groups 1 and 2 (Figure A-1).

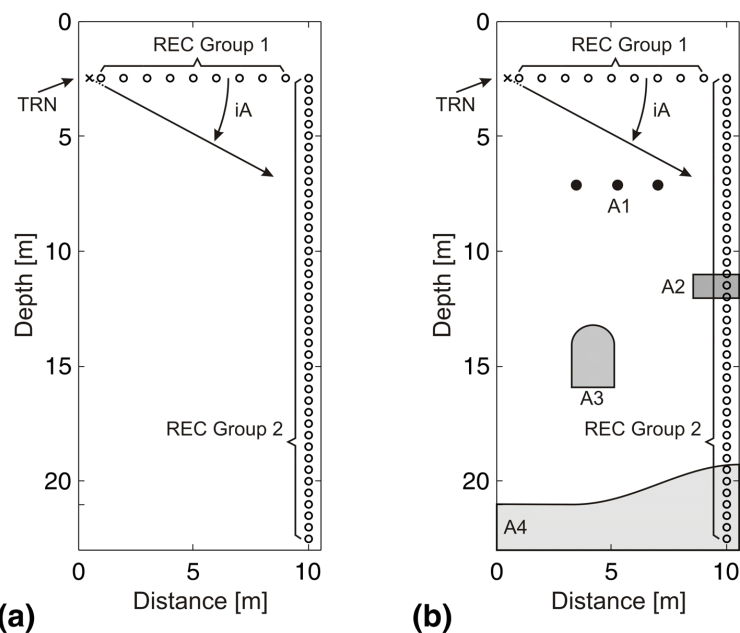


**Figure A-1:** Sketch of models used for testing the transformation scheme. (a) homogeneous model used for Test 1 and (b) stochastic model with deterministic anomalies A1 to A4 used for Test 2. TRN - transmitter; REC Group 1 and 2 - receivers used for testing the distance and angle dependence;  $iA$  - incidence angle (see Table A-1 for a detailed description of the media parameters).

The REC Group 1 receivers were used to test for distance-dependence variations, whereas the REC Group 2 receivers were used to test for angle-dependence variations. Ideally, the

transformed quasi-3-D to 2-D radar section should be identical to the true 2-D section. Figure A-2 demonstrates that differences between the two sections are negligibly small over all tested distances and incident angles. These differences between the squares of the values (percent differences in "energy" in the figure) are at least 20 times smaller than those between the quasi-3D and true 2-D sections (compare the black and red lines in Figure A-2).

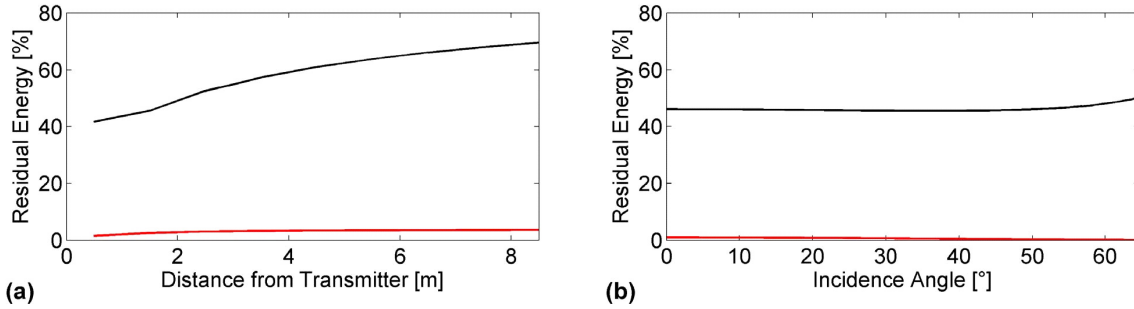


**Figure A-2:** (a) Distance- (REC group 1) and (b) angle- (REC group 2) dependent residual energies obtained from testing the homogeneous permittivity and conductivity models (Figure A-1a). Black and red lines are residual energies computed from differences between the quasi-3-D and true 2-D data and the transformed quasi-3-D and true 2-D data, respectively.

## A.2. TEST 2: STOCHASTIC MEDIA WITH DETERMINISTIC ANOMALIES

The second tests were conducted on models with more realistic media parameter distributions (Tests 2a and 2b in Table A-1; Figure 1b). The mean permittivity and conductivity of the stochastic models were  $\epsilon_{\text{rm}}^{\text{mean}} = 3.7$  and  $\sigma_{\text{m}}^{\text{mean}} = 1.6$  mS/m and the corresponding standard deviations were  $\epsilon_{\text{rm}}^{\text{std}} = 0.5$  and  $\sigma_{\text{m}}^{\text{std}} = 0.3$  mS/m. The stochastic variations were defined by exponential covariance functions with correlation lengths of 1.0 and 0.2 m in the horizontal and vertical directions. Figure A-3 demonstrates that differences between the transformed quasi-3-D to 2-D and true 2-D radar sections are negligibly small over all tested distances and incident angles up to  $45^\circ$ . The relatively large differences at

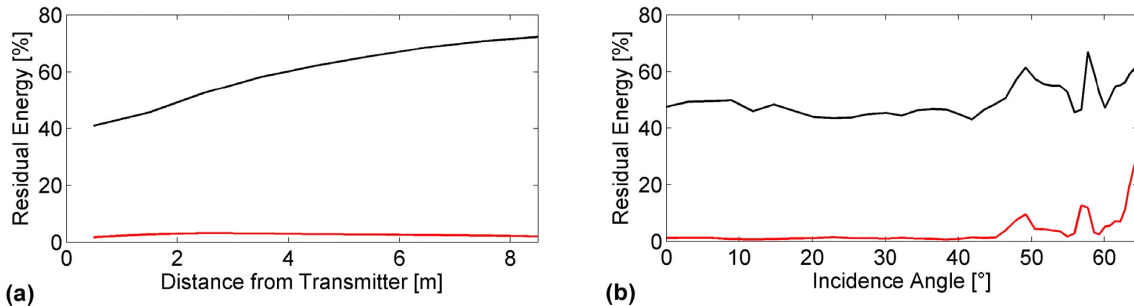


**Figure A-3:** (a) Distance- (REC group 1) and (b) angle- (REC group 2) dependent residual energies obtained from testing the heterogeneous permittivity and conductivity models (Figure A-1b). Black and red lines are residual energies computed from differences between the quasi-3-D and true 2-D data and the transformed quasi-3-D and true 2-D data, respectively.

larger angles are due to the slightly erroneous mean dielectric permittivity employed for computing the transformation (see Chapter 4-A: Accounting for 3-D effects, equation 4.A-1) and the low amplitudes at these angles. Furthermore, traces at incidence angles between  $45^\circ$  and  $67^\circ$  are strongly influenced by the rectangular (A2), tunnel (A3) and/or layer (A4) anomalies (Figure A-1b). Figure A-4 compares every 4<sup>th</sup> trace of the true 2-D data simulated for receivers in the REC Group 2 of Figure A-1b with the corresponding quasi-3-D and transformed quasi-3-D to 2-D traces. The residual traces in Figure A-4c clearly show the benefits of transforming the quasi-3-D data.

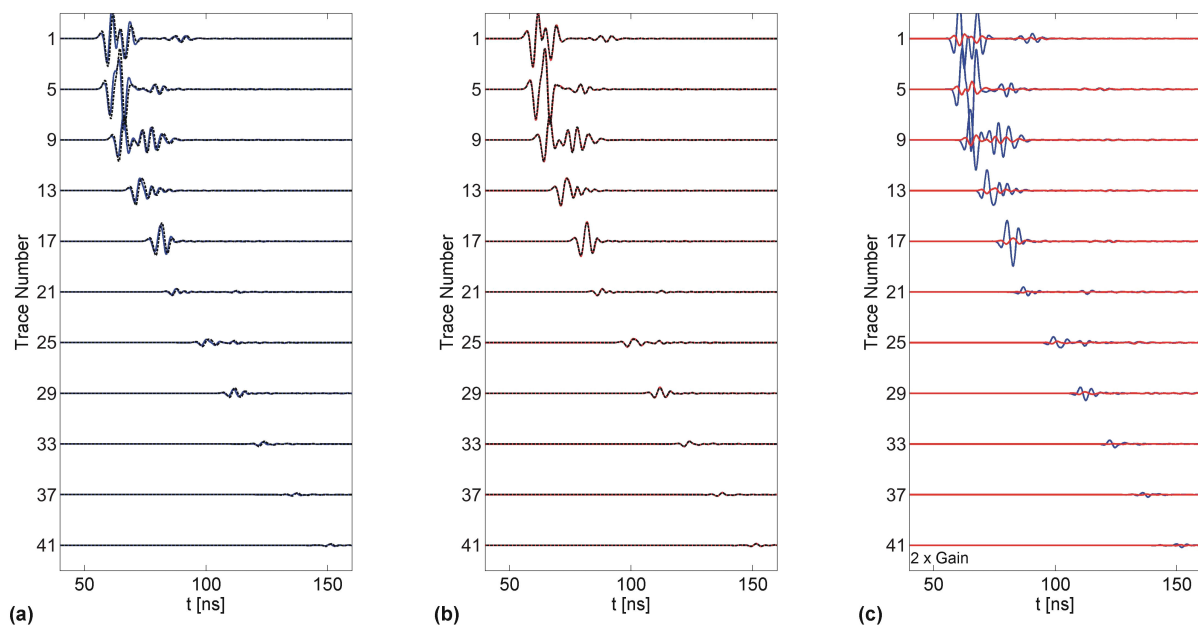


**Figure A-4:** (a) and (b) Radar sections for transmitter TRN and every fourth receiver from REC group 2 (Figure A-1b). The dashed black (barely visible) and solid blue and red lines show traces obtained from the true 2-D, quasi-3-D and transformed quasi-3-D data generated from the heterogeneous model shown in Figure A-1b. (c) Blue and red lines show differences between the blue and dashed black lines in (a) and the red and dashed black lines in (b). Amplitudes in all panels are normalized with respect to the maximum amplitude of the true 2-D data. The amplitudes of the residuals in (c) are gained by a factor of 2 relative to the respective radar traces.

### A.3. CONCLUSION

My implementation of the quasi-3-D to 2-D transformation algorithm performs well for minor to moderate media parameter variations. For media characterized by large contrasts, it is likely to yield inaccurate results at relatively large angles and for certain pathological cases that could be avoided by using variable permittivities in the transformation process. Indeed, Bleistein's (1986) approach is designed to work with variable media parameters (see

also Williamson and Pratt, 1995). However, variable permittivities would require the computation of rays from all transmitters to all receiver locations, the allocation of traveltime fractions to each grid cell, and the derivation of final correction factors (see Equation 4.A-1). In many cases, the assumption of small variations is valid, such that my simple approach is likely to yield reliable information.





# **APPENDIX B**

## **REALISTIC MODELING OF BOREHOLE GEORADAR ANTENNA RADIATION**

**Jacques R. Ernst**, Klaus Holliger and Hansruedi Maurer

73<sup>rd</sup> Annual International Meeting: Society of Exploration Geophysicists, 1162-1165 (2003).

### **B.1. SUMMARY**

High-frequency electromagnetic wave propagation phenomena associated with borehole georadar experiments are complex. To improve our understanding of the governing physical processes, we present a suitable finite-difference time-domain (FDTD) solution of Maxwell's equations in cylindrical coordinates. An important feature of this algorithm is the use of a powerful grid refinement technique that enables us to account efficiently for detailed design aspects of georadar antennas as well as materials with very high dielectric permittivities. This type of modeling provides the basis for improving the ray-based inversion of the first-cycle amplitudes and/or for performing the full-waveform inversion of crosshole georadar data. We first validate the accuracy of the algorithm with respect to the solutions for an infinitesimal electric dipole source as well as a wire-type dipole antenna and then apply it to explore the radiative properties of realistic antenna designs used in borehole georadar.

## B.2. INTRODUCTION

Borehole georadar is an increasingly popular method for high-resolution probing of the shallow subsurface. A typical setup for a borehole georadar experiment consists of an emitting dipole-type antenna located in a borehole and a corresponding receiving antenna in a neighboring borehole (Peterson, 2001). Tomographic inversions of travel-times and amplitudes provide information about the electromagnetic velocity/dielectric permittivity and the electric conductivity/attenuation structure, respectively (Olsson et al., 1992). Simultaneous inversion of the travel-times and amplitudes therefore holds the promise of separating the effects of dielectric permittivity and of electrical conductivity on electromagnetic wave propagation. This in turn could allow us to better constrain the distributions of important environmental, engineering, and hydrological parameters, such as porosity, water content, salinity, clay fraction, or ore grade within the probed region (Topp et al., 1980; Fullagar et al., 2000).

Both ray-based and full-waveform inversion of amplitude information requires a priori assumptions about the radiative properties of the borehole georadar emitters and receivers. A common approach is to assume that the radiation pattern of dipole-type borehole georadar antennas corresponds to the far-field radiation of an infinitesimal electric dipole, or a half-wave dipole antenna in a homogeneous medium (Olsson et al., 1992; Peterson, 2001). It is, however, not clear to what extent this assumption is justified and model studies are required to clarify this issue.

We present a versatile finite-difference time-domain (FDTD) solution of Maxwell's equations in cylindrical coordinates suitable for modeling pertinent aspects of typical borehole georadar antennas and experiments. This algorithm represents an extension of the method presented by Holliger and Bergmann (2002). The algorithm is first benchmarked against analytical solutions available for an infinitesimal electric dipole source and a basic thin-wire antenna and then applied to explore the radiation characteristics of typical borehole georadar antenna designs.

## B.3. MODELING APPROACH

Our modeling approach is based on a FDTD solution of Maxwell's equations in cylindrical coordinates. The algorithm is staggered and second-order accurate in both time and space (Yee, 1966; Holliger and Bergmann, 2002). The temporal and spatial discretizations are chosen to conform to standard numerical stability and dispersion criteria. The use of a cylindrical coordinate system implies that the models are rotationally symmetric

with respect to the vertical symmetry axis (i.e., the left-hand model edge). This is computationally efficient, correctly accounts for the radiative properties of the dipole-type transmitters as well as the geometric spreading characteristics of the electromagnetic wavefields, and is the most effective way to discretize small-diameter boreholes.

The assumption of cylindrical symmetry does, however, imply that the transmitters must lie on the cylindrical symmetry axis and that only the transmitter antennas can be explicitly modeled. Unless mentioned otherwise, the radiative properties of the receiver antenna are therefore emulated by recording the vertical component of the electric field, which approximates a vertical infinitesimal electric dipole receiver. The transmitter antenna is modeled either as an infinitesimal vertical electric dipole or as a finite-length dipole-type antenna. The metal parts of such transmitter antennas can be modeled as perfect electrical conductors by setting to zero the electric field components tangential to the metal surfaces. Alternatively, we can also simulate arbitrary distributions of the electrical conductivity within the metal parts of the antennas. The latter is achieved by defining the antenna by special “resistor cells” (Maloney and Smith, 1992). The transmitters are excited by a compact Gaussian voltage pulse, whose amplitude spectrum is essentially white in the frequency range of interest.

To avoid artificial reflections from the model boundaries, we use cylindrical symmetry conditions along the left-hand edge and add a highly conductive and hence highly diffusive buffer zone along the top, bottom and right-hand edges of the model space. Cylindrical symmetry with regard to the left-hand model edge is achieved by setting to zero the tangential component of the magnetic field located directly on the symmetry axis and mirroring the values of the vertical component of the electric field located closest to the symmetry axis. The conductivity in the absorbing buffer zone is gradually increasing so that the quality factor  $Q$  for the center frequency reaches a value of  $\sim 2$  at its outer edges. The width of the diffusive buffer zone corresponds to  $\sim 2$  dominant wavelengths.

The simulation of georadar antennas involves the discretization of small intricate structures. Moreover, parts of the model space, such as a water-filled borehole, may be characterized by very high dielectric permittivities and correspondingly short wavelengths. Using a uniformly fine grid to accommodate such features is computationally inefficient and severely limits the size and realism of the models that can be studied. This problem is circumvented by using an adaptation of the grid refinement technique described by Robertsson and Holliger (1997). This technique allows for local refinements of the spatial

discretization by an integer factor with regard to the master grid. In our experience, odd integer refinement factors are clearly preferable, because they require less extensive interpolation of the electromagnetic wavefield and hence introduce less numerical inaccuracies compared to even refinement factors.

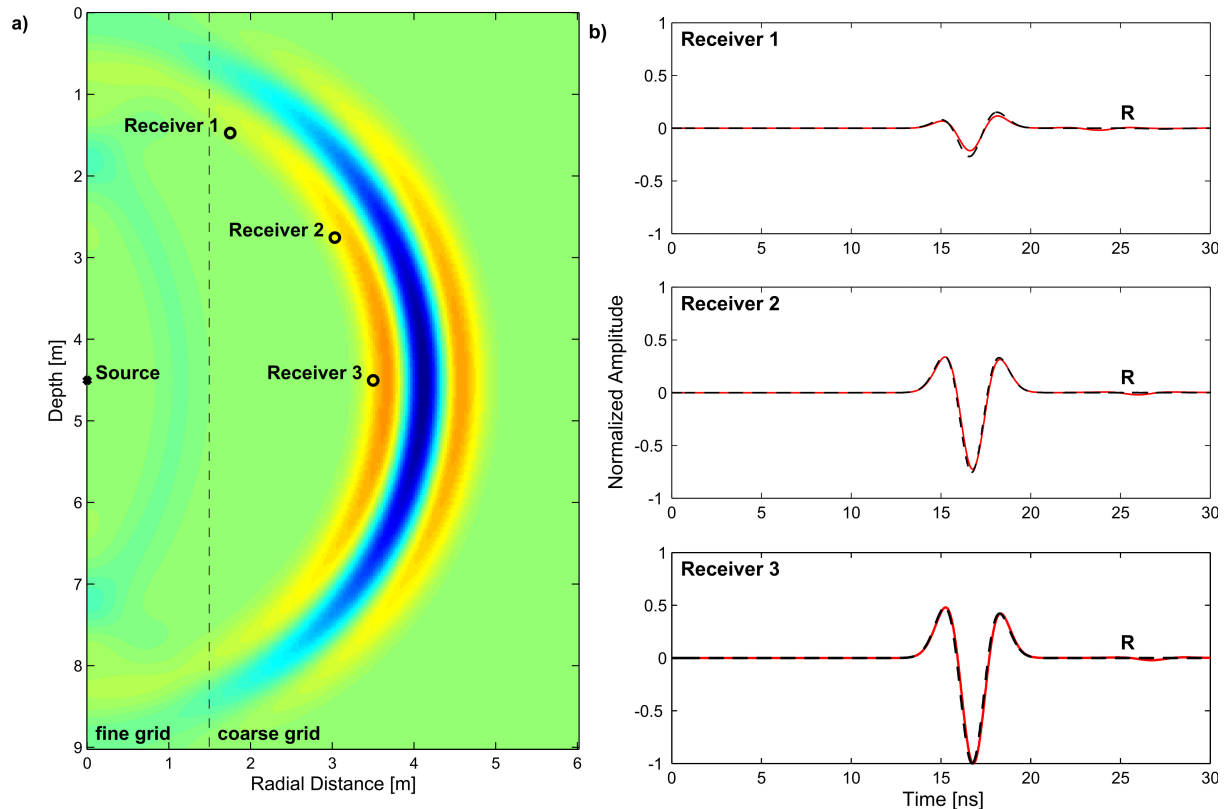


**Figure B-1:** (a) Snapshot of the vertical component of the electric field and (b) corresponding radargrams for models with (solid lines) and without (dashed lines) grid refinement. R: reflection from boundary between fine and coarse grid regions.

#### B.4. VALIDATION AND APPLICATION OF THE ALGORITHM

Figure B-1 serves to illustrate the validity and accuracy of the modelling approach described above. Figure B-1a shows a snapshot of the vertical component of the electric field radiated from an infinitesimal vertical electric dipole source. In this example, we used a grid refinement factor of 5. The snapshot was taken after the electromagnetic wavefield had propagated for 18 ns or  $\sim 3$  dominant wavelengths. The boundary between the finer and coarser regions of the grid is indicated by a vertical dashed line. The wavefield appears to be smooth and continuous across this “discontinuity” and there is no evidence for reflected or “parasitic” stationary energy thus indicating that the algorithm is working properly. This impression is quantitatively confirmed by Figure B-1b, which compares individual radargrams for the above model and a model with a uniformly fine grid spacing recorded at a constant radial distance of 3.5 m at angles of  $30^\circ$ ,  $60^\circ$ , and  $90^\circ$  with respect to the vertical.

The accuracy of the latter has been previously confirmed by comparison with the analytical solution (Holliger and Bergmann, 2002). With the exception of a minor reflection from the boundary between the finely and coarsely discretized regions of the grid and small phase differences due to differing amounts of numerical dispersion the two solutions are identical.

The next step is to test the validity of our algorithm when the electromagnetic wavefield is radiated from a realistic finite-length antenna. For this purpose we have implemented a wire-type dipole antenna with a radius of 2.5 mm and a length of 45 cm. The antenna wire is assumed to be a perfect electrical conductor, which is emulated by setting to zero the components of the electric field within the antenna and tangential to its surface. The source signal is a Gaussian voltage pulse fed into the central gap, or terminal, of the antenna. To evaluate the radiation patterns, the radial and vertical components of the electric field have been recorded at a constant distance of 3.5 m, or about  $\sim 3$  dominant wavelengths, from the center of the antenna. From these recordings we calculate the tangential components of the

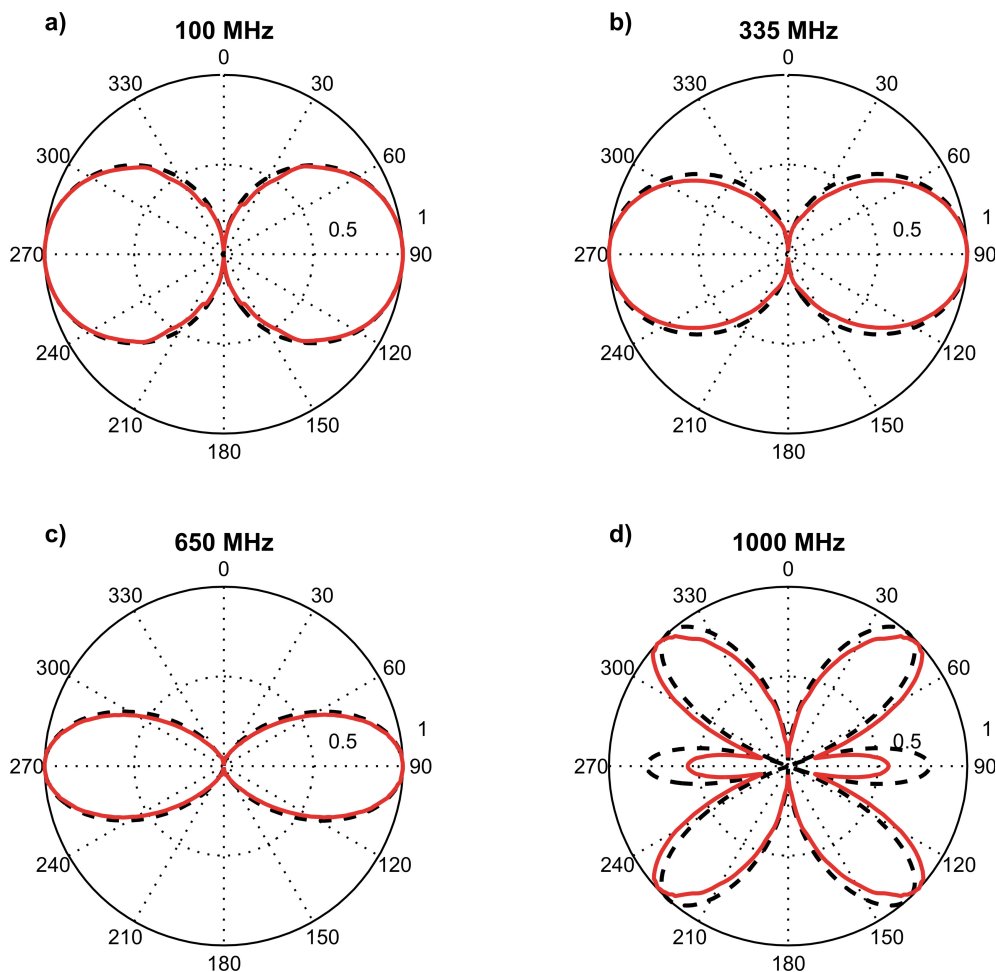


**Figure B-2:** Numerical (solid lines) and analytical (dashed lines) radiation patterns of the tangential component of the electric field for a wire-type dipole antenna at various frequencies. The modeled antenna is 45 cm long and has a radius of 2.5 mm. The half-wave tuning frequency of this antenna in the considered medium (vacuum) is  $\sim 335$  MHz.

electric field and determine the amplitude spectra to evaluate the corresponding radiation patterns at various frequencies.

In Figure B-2 we compare the resulting radiation patterns with corresponding analytical far-field radiation patterns for a thin-wire antenna of the same length (Stutzman and Thiele, 1998). Radiation patterns are shown for frequencies of 100, 335, 650, and 1000 MHz. The half-wave tuning frequency of this antenna is  $\sim 335$  MHz. Overall, there is quite good agreement between the numerical and analytical radiation patterns. At all frequencies, the largest discrepancies occur at angles close to the vertical, where also the artificial reflections from boundary between the finer and the coarser parts of the grid are largest (Figure B-1b). The somewhat larger discrepancies at 1000 MHz are probably due to the fact that at this high frequency the radiated amplitude of our modeled antenna is already quite low and correspondingly contaminated by numerical noise.

Finally, we apply the algorithm to realistic georadar antenna designs and compare the corresponding radiative properties and signal characteristics. A key characteristic of a well-designed pulsed georadar antenna is that the signal shape of the radiated electromagnetic field should be compact and closely resemble the input voltage pulse. For finite-length dipole-type antennas, this implies that internal reflections within the antenna rod must be minimized. This can be achieved through appropriate resistive loading of the antenna. The two most common ways to achieve this are through a near-constant resistive load along the entire antenna or through so-called Wu-King-type resistivity profiles (Wu and King, 1965). The latter emulate conductivity profiles within antenna wires that scale hyperbolically with the distance from the

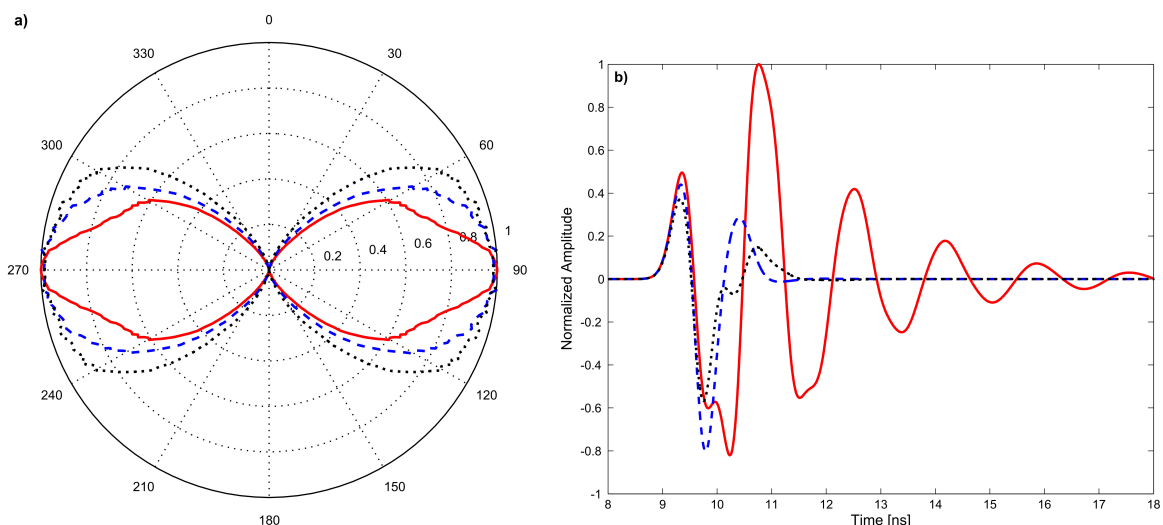


**Figure B-3:** (a) Radiation patterns as defined by the Poynting vector and (b) radargrams for a perfectly conducting (solid lines), constant conductivity (dashed lines), and “Wu-King-optimized” (dotted lines) wire-type dipole antennas. The radargrams correspond to the vertical components of the electric field recorded at a horizontal distance of 2.5 m from the antenna terminals.

terminal. Figures B-3a and B-3b compare the radiation patterns and waveforms of the radiated signal, respectively, for antennas with a constant resistive load ( $10 \Omega$ ) and Wu-King-type optimized resistive loading with those for a perfectly conducting wire-type antenna. For all antennas the wire is 46 cm long and has a radius of 2.5 mm. The radiation patterns are represented by the time-averaged Poynting vector, which is indicative on the energy flux of the radiated electromagnetic field. Figure B-3a shows that there are significant differences in the radiative properties of these basic antenna types. This information is critical for quantitative interpretation of the amplitude information recorded in crosshole georadar experiments. Figure B-3b shows the vertical component of the electric field radiated from these antennas recorded at a horizontal distance of 2.5 m from the center of the antennas. The signal character for the perfectly conducting antenna is indeed very “ringy”, whereas the waveforms radiated from the loaded antennas exhibit the desired “crispness”.

## **B.5. CONCLUSIONS**

We have developed a FDTD solution of Maxwell's equations in cylindrical coordinates that is suitable for modeling the detailed radiation characteristics of realistic borehole georadar antenna designs. The use of a powerful grid refinement technique greatly enhances the numerical accuracy and efficiency of the algorithm and allows us to simulate even detailed design aspects of transmitter antennas in an explicit fashion. Although the use of a cylindrical symmetry system only allows for the explicit modeling of the transmitter antennas, these results are also fully applicable to corresponding receiver antennas due to the validity of the reciprocity theorem in antenna theory. This information is a key prerequisite to take full advantage of amplitude information of crosshole georadar data through a full-waveform inversion approach as well as for the optimized design of novel antenna systems.





# APPENDIX C

## FDTD MODELING OF BOREHOLE GEORADAR DATA

Jacques R. Ernst, Klaus Holliger and Hansruedi Maurer

10<sup>th</sup> International Conference on Ground Penetrating Radar, 229-232 (2004).

### C.1. ABSTRACT

We present a finite-difference time-domain (FDTD) algorithm to realistically model the radiative properties of borehole georadar antenna systems and therefore to improve our understanding of the governing physical processes. Using a grid refinement technique and uniaxial perfectly matched layer (UPML) absorbing boundary conditions enables us to account efficiently and accurately for detailed aspects of antenna design and borehole environment, particularly, materials with very high dielectric permittivities such as water. Our FDTD-approach provides a suitable basis for improving the ray-based inversion of the first-cycle amplitudes as well as for performing full-waveform inversions of crosshole georadar data. The algorithm is applied to constrain the impact of air-filled boreholes on the radiative characteristics of typical georadar antennas. A crosshole data set was acquired under well-constrained conditions and used to compute a ray-based inversion. The wavefield modeled by using the resulting dielectric permittivity and attenuation tomograms is then compared to the measured data.

## C.2. INTRODUCTION

Borehole georadar is a popular high-resolution method for imaging the shallow subsurface. A typical setup for a borehole georadar survey consists of an emitting dipole-type antenna and a corresponding receiving antenna in a nearby borehole (Peterson, 2001). Tomographic inversion of crosshole georadar traveltimes and amplitudes provide information about the dielectric permittivity and the electric conductivity (Olsson et al., 1992). This information allows us to constrain better the distributions of important environmental, engineering, and hydrological parameters (e.g., porosity, water content, salinity, clay fraction, ore grade) within the probed region (Topp et al., 1980).

Ray-based and full-waveform inversions of crosshole georadar amplitudes require a priori knowledge about the radiative properties of the borehole antennas. A common approach is to assume that the radiation pattern of a dipole-type borehole antenna corresponds to the far-field radiation pattern of an infinitesimal electric dipole or a half-wave dipole antenna in a homogeneous medium (Olsson et al., 1992). It is, however, not clear to what extent this assumption is justified. Realistic model studies are required to clarify this issue. Reference (Holliger and Bergmann, 2002) uses a finite-difference time-domain (FDTD) approach to explore the effects of borehole on the radiative properties of an infinitesimal electric dipole transmitter. To extend this study, we present a versatile FDTD solution of Maxwell's equations in cylindrical coordinates that is capable of modeling typical borehole georadar antenna systems under realistic operating conditions. First, we compare the radiative properties of a realistic borehole georadar antenna in a homogeneous medium and in an air-filled borehole with the analytic full-space solutions for an infinitesimal electric dipole. Then, the algorithm is applied to model a crosshole georadar data set acquired under well-controlled conditions in the Grimsel Rock Laboratory in the central Swiss Alps. The Swiss Cooperative for the Storage of Nuclear Waste (NAGRA) operates this facility.

## C.3. METHODOLOGY

The cylindrical geometry of boreholes and georadar antennas prefers the use of a rotationally symmetric cylindrical coordinate system. Employing a cylindrical coordinate system and assuming rotational symmetry not only represents the geometry perfectly, it also reduces the computational cost to that of a 2-D problem, while correctly accounting for the 3-D geometrical spreading and radiation characteristics of dipole-type transmitters. Transforming Maxwell's equations to a 2-D cylindrical coordinate system yields to two sets of equivalent coupled partial-differential equations; the transverse magnetic mode (TM) and

the transverse electric mode (TE) equations. In a borehole georadar setup, it is the vertically oriented electric fields that are important, so we use the TM-mode equations in our approach. They are discretized using a staggered leapfrog FDTD scheme that is second order accurate in both, time and space (Yee, 1966). The temporal and spatial discretizations are chosen to conform to standard numerical stability and dispersion criteria.

Using a cylindrical coordinate system, however, implies that the transmitting antenna must be placed on the symmetry axis (cylinder axis) and that only transmitters can be explicitly modeled. The receiving antennas are therefore approximated with a vertical infinitesimal electric dipole, whereas the transmitting antennas are modeled as either an infinitesimal vertical electric dipole or as a finite-length dipole-type antenna. A realistic antenna often consists of a number of resistors fixed along the metallic parts of the antenna to minimize internal reflections. This kind of antennas can be simulated for instance by changing the resistivity of the cells defining the metallic part of the antenna as proposed by Wu and King (1965) or Maloney and Smith (1992). The antenna is excited by feeding a compact Gaussian voltage pulse into its central gap, whose amplitude spectrum is essentially white in

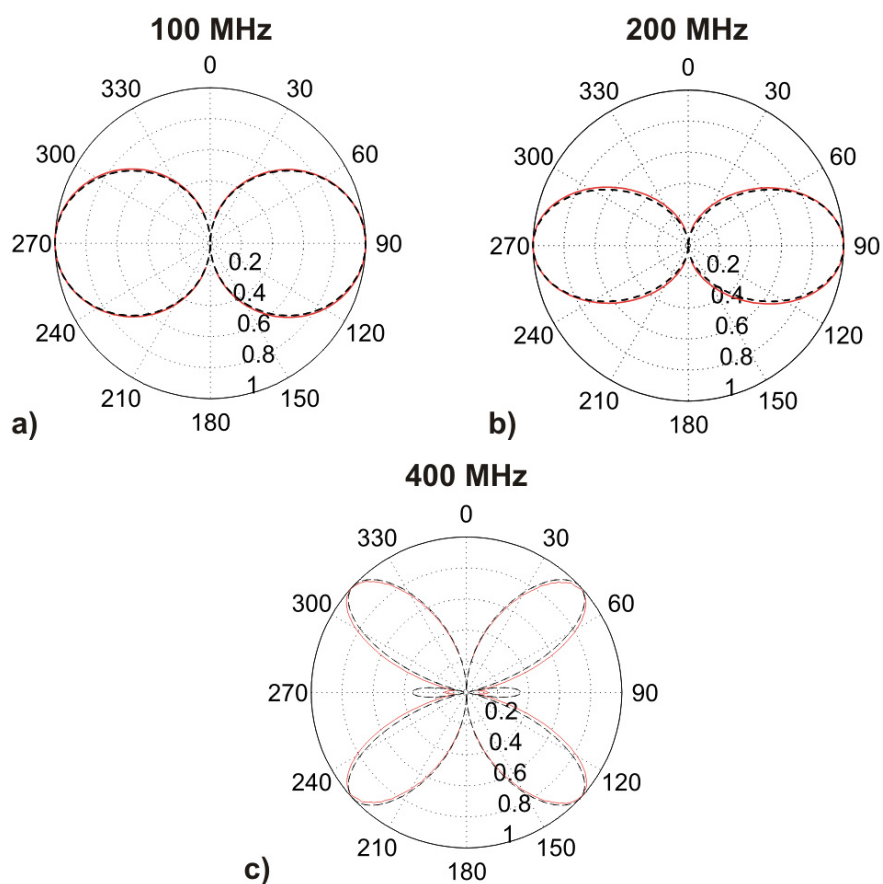


**Figure C-1:** Numerical radiation patterns calculated using a homogeneous model with an PEC antenna (red) and the analytical radiation pattern for a PEC antenna (black-dashed) for diverent frequencies.

the frequency range of interest. To allow simulations of finite-length antennas using millimeter-range cell sizes, we implemented a locally refined grid in the vicinity of the transmitter borehole as described by Robertsson and Holliger (1997). The refinement is achieved by splitting cells, such that the coarse-grid spacing is an integer times the fine-grid spacing. It is especially suitable for representing regions of unusually low velocities (i.e. high dielectric permittivities), such as water-filled boreholes.

To avoid artificial reflections from the model boundaries, we apply absorbing boundary conditions along the top, bottom and right model edges. Cylindrical symmetry conditions are employed along the left model edge, by mirroring the electric and magnetic field components in the immediate vicinity of the cylinder symmetry axis. For the absorbing boundary conditions, we use the perfectly matched layer (PML) approach (Berenger, 1994), suitably modified for uniaxial anisotropic medium (Taflove and Hagness, 2000). Our uniaxial perfectly matched layer (UPML) algorithm is particularly suitable and computationally efficient for heterogeneous media and for the low electrical conductivities that prevail in the georadar regime of electromagnetic wave propagation.

#### **C.4. VALIDATION AND APPLICATION OF THE ALGORITHM**

To validate our algorithm, we modeled the electromagnetic wavefield radiated from a realistic finite-length antenna. For this purpose, we implemented a wire-type dipole antenna with a radius of 1 mm and a total length of 40 cm in a 4.5 x 9 m homogeneous model (dielectric permittivity  $\varepsilon = 9\varepsilon_0$ , with  $\varepsilon_0$  the vacuum permittivity and conductivity  $\sigma = 5 \text{ mS/m}$ ). The antenna wire is assumed to be a perfect electrical conductor (PEC), which is achieved by setting the conductivity in the metallic parts of the antenna to that of copper ( $5 \cdot 10^7 \text{ S/m}$ ). In this case we are working with a half-wave tuning frequency of about 200 MHz. The antenna is excited by feeding a Gaussian voltage pulse into its central gap (terminal). The radiation characteristic can then be evaluated by calculating the tangential electric field. It can be obtained using the radial and vertical electric field components, recorded in a constant distance of 1.6 m, or about 4 dominant wavelengths, from the center of the transmitter antenna. Calculating the amplitude spectra of the tangential field allows the evaluation of the radiation pattern at various frequencies. In Figure C-1 we compare numerically computed radiation patterns (red) with the corresponding analytical solutions (black) (Stutzman and Thiele, 1998) for frequencies of 100, 200, and 400 MHz. The radiation patterns for low to intermediate frequencies (Figure C-1a and C-1b) agree very well with their analytical counterpart. The major side-lobes in the radiation pattern at 400 MHz (Figure C-1c) show

good agreement with the analytic solution. Whereas the two small lobes at angles close to the horizontal show large discrepancies, probably due to the fact, that amplitudes are relatively small at high frequencies and the increased influence of the numerical noise.

We now want to analyze the influence of an air-filled borehole on the radiation pattern. For this purpose, we modified the antenna wire such that no reflections inside the metallic parts occur. This is achieved by hyperbolically increase the resistivity of the cells corresponding to the metallic parts of the antenna. The resistivity-distribution was chosen as proposed by Wu and King (1965). Figure C-2 shows the radiation patterns for an insulated antenna in an air-filled borehole (black) compared to the simulation with a similar setup, but without insulation and borehole (red) and to the infinitesimal vertical electric dipole approximation (blue-dashed) at frequencies of 100, 200 and 400 MHz. All models have the same dimensions and material properties as in the previous simulation. A 5 cm radius borehole with vacuum properties and a 1.25 cm radius insulation ( $\epsilon_{\text{ins}} = 4\epsilon_0$  and  $\sigma_{\text{ins}} = 0$  mS/m) are centered along the symmetry axis. Good agreement between the shapes of the patterns for all solutions is found again at low to intermediate frequencies (Figure C-2a and

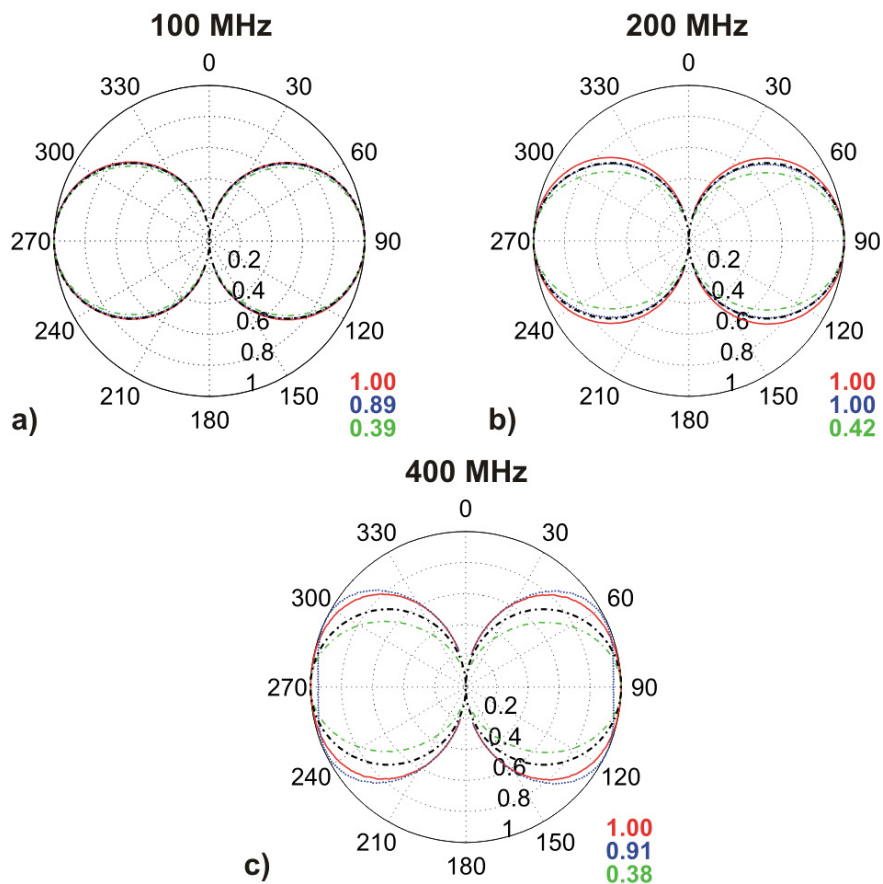


**Figure C-2:** Radiation patterns for a Wu-King type antenna in a homogeneous model (red), in a homogeneous model and insulated antenna (green), homogeneous model and borehole and insulated antenna (blue), and the pattern for an infinitesimal vertical electric dipole (black).

C-2b), while at higher frequencies (Figure. C-2c) the discrepancies are larger. High amplitude decay is observed in case of the presence of an air-filled borehole for all frequencies, whereas the insulation has only minor effects on the maximum amplitude. The infinitesimal vertical electric dipole approximation is particularly a good first order approximation in the low to intermediate frequency range.

We could show that only miniscule differences between the homogeneous model without insulation and borehole and the corresponding model with insulation and borehole occur in the relevant frequency range of typical georadar systems. To test these observations, we acquired a crosshole georadar dataset in an almost homogeneous environment in NAGRA's Grimsel rock laboratory in central Swiss Alps. In the following, we are going to investigate the influence of different modeling approaches on the wavefield. This is achieved by estimating the electromagnetic properties of the survey area using a ray-based inversion scheme (Paige and Saunders, 1982). Implementing these results in our FDTD-forward solver allows us to evaluate the wavefield with respect to the measured data. The two perfectly parallel boreholes, each 20 m long and 10 m apart, define the survey area on which we are focusing.

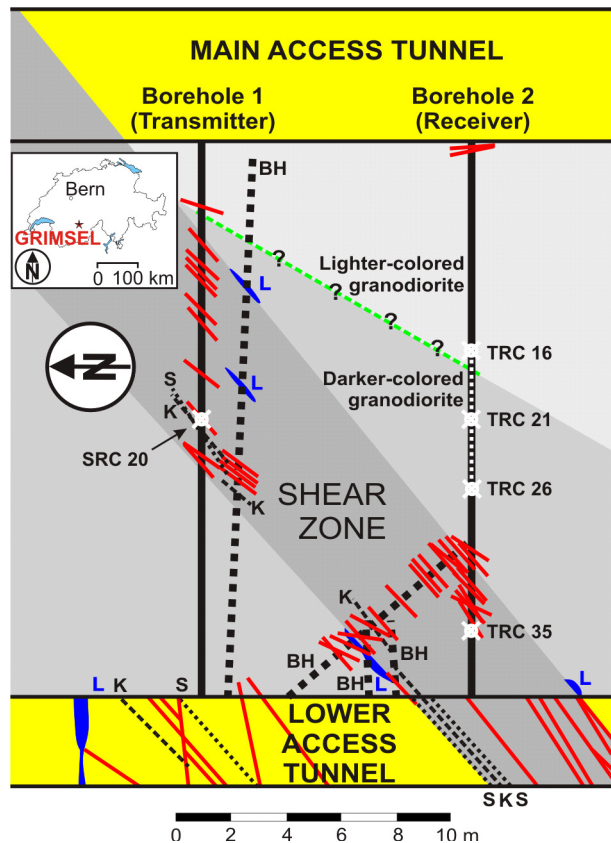


**Figure C-3:** Geometry and geologic interpretation of our survey area (after Majer et al., 1990). Bold lines show boreholes used for our radar inversion, BH are boreholes used for geologic interpretations, dotted lines (S) are thin shear bands and dashed lines (K) are cataclasite zones. Blue areas (L) are lamprophyres and red lines (unlabeled) are fractures.

Previous seismic, geologic and geomechanical investigations of the area (Figure C-3) show a major shear zone (Majer et al., 1990). The survey was carried out with two 250MHz RAMAC borehole georadar antennas, with a transmitting antenna in borehole 1 and a receiving antenna in borehole 2. Traces were recorded every 0.5 m for both, transmitter and receiver, resulting in a total amount of 40 shot and 41 recording positions. We used a sample interval of 0.32 ns and a total recording time of 480 ns. To be able to compare measured and modeled traces, we compute dielectric permittivity and conductivity tomograms with a ray-

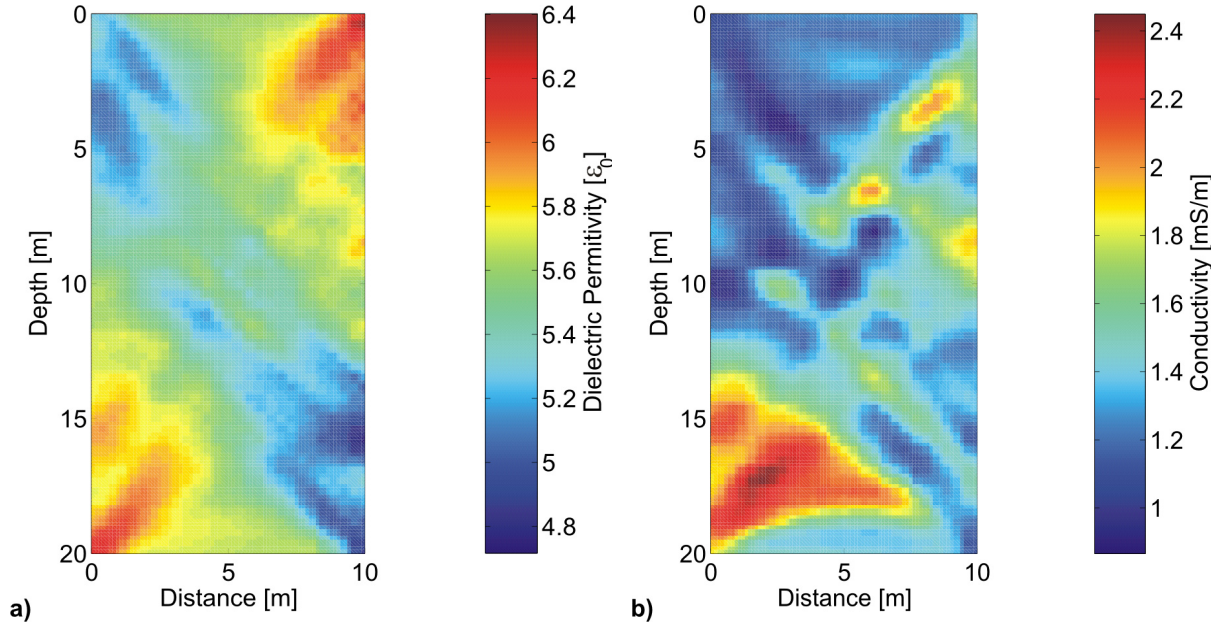


**Figure C-4:** (a) dielectric permittivity tomogram and (b) conductivity tomogram

based inversion of traveltimes and amplitude data. Traveltimes were found by picking the first arrivals of each measured trace. To obtain the amplitude data, we calculated the Hilbert transform of each trace and picked the maximum amplitude in a 12 ns time-window starting at the first-arrival time. While we manually have to account for the radiation characteristic by applying a first order approximation of an infinitesimal vertical electric dipole, the geometrical spreading is corrected automatically during the inversion. The resulting dielectric permittivity and conductivity tomograms are plotted in Figure C-4. Comparing the results with the geologic interpretation (Figure C-3), we find low permittivity and conductivity values in the shear zone (high velocities and low attenuations). This area can therefore be interpreted as an air-filled fracture zone. The high permittivity and conductivity anomaly in the lower left corner of the model could indicate a water-saturated area. The variations for both, the dielectric permittivity and conductivity is small, with less than  $2\epsilon_0$  for the permittivity and 2 mS/m for the conductivity.

The deduced dielectric permittivity and conductivity tomograms are now implemented in our FDTD algorithm. The transmitting antenna is implemented at the position SRC 20 (Figure C-3), as a finite-length wire type antenna with resistive loading and an insulation ( $\epsilon_{\text{ins}} = 4\epsilon_0$  and  $\sigma_{\text{ins}} = 0$  mS/m). The antenna is excited by feeding a wavelet that is estimated using an averaged and to the first cycle tapered recorded trace in to the antenna-terminal. The receivers are approximated as infinitesimal vertical electric dipoles at the same positions as for the measured data. Both, transmitter and receivers are placed in air-filled boreholes. In Figure C-5a we compare simulated traces from the central part of the model with their

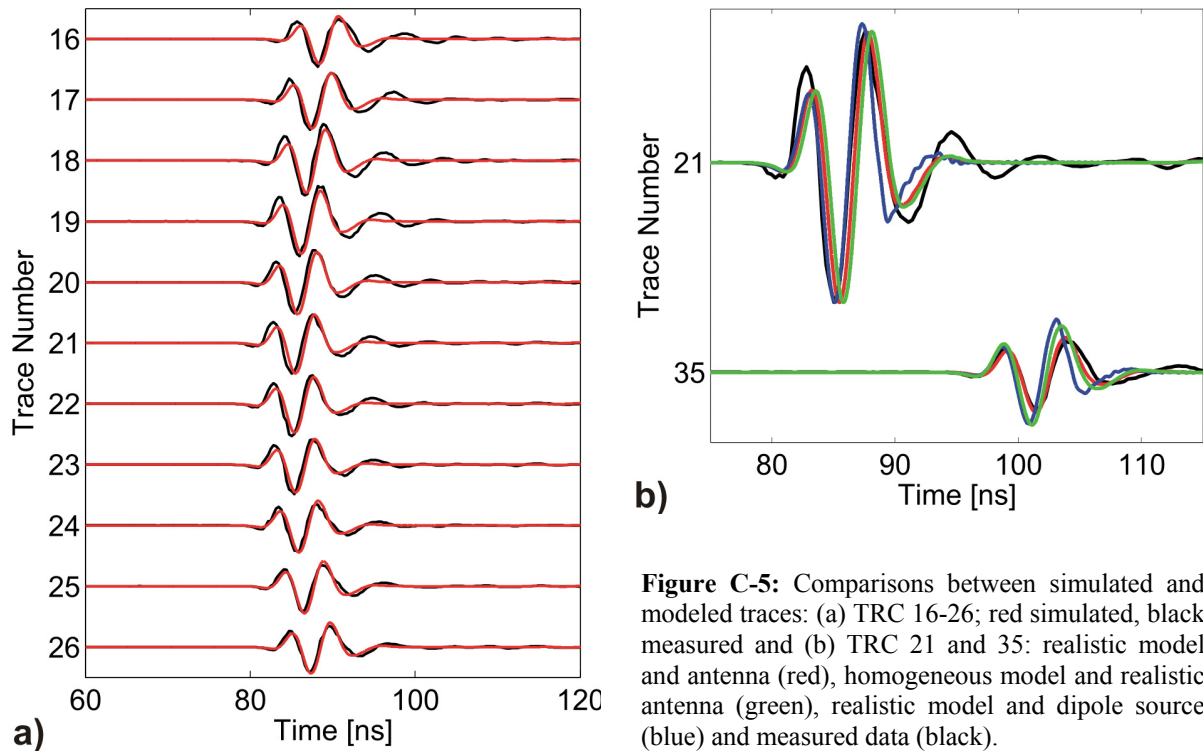


**Figure C-5:** Comparisons between simulated and modeled traces: (a) TRC 16-26; red simulated, black measured and (b) TRC 21 and 35: realistic model and antenna (red), homogeneous model and realistic antenna (green), realistic model and dipole source (blue) and measured data (black).

measured counterparts (TRC 16-26). Overall, a very good match for wavelet onsets, amplitudes and phases is found. Similar simulations were computed: (1) for a realistic, insulated antenna in an air-filled borehole, but only using an averaged homogeneous model ( $\epsilon_{\text{ins}} = 5.5\epsilon_0$  and  $\sigma_{\text{ins}} = 1.5 \text{ mS/m}$ ) and (2) for a infinitesimal vertical electric dipole using the previously calculated tomograms. Figure C-5b shows that the match between the numerical and the measured traces is still good, particularly in case of the averaged homogeneous model (green). Using the dipole approximation (blue), we find larger discrepancies as well as in the onset, the amplitude and also the phase.

### C.5. CONCLUSIONS

We developed a FDTD solution of Maxwell's equations in cylindrical coordinates that is suitable for modeling the detailed radiation characteristics of realistic borehole georadar antennas. Our approach allows us to accurately and efficiently model detailed aspects of transmitter antennas. In the low to intermediate frequency range, we find good agreement between the numerical solution of Wu-King antennas and the full-space radiation pattern of an infinitesimal electric dipole even if an air-filled borehole is present. Real data experiments in an almost homogeneous environment show a good match between numerical simulation with a realistic antenna and a realistic model. Even using a nearly homogeneous survey area



didn't inhibit in case of the infinitesimal dipole approximation severe discrepancies to the measured data at large radiation angles. Only small radiation angles and large offsets are problematic. Using a realistic antenna in an averaged homogeneous model produces better results but still leaves some smaller phase shifts and amplitude mismatches unresolved.



# **APPENDIX D**

## **FULL-WAVEFORM INVERSION OF CROSSHOLE GEORADAR DATA**

**Jacques R. Ernst**, Klaus Holliger and Hansruedi Maurer

75<sup>th</sup> Annual International Meeting: Society of Exploration Geophysicists, 2573-2576 (2005).

### **D.1. SUMMARY**

We present a full-waveform inversion scheme for crosshole georadar data based on a finite-difference time-domain (FDTD) solution of Maxwell's equations and test it on pertinent synthetic data. Existing tomographic inversion techniques for crosshole georadar data are based on geometric ray theory. Such techniques only consider limited aspects of the recorded data, only account for first-order wave propagation effects, and hence only resolve large-scale components of the subsurface. In contrast, FDTD-based waveform inversions of crosshole georadar account for all relevant wave propagation effects. The corresponding results demonstrate that our waveform inversion approach is capable of adequately resolving both the geometry and the parameter distribution of anomalies whose spatial extent is considerably smaller than a dominant wavelength.

## D.2. INTRODUCTION

Borehole georadar is an increasingly popular method for probing the shallow subsurface. A typical setup for a crosshole georadar experiment consists of an emitting dipole-type antenna located in a borehole and a corresponding receiver antenna located in a neighboring borehole. The nominal center frequencies of commonly used antennas range from  $\sim 20$  to  $\sim 200$  MHz, which correspond to dominant wavelengths of  $\sim 5$  to  $\sim 0.5$  m, in the subsurface. To date, tomographic inversions of crosshole georadar data have been based on ray methods. Ray-based inversions of first-arrival traveltimes and the maximum first-cycle amplitudes allow us to determine the electromagnetic velocity and attenuation structures of the probed regions. These parameters can then be used to resolve dielectric permittivity and electrical conductivity distributions, which may provide key constraints on engineering parameters, such as water content, salinity, porosity, clay fraction or ore grade.

Ray-based inversion methods consider only a very limited portion of the recorded georadar signal, namely the onset time of the first arriving wave trains and the peak amplitudes of the first cycles. As a consequence, these methods suffer from a number of inherent limitations. In particular, they can only resolve structures that are relatively large and smooth with respect to the dominant wavelength of the signal. Williamson and Worthington (1993) argue that, to a first approximation, the resolution of ray-based inversion methods scales with the diameter of the first Fresnel zone, whereas that of wave-equation-based methods is approximately half a dominant wavelength.

By considering the detailed waveforms of recorded georadar signals and correctly accounting for wave propagation effects in the inversion process, we can therefore expect to improve our resolution by nearly an order-of-magnitude. The expected sub-meter resolution is comparable to that of expensive and inherently 1D borehole-based studies, such as geophysical logging, core sampling and direct-push techniques. In the following, we shall first outline the methodological background of our waveform approach, test it on pertinent synthetic data and compare its performance with that of standard ray-based inversion techniques.

## D.3. METHODOLOGY

To our knowledge, no attempts to develop full-waveform inversion schemes for georadar data have been made so far. In contrast, waveform inversion strategies for seismic data have been around for almost two decades. Most seismic waveform inversion schemes are based on finite-difference solutions of the wave equation. These forward modeling schemes

are accurate, can accommodate strongly heterogeneous media and automatically include all wave types of the considered wave propagation regime, such as diffracted or multiply scattered waves. In the following, we briefly review what we consider to be the most promising and successful approaches for the seismic waveform inversion, discuss the pertinent differences between seismic and georadar data, and then describe our algorithm.

Tarantola (1984a) introduced the concept of full-waveform inversion to exploration seismology. Gauthier et al. (1986) and Mora (1987) clarified many of Tarantola's formalisms, presented complete waveform inversion algorithms for acoustic and elastic seismic reflection data. Their approaches were based on finite-difference time-domain (FDTD) solutions of the acoustic and elastic wave equations. Pratt (1999) clarified and extended earlier work on waveform inversion schemes based on a frequency-domain solution of the wave equation. Compared to the time-domain approaches pursued by many other workers, his scheme ideally allows the solution of the inverse problem to be limited to a number of signal frequencies, which may greatly enhance the efficiency of the inversion process. Two decades after Tarantola's (1984a) pioneering work, 2D waveform inversion of seismic reflection and crosshole data is clearly feasible. However, the method is still far from being applied routinely, primarily because elastic waveform inversion is computationally very expensive and acoustic full-waveform inversion does not account for "elastic-wave complications" in observed seismograms (e.g., shear, converted and surface waves). Furthermore, strong local variations in source and receiver coupling as well as three-dimensional effects may result in significant data inconsistencies.

Finite-difference solutions of Maxwell's equations require comparable computational efforts to corresponding solutions of the acoustic wave equation. However, in contrast to acoustic modeling of seismic data, finite-difference solutions of Maxwell's equations contain all wave phenomena present in georadar data. Moreover, unlike for seismic sources and receivers, the system responses of georadar antennas can be reliably simulated via appropriate finite-difference solutions of Maxwell's equations. The same is true for other complications, such as waveguide effects in water-filled boreholes or the presence of transmitters and/or receivers near the Earth's surface or other discontinuities.

The full-waveform inversion algorithm for crosshole georadar data presented in this study is based on a FDTD solution of Maxwell's equations in 2D Cartesian coordinates. This choice was largely based on our expertise in FDTD forward modeling (e.g., Lampe and Holliger, 2003; Ernst et al., 2006) as well as on the intriguing conceptual simplicity of these

techniques. Once one has decided on the underlying forward algorithm, all waveform inversion approaches proceed by evaluating the gradient of the target parameters through iterative minimizations of the misfit between observed and simulated data.

In the case of borehole georadar experiments, the observed data generally correspond to the vertical component of the electrical field  $E_z$  and the target parameters are the dielectric permittivity  $\varepsilon$  and the electrical conductivity  $\sigma$  (e.g., Holliger et al., 2001). In this pilot study, we shall limit ourselves to the inversion of the dielectric permittivity, which is generally expected to have a dominant influence on the observed waveforms. The corresponding gradient can then be regarded as a cross-correlation between the time derivatives of the forward-propagated vertical component of the electrical field and the back-propagated residuals between the observed and simulated vertical electric field (e.g., Gauthier et al., 1986):

$$\delta\varepsilon(\mathbf{x})|_n = \varepsilon^2 \sum_{Tr=1}^{N_{Tr}} \int_0^{T_{max}} \dot{E}_z(\mathbf{x}, t; \mathbf{x}_{Tr}) \dot{E}_z^{residual}(\mathbf{x}, t; \mathbf{x}_{Tr}) dt, \quad (\text{D.1})$$

where  $Tr$  denotes the transmitter number,  $N_{Tr}$  the total number of transmitters,  $T_{max}$  the record length,  $t$  the traveltime,  $\mathbf{x}$  a particular location in the tomographic plane,  $\mathbf{x}_{Tr}$  the transmitter location, and  $n$  the iteration number. The distribution of the dielectric permittivity in the imaged tomographic plane is then updated as:

$$\varepsilon(\mathbf{x})|_{n+1} = \varepsilon(\mathbf{x})|_n - \eta|_n \cdot \delta\varepsilon(\mathbf{x})|_n. \quad (\text{D.2})$$

The step-length  $\eta$  is evaluated as (Pica et al., 1990):

$$\eta|_n = s \cdot \frac{(E_z^{pert} - E_z^{syn})^T (E_z^{syn} - E_z^{obs})}{(E_z^{pert} - E_z^{syn})^T (E_z^{pert} - E_z^{syn})}, \quad (\text{D.3})$$

where  $T$  is the transpose operator,  $s$  denotes a ‘‘small number’’ and the superscripts *syn*, *obs* and *pert* refer to synthetic, observed and perturbed data, respectively. The perturbed data are obtained by adding  $s\delta\varepsilon(\mathbf{x})|_n$  to the dielectric permittivity model resulting from the  $n^{\text{th}}$ -iteration and performing another forward simulation. Based on the work of Pica et al. (1990), we chose  $s = 0.01$ .

#### D.4. RESULTS

To test the validity and accuracy of our full-waveform inversion approach, we have applied it to a variety of synthetic datasets. In the following, we report on the results of two such test cases, which we consider to be particularly challenging and illustrative with regard

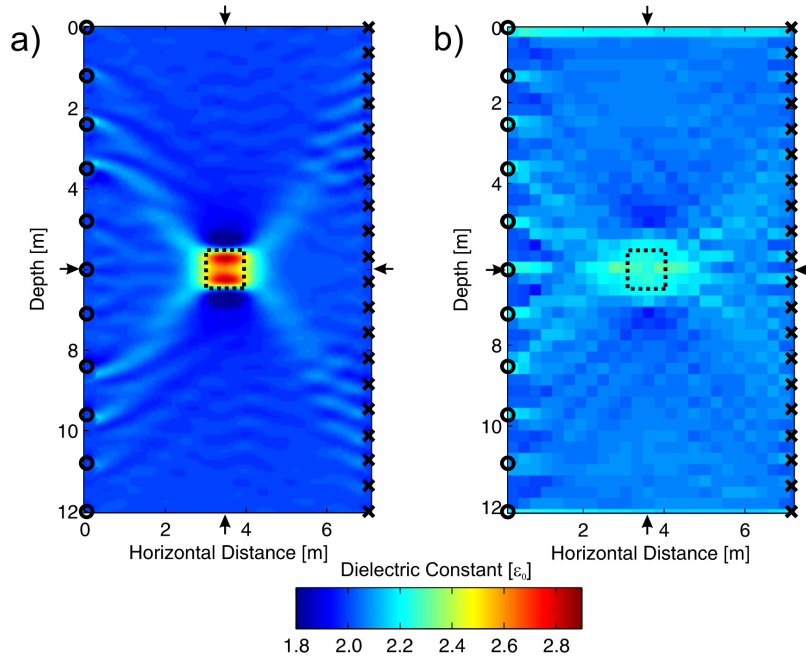


**Figure D-1:** Comparison of tomograms of a square-shaped low-velocity anomaly (dashed line) resulting from (a) full-waveform inversion and (b) ray-based inversion of first-arrival traveltimes. Arrows denote the locations of the cross-sections shown in Figure D-2.

to the potential of our algorithm. All models considered here are 7 m wide and 12 m deep and are characterized by a central low-velocity/high- $\varepsilon$  anomaly embedded in an otherwise homogeneous matrix. Transmitters and receivers are located along the left and right model edges with spacings of 1 m and  $\sim 0.6$  m, respectively. The models are uniformly non-magnetic and weakly conductive ( $\sigma = 0.5$  mS/m). The embedding matrix and the anomalies of the models are characterized by dielectric permittivities of  $2\varepsilon_0$  and  $3\varepsilon_0$ , respectively, with  $\varepsilon_0$  denoting the free-space permittivity.

The forward modeling and waveform inversion procedures are based on a FDTD solution of Maxwell's equations in 2D Cartesian coordinates that is second-order accurate in both time and space. The model space is surrounded by highly effective generalized perfectly matched layer (GPML) absorbing boundary conditions in order to avoid artifacts due to reflections from the edges of the computational domain (e.g., Lampe et al., 2003). The emitted wavelet corresponds to the first derivative of a Gaussian with a dominant frequency of  $\sim 160$  MHz and a bandwidth of 2-3 octaves. This yields a dominant wavelength of  $\sim 1.4$  m.

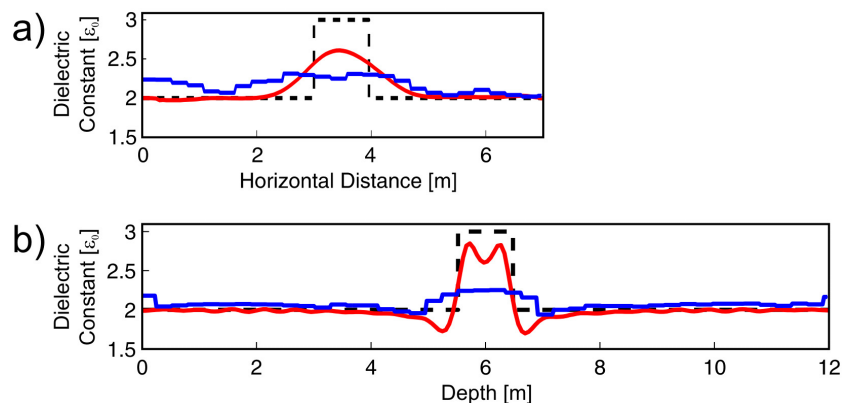


**Figure D-2:** (a) Horizontal and (b) vertical cross-section through the full-waveform (red lines) and ray-based (blue lines) tomograms shown in Figure D-1. The dashed line denotes the actual anomaly.

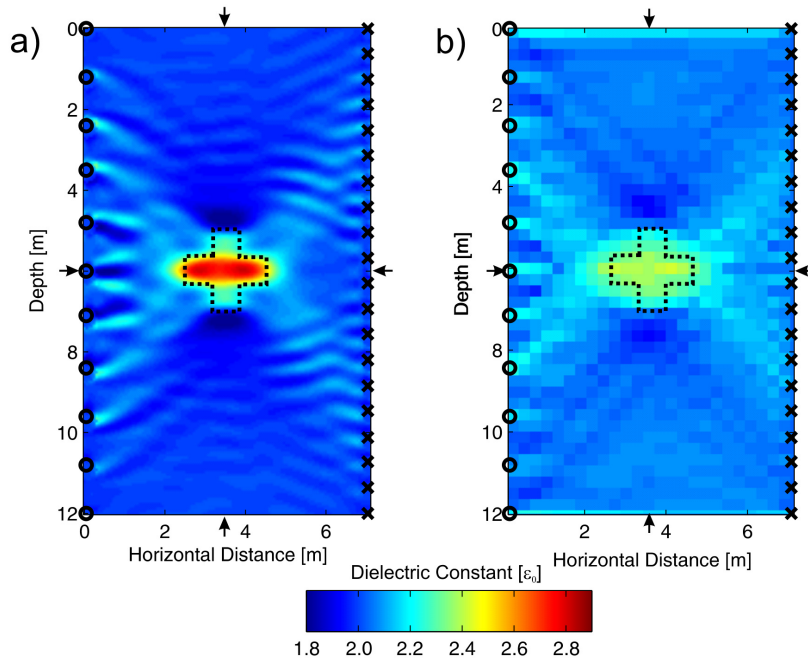


**Figure D-3:** Comparison of tomograms of a cross-shaped low-velocity anomaly (dashed line) resulting from (a) full-waveform inversion and (b) ray-based inversion of first-arrival traveltimes. Arrows denote the locations of the cross-sections shown in Figure D-4.

The results of our tests are summarized in Figures D-1 - D-5 by comparing the results of the waveform inversions to those of corresponding ray-based inversions of the first-arrival travel-times. For all inversions we used a homogeneous starting model with a constant dielectric permittivity of  $2\epsilon_0$ . The anomaly of our first test model corresponds to a square

1.0m-by-1.0m low velocity ( $\epsilon = 3\epsilon_0$ ) anomaly (Figures D-1 and D-2). To reduce numerical artifacts related to high values in the vicinity of the transmitter and receiver locations, which correspond to the most severely underdetermined regions (“null-space”), the inversion process is *a posteriori* regularized by applying a taper at these locations and by smoothing the inversion results with a five-point spatial weighted-average filter. Despite the fact that the dimensions of this square-shaped anomaly are much smaller than the dominant wavelength, the inversion of the waveforms provides a remarkably accurate reconstruction of both the shape and the dielectric permittivity of the anomaly. Conversely, the ray-based inversion approach barely manages to detect the presence of this anomaly and clearly fails at resolving its shape and dielectric permittivity.

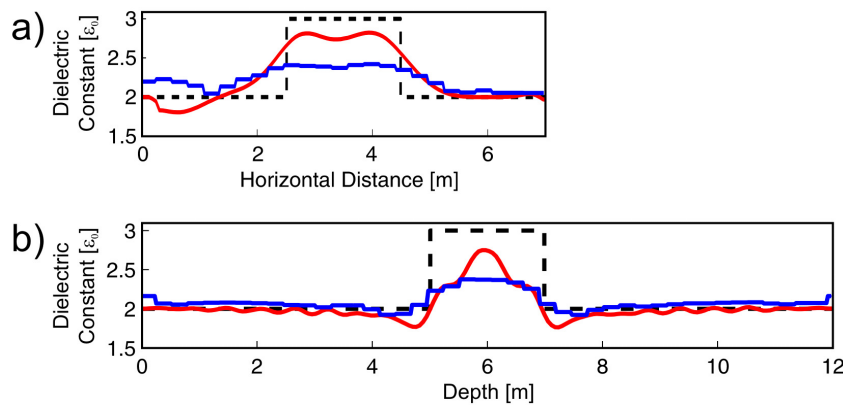


**Figure D-4:** (a) Horizontal and (b) vertical cross-section through the full-waveform (red lines) and ray-based (blue lines) tomograms shown in Figure D-3. The dashed line denotes the actual anomaly.



The anomaly of our second test corresponds to a low-velocity ( $\varepsilon = 3\varepsilon_0$ ) cross, composed of five 0.7 m-by-0.7 m square elements (Figures D-3 and D-4). Compared to the previously considered anomaly, this cross-shaped anomaly is characterized by a larger spatial extent and a more complex shape. The inversion of the waveform allows for an accurate reconstruction of the geometrical outline of the anomaly and provides a remarkably accurate estimate of the dielectric permittivity for the entire horizontal arm of the cross, but not for its upper and lower tips. The latter is most likely to be due to the sparse transmitter and receiver spacings as well as to the rather limited angular coverage characterizing the synthetic data. The ray-based inversion of the first-arrival traveltimes again fails to adequately resolve both the shape and the dielectric permittivity of the anomaly. Indeed, based on the ray-based inversions alone, it is impossible to distinguish between the two anomalies.

Finally, Figures D-5a and D-5b compare the “observed” and inverted radargrams of a receiver gather corresponding to a transmitter depth of 6 m for the second test case (Figures D-3 and D-4) before the first and after the 20<sup>th</sup> and final iteration. We see that before the start of the inversion procedure there are significant mismatches between the “observed” and simulated traces, both in terms of their amplitudes and phases, and that, despite phase mismatches of up to  $90^\circ$ , our waveform inversion approach achieves a near-perfect fit. It is also important to note that, at least for the experimental setup considered in this study, the computational effort was quite moderate, as each iteration only took  $\sim 30$  minutes on a standard desktop computer with two 2.4 GHz processors.

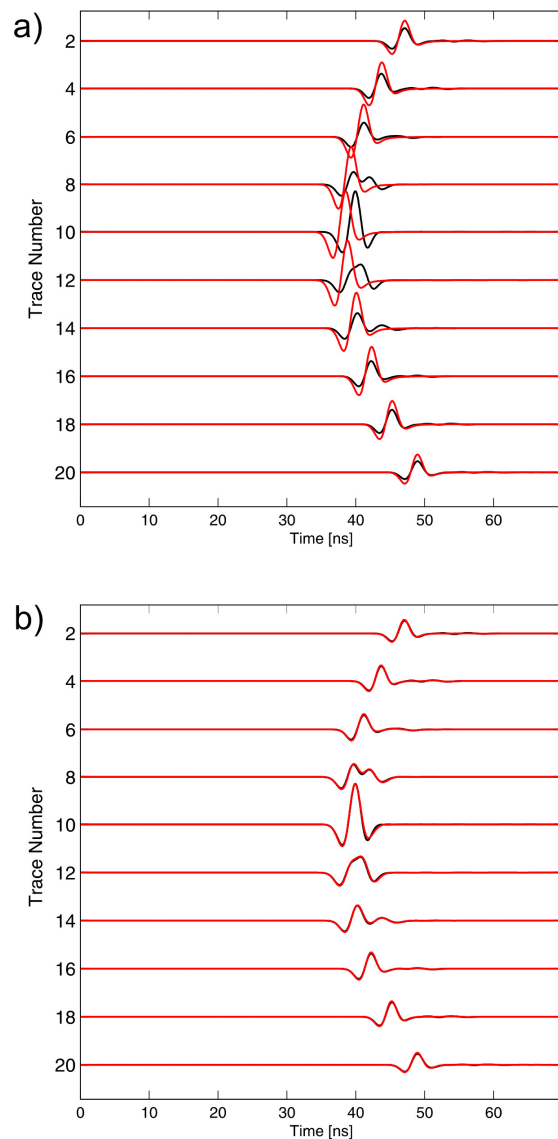


**Figure D-5:** “Observed” (black) and simulated (red) traces for the model containing the cross-shaped low-velocity anomaly (Figures D-3 and D-4) (a) before the first and (b) after the 20<sup>th</sup> and final iteration of the waveform inversion procedure.

## D.5. CONCLUSIONS

We have presented a full-waveform inversion approach for crosshole georadar data based on a FDTD solution of Maxwell's equations in 2D Cartesian coordinates. Tests on synthetic data for challenging low-velocity-anomaly models demonstrate that this approach is clearly superior to standard ray-based approaches. We find that our waveform inversion approach is capable of resolving both the shape and dielectric permittivity of low-velocity anomalies whose spatial extent is considerably smaller than a dominant wavelength. In this pilot study, we have limited ourselves to synthetic data and to inverting only for the dielectric permittivity. In future, we plan to extend our algorithm to jointly invert for the dielectric permittivity and electrical conductivity and apply it to a variety of observed data. The latter will require the data to be adequately corrected for the 3D radiation and spreading characteristics. The generally underdetermined nature of these problems as well as the inherently noisy nature of real data may also mandate a more sophisticated regularization of the inversion process.

# BIBLIOGRAPHY

- Appleton, E. V., and M. A. F. Barnett, 1925a, Local reflection of wireless waves from the upper atmosphere: *Nature*, **115**, 333-334.
- Appleton, E. V., and M. A. F. Barnett, 1925b, On some direct evidence for downward atmospheric reflection of electric rays: *Proceedings of the Royal Society of London Series a-Containing Papers of a Mathematical and Physical Character*, **109**, 621-641.
- Arcone, S. A., 1991, Dielectric constant and layer-thickness interpretation of helicopter-borne short-pulse radar waveforms reflected from wet and dry river-ice sheets: *Geoscience and Remote Sensing, IEEE Transactions on*, **29**, 768-777.
- Balanis, C., 1982, *Antenna theory: Analysis and design*: Wiley.
- Bano, M., 1996, Constant dielectric losses of ground-penetrating radar waves: *Geophysical Journal International*, **124**, 279-288.
- Barrash, W., and T. Clemo, 2002, Hierarchical geostatistics and multifacies systems: Boise Hydrogeophysical Research Site, Boise, Idaho: *Water Resources Research*, **38**, 1196, doi:1110.1029/2002WR001436.
- Barrash, W., and E. C. Reboulet, 2004, Significance of porosity for stratigraphy and textural composition in subsurface, coarse fluvial deposits: Boise Hydrogeophysical Research Site: *Geological Society of America Bulletin*, **116**, 1059-1073.
- Bauer, A. O., 2004, Hülsmeyer and the early days of radar inventions, sense and nonsense, a survey ([http://www.xs4all.nl/~aobauer/radar\\_i.htm](http://www.xs4all.nl/~aobauer/radar_i.htm)).
- Belina, F. A., 2006, Vollwellenfeldtomographie seismischer Durchschallungsmessungen basierend auf elektromagnetisch-akustischen Analogien, Master Arbeit am Institut für Geophysik, ETH Zürich.
- Bellefleur, G., and M. Chouteau, 2001, Massive sulphide delineation using borehole radar: tests at the McConnell nickel deposit, Sudbury, Ontario: *Journal of Applied Geophysics*, **47**, 45-61.
- Bently, J. O., 1928, Airplane altitude indicating system: US Patents 2011392.
- Berenger, J. P., 1994, A perfectly matched layer for the absorption of electromagnetic-waves: *Journal of Computational Physics*, **114**, 185-200.
- Bergmann, T., J. O. Blanch, J. O. A. Robertsson, and K. Holliger, 1999, A simplified Lax-Wendroff correction for staggered-grid FDTD modeling of electromagnetic wave propagation in frequency-dependent media: *Geophysics*, **64**, 1369-1377.
- Bergmann, T., J. O. A. Robertsson, and K. Holliger, 1996, Numerical properties of staggered finite-difference solutions of Maxwell's equations for ground-penetrating radar modeling: *Geophysical Research Letters*, **23**, 45-48.

- Bergmann, T., J. O. A. Robertsson, and K. Holliger, 1998, Finite-difference modeling of electromagnetic wave propagation in dispersive and attenuating media: *Geophysics*, **63**, 856-867.
- Beydoun, W. B., J. Delvaux, M. Mendes, G. Noual, and A. Tarantola, 1989, Practical aspects of an elastic migration - inversion of crosshole data for reservoir characterization - a Paris basin example: *Geophysics*, **54**, 1587-1595.
- Bleistein, N., 1986, 2-1/2 dimensional inplane wave-propagation: *Geophysical Prospecting*, **34**, 686-703.
- Brown, L., 1999, *A radar history of World War II: Technical and military imperatives*: Taylor & Francis.
- Brown, R. A., Bumgarne, W. C., D. Sirmans, and K. C. Crawford, 1971, Preliminary doppler velocity measurements in a developing radar hook echo: *Bulletin of the American Meteorological Society*, **52**, 1186-&.
- Brune, D. E., and J. Doolittle, 1990, Locating lagoon seepage with radar and electromagnetic survey: *Environmental Geology*, **16**, 195-207.
- Bruschini, C., B. Gros, F. Guerne, P.-Y. Piece, and O. Carmona, 1998, Ground penetrating radar and imaging metal detector for antipersonnel mine detection: *Journal of Applied Geophysics*, **40**, 59-71.
- Cai, W. Y., F. H. Qin, and G. T. Schuster, 1996, Electromagnetic velocity inversion using 2-D Maxwell's equations: *Geophysics*, **61**, 1007-1021.
- Carcione, J. M., 1996, Ground radar simulation for archaeological applications: *Geophysical Prospecting*, **44**, 871-888.
- Carcione, J. M., and F. Cavallini, 1995, On the acoustic electromagnetic analogy: *Wave Motion*, **21**, 149-162.
- Carlsten, S., S. Johansson, and A. Worman, 1995, Radar techniques for indicating internal erosion in embankment dams: *Journal of Applied Geophysics*, **33**, 143-156.
- Cassiani, G., C. Strobbia, and L. Gallotti, 2004, Vertical radar profiles for the characterization of deep vadose zones: *Vadose Zone J*, **3**, 1093-1105.
- Cervený, V., and J. E. P. Soares, 1992, Fresnel volume ray tracing: *Geophysics*, **57**, 902-915.
- Chen, Y.-L., and J. Chow, 2007, Ground penetrating radar signal processing improves mapping accuracy of underground voids and seawater table: an application in deteriorating coastal structure, Nanfangao Port, Taiwan: *Environmental Geology*.
- Chevalier, M. W., R. J. Luebbers, and V. P. Cable, 1997, FDTD local grid with material traverse: *Ieee Transactions on Antennas and Propagation*, **45**, 411-421.
- Chew, W. C., and Y. M. Wang, 1990, Reconstruction of 2-dimensional permittivity distribution using the distorted Born iterative method: *IEEE Transactions on Medical Imaging*, **9**, 218-225.

- Clement, W. P., and W. Barrash, 2006, Crosshole radar tomography in a fluvial aquifer near Boise, Idaho: *Journal of Environmental and Engineering Geophysics*, **11**, 171-184.
- Clement, W. P., M. D. Knoll, L. M. Liberty, P. R. Donaldson, P. Michaels, W. Barrash, and J. R. Pelton, 1999, Geophysical surveys across the Boise Hydrogeophysical Research Site to determine geophysical parameters of a shallow, alluvial aquifer, *Proceedings of Symposium on the Application of Geophysics to Engineering and Environmental Problems (SAGEEP99)*, 399-408.
- Coffey, T., J. Dahlburg, and E. Zimet, 2005, *The S&T innovation conundrum*: N. D. U. Center for Technology and National Security Policy, 17.
- Conyers, L. B., 2004, *Ground-penetrating radar for archaeology*: Altamira Press.
- Cui, T. J., and W. C. Chew, 2000, Novel diffraction tomographic algorithm for imaging two-dimensional targets buried under a lossy earth: *IEEE Transactions on Geoscience and Remote Sensing*, **38**, 2033-2041.
- Cui, T. J., and W. C. Chew, 2002, Diffraction tomographic algorithm for the detection of three-dimensional objects buried in a lossy half-space: *IEEE Transactions on Antennas and Propagation*, **50**, 42-49.
- Cui, T. J., W. C. Chew, A. A. Aydinler, and S. Y. Chen, 2001, Inverse scattering of two-dimensional dielectric objects buried in a lossy earth using the distorted Born iterative method: *IEEE Transactions on Geoscience and Remote Sensing*, **39**, 339-346.
- Cui, T. J., Y. Qin, G. Y. Wang, and W. C. Chew, 2004, Low-frequency detection of two-dimensional buried objects using high-order extended Born approximations: *Inverse Problems*, **20**, S41-S62.
- Davenport, G. C., J. W. Lindemann, T. J. Griffin, and J. E. Borowski, 1988, Crime scene investigation techniques: *The Leading Edge*, **7**, 64-66.
- Davis, J. L., and A. P. Annan, 1989, Ground-penetrating radar for high-resolution mapping of soil and rock stratigraphy: *Geophysical Prospecting*, **37**, 531-551.
- de Hoop, A. T., 1995, *Handbook of radiation and scattering of waves: acoustic waves in fluids, elastic waves in solids, electromagnetic waves*: Academic Press.
- Dessa, J. X., and G. Pascal, 2003, Combined travelttime and frequency-domain seismic waveform inversion: a case study on multi-offset ultrasonic data: *Geophysical Journal International*, **154**, 117-133.
- Devaney, A. J., 1984, Geophysical diffraction tomography: *IEEE Transactions on Geoscience and Remote Sensing*, **22**, 3-13.
- Dickens, T. A., 1994, Diffraction tomography for crosswell imaging of nearly layered media: *Geophysics*, **59**, 694-706.
- Engquist, B., and A. Majda, 1977, Absorbing boundary-conditions for numerical-simulation of waves: *Mathematics of Computation*, **31**, 629-651.

- Ernst, J. R., K. Holliger, H. Maurer, and A. G. Green, 2005, Full-waveform inversion of crosshole georadar data: SEG International Exposition and Seventy-Fifth Annual Meeting, The Society, 2573-2577.
- Ernst, J. R., K. Holliger, H. Maurer, and A. G. Green, 2006, Realistic FDTD modelling of borehole georadar antenna radiation: Methodology and application: *Near Surface Geophysics*, **4**, 19-30.
- Ernst, J. R., H. Maurer, A. G. Green, and K. Holliger, 2007, Full-waveform inversion of crosshole radar data based on 2-D finite-difference time-domain (FDTD) solutions of Maxwell's equations: *IEEE Transactions on Geoscience and Remote Sensing*, **45**, 2807-2828.
- Falk, J., E. Tessmer, and D. Gajewski, 1996, Tube wave modeling by the finite-difference method with varying grid spacing: *Pure and Applied Geophysics*, **V148**, 77-93.
- Fang, J. Y., and Z. H. Wu, 1996, Generalized perfectly matched layer for the absorption of propagating and evanescent waves in lossless and lossy media: *IEEE Transactions on Microwave Theory and Techniques*, **44**, 2216-2222.
- Fokkema, J. T., 2003, Analysis of georadar reflection responses, 1-4.
- Fujita, T. T., 1981, Tornadoes and downbursts in the context of generalized planetary scales: *Journal of the Atmospheric Sciences*, **38**, 1511-1534.
- Fullagar, P. K., D. W. Livelybrooks, P. Zhang, A. J. Calvert, and Y. R. Wu, 2000, Radio tomography and borehole radar delineation of the McConnell nickel sulfide deposit, Sudbury, Ontario, Canada: *Geophysics*, **65**, 1920-1930.
- Gauthier, O., J. Virieux, and A. Tarantola, 1986, Two-dimensional nonlinear inversion of seismic wave-forms - numerical results: *Geophysics*, **51**, 1387-1403.
- Gedney, S. D., 1996, An anisotropic perfectly matched layer-absorbing medium for the truncation of FDTD lattices: *Antennas and Propagation, IEEE Transactions on*, **44**, 1630-1639.
- Gernsbacher, H., 1911, Ralph 124c 41 +  
(e.g., <http://www.technovelgy.com/ct/content.asp?Bnum=651>).
- Goff, J. A., and J. W. Jennings, 1999, Improvement of Fourier-based unconditional and conditional simulations for band limited fractal (von Karman) statistical models: *Mathematical Geology*, **31**, 627-649.
- Gogineni, S., D. Tammana, D. Braaten, C. Leuschen, T. Akins, J. Legarsky, P. Kanagaratnam, J. Stiles, C. Allen, and K. Jezek, 2001, Coherent radar ice thickness measurements over the Greenland ice sheet: *Journal of Geophysical Research*, **106**, 33761-33772.
- Goodman, D., 1994, Ground-penetrating radar simulation in engineering and archaeology: *Geophysics*, **59**, 224-232.

- 
- Grandjean, G., J. C. Gourry, and A. Bitri, 2000, Evaluation of GPR techniques for civil-engineering applications: study on a test site: *Journal of Applied Geophysics*, **45**, 141-156.
- Grasmueck, M., and D. A. Viggiano, 2007, Integration of ground-penetrating radar and laser position sensors for real-time 3-D data fusion: *IEEE Transactions on Geoscience and Remote Sensing*, **45**, 130-137.
- Greaves, R. J., D. P. Lesmes, J. M. Lee, and M. N. Toksoz, 1996, Velocity variations and water content estimated from multi-offset, ground-penetrating radar: *Geophysics*, **61**, 683-695.
- Gross, R., A. G. Green, H. Horstmeyer, and J. H. Begg, 2004, Location and geometry of the Wellington Fault (New Zealand) defined by detailed three-dimensional georadar data: *Journal of Geophysical Research-Solid Earth*, **109**.
- Gross, R., A. G. Green, H. Horstmeyer, K. Holliger, and J. Baldwin, 2003, 3-D georadar images of an active fault: Efficient data acquisition, processing and interpretation strategies: *Subsurface Sensing Technologies and Applications*, **4**, 19-40.
- Guy, E. D., J. J. Daniels, J. Holt, S. J. Radzevicius, and M. Vendl, 2000, Electromagnetic induction and GPR measurements for creosote contaminant investigation: *Journal of Environmental and Engineering Geophysics*, **5**, 11-19.
- Hafner, C., 1999, *Post-modern electromagnetics: using intelligent Maxwell solvers*: Wiley.
- Hammon, W. S., G. A. McMechan, and X. Zeng, 2000, Forensic GPR: finite-difference simulations of responses from buried human remains: *Journal of Applied Geophysics*, **45**, 171-186.
- Hansen, T. B., and P. M. Johansen, 2000, Inversion scheme for ground penetrating radar that takes into account the planar air-soil interface: *Geoscience and Remote Sensing, IEEE Transactions on*, **38**, 496-506.
- Harris, J. M., and G. Y. Wang, 1996, Diffraction tomography for inhomogeneities in layered background medium: *Geophysics*, **61**, 570-583.
- Heincke, B., A. G. Green, J. van der Kruk, and H. Horstmeyer, 2005, Acquisition and processing strategies for 3D georadar surveying a region characterized by rugged topography: *Geophysics*, **70**, K53-K61.
- Heincke, B., J. van der Kruk, A. G. Green, and H. Horstmeyer, 2004, Processing strategy for 3-D georadar data acquired in areas characterized by rugged topography, 283-286.
- Hesthaven, J. S., and T. Warburton, 2002, Nodal high-order methods on unstructured grids: *Journal of Computational Physics*, **181**, 186-221.
- Hewett, T. A., 1986, Fractal distribution of reservoir heterogeneity and their influence on fluid transport: SPE 15386, 61st Annual Technical Conference of SPE, New Orleans, Louisiana, 1-16.

- Hicks, G. J., and R. G. Pratt, 2001, Reflection waveform inversion using local descent methods: Estimating attenuation and velocity over a gas-sand deposit: *Geophysics*, **66**, 598-612.
- Holliger, K., and T. Bergmann, 1998, Accurate and efficient FDTD modeling of ground-penetrating radar antenna radiation: *Geophysical Research Letters*, **25**, 3883-3886.
- Holliger, K., and T. Bergmann, 2002, Numerical modeling of borehole georadar data: *Geophysics*, **67**, 1249-1257.
- Holliger, K., and H. Maurer, 2004, Effects of stochastic heterogeneity on ray-based tomographic inversion of crosshole georadar amplitude data: *Journal of Applied Geophysics*, **56**, 177-193.
- Holliger, K., M. Musil, and H. R. Maurer, 2001, Ray-based amplitude tomography for crosshole georadar data: a numerical assessment: *Journal of Applied Geophysics*, **47**, 285-298.
- Hollmann, M., 2001, Christian Hülsmeier, the inventor:  
[www.radarworld.org/huelsmeyer.html](http://www.radarworld.org/huelsmeyer.html).
- Hugenschmidt, J., M. N. Partl, and H. de Witte, 1998, GPR inspection of a mountain motorway in Switzerland: *Journal of Applied Geophysics*, **40**, 95-104.
- Hülsenbeck & Co, 1926, Verfahren zur elektrischen Bodenerforschung: German Patents 489434.
- Hülsmeier, C., 1904, Hertzian-wave projecting and receiving apparatus adapted to indicate or give warning of the presence of a metallic body, such as a ship or a train, in the line of projection of such waves. : GB Patents 190413170A.
- Irving, J. D., and R. J. Knight, 2005, Effect of antennas on velocity estimates obtained from crosshole GPR data: *Geophysics*, **70**, K39-K42.
- Irving, J. D., M. D. Knoll, and R. J. Knight, 2007, Improving crosshole radar velocity tomograms: A new approach to incorporating high-angle travelttime data: *Geophysics*, **72**, J31-J41.
- Jackson, J. D., 1975, *Classical electrodynamics*: Wiley.
- Jia, H. T., T. Takenaka, and T. Tanaka, 2002, Time-domain inverse scattering method for cross-borehole radar imaging: *IEEE Transactions on Geoscience and Remote Sensing*, **40**, 1640-1647.
- Johnson, T. C., P. S. Routh, and M. D. Knoll, 2005, Fresnel volume georadar attenuation-difference tomography: *Geophysical Journal International*, **162**, 9-24.
- Jung-Ho, K., Y. Myeong-Jong, S. Jeong-Sul, C. Seong-Jun, and P. Sam-Gyu, 2005, Effective 3D GPR survey and its application to the exploration of old remains, 4 pp.
- Kennett, B. L. N., M. S. Sambridge, and P. R. Williamson, 1988, Subspace methods for large inverse problems with multiple parameter classes: *Geophysical Journal International*, **94**, 237-247.



- 
- Khalil, A. I., and M. B. Steer, 1999, A generalized scattering matrix method using the method of moments for electromagnetic analysis of multilayered structures in waveguide: *IEEE Transactions on Microwave Theory and Techniques*, **47**, 2151-2157.
- Knödel, K., H. Krummel, G. Lange, and A. Berktold, 1997, *Geophysik*: Springer.
- Kuroda, S., M. Takeuchi, and H. J. Kim, 2005, Full waveform inversion algorithm for interpreting cross-borehole GPR data: *SEG International Exposition and Seventy-Fifth Annual Meeting*, The Society, 1176-1180.
- Lampe, B., and K. Holliger, 2003, Effects of fractal fluctuations in topographic relief, permittivity and conductivity on ground-penetrating radar antenna radiation: *Geophysics*, **68**, 1934-1944.
- Lampe, B., and K. Holliger, 2005, Resistively loaded antennas for ground-penetrating radar: A modeling approach: *Geophysics*, **70**, K23-K32.
- Lampe, B., K. Holliger, and A. G. Green, 2003, A finite-difference time-domain simulation tool for ground-penetrating radar antennas: *Geophysics*, **68**, 971-987.
- Lanz, E., H. Maurer, and A. G. Green, 1998, Refraction tomography over a buried waste disposal site: *Geophysics*, **63**, 1414-1433.
- Leckebusch, J., 2005, Use of antenna arrays for GPR surveying in archaeology: *Near Surface Geophysics*, **3**, 111-115.
- Lehmann, F., and A. G. Green, 1999, Semiautomated georadar data acquisition in three dimensions: *Geophysics*, **64**, 719-731.
- Leimbach, G., and H. Löwy, 1911, A method of indicating the presence and determining the position of veins of metallic ore or subterranean water levels: *GB Patents* 191111737A.
- Luo, Y., and G. T. Schuster, 1991, Wave-equation travelttime inversion: *Geophysics*, **56**, 645-653.
- Majer, E. L., L. R. Myer, J. E. Peterson, K. Karasaki, J. C. S. Long, S. J. Martel, P. Blümling, and S. Vomvoris, 1990, Joint seismic, hydrogeological, and geomechanical investigations of a fractured zone in the Grimsel Rock Laboratory, Switzerland.: *NAGRA - DOE Cooperative Project Report*.
- Maloney, J. G., and G. S. Smith, 1992, The efficient modeling of thin material sheets in the finite-difference time-domain (FDTD) method: *Antennas and Propagation, IEEE Transactions on*, **40**, 323-330.
- Maurer, H., and A. G. Green, 1997, Potential coordinate mislocations in crosshole tomography: Results from the Grimsel test site, Switzerland: *Geophysics*, **62**, 1696-1709.
- Maurer, H. R., 1996, Systematic errors in seismic crosshole data: Application of the coupled inverse technique: *Geophysical Research Letters*, **23**, 2681-2684.

- Moghaddam, M., and W. C. Chew, 1992, Nonlinear 2-dimensional velocity profile inversion using time domain data: *IEEE Transactions on Geoscience and Remote Sensing*, **30**, 147-156.
- Moghaddam, M., and W. C. Chew, 1993, Study of some practical issues in inversion with the Born iterative method using time-domain data: *IEEE Transactions on Antennas and Propagation*, **41**, 177-184.
- Moghaddam, M., W. C. Chew, and M. Oristaglio, 1991, Comparison of the Born iterative method and Tarantola's method for an electromagnetic time-domain inverse problem: *International Journal of Imaging Systems and Technology*, **3**, 318-333.
- Monk, P., 2003, *Finite element methods for Maxwell's equations*: Clarendon Press.
- Mora, P., 1987, Nonlinear two-dimensional elastic inversion of multioffset seismic data: *Geophysics*, **52**, 1211-1228.
- Mora, P., 1988, Elastic wave-field inversion of reflection and transmission data: *Geophysics*, **53**, 750-759.
- Morey, R. M., 1972, *Geophysical surveying system employing electromagnetic impulses*: US Patents 3806795.
- Mur, G., 1981, Absorbing boundary-conditions for the finite-difference approximation of the time-domain electromagnetic-field equations: *IEEE Transactions on Electromagnetic Compatibility*, **23**, 377-382.
- Musil, M., H. Maurer, K. Hollinger, and A. G. Green, 2006, Internal structure of an alpine rock glacier based on crosshole georadar traveltimes and amplitudes: *Geophysical Prospecting*, **54**, 273-285.
- Nolet, G., 1987, *Seismic wave propagation and seismic tomography: Seismic tomography with application in global seismology and exploration geophysics* (ed. Nolet, G.): D. Reidel Publishing Company.
- Olhoeft, G. R., 2002, Applications and frustrations in using ground penetrating radar: *IEEE Aerospace and Electronic Systems Magazine*, **17**, 12-20.
- Olsson, O., L. Falk, O. Forslund, L. Lundmark, and E. Sandberg, 1992, Borehole radar applied to the characterization of hydraulically conductive fracture-zones in crystalline rock: *Geophysical Prospecting*, **40**, 109-142.
- Paasche, H., J. Tronicke, K. Holliger, A. G. Green, and H. Maurer, 2006, Integration of diverse physical-property models: Subsurface zonation and petrophysical parameter estimation based on fuzzy c-means cluster analyses: *Geophysics*, **71**, H33-H44.
- Paige, C. C., and M. A. Saunders, 1982, LSQR: an algorithm for sparse linear equations and sparse least squares: *ACM Transactions on Mathematical Software*, **8**, 43-71.
- Peters, L. P., Jr., J. J. Daniels, and J. D. Young, 1994, Ground penetrating radar as a subsurface environmental sensing tool: *Proceedings of the IEEE*, **82**, 1802-1822.

- 
- Peterson, J. E., 2001, Pre-inversion corrections and analysis of radar tomographic data: *Journal of Environmental and Engineering Geophysics*, **6**, 1-18.
- Pica, A., J. P. Diet, and A. Tarantola, 1990, Nonlinear inversion of seismic-reflection data in a laterally invariant medium: *Geophysics*, **55**, 284-292.
- Polak, E., and G. Ribière, 1969, Note on convergence of conjugate direction methods: *Revue Française d'Informatique de Recherche Opérationnelle*, **3**, 35-43.
- Popovic, M., and A. Taflove, 2004, Two-dimensional FDTD inverse-scattering scheme for determination of near-surface material properties at microwave frequencies: *Antennas and Propagation, IEEE Transactions on*, **52**, 2366-2373.
- Porcello, L. J., R. L. Jordan, J. S. Zelenka, G. F. Adams, R. J. Phillips, W. E. Brown, S. H. Ward, and P. L. Jackson, 1974, Apollo lunar sounder radar system: *Proceedings of the IEEE*, **62**, 769-783.
- Porsani, J. L., W. M. Filho, V. R. Elis, F. Shimeles, J. C. Dourado, and H. P. Moura, 2004, The use of GPR and VES in delineating a contamination plume in a landfill site: a case study in SE Brazil: *Journal of Applied Geophysics*, **55**, 199-209.
- Pratt, R. G., 1990a, Frequency-domain elastic wave modeling by finite-differences - a tool for crosshole seismic imaging: *Geophysics*, **55**, 626-632.
- Pratt, R. G., 1990b, Inverse-theory applied to multisource cross-hole tomography. Part 2: Elastic wave-equation method: *Geophysical Prospecting*, **38**, 311-329.
- Pratt, R. G., 1999, Seismic waveform inversion in the frequency domain, Part 1: Theory and verification in a physical scale model: *Geophysics*, **64**, 888-901.
- Pratt, R. G., and N. R. Goult, 1991, Combining wave-equation imaging with travelttime tomography to form high-resolution images from crosshole data: *Geophysics*, **56**, 208-224.
- Pratt, R. G., Q. Li, B. C. Dyer, N. R. Goult, and M. H. Worthington, 1991, Algorithms for eor imaging using crosshole seismic data - an experiment with scale-model data: *Geoexploration*, **28**, 193-220.
- Pratt, R. G., C. Shin, and G. J. Hicks, 1998, Gauss-Newton and full Newton methods in frequency-space seismic waveform inversion: *Geophysical Journal International*, **133**, 341-362.
- Pratt, R. G., and R. M. Shipp, 1999, Seismic waveform inversion in the frequency domain, Part 2: Fault delineation in sediments using crosshole data: *Geophysics*, **64**, 902-914.
- Pratt, R. G., and M. H. Worthington, 1988, The application of diffraction tomography to cross-hole seismic data: *Geophysics*, **53**, 1284-1294.
- Pratt, R. G., and M. H. Worthington, 1990, Inverse-theory applied to multisource cross-hole tomography. Part 1: Acoustic wave-equation method: *Geophysical Prospecting*, **38**, 287-310.

- Reiter, D. T., and W. Rodi, 1996, Nonlinear waveform tomography applied to crosshole seismic data: *Geophysics*, **61**, 902-913.
- Robertsson, J. O. A., and K. Holliger, 1997, Modeling of seismic wave propagation near the earth's surface: *Physics of the Earth and Planetary Interiors*, **104**, 193-211.
- Ruffell, A., and J. McKinley, 2005, Forensic geoscience: applications of geology, geomorphology and geophysics to criminal investigations: *Earth-Science Reviews*, **69**, 235-247.
- Saarenketo, T., and T. Scullion, 2000, Road evaluation with ground penetrating radar: *Journal of Applied Geophysics*, **43**, 119-138.
- Sambridge, M. S., A. Tarantola, and B. L. N. Kennett, 1991, An alternative strategy for non-linear inversion of seismic waveforms: *Geophysical Prospecting*, **39**, 723-736.
- Sena, A. G., and M. N. Toksoz, 1990, Simultaneous reconstruction of permittivity and conductivity for crosshole geometries: *Geophysics*, **55**, 1302-1311.
- Sinclair, C., S. A. Greenhalgh, and B. Zhou, 2007, 2.5-D modelling of elastic waves in anisotropic media using the spectral element method: *Exploration Geophysics (Australia)*, in press.
- Song, Z. M., and P. R. Williamson, 1995, Frequency-domain acoustic-wave modeling and inversion of crosshole data. Part 1. 2.5-D modeling method: *Geophysics*, **60**, 784-795.
- Song, Z. M., P. R. Williamson, and R. G. Pratt, 1995, Frequency-domain acoustic-wave modeling and inversion of crosshole data. Part 2. Inversion method, synthetic experiments and real-data results: *Geophysics*, **60**, 796-809.
- Spetzler, J., and R. Snieder, 2004, The Fresnel volume and transmitted waves: *Geophysics*, **69**, 653-663.
- Spillmann, T., H. Maurer, H. Willenberg, K. F. Evans, B. Heincke, and A. G. Green, 2007, Characterization of an unstable rock mass based on borehole logs and diverse borehole radar data: *Journal of Applied Geophysics*, **61**, 16-38.
- Spitz, S., 1991, Seismic trace interpolation in the F-X domain: *Geophysics*, **56**, 785-794.
- Stern, W., 1929, Versuch einer elektrodynamischen Dickemessung von Gletschereis: *Gerlands Beiträge zur Geophysik*, **23**, 292-333.
- Stern, W., 1930, Über Grundlagen, Methodik und bisherige Ergebnisse elektrodynamischer Dickenmessung von Gletschereis: *Zeitschrift für Gletscherkunde*, **18**, 24-30.
- Sternberg, B. K., and J. W. McGill, 1995, Archaeology studies in southern Arizona using ground penetrating radar: *Journal of Applied Geophysics*, **33**, 209-225.
- Streich, R., and J. Van der Kruk, 2006, Characterizing a GPR-antenna system by near-field electric field measurements: *SEG International Exposition and Seventy-Six Annual Meeting, The Society*, 1426-1430.

- 
- Streich, R., J. Van der Kruk, and A. G. Green, 2007, Efficient vector-migration of standard co-polarized 3-D GPR data: submitted to Geophysics.
- Strickel, M., A. Taflove, and K. Umashankar, 1994, Finite-difference time-domain formulation of an inverse scattering scheme for remote-sensing of conducting and dielectric targets: Part 2: 2-dimensional case: *Journal of Electromagnetic Waves and Applications*, **8**, 509-529.
- Stutzman, W. L., and G. A. Thiele, 1998, *Antenna theory and design*: Wiley.
- Sun, Y., and J. Li, 2003, Time-frequency analysis for plastic landmine detection via forward-looking ground penetrating radar: *Radar, Sonar and Navigation, IEE Proceedings -*, **150**, 253-261.
- Taflove, A., and S. C. Hagness, 2000, *Computational electrodynamics the finite-difference time-domain method*: Artech House.
- Takenaka, T., H. Zhou, and T. Tanaka, 2003, Inverse scattering for a three-dimensional object in the time domain: *Journal of the Optical Society of America a-Optics Image Science and Vision*, **20**, 1867-1874.
- Tarantola, A., 1984a, Inversion of seismic-reflection data in the acoustic approximation: *Geophysics*, **49**, 1259-1266.
- Tarantola, A., 1984b, The seismic reflection inverse problem, in Santosa, F., Pao, Y.-H., Symes, W., and Holland, C.: *Inverse problems of acoustic and elastic waves*: Society for Industrial and Applied Mathematics.
- Tarantola, A., 1986, A strategy for nonlinear elastic inversion of seismic-reflection data: *Geophysics*, **51**, 1893-1903.
- Tarantola, A., 2005, *Inverse problem theory and methods for model parameter estimation*: Society for Industrial and Applied Mathematics.
- Tarantola, A., and B. Valette, 1982, Generalized non-linear inverse problems solved using the least-squares criterion: *Reviews of Geophysics*, **20**, 219-232.
- Topp, G. C., J. L. Davis, and A. P. Annan, 1980, Electromagnetic determination of soil-water content - Measurements in coaxial transmission-lines: *Water Resources Research*, **16**, 574-582.
- Tronicke, J., P. Dietrich, U. Wahlig, and E. Appel, 2002, Integrating surface georadar and crosshole radar tomography: A validation experiment in braided stream deposits: *Geophysics*, **67**, 1516-1523.
- Tronicke, J., and K. Holliger, 2005, Quantitative integration of hydrogeophysical data: Conditional geostatistical simulation for characterizing heterogeneous alluvial aquifers: *Geophysics*, **70**, H1-H10.
- Tronicke, J., K. Holliger, W. Barrash, and M. D. Knoll, 2004, Multivariate analysis of cross-hole georadar velocity and attenuation tomograms for aquifer zonation: *Water Resources Research*, **40**, W01519, doi:01510.01029/02003WR002031.

- Tronicke, J., D. R. Tweeton, P. Dietrich, and E. Appel, 2001, Improved crosshole radar tomography by using direct and reflected arrival times: *Journal of Applied Geophysics*, **47**, 97-105.
- Tura, M. A. C., L. R. Johnson, E. L. Majer, and J. E. Peterson, 1992, Application of diffraction tomography to fracture detection: *Geophysics*, **57**, 245-257.
- Umashankar, K. R., A. Taflove, and B. Beker, 1987, Calculation and experimental validation of induced currents on coupled wires in an arbitrary shaped cavity: *Ieee Transactions on Antennas and Propagation*, **35**, 1248-1257.
- Vasco, D. W., 1991, Bounding seismic velocities using a tomographic method: *Geophysics*, **56**, 472-482.
- Vasco, D. W., and E. L. Majer, 1993, Wavepath travel-time tomography: *Geophysical Journal International*, **115**, 1055-1069.
- Vasco, D. W., J. E. Peterson, and E. L. Majer, 1998, Resolving seismic anisotropy: Sparse matrix methods for geophysical inverse problems: *Geophysics*, **63**, 970-983.
- Wang, Y., 2002, Seismic trace interpolation in the f-x-y domain: *Geophysics*, **67**, 1232-1239.
- Wang, Y. M., and W. C. Chew, 1989, An iterative solution of the two-dimensional electromagnetic inverse scattering problem: *International Journal of Imaging Systems and Technology*, **1**, 100-108.
- Watanabe, T., K. T. Nihei, S. Nakagawa, and L. R. Myer, 2004, Viscoacoustic waveform inversion of transmission data for velocity and attenuation: *Journal of the Acoustical Society of America*, **115**, 3059-3067.
- Wielandt, E., 1987, On the validity of the ray approximation for interpreting delay times: *Seismic tomography with applications in global seismology and exploration geophysics* (ed. Nolet, G.): D. Reidel Publishing Company.
- Williamson, P. R., and R. G. Pratt, 1995, A critical review of acoustic wave modeling procedures in 2.5 dimensions: *Geophysics*, **60**, 591-595.
- Williamson, P. R., and M. H. Worthington, 1993, Resolution limits in ray tomography due to wave behavior - numerical experiments: *Geophysics*, **58**, 727-735.
- Woodward, M. J., 1992, Wave-equation tomography: *Geophysics*, **57**, 15-26.
- Wu, R. S., and M. N. Toksoz, 1987, Diffraction tomography and multisource holography applied to seismic imaging: *Geophysics*, **52**, 11-25.
- Wu, T. T., and R. W. P. King, 1965, Cylindrical antenna with nonreflecting resistive loading: *IEEE Transactions on Antennas and Propagation*, **13**, 369-373.
- Yashiro, K., and S. Ohkawa, 1985, Boundary element method for electromagnetic scattering from cylinders: *IEEE Transactions on Antennas and Propagation*, **33**, 383-390.

- 
- Yee, K. S., 1966, Numerical solution of initial boundary value problems involving Maxwell's equations in isotropic media: *IEEE Transactions on Antennas and Propagation*, **14**, 302-307.
- Yuan, X. J., D. Borup, J. W. Wiskin, M. Berggren, R. Eidsens, and S. A. Johnson, 1997, Formulation and validation of Berenger's PML absorbing boundary for the FDTD simulation of acoustic scattering: *IEEE Transactions on Ultrasonics Ferroelectrics and Frequency Control*, **44**, 816-822.
- Zhou, B., and S. A. Greenhalgh, 1998a, Crosshole acoustic velocity imaging with the full-waveform spectral data: 2.5-D numerical simulations: *Exploration Geophysics*, **29**, 680-684.
- Zhou, B., and S. A. Greenhalgh, 1998b, A damping method for 2.5-D Green's function for arbitrary acoustic media: *Geophysical Journal International*, **144**, 111-120.
- Zhou, B., and S. A. Greenhalgh, 2003, Crosshole seismic inversion with normalized full-waveform amplitude data: *Geophysics*, **68**, 1320-1330.
- Zhou, C. G., and L. B. Liu, 2000, Radar-diffraction tomography using the modified quasi-linear approximation: *IEEE Transactions on Geoscience and Remote Sensing*, **38**, 404-415.
- Zhou, C. X., W. Y. Cai, Y. Luo, G. T. Schuster, and S. Hassanzadeh, 1995, Acoustic wave-equation travel-time and wave-form inversion of crosshole seismic data: *Geophysics*, **60**, 765-773.
- Zhou, C. X., G. T. Schuster, S. Hassanzadeh, and J. M. Harris, 1997, Elastic wave equation travelttime and waveform inversion of crosswell data: *Geophysics*, **62**, 853-868.
- Zhou, H., T. Takenaka, and T. Tanaka, 2003, Three-dimensional reconstruction of a shallowly buried mine using time-domain data: *Microwave and Optical Technology Letters*, **39**, 276-280.





# CURRICULUM VITAE

## PERSONAL DETAILS

**Name:** Ernst, Jacques Robert  
**Address:** Ebnetstrasse 8a  
 8424 Embrach  
 Switzerland  
**Telephone:** +41 44 633 35 66 (office ETH)  
 +41 44 865 42 30 (private)  
**Mobile:** +41 79 655 19 37  
**E-mail:** jack@aug.ig.erdw.ethz.ch  
**Date of birth:** January 10<sup>th</sup>, 1973  
**Nationality:** Swiss



## EDUCATION

**PhD in Geophysics at Swiss Federal Institute of Technology, Zurich (ETH)**

11/02 - 04/07

**Studies in Geophysics at Swiss Federal Institute of Technology, Zurich (ETH)**

10/97 - /04/02

**Studies in Mathematics and Physics at Swiss Federal Institute of Technology, Zurich (ETH)**

10/94 - 10/96

**Matura in mathematical and natural sciences at Kantonschule Zurich-Unterland, Switzerland**

08/89 - 01/94

## EMPLOYMENT HISTORY

**Assistant at ETH**

11/02 04/07

**Scientific Research Assistant at ETH**

04/02 - 10/02

**Assistant at ETH (during studies)**

01/00 - 01/01

**Truck-driver (various companies)**

01/94 - 01/01

**PROFESSIONAL QUALIFICATIONS****COMPUTER SKILLS**

- DOS and MS Windows (9x, NT, 2000, XP) and working knowledge in LINUX and UNIX
- MatLab and Mathematica
- Office applications (MS Office, Corel Graphics, Adobe)
- LaTeX
- Experience with ProMax™ and REFLEX™ (Seismic Data Processing Software)

**PROGRAMMING SKILLS:**

- C, C++
- Pascal
- HTML

**LANGUAGES**

- German      Fluent speaking and writing (native)
- English      Fluent speaking and writing (working knowledge)
- French      Good speaking and writing (but not regularly used)

**CURRENT DETAILS****PRIVATE**

**Name:** Ernst, Jacques Robert  
**Address:** Querstrasse 1  
CH-8424 Embrach  
**Mobile:** +41 79 655 19 37  
**E-mail:** Jacques.Ernst@gmail.com

**BUSINESS**

**Address:** UBS AG  
Investment Bank Switzerland  
Market Risk Control, MCC  
Europastrasse 1  
CH-8152 Opfikon  
**Telephone:** +41 44 239 37 69  
**Fax:** +41 44 239 35 15  
**E-mail:** Jacques.Ernst@ubs.com

## ACKNOWLEDGMENTS

Without the help, contributions and constant encouragement of many special people from within the ETH Institute of Geophysics and from outside ETH, I would not yet be at the end of my dissertation. For this great support, I wish to thank everyone who contributed in one or another way to my success.

First and foremost, I would like to express my gratitude to Prof. Dr. Klaus Holliger for his outstanding supervision. His belief in my abilities, his open ears for my problems and his kindness, in quiet as well as hectic times, remained even after he left ETH, and built a stable foundation for my work. Klaus' remarkable knowledge and experience, his clear and straight-forward way of approaching problems and finding appropriate solutions not only positively influenced my project but also my own working style.

I am particularly grateful to Prof. Dr. Alan Green who took over the supervision of my thesis after Klaus left. His enormous knowledge and his extremely fast way of adapting to new challenges (e.g., the waveform inversion I presented in this thesis) are indeed very impressive and greatly contributed to the quality of my work. Without his patience in reading and re-reading through my manuscripts and continually improving them, they would never have reached the professional language level, sharpness and precision required for publication.

I wish to further express my thanks to Dr. Hansruedi Maurer. He always had good ideas at hand to help me when I was trapped at a dead end. Hansruedi's patience and constant support greatly improved my thesis research. I would also like to thank him for giving me the opportunity to participate in field trips, which were a very welcome change in the everyday life of a theoretician.

During the first year of my PhD studies, I had the chance to visit Prof. Dr. Gerhard Pratt at Queens University in Kingston, Canada. I look upon this trip as a highlight in my education, not only because it was my first long distance trip, but also because of Gerhard's hospitality and generosity in introducing me to his way of performing full-waveform inversions.

I would like to acknowledge several people who considerably helped me in my work. Foremost, I would like to express my sincere thanks to the Asgard/Hreidar cluster group at ETH. They provided me with more computer power than I could ever wish to have access to - well, that's not exactly true, but comes very close to the truth. Inversion of real data using a time-domain full-waveform scheme not only requires a supercomputer but also data. I had the chance to acquire crosshole radar data at the Grimsel Rock Laboratory and would therefore like to thank the people from Nagra who made this survey possible. A second data set was acquired at the Boise Hydrogeophysical Research Site in the US. I would like to thank Prof. Dr. Jens Tronicke, Prof. Dr. Warren Barrash and Prof. Dr. Michael Knoll for sharing their data and providing helpful information.

Working in the AUG group gave me the opportunity to meet many great colleagues and friends. I would like to particularly thank Heinrich Horstmeyer for supporting me whenever I was stuck with a computer problem (yes, it indeed happened!) or with some data processing questions. He also gave me more than once a ride home for which I owe him my sincere gratitude. I would also like to acknowledge Elisabeth Läderach, Chrissy Chatzidis and André Blanchard for the interesting occasional discussions we had and for their administrative assistance whenever it was required.

I wish to especially thank Tom Spillmann, Christian Schmid, Peter Stummer, Bernhard Lampe, Peter Hetely and Constantin Lazari for the good times we had with interesting, challenging and sometimes a bit too philosophical discussions. I'm particularly grateful to Tom, Christian, Peter Hetely and Constantin for being good smoking companions during times when smokers being more and more treated as criminals. Additionally, I would like to thank Anna Kaiser, Fiona Campbell and the rest of the New Zealand field crew for the great times in New Zealand.

I'm deeply indebted to my parents and my sister. Without their constant support, kindness and endless love over the years, I would never have been able to complete my dissertation.

Last but not least, my apologies to all those who I forgot to mention...

Gavin Winsborrow, I will keep you in good memories!